GHENT
UNIVERSITY

FACULTY OF
BIOSCIENCE ENGINEERING

MODEL-BASED ANALYSIS AS A TOOL FOR INTENSIFICATION OF A BIOCATALYTIC PROCESS IN A MICROREACTOR

ir. Timothy Van Daele

Thesis submitted in fulfillment of the requirements for the degree of
Doctor (Ph.D) in Applied Biological Sciences
Academic year 2016-2017

BIOMATH

BIO INTENSE

"De omnibus dubitandum."

René Descartes

*"An expert is a man who has made all the mistakes
which can be made in a very narrow field."*

Niels Bohr

*"Everything should be made as simple as possible,
but not simpler."*

Albert Einstein

Examination Committee: Prof. dr. ir. Nico Boon
Chairman
Center for Microbial Ecology and Technology
Ghent University, Belgium

Prof. dr. ir. Frederik Ronsse
Secretary
Department of Biosystems Engineering
Ghent University, Belgium

Prof. dr. ir. Joris Thybaut
Department of Chemical Engineering
and Technical Chemistry
Ghent University, Belgium

Prof. dr. ir. Kristel Bernaerts
Department of Chemical Engineering (CIT)
KU Leuven, Belgium

dr. Roland Wohlgemuth
Sigma-Aldrich (Merck), Switzerland

Supervisors: Prof. dr. ir. Ingmar Nopens
Department of Mathematical Modelling,
Statistics and Bioinformatics (BIOMATH)
Ghent University, Belgium

Prof. dr. ir. Krist V. Gernaey
Department of Chemical and Biochemical Engineering
DTU, Denmark

Dean: Prof. dr. ir. Marc Van Meirvenne

Rector: Prof. dr. Anne De Paepe

ir. Timothy Van Daele

Model-based analysis as a tool for intensification of a biocatalytic process in a microreactor

Thesis submitted in fulfillment of the requirements for the degree of

Doctor (Ph.D) in Applied Biological Sciences

Academic year 2016-2017

Dutch translation of the title:
Modelgebaseerde analyse als hulpmiddel voor de intensificatie van een biokatalytisch proces in een microreactor

Please refer to this work as follows:
Timothy Van Daele (**2016**). *Model-based analysis as a tool for intensification of a biocatalytic process in a microreactor*, PhD Thesis, Department of Mathematical Modelling, Statistics and Bioinformatics, Ghent University, Ghent, Belgium.

ISBN 978-90-5989-953-7

DANKWOORD

Het is alweer een dikke vier jaar geleden dat ik besloot om een doctoraat te starten bij BIOMATH. Gedurende die vier jaar vol hindernissen, leerde ik meerdere "partners in crime" kennen die me hielpen om het parcours succesvol af te leggen. In dat opzicht wil ik allereerst Ingmar bedanken voor de opportuniteit die hij mij toen geboden heeft. Ingmar steunde ten allen tijde de inspanningen die ik deed en gaf daartoe ook de nodige vrijheden/mogelijkheden. Tevens wil ik ook mijn co-promotor Krist bedanken voor de vele interessante gesprekken die we gevoerd hebben :-). Je was er al van in het begin bij betrokken, maar ik leerde je pas echt kennen tijdens de BIOPRO World Talent Campus in 2013. Deze cursus was echt een geweldige sociale en wetenschappelijke ervaring.

Naast mijn promotoren waren er natuurlijk ook vele collega's die ik beter heb leren kennen. Stijn en Joris, ik ben de laatste van de eerste generatie "Pythoneers" in het simulatielab, maar jullie niveau van kennis, inzet, behulpzaamheid,... in Python zal ik niet snel bereiken. Stijn, ook bedankt om de voorbije jaren te fungeren als mijn persoonlijk klankbord ("my personal post-doc") en mij te ondersteunen in mijn wetenschappelijke zoektocht. Je stond altijd klaar om problemen mee op te lossen, ook al moest je je eigen werk daarvoor laten liggen. I would also like to thank my thesis students for the nice work they have performed. Daan and David, thanks for the outstanding work you have done in your master theses and within the Biointense project. Voor de meer sociale activiteiten waren de BIOMATH weekends zeker geniaal, maar zonder de meer frequente sociale activiteiten, was ik die vier jaar niet doorgekomen. Niels, merci voor het sociale luik, maar ook om de voorbije jaren mijn badmintonskills aan te scherpen. Tinne, merci voor de lekkere dessertjes gedurende de voorbije jaren, maar sinds de "chocomousse battle" weet je dat er kapers op de kust zijn :-). Al wat langer geleden: Katrijn bedankt om mij tijdens de allereerste Biointense meeting in 2012 te vergezellen en mij op mijn gemak te stellen :-). José ("el mexicano"), ik vind het echt knap dat je altijd probeert om Nederlands te praten met de "locals". Blijf zo voort doen ;-) Natuurlijk zijn er nog vele andere collega's waar ik leuke en blijvende herinneringen aan heb, dus aan allen die ik hier nog niet expliciet vermeld heb (zoals bierbrouwende Wouter, Aziatische Michael, botsende Sophie,...) : Merci!/Thank you!

Magali, Marjolein, Caroline, Sanne en Robin (AKA de In-Gent-Blijvers), merci voor de leuke bijeenkomsten de voorbije jaren. Samen eens stoom aflaten, het deed me veel deugd en liet me ook toe de dingen wat te relativeren. Daarnaast waren de weekends met de Antwerpse bio-ingenieurs natuurlijk ook altijd een fijne uitlaatklep en een goed moment om elkaar terug te zien. De vrienden van Land en Water (Brecht, Niels, Sacha en Jeroen) mag ik zeker niet vergeten! Altijd fijn om de meer nerdy toer op te gaan :-). Ik hoop dat ik na deze hectische periode terug wat meer tijd heb om weer wat sociale activiteiten mee te pikken^^.

Last but not least: de familie. Eerst en vooral wil ik mijn ouders bedanken voor de mogelijkheden die ze me geboden hebben, maar ook voor de ondersteuning in de moeilijkere momenten. Cassandra, ik vond het tof dat je de voorbije jaren met mij wilde tennissen in de dubbel gemengd reeks. Merci voor de gevatte opmerkingen, maar ook om mij met rust te laten als het daar "niet het moment voor was...". Daarnaast wil ik ook mijn Bomma en Bompa en de rest van de familie bedanken voor hun belangstelling in de "bio-dinges". Ik hoop dat het voor jullie tijdens de verdediging duidelijk zal worden wat ik de voorbije jaren heb uitgestoken :-).

Timothy
Gent, December 2016

SUMMARY

Chiral amines are highly valuable functionalised molecules which play an important role in the pharmaceutical, agrochemical and chemical industry. Nowadays, the asymmetric pathway, which is catalysed by ω-transaminase, receives a lot of attention in order to produce these optically active molecules. However, the pathway generally suffers from low productivity and thus must be intensified to meet industrial requirements. To evaluate potential intensification strategies in an efficient and fast way, microreactors can be used since they provide an ideal screening platform which can also be used for production by a so-called scaling-out. To limit the required experimental effort, mathematical models can be used. In this dissertation two types of mathematical models are used, i.e. kinetic and computational fluid dynamic (CFD) models. On the one hand, the kinetic model is used to characterise the kinetic behaviour of the enzyme, which makes it possible to optimise the process conditions or to determine its performance compared to other enzymes. On the other hand, CFD models provide insight into the mass transfer processes, and are used to identify conditions where mass transfer limitations drastically reduce the overall productivity. These models are used to gather process knowledge, and indicate which intensification strategies will prove more successful.

The first part of the dissertation deals with the kinetic characterisation of the ω-transaminase under study. The kinetic behaviour of the enzyme can be represented by the plain ping-pong bi-bi model. The kinetic parameters need to be estimated from experimental data before such a model can be used for any process analysis. Since every kinetic parameter has a physical or chemical meaning, it should have one unique and physically realistic value. When a multitude of parameter values yield the same model output, it is impossible to know which combination is the true one. However, this important feature does in many cases hold true, but should be verified when performing a parameter estimation. This type of problem is often related with poor model structures, overparameterised models or non-informative

data, but can be detected by using a so-called identifiability analysis. First, a structural identifiability analysis is performed to determine whether it is possible to retrieve the real parameter values when perfect and unlimited data are available. Second, a practical identifiability analysis is performed to assess whether the parameters can still be retrieved when only a limited amount of noise-corrupted data are available. In this respect, a numerical identifiability method is developed to assess both types of identifiabilities. The application of this numerical identifiability method yielded that the plain ping-pong bi-bi model is (at least locally) structurally identifiable. However, for the parameter values found in literature, it is found that not all the parameters are practically identifiable, which indicates that the experiments conducted to estimate those parameters are not sufficiently informative. Moreover, it is shown that the parameters are only practically identifiable for low measurement errors. The results of the numerical identifiability confirm that a proper parameter estimation should always be followed by an estimation of the parameter estimate uncertainties.

Since the plain ping-pong bi-bi model is found to be (at least locally) structurally identifiable, a parameter estimation can be performed. In this respect, it is chosen to use a model-based optimal experimental design. The aim of such a design approach is to reduce the total experimental effort by proposing highly informative experiments. However, for nonlinear models like the plain ping-pong bi-bi model, proposing an optimal experimental design is a nontrivial task. Such an experimental design is highly dependent on the intrinsic (i.e. “real”) values of the kinetic parameters, but since these kinetic parameter values are *a priori* unknown, it is impossible to propose an optimal design. To overcome this problem, an iterative approach is required to estimate the kinetic parameter values. First, some experiments are performed in real-life. This additional experimental information is used to update the current model parameters, and afterwards used to propose new experiments. However, the current experimental design is still highly dependent on the current parameter values, and thus a more advanced design method is required. By using a so-called iterative robust model-based optimal experimental design method, more robust experimental designs are proposed which are suitable for a range of parameter values instead of only one specific value. It is shown that by using such an iterative experimental design approach, the parameters can be estimated more accurately compared to a standard uniform design where the collected information is not used to optimise the experimental design. By applying this methodology, the plain ping-pong bi-bi model is properly calibrated and found to be practically identifiable.

To ensure that the calibrated parameter values represent the intrinsic parameter values, the measurements of such a parameter estimation exercise need to be conducted at conditions where there are no mass transfer limitations. This is an important condition, since this will determine whether microreactors can be successfully used as a screening device for biocatalytic reactions. For simple reactions and microreactor geometries, the mass transfer limitations can be easily calculated using dimensionless numbers. However, the ping-pong bi-bi reaction under study is more complex and thus these dimensionless numbers will only yield qualitative measures (i.e. high, medium, low). Moreover, these dimensionless numbers are only applicable for simple microreactor geometries, and thus the mass transfer limitations cannot be assessed for more complex microreactor geometries yet. To overcome this problem, a generic methodology is developed which is applicable for any kinetic model and microreactor geometry. For two simple microreactor configurations, this generic methodology is applied and its results coincide with those of the traditional approach of dimensionless numbers. These observations confirm that the generic methodology is valid and can be used to calculate productivity decreases due to these mass transfer limitations. The general applicability makes the method superior to the use of dimensionless numbers.

As stated above, kinetic parameters are typically estimated under the absence of any mass transfer limitations or at least this assumption is made. To achieve these so-called kinetically limited conditions in batch reactors, mixing is typically increased until no further improvement is seen with respect to the reactor productivity. However, the increase of the shear stresses can lead to the denaturation of the enzyme, which would yield a decrease in the reactor productivity. Moreover, increasing the mixing rate is not straightforward in microreactors and other solutions need to be found. In this respect, the aim of the final part of this dissertation is to investigate whether it is possible to calibrate kinetic parameters under mass transfer limited conditions. For a simple, irreversible enzymatic reaction it is proven that the parameter values can be estimated properly as long as the mass transfer limitations are not too severe. However, the quality of the parameter estimate is strongly related with the experimental conditions (e.g. the measurement error) and design (e.g. the measurement time). These observations indicate that a proper experimental design remains important to perform a parameter estimation under mass transfer limiting conditions. To optimise the experimental design, the Fisher information matrix is often used for kinetic models. For the coupled CFD-kinetic model, the Fisher information matrix showed good correspondence with the "exact" confidence interval, which is sampled directly from the objective function.

The main outcome of this dissertation is the indepth knowledge which was gained about the model calibration of biocatalytic processes and mass transfer limitations. Moreover, this dissertation led to a new generic methodology to assess mass transfer limitations in a (micro)reactor, but it was also illustrated that it is possible to calibrate of kinetic parameters under mass transfer limited conditions. The results of this dissertation will help future researcher to speed up both the enzyme characterisation and reactor development. These two factors are considered crucial with respect to the reduction of the lab-to-market time.

SAMENVATTING

Chirale amines zijn waardevolle, functionele moleculen die belangrijk zijn voor de farmaceutische, agrochemische en chemische industrie. Om deze optisch actieve moleculen te produceren, wordt de asymmetrische *pathway*, welke gekatalyseerd wordt door ω-transaminase, momenteel uitvoerig bestudeerd. Deze *pathway* heeft echter een lage productiviteit en dient geïntensifieerd te worden om te voldoen aan de industriële vereisten. Om de verschillende intensifieringstrategiën op een snelle en efficiënte manier te evalueren, worden typisch microreactoren gebruikt omdat deze een ideaal onderzoeksplatform bieden, dat tevens gebruikt kan worden voor de productie door een zogenaamde *scaling-out*. De totale experimentele inspanning dient echter haalbaar te zijn, maar kan beperkt worden door beroep te doen op wiskundige modellen. In deze thesis zullen twee types van wiskundige modellen gebruikt worden. Enerzijds de kinetische modellen die gebruikt worden om de kinetische karakteristieken van een enzym te achterhalen. Deze karakteristieken kunnen nadien gebruikt worden om de procescondities te optimaliseren of om de performantie met andere enzymen te vergelijken. Anderzijds zijn er de numerieke stromingsleermodellen die inzicht bieden in de massatransportprocessen en gebruikt worden om te identificeren wanneer de productiviteit gelimiteerd wordt door een (te) beperkt massatransport. Het gebruik van beide modeltypes laat toe om kennis op te bouwen, maar ook om te kijken welke intensifieringstrategiën mogelijks succesvol kunnen zijn.

In het eerste deel van deze thesis wordt de kinetische karakterisatie van ω-transaminase bestudeerd. Het kinetische gedrag van dit enzym kan worden voorgesteld door het zogenaamde ping-pong bi-bi model. De kinetische modelparameters dienen geschat te worden met behulp van experimentele data vooraleer het model effectief gebruikt kan worden voor enige procesanalyse. Tevens heeft elke kinetische parameter ook een kinetische of chemische betekenis en dus dient het ook een unieke en fysisch realistische waarde te verkrijgen. Deze belangrijke eigenschap is geldig in meeste gevallen, maar dient gevalideerd te worden bij het uitvoeren van

een parameterschatting. Indien een hele verzameling parameterwaarden éénzelfde modelvoorspelling oplevert, wordt het onmogelijk om de correcte parameterwaarde te selecteren. In zulke gevallen is het model vaak overgeparametriseerd, betreft het een gebrekkige modelstructuur of is the data niet voldoende informatief. Om deze modeldeficiënties te achterhalen, wordt een zogenaamde identificeerbaarheidsanalyse uitgevoerd. Allereerst wordt een structurele identificeerbaarheidsanalyse uitgevoerd om te detecteren of het mogelijk is om the reëele parameterwaarden te achterhalen wanneer er een oneindige hoeveelheid perfecte data beschikbaar is. Ten tweede wordt een praktische identificeerbaarheidsanalyse uitgevoerd om te achterhalen of het nog steeds mogelijk is de parameterwaarden te achterhalen wanneer er slechts een beperkte hoeveelheid onzekere data beschikbaar is. Om beide identificeerbaarheidsanalyses uit te voeren, is er in deze thesis een numerieke identificeerbaarheidsmethode ontwikkeld. De toepassing van deze methode leidt tot de conclusie dat het ping-pong bi-bi model (ten minste lokaal) structureel identificeerbaar is. Echter voor de parameterwaarden uit de literatuur blijkt dat niet alle parameters praktisch identificeerbaar zijn, wat erop duidt dat de experimenten niet voldoende informatief waren om deze waarden ook effectief te schatten. Bovendien wordt ook getoond dat de overige parameters enkel praktisch zijn bij een lage meetonzekerheid. De resultaten van de numerieke identificeerbaarheidsmethode bevestigen dat een degelijke parameterschatting altijd gevolgd moet worden door een schatting van de parameteronzekerheden.

Aangezien het ping-pong bi-bi model (ten minste lokaal) structureel identificeerbaar is, kan een parameterschatting uitgevoerd worden. Om dit te realiseren, wordt gebruik gemaakt van een modelgebaseerd optimaal experimenteel ontwerp. Het doel van zulk ontwerp is om de totale experimentele inspanning te reduceren door enkel hoog informatieve metingen te ontwerpen en uit te voeren. Echter, het berekenen van een optimaal experimenteel ontwerp is niet triviaal voor niet-lineaire modellen zoals het ping-pong bi-bi model. Een experimenteel ontwerp is voor zulke modellen zeer afhankelijk van de intrinsieke parameterwaarden, maar deze parameterwaarden zijn initieel onbekend zodat het onmogelijk is om een geschikt optimaal experimenteel ontwerp voor te stellen. Om dit probleem te omzeilen, is een iteratieve procedure vereist om de parameterwaarden te schatten. Allereerst dienen enkele experimenten uitgevoerd te worden. Deze experimentele data kan nadien gebruikt worden om de huidige parameterwaarden te updaten. Deze verbeterde informatie kan vervolgens gebruikt worden om terug enkele (meer informatieve) experimenten voor te stellen. Aangezien deze experimentele ontwerpen nog steeds sterk afhankelijk zijn van de huidige parameterwaarden, dient een meer geavanceerde ontwerpmethode gebruikt te worden. Door gebruik te maken van zogenaamde robuuste modelgebaseerde optimale experimentele ontwerpmethoden, kunnen meer robuuste experimentele ontwerpen voorgesteld worden die geschikt zijn voor een groot bereik aan parameterwaarden in plaats van slechts één specifieke parameterwaarde. Het gebruik van zulke iteratieve experimentele ontwerpmethode die ook robuust is, kunnen meer accurate parameterschattingen bekomen worden in vergelijking met een standaard uniform ontwerp waar de vergaarde informatie niet gebruikt wordt om het experimenteel ontwerp te optimaliseren. De toepassing van deze methode leidt tot een degelijk gecalibreerd ping-pong bi-bi model dat tevens praktisch identificeerbaar is.

Om te garanderen dat de geschatte parameterwaarden de intrinsieke parameterwaarden voorstellen, moeten de metingen voor zulke parmaterschatting gebeuren onder condities waar massatransport geen limitatie vormt. Dit is een belangrijke voorwaarde, aangezien dit bepaalt of microreactoren geschikt zijn als onderzoeksplatform voor biokatalytische reacties. Voor eenvoudige reacties en microreactor geometriën kunnen de massatransportlimitaties al eenvoudig berekend worden met behulp van dimensieloze getallen. Het ping-pong bi-bi model is echter complexer en dus kunnen deze dimensieloze getalllen enkel gebruikt worden om een kwalitatieve schatting te maken. Bovendien zijn deze dimensieloze getallen enkel toepasbaar voor zeer eenvoudige microreactor geometriën en dus kunnen massatransportlimitaties niet exact bepaald worden voor meer complexe reactoren. Om deze problemen het hoofd te bieden, wordt een generieke methode ontwikkeld die toepasbaar is voor elk kinetische model en microreactor geometrie. Deze generieke methodologie wordt toegepast voor twee eenvoudige microreactor configuraties en levert dezelfde resultaten op als de traditionele aanpak met behulp van dimensieloze getallen. Dit bevestigt dat de generieke methode geschikt is om productiviteitsdalingen ten gevolge van massatransport limitaties te berekenen. De algemene toepasbaarheid van de generieke methode maakt deze superieur tegenover het gebruik van dimensieloze getallen.

Zoals eerder gesteld worden kinetische parameters typisch geschat in de afwezigheid van massatransport limitaties of dit wordt toch verondersteld. Om zogenaamde kinetisch gelimiteerde condities te verkrijgen in *batch* reactoren, wordt typisch de mengsnelheid verhoogd tot er geen verdere verbetering wordt opgemerkt qua productiviteit. Dit leidt tot een toename van de schuifspanningen die aanleiding kunnen geven tot de denaturatie van het enzym. Bovendien is het niet voor de hand liggend om de mengsnelheid te verhogen in een microreactor en dus dienen andere oplossingen gezocht te worden. In het laatste deel van deze thesis wordt onderzocht of het mogelijk is om de kinetische parameters te schatten onder massatransport gelimiteerde condities. Voor een eenvoudige, irreversibele enzymatische reactie kan aangetoond worden dat de parameterwaarden kunnen worden geschat zolang de massatransportlimitaties niet onredelijk hoog zijn. Echter, de kwaliteit van de parameterschattingen is sterk gerelateerd met de experimentele condities (bijv. de meetonzekerheid) en het ontwerp (bijv. het meettijdstip). Deze observaties tonen aan dat een degelijk experimenteel ontwerp belangrijk blijft om een degelijke parameterschatting uit te voeren onder massatransport gelimiteerde condities. Om het experimenteel ontwerp van kinetische modellen te optimaliseren wordt vaak de Fisher informatie matrix gebruikt. Voor het gekoppelde CFD-kinetisch model toont de Fisher informatie matrix een goede overeenkomst met het “exacte” betrouwbaarheidsinterval dat rechtstreeks verkregen is van de objectieffunctie.

CONTENTS

LIST OF ABBREVIATIONS

ACE	acetone
α-TA	α-transaminase
BA	benzylacetone
CFD	computational fluid dynamics
CI	confidence interval
DOF	degree of freedom
HPLC	high-performance liquid chromatography
IPA	isopropylamine
LSA	local sensitivity analysis
MPPA	1-methyl-3-phenylpropylamine
ODE	ordinary differential equation
OED	optimal experimental design
ω-TA	ω-transaminase
SD	standard deviation
SSE	sum of squared errors

TA	transaminase
WSSE	weighted sum of squared errors

LIST OF SYMBOLS

Symbol	Description	Unit
D	diffusion coefficient solute	m^2/s
$\mathrm{Da_{II}}$	second Damköhler number	–
D_{E}	diffusion coefficient enzyme	m^2/s
ΔG	change in Gibbs free energy	kJ/mol
d_{H}	hydraulic diameter microreactor	m
$\mathbf{D}$	dispersion coefficient	m^2/s
$[E]$	enzyme concentration	g/L
$\mathbf{FIM}$	Fisher Information matrix	
F_{S}	flow of substrate S	mol/L
H	microreactor height	m
$\mathbf{H}$	Hessian matrix	
J	objective function	
K	thermodynamic equilibrium constant	
K_{ACE}	Michaelis constant $[ACE]$	mM
K_{BA}	Michaelis constant $[BA]$	mM
k_{cat}	second-order kinetic constant	L/(g s)
K_{eq}	equilibrium constant	–
k_{f}	forward kinetic constant	$L/(g \cdot s)$
K_{ia}	dissociation constant $E + A <=> EA$	mM
K_{iIPA}	dissociation constant $E + IPA <=> E\,IPA$	mM
K_{iMPPA}	dissociation constant $F\,MPPA <=> F + MPPA$	mM
K_{IPA}	Michaelis constant $[IPA]$	mM

Symbol	Description	Unit
K_{iq}	dissociation constant $FQ <=> E + Q$	mM
K_m	Michaelis constant	mM
K_{m_A}	Michaelis constant $[A]$	mM
K_{m_B}	Michaelis constant $[B]$	mM
K_{m_P}	Michaelis constant $[P]$	mM
K_{MPPA}	Michaelis constant $[MPPA]$	mM
K_{m_Q}	Michaelis constant $[Q]$	mM
Kn	Knudsen number	
k_r	backward kinetic constant	$L/(g \cdot s)$
L	microreactor length	m
λ_{IM}	intermolecular length between the fluid molecules	m
λ_M	molecular mean free path length	m
$lb_{[P]}$	lower bound measurement error	mM
l_{char}	characteristic length	m
Ma	Mach number	
$\mathbf{\Sigma}$	measurement error covariance matrix	
μ	dynamic viscosity	Pa s
N	number of samples	
n_{enzyme}	total amount of enzyme	g
$[P]$	concentration of product P	mM
P	number of parameters	
p	rho-normalised pressure	m^2/s^2
Pe	Péclet number	–
Pe_{2D}	two-dimensional Péclet number	–
$\mathbf{\Phi}$	parameter estimates error covariance matrix	
pK_a	logarithmic acid dissociation constant	–
$\mathbf{Q}$	weight matrix	
R	universal gas constant	8.31 J/(molK)
RD	relative difference [%] between $[P]_{out,PF}$ and $[P]_{out,CFD}$	–
Re	Reynolds number	–
ρ	density of the fluid	kg/m^3

Symbol	Description	Unit
r_{max}	maximum reaction rate	mM/s
r_{S}	substrate consumption rate	mM/s
$[S]$	concentration of substrate S	mM
σ_{rel}	relative standard deviation measurements	–
$[S]_{\mathrm{in}}$	inlet concentration of substrate S	mM
T	temperature	K
t	time	min
τ	residence time	min
τ_{mod}	modified residence time (Walter et al., 2005)	min
TC	total conversion	–
$\boldsymbol{\Theta}$	parameter space	
$\boldsymbol{\theta}$	parameter set	
$\mathbf{u}$	velocity vector	m/s
$\mathbf{u}_{\mathrm{sound}}$	velocity of the sound waves in the fluidum	m/s
u_{x}	fluid velocity in x-direction	m/s
V_{f}	maximum forward reaction rate	nmol/(Umin)
V_{max}	maximum reaction rate	mM/s
V_{r}	maximum backward reaction rate	nmol/(Umin)
W	width of the microreactor	m
x	average displacement of a Brownian particle	m
$\boldsymbol{\psi}$	independent variables	
$\boldsymbol{\Psi}$	design space	
$\mathbf{y}$	measurements	
$\hat{\mathbf{y}}$	measurable model outputs	

LIST OF FIGURES

LIST OF TABLES

CHAPTER 1

PROBLEM STATEMENT, RESEARCH OBJECTIVES AND OUTLINE

1.1 Introduction

Chiral amines are highly valuable functionalised molecules which play an important role in the pharmaceutical, agrochemical and chemical industry (Nugent and El-Shazly, 2010; Turner and Truppo, 2010; Schätzle et al., 2011). These optically active molecules are frequently used for the synthesis of biologically active compounds such as drugs, for which some examples are given in Figure 1.1. It is estimated that about 40 % of all pharmaceuticals contain a chiral amine component (Ghislieri and Turner, 2014). Despite its importance for these industries, the production of optically pure chiral amines remains challenging (Nugent and El-Shazly, 2010) and thus the pharmaceutical industry has identified its sustainable production as a key research priority (Constable et al., 2007; Green et al., 2014). Currently, the major (chemical) route for producing optically pure amines still consists of the resolution of racemates by crystallisation of diastereomeric salts (Breuer et al., 2004; Höhne and Bornscheuer, 2009). However, the chemical pathways to produce these molecules in many cases require specialised equipment, multiple steps and purifications, and rare metal catalysts and can thus be regarded as expensive and inefficient (Hansen et al., 2005; Savile et al., 2010; Dunn, 2012).

Another approach is to use enzymes to produce the chiral amines. Various enzymatic routes exist which can be used for its synthesis using transferases, hydrolases or oxidoreductases (Höhne and Bornscheuer, 2009; Schätzle et al., 2011). All

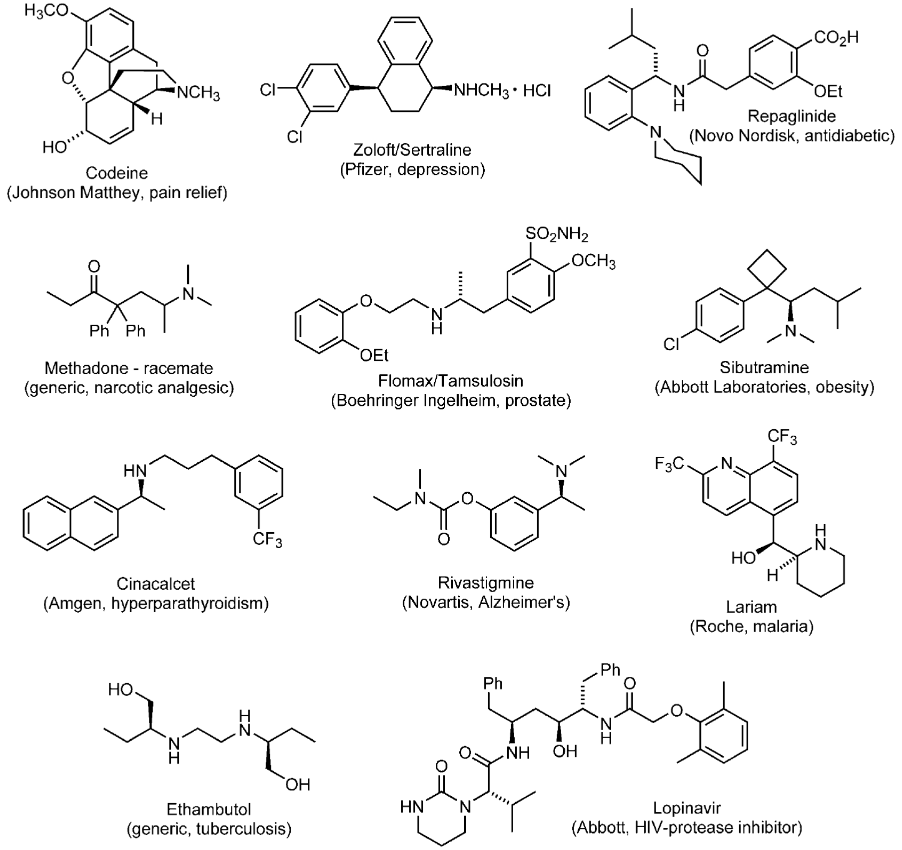

Figure 1.1: Examples of non-amino based chiral amine pharmaceutical drugs (Nugent and El-Shazly, 2010).

routes have their advantages and disadvantages, but only by using ω-transaminases (ω-TAs) and the asymmetric synthesis route optically active amines (or β-amino acids) can be synthesised directly from prostereogenic ketones with a theoretically quantitative yield (Höhne and Bornscheuer, 2009). ω-TAs represent a subgroup of TAs (EC 2.6.1.18), which in contrast to α-TAs do not require the presence of a carboxylic acid group in the α position to the keto or amine functionality, and thus are more useful since they in principle accept any ketone or amine (Höhne and Bornscheuer, 2009). The asymmetric synthesis offers some advantages, i.e. the possible theoretical yield of 100 %, the use of a prochiral substrate, and the product enantiomeric excess which is independent from the conversion (Höhne and Bornscheuer, 2009). In some cases, industry has already successfully switched from a chemical to a biocatalytic pathway, e.g. Merck and Codexis now produce sitagliptin (i.e. a medicine for the treatment of type II diabetes) by using the asymmetric synthesis using ω-TA. In this way they were able to increase the overall yield by 10 %, realise a 53 % increase in productivity (kg/L), reduce the total waste by 19 %, eliminate all heavy metals, and reduce the total manufacturing cost (Savile et al., 2010). This real-life example shows that shifting to ω-TAs for the production of chiral amines can be advantageous. However the use of asymmetric synthesis also has some drawbacks. First, the synthesis suffers from an unfavourable thermodynamical equilibrium, and thus the equilibrium has to be shifted to reach a high conversion. Second, the enzyme suffers from product and substrate inhibition, which makes it difficult to achieve economically viable product concentrations. To overcome these different process challenges, Tufvesson et al. (2011) described possible strategies to make such an enzymatic process economically interesting. However, the authors stated that there is a need for the development of platform technologies to facilitate implementation and shortening of development times. In this respect, microreactors are an interesting candidate for building such a platform. Indeed, microreactors typically have dimensions smaller than 1 mm, which allows to reduce mass transfer limitations inside the reactor. Other interesting features of microreactors are the high surface-to-volume ratio, the continuous operation, and the limited need for chemicals. These advantages make microreactors the ideal platform for the rapid screening of biocatalysts and the assessment of different experimental conditions at a limited cost (Kerby et al., 2006; Tišma et al., 2009). Moreover, the development time from lab to industrial scale can be drastically decreased by using microreactors (Asano et al., 2010). The conventional batch method requires a number of scale-up processes from the R&D phase, through pilot plants, to full-scale production (Figure 1.2). The scale-up approach generally has two drawbacks. First, the process efficiency is generally decreased in large scale reactors (Tufvesson et al., 2010). Second, the stepwise scaling procedure is time-consuming and thus the time to market is increased (Plumb, 2005; Marques and Fernandes, 2011). These problems can be overcome by using the numbering-up strategy (Figure 1.2), in which the production is increased by using multiple microreactors in parallel. Since the original development was already performed in these microreactors, scale-up costs can be eliminated.

Within the BIOINTENSE project, the expertise of both biocatalysis and microtechnology was brought together in order to address the challenges of low productivity and process intensification. The BIOINTENSE project was supported by the European Union as a FP7 project (Grant Agreement Number 312148).

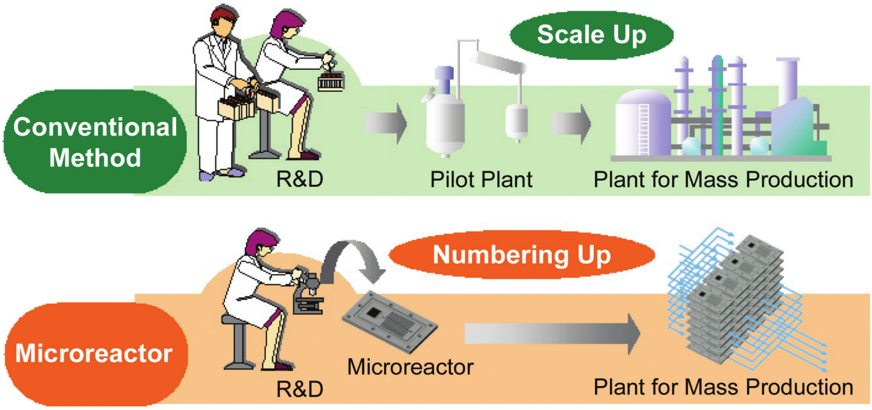

Figure 1.2: Processes from R&D to plant construction using the conventional batch method and a microreactor (Asano et al., 2010).

1.2 Problem Statement

The aim of combining biocatalysis and microreactors, is to overcome low productivity and improve process intensity which frequently hampers the implementation of bioprocesses in industry. In practice this proves to be more difficult than it sounds. In this dissertation, ω-TA is selected as the biocatalyst of interest since it is promising with respect to the production of chiral amines. To overcome low productivity of the asymmetric synthesis, the enzyme structure and process design and operation need to be optimised. In this dissertation, the focus will be on the use of mathematical modelling and techniques to characterise enzymes, calibrate overparameterised models, optimise process conditions but also to gather more fundamental knowledge.

1.3 Research objectives

To overcome the problem of low productivity commonly encountered with the asymmetric synthesis, three main objectives are formulated:

1. estimate the intrinsic parameter values describing the conversion by ω-TA in an efficient and reliable way,
2. gain fundamental knowledge about the productivity improvements of enzymes in microreactors,

3. determine whether intrinsic parameter values can be estimated properly under mass transfer limited conditions.

These three research objectives need to be met in order to get a more fundamental understanding and allow a thorough (model-based) process optimisation. Therefore, these objectives need to be translated to more detailed research questions which will be answered throughout this dissertation.

1.4 Research questions

The research objectives introduced above can be translated in four detailed research questions:

RQ 1. Is the ping-pong bi-bi model identifiable?

The ping-pong bi-bi model is generally considered as the appropriate model to describe the asymmetric synthesis by ω-TA. However, the quasi steady-state equation of the plain ping-pong bi-bi model contains 8 parameters which need to be estimated from limited experimental data. First, it needs to be verified whether it is possible to properly estimate the kinetic parameter values when unlimited, noise-free data are available. This ideal approach is often referred to as theoretical identifiability. In practice, only a limited amount of noise-corrupted data are available which can be used to perform a parameter estimation. Depending on the level of noise and amount of data, the parameters will (not) be practically identifiable. The identifiability problem is important, since it allows to determine whether the obtained parameter values, which represent the kinetic characteristics of the enzyme, can be uniquely determined given a certain set of experimental data.

Can the uncertainty of kinetic parameter estimates be reduced by optimising the experimental design?

As stated in research question 1 (RQ 1), the kinetic parameter values need to be estimated from the kinetic data. In that respect, both a high information content and a low noise level are important to yield qualitative data for parameter estimation. In other words, the information content of the data needs to be sufficiently high to acquire accurate parameter estimates, e.g. when one wants to gain knowledge about the maximum reaction rate of an enzyme, it makes no sense to perform measurements at low substrate concentrations. Mathematically, this can be represented by the Fisher Information Matrix which allows to quantify the level of available information and parameter estimate uncertainties. In most literature, this kind of approach is performed *in silico*, but in this dissertation the aim is to use Fisher Information Matrix as a guidance to design real-life, informative lab experiments. In this way, it may be possible to obtain more accurate parameter estimates for a similar experimental cost.

RQ 3. How can mass transfer limitations be quantified in (complex) microreactors?

To assess mass transfer limitations, dimensionless numbers are still frequently used, e.g. the second Damköhler number, which represents the ratio between the reaction rate and diffusion rate, is often used to determine whether a microreactor suffers from mass transfer limitations or not. However, these dimensionless numbers have a very limited range of applicability, i.e. only for simple reactor configurations. This is why currently no assessment of the mass transfer limitations can be done for more complex reactor configurations. The aim is to develop a generic methodology which allows to quantify the mass transfer limitations for any microreactor configuration. Moreover, an accurate quantification of the mass transfer limitations allows to estimate the reduction in enzymatic productivity.

RQ 4. Is it possible to (properly) estimate kinetic parameters under mass transfer limited conditions?

In most of the literature, it is stated that mass transfer limitations need to be eliminated in order to properly estimate the kinetic parameter values. When using mass transfer limited data, the parameter estimates will not reflect the "real" parameter values. In some older literature, derivations are presented which predict the "apparent" parameter value in function of the "real" parameter value and the level of mass transfer limitation. However, the question arises whether it is also possible to do this exercise the other way around since this is what would happen in reality. Moreover, such an exercise was not yet performed for noise-corrupted, mass transfer limited data. Therefore, the reliability of the "real" parameter value will always be assessed and it will be determined whether it is possible to optimise the experimental conditions to improve the parameter reliability.

1.5 Roadmap through this dissertation

In **chapter 2**, some basic modelling concepts like parameter estimation and local sensitivity analysis are introduced. In order to analyse the kinetic models, a Python package is developed and introduced. In **chapter 3**, the ping-pong bi-bi model is introduced and its theoretical and practical identifiability is analysed using a numerical method.

In **chapter 4**, the ping-pong bi-bi model is introduced which describes the conversion of isopropylamine and benzylacetone to (S)-4-phenyl-2-butylamine and acetone by a wild type variant of ω-TA. The parameters of the model are calibrated using robust model-based optimal experimental design (rMbOED). The use of this methodology allows to propose design experiments which are highly informative, and thus reduce the overall experimental effort.

In **chapter 5**, the flow and convection-diffusion-reaction equations are simulated for different microreactor geometries using the computational fluid dynamics (CFD) library OpenFOAM. The results of these simulations are used to determine the level of mass transfer limitations by comparing them with ideal plug flow models. To ensure that the developed methodology is correct, the results are compared with the traditional approach of dimensionless numbers.

In **chapter 6**, the aim is to properly estimate the intrinsic kinetic parameters under mass transfer limited conditions. It can thus be regarded as a continuation of chapters 4 & 5, since it combines parameter estimation/uncertainty, practical identifiability and experimental design (chapter 4) with the effect of mass transfer limitations (chapter 5).

Finally, the conclusions and suggestions for future research are formulated in **chapter 7**. To structure the conclusions section, the research questions formulated above will be used and answered.

An overview of the roadmap through this dissertation is given in Figure 1.3.

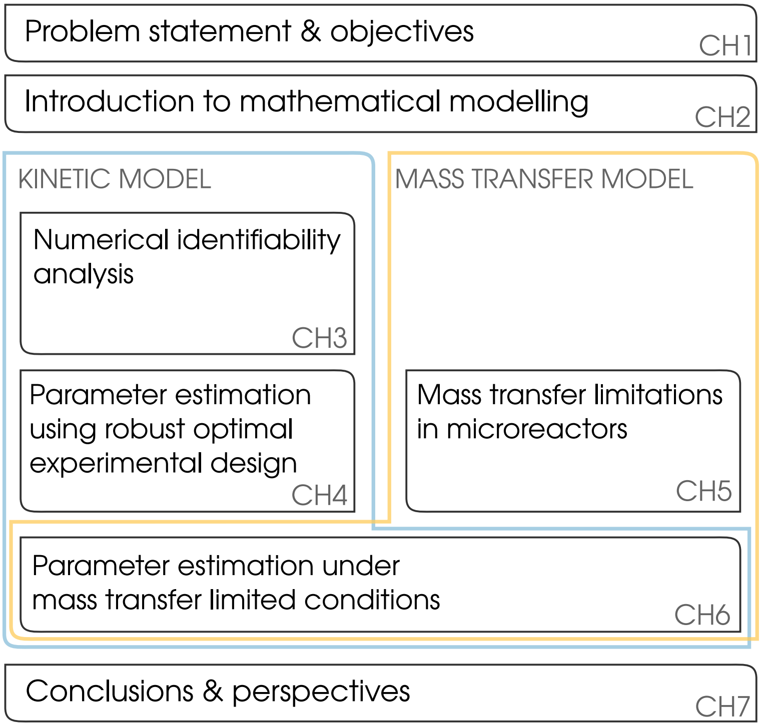

Figure 1.3: Roadmap through this dissertation.

CHAPTER 2

INTRODUCTION TO MATHEMATICAL MODELLING OF KINETICS AND MICROREACTORS

Partially redrafted from

Van Daele, T., Van Hoey, S., Nopens, I. (2015) pyIDEAS: an open source Python package for model analysis, *Comput Aided Chem Eng*, 37, p569-574, doi:10.1016/B978-0-444-63578-5.50090-6

Abstract

In this chapter, first the concept of microreactors as well as their current use in the biotechnological field is introduced. Next, the modelling approach and assumptions for modelling these microscale reactors is discussed. Afterwards, the general model representation and the Michaelis-Menten and the ping-pong bi-bi model are introduced. Finally, some basic "kinetic" modelling concepts such as parameter estimation, local sensitivity analysis, parameter estimates' uncertainty, model prediction uncertainty, and optimal experimental design will be discussed for the reader who is unfamiliar with these concepts. These concepts will be used often in the subsequent chapters, or will be used as a basis for more advanced applications, and thus are critical for the understanding of the work performed in this dissertation.

2.1 Microreactor modelling

2.1.1 Microreactor configurations

In recent years, microreactors have received increased attention in the biocatalytic field. Microreactors can be described as devices with narrow channels (typically less than 1 mm) constructed from stable inert materials (e.g. glass, silicon, stainless steel, ceramics, or polymers), and equipped with a tunable pumping system, two or three reservoirs for reagents, and a system for the selective collection of the reaction products (Wiles and Watts, 2008; Frost and Mutton, 2010). The reaction volume of these microreactors is typically below 1000 µL, and its residence time can be regulated by the pump rate. Thanks to its microscale dimensions and high surface-to-volume ratio, rapid heat exchange and mass transfer can happen, which results in higher reaction yields and reaction rates compared to conventional reactors (Laurenti and dos Santos Vianna Jr., 2016). The improved performance combined with its continuous operation allows for rapid prototyping, such as rapid screening of different process conditions, reactor configurations and biocatalyst alternatives (Bodla et al., 2013).

In several publications, microreactors have been successfully used for different enzymatic reactor configurations. The most common microreactor configurations are shown in Figure 2.1. These microreactor configurations can be divided in two major classes, i.e. the microreactors with free enzyme and those with immobilised enzyme. The microreactors with free enzyme are considered as simpler, since it only requires the introduction of both substrate and enzyme solutions from separate inlets, typically by syringe pumps, and proceeds with a continuous flow of reagents for the entire measurement time (Ristenpart et al., 2008; Tišma et al., 2009; Swarts et al., 2010). However, this simpler method yields a mixture of free enzyme, substrates, and products, which need to be separated somehow. This has already been resolved in multistep chemical syntheses, where the use of a network of microreactors and separators allows for efficient continuous synthetic systems (Sahoo et al., 2007; Hartman et al., 2010). However, for enzymatic systems the separation and reuse of the enzyme remains an important factor. To allow the reuse of the free enzymes, O'Sullivan et al. (2012) developed an in-line tangential flow filtration system which allowed to recirculate the enzyme in one-phase systems. At the other hand, multiphase biocatalytic microreactors have received increased attention (Pohar et al., 2009; Žnidaršič-Plazl and Plazl, 2009; Karande et al., 2010; Novak et al., 2012). Moreover, these multiphase systems allow to reduce substrate and/or product inhibition, provide high concentrations for substrates with low solubility, and overall increase the productivity.

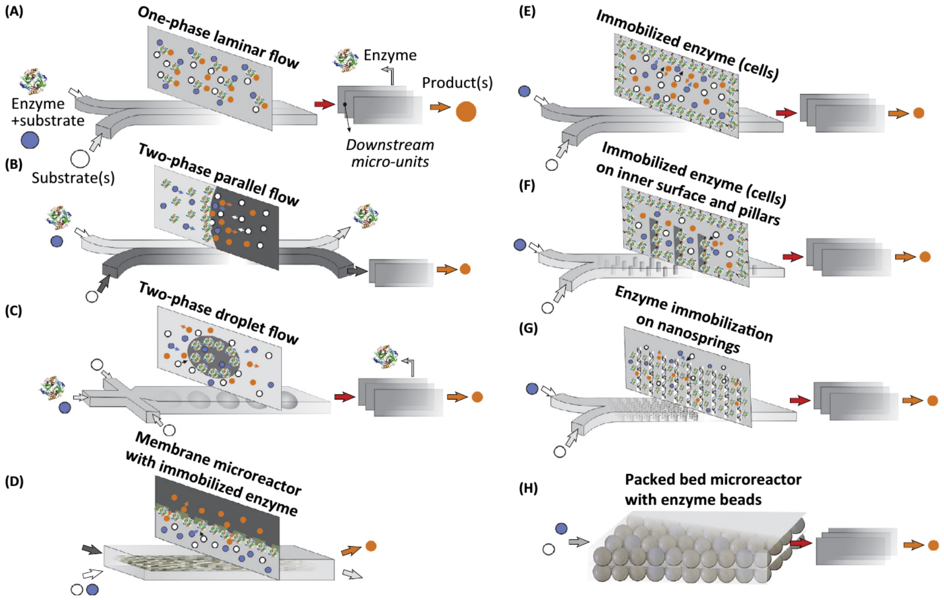

Figure 2.1: Schematic representation of enzymatic microreactors: **(A)** free enzyme in a homogeneous system; **(B)** free enzyme in a two-phase parallel flow; **(C)** free enzyme in a droplet flow; **(D)** membrane microreactor with enzyme immobilised on the membrane; **(E)** immobilised biocatalyst on the inner surface of a microchannel; **(F)** immobilised biocatalyst on the inner surface and pillars; **(G)** nanospring supports to increase surface area and biocatalyst loading in the microchannel; and **(H)** packed-bed microreactor with beads containing biocatalyst (Wohlgemuth et al., 2015).

A more straightforward approach to improve the lifetime of the enzyme, can be realised by immobilising it. Such an immobilisation prevents the contamination of the products by the enzyme, suppresses undesirable side reactions, and yields a more consistent performance and lower costs in comparison with the free enzyme approach. However, in practice it has been shown that enzyme immobilisation may lead to changes in the kinetic behaviour of the enzyme (Kerby et al., 2006). Four different main categories can be distinguished (Laurenti and dos Santos Vianna Jr., 2016):

- Surface-immobilised enzymes: enzymes are linked to the surface of a microreactor and are exposed to the flow of reagents;

- Enzyme activated beads: an appropriate amount of porous beads, previously functionalised with enzymes, are packed together to fill the chamber of a microreactor;
- Enzyme-containing monoliths: meso- or macroporous monoliths are coated with a resistant layer or directly prepared in a microchannel and functionalised with enzymes;
- Membranes: enzymes are immobilised onto a selective ultrafiltration membrane.

For all the immobilised microreactor types listed above, the enzyme needs to be immobilised onto a solid support by methods such as covalent binding , entrapment, or adsorption (Tufvesson et al., 2011).

Throughout this dissertation the focus will only lie on one-phase microreactor configurations, i.e. a microreactor where the enzyme is immobilised at the walls and a parallel-flow free-enzyme microreactor. Both microreactor configurations are introduced in more detail in Chapter 5.

2.1.2 Flow and reaction modelling

The fluid regime in microreactors is laminar due to the combined effect of small scale pipes (low hydraulic diameter) and low fluid velocity. The analysis of the flow properties can be performed by using dimensionless numbers (Hessel et al., 2005). The laminar fluid regime has both a low Reynolds (Re, see Equation 2.1) and Mach number (Ma, see Equation 2.2), and the fluid is considered an incompressible Newtonian fluid (Koo and Kleinstreuer, 2003). In Equation 2.1, $\mathbf{u}$ is the fluid velocity, d_H is the hydraulic diameter, ρ is the density of the fluid under study and μ is its dynamic viscosity. In Equation 2.2, $\mathbf{u}_\mathrm{sound}$ stands for the speed of sound waves in the fluid under study.

$$\mathrm{Re} = \frac{\rho \mathbf{u} d_\mathrm{H}}{\mu} \tag{2.1}$$

$$\mathrm{Ma} = \frac{\mathbf{u}}{\mathbf{u}_\mathrm{sound}} \tag{2.2}$$

When applying computational fluid dynamics (CFD), it needs to be verified whether the fluid in microreactors can be regarded as a continuum (Koo and Kleinstreuer, 2003). This can be quantified by the Knudsen number Kn (Equation 2.3), which equals the ratio of the molecular free path (λ_M) to a representative physical scale length (L, e.g. hydraulic diameter, d_H).

$$\mathrm{Kn} = \frac{\lambda_{\mathrm{M}}}{L} = \sqrt{\frac{\pi\gamma}{2}}\frac{\mathrm{Ma}}{\mathrm{Re}} \tag{2.3}$$

Depending on the value of the Knudsen number, several regimes can be distinguished (Table 2.1). From free molecular flow at high Knudsen numbers, to Navier-Stokes and Euler regime at low Knudsen numbers. For liquids, Kleinstreuer (2003) suggests a modification of this condition: the general Knudsen number for liquids (equation 2.4).

$$\mathrm{Kn}_l = \frac{\lambda_{\mathrm{IM}}}{L} \tag{2.4}$$

The general Knudsen number for liquids equals the ratio of the intermolecular length for the fluid molecules (λ_{IM}) to a representative physical scale (L). Given that the intermolecular length for water molecules is 30 nm, the Navier-Stokes equations with no-slip boundary condition hold up to microreactors with a hydraulic diameter as low as 0.3 µm (Kleinstreuer, 2003). Koo and Kleinstreuer (2003) state that the surface roughness effects should only be taken into account for $d_{\mathrm{H}} \leq 10\,\mu\mathrm{m}$ and turbulence effects only become important when the Reynolds number exceeds 1000. Koo and Kleinstreuer (2003) also state that viscous dissipation effects are not negligible for conduits with $d_{\mathrm{H}} \leq 100\,\mu\mathrm{m}$. Sharp (2001) states that non-Newtonian fluid behaviour only occurs when there exist long chain polymers or when fine particle suspensions are considered. Hence, it is concluded that under the assumptions made above the Navier-Stokes equations are generally valid for describing fluid flow in microreactors.

Table 2.1: Different Knudsen regimes for fluids (Gad-el Hak, 1999).

Fluid regime	Condition
Euler equations (neglect molecular diffusion)	$\mathrm{Kn} \to 0$ ($\mathrm{Re} \to \infty$)
Navier-Stokes equations with no-slip boundary conditions	$\mathrm{Kn} \leq 10^{-3}$
Navier-Stokes equations with slip boundary conditions	$10^{-3} \leq \mathrm{Kn} \leq 10^{-1}$
Transition regime	$10^{-1} \leq \mathrm{Kn} \leq 10$
Free-molecule flow	$\mathrm{Kn} > 10$

In contrast to the Navier-Stokes equations, the Boltzmann transport equation, an integral-differential equation which characterises the dynamics and kinetics of the distribution of micro-scale particles, is applicable over the entire domain of Kn. Next to the Navier-Stokes equations, it is also possible to derive the continuity and the energy equation from the Boltzmann equation (Li, 2006). The Lattice

Boltzmann method has some distinct advantages over the more frequently used Navier-Stokes system, since it is easier to implement complex and moving geometries (Zimny et al., 2013), has an intrinsic linear scalability in parallel computing and efficient inter-phase interaction handling for multiphase flow. The downsides of the approach overwhelm the upsides, since it is computationally very expensive, has issues regarding turbulence modelling and boundary conditions, and it is impossible to run steady-state simulations. Due to its maturity, the Navier-Stokes system is still the most reliable approach for the simulation of fluid flow (Shengwei, 2011). Consequently, the Navier-Stokes equations will be used throughout this dissertation.

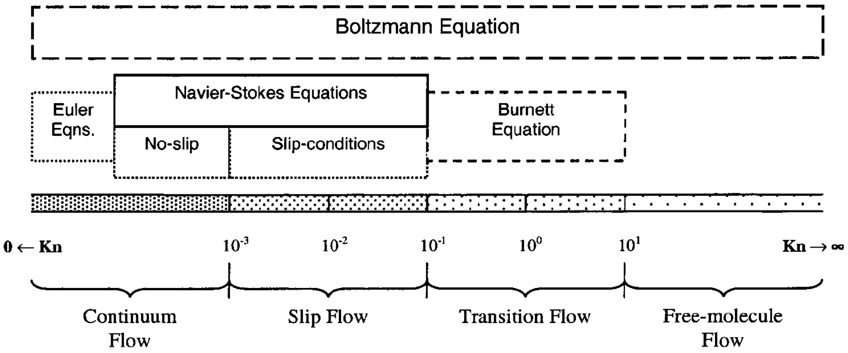

Figure 2.2: Classification of flows from free molecular flow to continuous flow in function of the Knudsen number (Roy et al., 2003).

2.2 Kinetic modelling

As stated above, the productivity of an enzymatic microreactor can be predicted by combining the CFD model with a kinetic model which represents the characterics of the enzyme. In order to obtain a kinetic model with large predictive power, an extended model-based analysis is necessary. This analysis roughly includes the estimation of the model parameters, identifiability study, and estimation of the parameter and model prediction uncertainty. The different aspects will be introduced in more detail in the following sections.

2.2.1 General model representation

A model can be regarded as a mathematical description of a certain process of interest, and can be used to predict the behaviour of that process under different conditions. Its application allows to make predictions which can be used to perform process control, but also to gain knowledge about the underlying process by testing the current model hypotheses and assumptions.

The deterministic (bio)kinetic models which are used throughout this dissertation can generally be presented as a set of (possibly mixed) differential and algebraic equations and can be represented by Equations 2.5 and 2.6.

$$\frac{\mathrm{d}\mathbf{x}}{\mathrm{d}t} = \mathbf{f}(\mathbf{x}, \boldsymbol{\theta}, t); \quad \mathbf{x}(t_0) = \mathbf{x}_0 \tag{2.5}$$

$$\hat{\mathbf{y}} = \mathbf{g}(\mathbf{x}, \boldsymbol{\theta}, t) \tag{2.6}$$

where t represents the independent variable time, $\mathbf{x}$ the n_s-dimensional vector of the time-dependent state variables, $\boldsymbol{\theta}$ represents the n_p-dimensional vector of model parameters, and $\hat{\mathbf{y}}$ represents the n_m-dimensional vector of measurable model predictions. Often $\mathbf{g}$ acts as a selector, selecting the state variables that are actually measured (Donckels, 2009).

2.2.2 Enzymatic models

In this dissertation, the main focus will be on the analysis of a kinetic model describing the behaviour of ω-transaminase. First, the generally well-known Michaelis-Menten model is introduced, since the derivation of this model is more straightforward but analogous to that of the ping-pong bi-bi model. Both models are derived using the quasi steady-state assumption, also referred to as pseudo steady-state assumption, and will be explained in more detail in the following section.

Michealis-Menten model

In many simple biochemical reactions, a substrate S is converted to product P by an enzyme E. Therefore, the substrate first reversibly binds to the enzyme to form an enzyme-substrate complex ES. This complex irreversibly breaks down into the original enzyme and the product with a certain rate k_cat (Segel and Slemrod, 1989). This is depicted in Figure 2.3.

$$\mathrm{E} \;+\; \mathrm{S} \;\underset{k_{-1}}{\overset{k_1}{\rightleftharpoons}}\; \mathrm{ES} \;\xrightarrow{k_\mathrm{cat}}\; \mathrm{E} \;+\; \mathrm{P}$$

Figure 2.3: The reaction scheme of the Michaelis-Menten model.

This reaction scheme can be represented as a set of ordinary differential equations (ODEs):

$$\frac{\mathrm{d}[S]}{\mathrm{d}t} = -k_1[E][S] + k_{-1}[ES] \tag{2.7}$$

$$\frac{\mathrm{d}[E]}{\mathrm{d}t} = -k_1[E][S] + (k_{-1} + k_{\mathrm{cat}})[ES] \tag{2.8}$$

$$\frac{\mathrm{d}[ES]}{\mathrm{d}t} = k_1[E][S] - (k_{-1} + k_{\mathrm{cat}})[ES] \tag{2.9}$$

$$\frac{\mathrm{d}[P]}{\mathrm{d}t} = k_{\mathrm{cat}}[ES] \tag{2.10}$$

where $[S]$ and $[P]$ respectively represent the concentrations of the substrate and product, $[E]$ and $[ES]$ the concentration of the enzyme and enzyme-substrate complex. k_1, k_{-1}, and k_{cat} represent the kinetic parameters. Since the total enzyme concentration $[E]_{\mathrm{t}}$ is constant, the sum of the different enzyme forms and complexes equals this concentration (Equation 2.11). This enzyme balance can also be derived from the summation of Equations 2.8 and 2.9.

$$[E]_{\mathrm{t}} = [E] + [ES] \tag{2.11}$$

The ODE system can, under certain circumstances, be simplified using the quasi steady-state assumption (QSSA). First, the experiments have to be performed after a relatively short *pre-steady-state period* but before the substrate concentration decays appreciably (Fersht, 1985). Second, it is assumed that the different enzyme forms and complexes are constant over time (Equation 2.12).

$$\frac{\mathrm{d}[E]}{\mathrm{d}t} = \frac{\mathrm{d}[ES]}{\mathrm{d}t} = 0 \tag{2.12}$$

This second assumption is only valid when the concentration of S is sufficiently high, because in that condition the free enzyme E will immediately combine with another molecule of S (Lehninger, 1982). These two assumptions are the essence of the quasi steady-state assumption. The concentration of $[EP]$ is not truly constant, but changes instantaneously to be in steady state with the present value of the substrate concentration (Segel and Slemrod, 1989). In other words, the reversible reaction in Figure 2.3 is much faster compared to the irreversible reaction, and thus k_{cat} is negligible in comparison with k_{-1} (Briggs and Haldane, 1925). Using both assumptions, Equation 2.9 can be simplified to an algebraic equation (Equation 2.13).

$$[ES] = \frac{[E]_\mathrm{t}[S]}{[S] + \dfrac{k_{-1} + k_\mathrm{cat}}{k_1}} \tag{2.13}$$

Equation 2.13 can be substituted in Equation 2.10, yielding the product conversion rate which equals the substrate consumption rate for the quasi steady-state assumption (Equation 2.14).

$$\frac{\mathrm{d}[P]}{\mathrm{d}t} = -\frac{\mathrm{d}[S]}{\mathrm{d}t} = \frac{k_\mathrm{cat}[E]_\mathrm{t}][S]}{[S] + \dfrac{k_{-1} + k_\mathrm{cat}}{k_1}} \tag{2.14}$$

Typically Equation 2.14 is reduced to Equation 2.15, since it is impossible to estimate all three rate constants from available data (Segel and Slemrod, 1989). In Equation 2.15 only two parameters, i.e. V_max and K_m are available.

$$\frac{\mathrm{d}[P]}{\mathrm{d}t} = v = \frac{V_\mathrm{max}[S]}{K_\mathrm{m} + [S]} \tag{2.15}$$

where K_m equals $\frac{k_{-1}+k_\mathrm{cat}}{k_1}$ and V_max equals $k_\mathrm{cat}[E]_\mathrm{t}$.

Ping-pong bi-bi mechanism

The asymmetric synthesis catalysed by the ω-transaminase cannot be described by the Michaelis-Menten model, but is typically described by the ping-pong bi-bi mechanism. The individual steps of the mechanism are shown in Figure 2.4 using the Cleland notation (Segel, 1975).

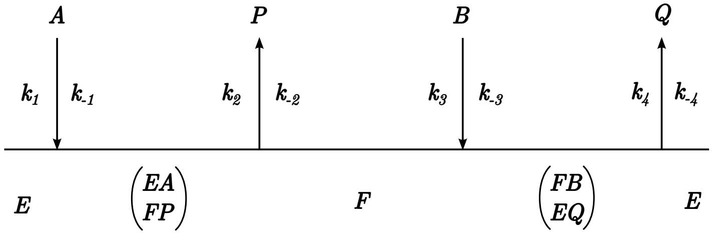

Figure 2.4: The ping-pong bi-bi mechanism without any inhibition using the Cleland notation (Segel, 1975).

First, the amino acid A binds with the enzyme E to form the enzyme-substrate complex EA in a reversible way. The amino group of A is transferred to the (cofactor of the) enzyme, leading to the formation of the amino enzyme-product complex FP. This enzyme complex reversibly releases the ketone P and yields the amino enzyme F. This second stable enzyme form catalyses the second reaction part by reacting with the ketone substrate B to yield the amino enzyme-substrate complex FB. The amino group of the enzyme is transferred to the ketone to form the enzyme-product complex EQ, which afterwards can split up in the free enzyme form E and an amine product Q.

For the ping-pong bi-bi mechanism the quasi steady-state assumption can also be used to reduce the ODE system to a single algebraic equation. However, for more complicated mechanisms such as the ping-pong bi-bi mechanism, this becomes a tedious task. To overcome this problem, multiple graphical methods have been developed based on the so-called King-Altman representation (Figure 2.5). However, these graphical methods are also prone to human errors and should therefore be avoided, e.g. Al-Haque et al. (2012) used such a graphical method to derive a ping-pong bi-bi model which incorporated both substrate and product inhibition. However, the manually derived equation presented by Al-Haque et al. (2012) does not match with the equation which is derived using the computational procedure presented by Ishikawa et al. (1988), indicating that the mechanism depicted in the King-Altman figure and the equation of Al-Haque et al. (2012) do not match. This makes the proposed equation useless for other scientist and raises questions about the modelling and calibration results. To avoid this kind of issues, Herries (1984) and Ishikawa et al. (1988) state that a computerised derivation approach should be the preferred approach.

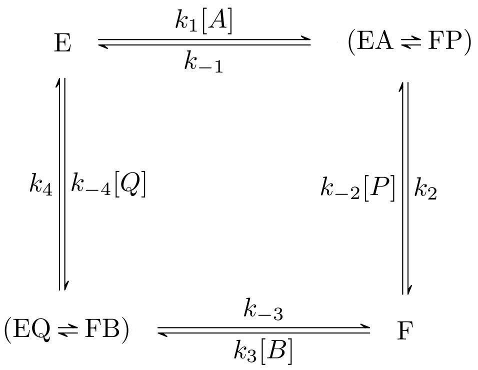

Figure 2.5: The King-Altman representation of the plain ping-pong bi-bi mechanism without any inhibition (Segel (1975)).

The application of the pseudo steady-state approximation to the plain ping-pong bi-bi mechanism, yields the model equation in Equation 2.16.

$$\frac{v}{[E]_t} = \frac{V_{\mathrm{f}} V_{\mathrm{r}} \left([A][B] - \frac{[P][Q]}{K_{\mathrm{eq}}} \right)}{\begin{aligned} & V_{\mathrm{r}} K_{\mathrm{m_B}} [A] + V_{\mathrm{r}} K_{\mathrm{m_A}} [B] + V_{\mathrm{r}} [A][B] + \frac{V_{\mathrm{f}} K_{\mathrm{m_Q}} [P]}{K_{\mathrm{eq}}} + \frac{V_{\mathrm{f}} K_{\mathrm{m_P}} [Q]}{K_{\mathrm{eq}}} \\ & + \frac{V_{\mathrm{f}} [P][Q]}{K_{\mathrm{eq}}} + \frac{V_{\mathrm{f}} K_{\mathrm{m_Q}} [A][P]}{K_{\mathrm{eq}} K_{\mathrm{ia}}} + \frac{V_{\mathrm{r}} K_{\mathrm{m_A}} [B][Q]}{K_{\mathrm{iq}}} \end{aligned}} \tag{2.16}$$

where V_{f} and V_{r} represent the maximum velocity, $K_{\mathrm{m_A}}$, $K_{\mathrm{m_B}}$, $K_{\mathrm{m_P}}$, and $K_{\mathrm{m_Q}}$ the Michaelis constants, K_{ia} and K_{iq} the dissociation constants, and K_{eq} the equilibrium constant (Segel, 1975). The relation between the kinetic constants of Equation 2.16 and the rate constants are given in Table 2.2. However, it needs to be noted that during a parameter estimation exercise the kinetic parameters are calibrated. The relations in Table 2.2 are only used to reparameterise the model, since it is impossible to retrieve the unique rate constant values from these relations.

Table 2.2: The relation between the kinetic parameters of the quasi steady-state equation and the rate constants for the plain ping-pong bi-bi mechanism.

Kinetic parameters	**Rate constants**
V_{f}	$\frac{k_2\, k_4}{k_2 + k_4}$
V_{r}	$\frac{k_{-1}\, k_{-3}}{k_{-1} + k_{-3}}$
$K_{\mathrm{m_A}}$	$\frac{k_4 (k_{-1} + k_2)}{k_1 (k_2 + k_4)}$
$K_{\mathrm{m_B}}$	$\frac{k_2 (k_{-3} + k_4)}{k_3 (k_2 + k_4)}$
$K_{\mathrm{m_P}}$	$\frac{k_{-3} (k_{-1} + k_2)}{k_{-2} (k_{-1} + k_{-3})}$
$K_{\mathrm{m_Q}}$	$\frac{k_{-1} (k_{-3} + k_4)}{k_{-4} (k_{-1} + k_{-3})}$
K_{ia}	$\frac{k_{-1}}{k_1}$
K_{iq}	$\frac{k_4}{k_{-4}}$
K_{eq}	$\left(\frac{V_{\mathrm{f}}}{V_{\mathrm{r}}}\right)^2 \frac{K_{\mathrm{m_P}} K_{\mathrm{m_Q}}}{K_{\mathrm{m_A}} K_{\mathrm{m_B}}}$

It is clear that by applying the quasi steady-state approximation, the ODE system has been reduced to a simple algebraic model (Equation 2.16), which describes the reaction rate for all substrates and products.

2.2.3 Parameter estimation

The general model represented by Equations 2.5 and 2.6 needs to be calibrated before it can be used for any practical application. The aim of such a parameter estimation, also commonly referred to as model calibration or inverse modelling, is to find unique parameter values which lead to a good agreement between the model predictions and the experimental data. In the literature, different approaches to estimate model parameters are available and this remains an important aspect of the modelling exercise. In order to find the actual optimal parameter set $\hat{\boldsymbol{\theta}}$, two major classes of methods can be distinguished, i.e. the linear plotting methods and nonlinear regression (Chen et al., 2008). The linear plotting methods are based on algebraic expressions of simplified kinetic differential equations at initial rate conditions to give a series of straight line equations. Different linear plotting methods exist (Chen et al., 2008): Lineweaver-Burk (Lineweaver and Burk, 1934), Hanes-Woolf (Hanes, 1932), Eadie-Hofstee (Eadie, 1942; Hofstee, 1952), the direct linear plot (Eisenthal and Cornish-Bowden, 1974), and the Dixon plot (Dixon, 1953) (which is used in particular for determining enzyme inhibition constants). It might seem that the choice of linear transformation is unimportant, since they are all variants of the same equation, and thus would yield an equal accuracy. However, this is only true if both the concentrations and measurements would be errorless (Dowd and Riggs, 1965). By transforming the equation, the error distribution is distorted depending on the kind of transformation or linearisation that is applied (Moser, 2012). Dowd and Riggs (1965) compared the accuracy of the Lineweaver-Burk plot, Hanes-Woolf plot, and Eadie-Hofstee plot and found that closeness of fit is always the best for the Lineweaver-Burk plot and worst for the Eadie-Hofstee. However, the accuracy with which the Michaelis constants were estimated is the greatest for Eadie-Hofstee and worst for the Lineweaver-Burk plot, leading to the paradox that the "worst fitting" line was yielding the "best" parameter estimates and *vice versa*. Dowd and Riggs (1965) stated that the popularity of the Lineweaver-Burk method may be based upon the ability to provide what seems a good fit even when the experimental data are poor. In the original paper, Lineweaver and Burk (1934) already stated that "*the relative weighting of the experimental observations alters in a definite matter when the form of the equation is altered, and if not taken into account may alter slightly the parameter constants obtained*". By applying the proper weighting, identical parameter estimates can be obtained as the Eadie-Hofstee approach. However, Dowd and Riggs (1965) stated that calculating the proper weighting factors is inconvenient, and often coupled with ignorance. Ranaldi et al. (1999) extended the analysis of Dowd and Riggs (1965) by also including the direct linear plot and the nonlinear regression. Nonlinear regression, also known as nonlinear optimisation, reduces the offset between the model and data using an objective function, without the need for linearising the model. Ranaldi et al. (1999) showed that using nonlinear regression, even without using the proper weighting factors, yields the most reliable estimates for the different parameter values. Linear methods are still useful as graphical methods, but not as quantitative methods to estimate parameter values.

In this dissertation, no linear methods are used to perform parameter estimations since they show a lower performance and are only applicable for linear(ised) models. The nonlinear optimisation is used to find a good agreement between the model outputs and experimental data. Mathematically, this can be expressed as a minimisation of an objective function in which the offset between the model and data is evaluated. This minimisation yields an optimal parameter set $\hat{\boldsymbol{\theta}}$ and is given by Equation 2.17.

$$\hat{\boldsymbol{\theta}} = \arg\min_{\boldsymbol{\theta}\in\boldsymbol{\Theta}} J(\boldsymbol{\theta}) \tag{2.17}$$

For the objective function $J(\boldsymbol{\theta})$ typically a weighted sum of squared errors (WSSE) is used (Equation 2.18).

$$J(\boldsymbol{\theta}) = \sum_{i=1}^{N} (\mathbf{y}_i - \hat{\mathbf{y}}(\boldsymbol{\theta}, t_i))^{\intercal} \, \mathbf{Q}_i \, (\mathbf{y}_i - \hat{\mathbf{y}}(\boldsymbol{\theta}, t_i)) \tag{2.18}$$

where $\mathbf{Q}_i$ represents a time-dependent $n_{\mathrm{m}} \times n_{\mathrm{m}}$ dimensional matrix, containing the weighting coefficients. Typically, $\mathbf{Q}$ is chosen as the inverse of the measurement error covariance matrix $\boldsymbol{\Sigma}$ (Omlin and Reichert, 1999; Marsili-Libelli et al., 2003; Donckels, 2009). In this way, the measurement uncertainty is incorporated in the objective function $J(\boldsymbol{\theta})$, which can be rewritten (Equation 2.19).

$$J(\boldsymbol{\theta}) = \sum_{i=1}^{N} (\mathbf{y}_i - \hat{\mathbf{y}}(\boldsymbol{\theta}, t_i))^{\intercal} \, \boldsymbol{\Sigma}_i^{-1} \, (\mathbf{y}_i - \hat{\mathbf{y}}(\boldsymbol{\theta}, t_i)) \tag{2.19}$$

where $\boldsymbol{\Sigma}_i$ represents the measurement error covariance matrix for the i^{th} sample. This representation of the objective function will be used throughout the entire dissertation.

As stated above, Equation 2.17 needs to be minimised to retrieve the optimal parameter set $\hat{\boldsymbol{\theta}}$. This can be achieved by different optimisation techniques, which can be divided in two major classes: local and global optimisation algorithms (Dochain and Vanrolleghem, 2001). As the name suggests, local optimisation algorithms try to find the minimal value of J in a local neighbourhood starting from an initial guess in the parameter space. However, when the objective function contains multiple local minima and one global minimum, it is likely that the local optimisation algorithm will not end up in the "real" minimum. To circumvent this problem, global optimisation algorithms are available which are less sensitive to these local minima, though typically are computationally more expensive. Optimisation methods from both classes will be used throughout this dissertation. The selection of the suitable strategy depends on the specific optimisation problem, and will therefore be discussed individually in each chapter.

2.2.4 Model identifiability

The aim of the parameter estimation performed above, is to retrieve the unique parameter set $\hat{\boldsymbol{\theta}}$ which is able to describe the acquired data. However, it is possible that not one but multiple parameter sets yield the same or comparable model prediction, making it impossible to determine the "real" parameter values, a situation which is referred to as an identifiability problem. The lack of identifiability can be related to the model structure itself (structural identifiability) or to the quantity and/or quality of the experimental data (practical identifiability) (Vanrolleghem et al., 1995).

Structural identifiability is studied under the assumption that unlimited and perfect (i.e. error-free and unbiased) measurements are available. This analysis can be performed in the absence of any prior information on the value of the parameters and even before collecting any data (De Pauw, 2005). The symbolic techniques which are used most often to assess structural identifiability are the Taylor series approach (TSA), the generating series approach (GSA) and the differential algebra approach (DAA) (Chis et al., 2011). All techniques require significant computational resources and the question whether the model is structural identifiable may remain unanswered. These drawbacks make the methods only applicable for relatively simple nonlinear models (De Pauw, 2005). The problem of structural identifiability was already encountered when deriving the Michaelis-Menten model, since the model in Equation 2.14 was shown to be unidentifiable. By reparameterising this model, the number of parameters reduced to 2, and the Michaelis-Menten model (Equation 2.15) was found to be structurally identifiable.

Practical identifiability is not only related to the model structure but also to the quality and availability of the data. In other words, the practical identifiability study is used to verify if the available data are sufficiently informative to identify the model parameters and give them a unique and accurate value (De Pauw, 2005). Typically the practical identifiability is quantified based on a sensitivity analysis of the model parameters in combination with information on the measurement uncertainty (Vanrolleghem et al., 1995; Brun et al., 2001; De Pauw and Vanrolleghem, 2006a).

The assessment of the practical identifiability is essential, since a parameter which is practically identifiable is also structurally identifiable but not *vice versa*. Since the use of noise-corrupted data will obscure the process characteristics, it is possible that a change in one parameter can be compensated almost completely by changing the other parameter values, while still producing a satisfying fit between the model outputs and the data. Structural identifiability can thus be regarded as the upper bound for the model identifiability which will probably not be reached in a practical situation (De Pauw, 2005).

The practical identifiability question is closely related to model predictive performance and overfitting/overparametrisation, and is illustrated in Figure 2.6. At a low model complexity, the model is not able to capture the underlying process characterics, and thus its calibration error and prediction error will be high. At high model complexity, the calibration error will be low and thus it is expected that the model will yield proper predictions. However, since the model is overfitted, not only the process characterics are described but also random behaviour of the measurement error. This makes that model predictions for new data will be much worse than expected, indicated as "optimism" in Figure 2.6. It is clear that by balancing model complexity and data availability, the model predictive performance will be higher. Marsili-Libelli et al. (2014) stated that in the presence of noise the potential for overfitting raises, and thus the practical identifiability of the model needs to be assessed.

2.2.5 Local sensitivity analysis

The model outputs are directly determined by the values of the model parameters. Therefore, it is interesting to calculate the so-called local parameter sensitivities, which indicate whether the model predictions ($\hat{\mathbf{y}}$) are sensitive to changes in the parameter values. A parameter can be regarded as sensitive when a small change in its value yields a significant change in (at least one of) the model outputs. In this dissertation, two different approaches were implemented and used to calculate

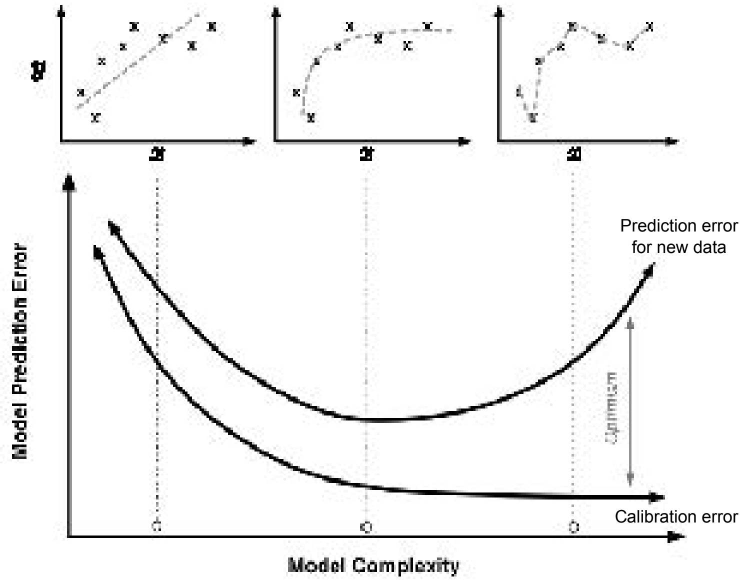

Figure 2.6: To ensure that a model is practically identifiable and has a good predictive performance, the model complexity and the available data need to be balanced (adapted from Fortmann-Roe (2012)).

the local sensitivity analyses, i.e. the indirect local sensitivity analysis LSA (also referred to as the brute-force LSA) and the direct LSA.

Indirect local sensitivity analysis

The indirect method is the simplest way to calculate the LSA, since it only requires the use of the finite difference approximation. Therefore, no additional code needs to be implemented beyond the original solver code (De Pauw, 2005). The partial derivative of one of the model predictions ($\hat{y}_i$) to a certain parameter (θ_j) can be approximated by using the forward difference (Equation 2.20).

$$\left.\frac{\partial \hat{y}_i}{\partial \theta_j}\right|_{\hat{\boldsymbol{\theta}}} = \lim_{\Delta\theta_j \to 0} \frac{\hat{y}_i(\boldsymbol{\theta} + \Delta\theta_j, t) - \hat{y}_i(\boldsymbol{\theta}, t)}{\Delta\theta_j} \tag{2.20}$$

To calculate the local sensitivities for all parameters using the finite difference method, the model needs to be evaluated once at its nominal parameter values, but also n_p times at the different pertubated parameter values ($\hat{\mathbf{y}}(\boldsymbol{\theta} + \theta_j)\,\forall j \in \{1, \ldots, n_\mathrm{p}\}$) where n_p represents the number of parameters which are involved in the sensitivity analysis. It should be noted that Equation 2.20 is only valid for an infinitesimally small perturbation of $\Delta\theta_j$. However, in practice it is unfeasible to select such small perturbations since they would result in numerical inaccuracies due to round-off errors. On the other hand, the perturbation should not be too large either, since the nonlinearity of the model will influence the calculation of the sensitivity functions yielding unreliable results. In order to select the most appropriate perturbation value for each parameter, the forward sensitivity (Equation 2.20) can be compared with the backward sensitivity (Equation 2.21).

$$\left.\frac{\partial \hat{y}_i}{\partial \theta_j}\right|_{\hat{\boldsymbol{\theta}}} = \lim_{\Delta\theta_j \to 0} \frac{\hat{y}_i(\boldsymbol{\theta}, t) - \hat{y}_i(\boldsymbol{\theta} - \Delta\theta_j, t)}{\Delta\theta_j} \tag{2.21}$$

In theory, both the forward and the backward difference should yield the same results, but due to the nonlinearity of the models under study the results will (slightly) differ. By comparing both the forward and the backward difference for different perturbation values, a perturbation value can be selected which yields the lowest difference between both approaches. However, this requires that the forward and backward sensitivities are calculated for a range of perturbation factors, to select the most optimal perturbation factor. The perturbation factor has to be determined for each parameter individually, making its optimisation calculation intensive for large and complex models. To quantify the quality of the sensitivity calculations (and its corresponding perturbation factor) different measures are available, i.e. sum of squared errors (SSE), sum of absolute errors (SAE), maximum relative error (MRE), and sum of relative errors (SRE). De Pauw and Vanrolleghem (2006a) presented a nice overview of the available methods and discussed the assessment of the quality of sensitivity calculations with respect to the perturbation value and solver settings in more detail.

Direct local sensitivity analysis

The indirect local sensitivity method is computationally expensive, especially for models where the sensitivity needs to be calculated for many parameters (De Pauw, 2005). Atherton et al. (1975) developed the direct method for the sensitivity analysis for a system of differential and algebraic equations. To calculate the local parameter sensitivities for the different measurable model predictions, the $n_{\mathrm{s}} \times n_{\mathrm{p}}$ additional differential equations (Equation 2.22) have to be defined and solved together with the actual model (Equations 2.5 and 2.6) (Atherton et al., 1975; Leis and Kramer, 1988; Donckels, 2009).

$$\frac{\mathrm{d}}{\mathrm{d}t}\left(\left.\frac{\partial \mathbf{x}(\boldsymbol{\theta})}{\partial \boldsymbol{\theta}}\right|_{\hat{\boldsymbol{\theta}}}\right) = \left.\frac{\partial \mathbf{f}(\mathbf{x}, \boldsymbol{\theta}, t)}{\partial \boldsymbol{\theta}}\right|_{\hat{\boldsymbol{\theta}}} + \left.\frac{\partial \mathbf{f}(\mathbf{x}, \boldsymbol{\theta}, t)}{\partial \mathbf{x}}\right|_{\hat{\boldsymbol{\theta}}} \left.\frac{\partial \mathbf{x}(\boldsymbol{\theta}, t)}{\partial \boldsymbol{\theta}}\right|_{\hat{\boldsymbol{\theta}}} \tag{2.22}$$

The solution of the system of ordinary differential equations of Equation 2.22, which is the sensitivity of the state variables in function of the different parameters, is afterwards used to calculate the sensitivity of the measurable model outputs in function of the different parameters (Equation 2.23).

$$\left.\frac{\partial \hat{\mathbf{y}}(\boldsymbol{\theta},t)}{\partial \boldsymbol{\theta}}\right|_{\hat{\boldsymbol{\theta}}} = \left.\frac{\partial \mathbf{g}(\mathbf{x},\boldsymbol{\theta},t)}{\partial \boldsymbol{\theta}}\right|_{\hat{\boldsymbol{\theta}}} + \left.\frac{\partial \mathbf{g}(\mathbf{x},\boldsymbol{\theta},t)}{\partial \mathbf{x}}\right|_{\hat{\boldsymbol{\theta}}} \left.\frac{\partial \mathbf{x}(\boldsymbol{\theta},t)}{\partial \boldsymbol{\theta}}\right|_{\hat{\boldsymbol{\theta}}} \tag{2.23}$$

As already stated earlier, it is often the case that some of the measurable model predictions $\hat{\mathbf{y}}$ are equal to one of the state variables $\mathbf{x}$. In this case the parameter sensitivities of these measurable model predictions equal those of the corresponding state variables. For large and complex systems, Equations 2.22 and 2.23 might become very complex and it will become practically unfeasible to calculate the parameter sensitivity directly. In such cases, the indirect methodology might be more appropriate (Donckels, 2009). In this dissertation, mainly the direct local sensitivity analysis will be used, since this approach proved to be much faster (at least factor 3 for small models).

2.2.6 Uncertainty on the parameter estimates

After finishing the parameter estimation procedure, a parameter set will be found which is able to properly predict the experimental data. Since the collected data are noise-corrupted, the parameter estimates will be uncertain to some extent. This parameter uncertainty needs to be estimated, since a parameter value can only be regarded as reliable if this uncertainty is sufficiently low. Therefore, a parameter estimation exercise should always be followed by an assessment of the parameter estimate uncertainty (Donckels, 2009). Seber and Wild (1989) stated that it is justifiable to base the confidence region of the parameter estimates on the contours of the objective function. This is illustrated for a model with only one calibrated parameter in Figure 2.7.

When the model parameter has a large influence on the model prediction (inner curve ① in Figure 2.7), the objective function will be narrow, yielding a large increase in objective function value when the parameter is slightly varied. On the other hand, when the calibrated parameter only has a limited impact on the model prediction (outer curve ② in Figure 2.7), the objective function value will only slightly vary, leading to a rather flat curve. It is obvious that the narrow objective function will yield a much more reliable parameter estimate and thus is preferable. To quantify this "narrowness", a confidence interval (or more generally confidence

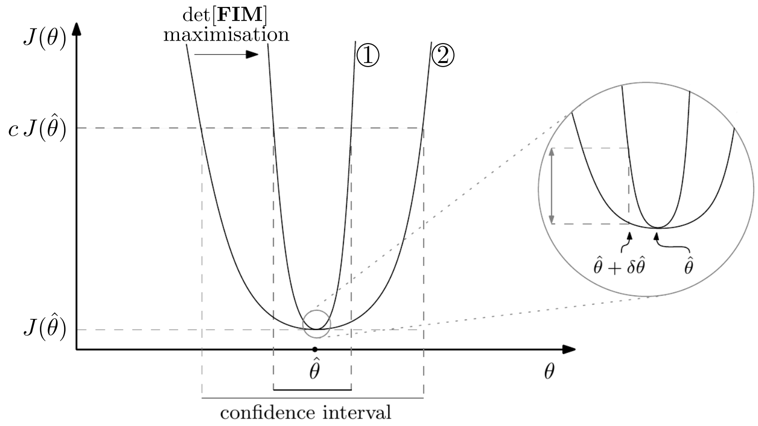

Figure 2.7: The uncertainty of the parameter estimates can be reduced by making the shape of the objective function more narrow (adapted from Donckels (2009)).

region for multi-parameter models) needs to be derived from the objective function which represents all the parameter values which lie below a certain threshold $c\,J(\hat{\boldsymbol{\theta}})$. Mathematically, such an *exact* confidence region can be determined using Equation 2.24.

$$\left\{\boldsymbol{\theta} : J(\boldsymbol{\theta}) \leq c\,J(\hat{\boldsymbol{\theta}})\right\} \tag{2.24}$$

for any $c > 1$. This confidence region is *exact* in the sense that it is not based on any approximation (Seber and Wild, 1989). However, for nonlinear models it is difficult to select a c value with any statistical significance. Instead of trying to find the exact confidence region, linear approximations are often used to construct the confidence region. These linear approximation methods are only sufficiently accurate to construct parameter confidence regions for nonlinear models under certain conditions. The linear approximation of the confidence regions will already be introduced shortly below, but a more extensive introduction about its limitations will be given in Chapter 4.

The parameter estimation error covariance matrix, which will be denoted as $\boldsymbol{\Phi}$ throughout this dissertation, is used to represent the uncertainty of the parameter estimates. The quality of the parameter estimates is determined by the information content of the experimental data from which they are determined (Donckels, 2009). Two major factors can be determined which will affect this quality: the measurement error and the local sensitivity of the parameter. For a high measurement uncertainty (and thus more noise), it will become harder to extract (small) changes and evolutions, and thus information with respect to the parameters will be lost. On the other hand, the conducted experiments need to contain information at conditions where the parameter is sensitive. If a parameter is not sensitive under the current conditions, it will not have any impact on the model predictions and thus its actual value will be uncertain. These two factors are combined in the so-called Fisher information matrix (**FIM**), and allow to quantify the information content of experimental data. According to the Cramér-Rao inequality (Ljung, 1999), the inverse of the **FIM** equals the lower bound of the parameter estimation error covariance matrix $\mathbf{\Phi}$ (Equation 2.25). However, this is only true when the measurement errors are independent samples from a normal distribution with zero mean (i.e. Gaussian white noise). Moreover, it is also required that the residuals are uncorrelated and white. The latter is something that unfortunately rarely happens for nonlinear systems (De Pauw, 2005).

$$\mathbf{\Phi} \geq \mathbf{FIM}^{-1} \tag{2.25}$$

The inverse of the **FIM** is therefore often used as an approximation of the parameter estimation error covariance matrix and is represented in Equation 2.26 (Vanrolleghem et al., 1995; Walter and Pronzato, 1997; Ljung, 1999; Asprey and Macchietto, 2002; Benabbas et al., 2005; Al-Haque et al., 2012; Goujot et al., 2012).

$$\mathbf{FIM} = \sum_{i=1}^{N} \left(\left. \frac{\partial \hat{\mathbf{y}}(\boldsymbol{\theta}, t_i)}{\partial \boldsymbol{\theta}} \right|_{\hat{\boldsymbol{\theta}}} \right)^{\mathsf{T}} \mathbf{\Sigma}_i^{-1} \left(\left. \frac{\partial \hat{\mathbf{y}}(\boldsymbol{\theta}, t_i)}{\partial \boldsymbol{\theta}} \right|_{\hat{\boldsymbol{\theta}}} \right) \tag{2.26}$$

where $\partial \hat{\mathbf{y}} / \partial \boldsymbol{\theta}$ represents the $n_{\mathrm{m}} \times n_{\mathrm{p}}$-dimensional parameter sensitivity matrix for measurement time t_i. The exact relationship between the objective function and the **FIM** is discussed in more detail in Chapter 4.

The diagonal elements of the parameter estimation error covariance matrix $\mathbf{\Phi}$ are the variances of the errors of the parameter estimates ($\sigma^2_{\theta_i}$) whereas the off-diagonal elements are the covariances between the parameter estimation errors (Equation 2.27).

$$\mathbf{\Phi} = \begin{bmatrix} \sigma^2_{\theta_1} & \mathrm{Cov}(\theta_1, \theta_2) & \dots & \mathrm{Cov}(\theta_1, \theta_{n_{\mathrm{p}}}) \\ \mathrm{Cov}(\theta_2, \theta_1) & \sigma^2_{\theta_2} & & \\ \vdots & & \ddots & \\ \mathrm{Cov}(\theta_{n_{\mathrm{p}}}, \theta_1) & & & \sigma^2_{\theta_{n_{\mathrm{p}}}} \end{bmatrix} \tag{2.27}$$

Based on these variances and covariances, the elements of the linear correlation matrix can be calculated (Equation 2.28) (Walter and Pronzato, 1997; Marsili-Libelli et al., 2003; De Pauw, 2005; Donckels, 2009).

$$\rho_{\boldsymbol{\Phi}}(i,j) = \frac{\boldsymbol{\Phi}(i,j)}{\sqrt{\boldsymbol{\Phi}(i,i)\,\boldsymbol{\Phi}(j,j)}} \tag{2.28}$$

The elements of the matrix give a measure for the linear correlation between two parameters and range between -1 and 1. For highly correlated parameters, the absolute value will be close to 1, while correlation coefficients close to zero imply low correlations (Donckels, 2009).

From the parameter estimation error covariance matrix, the $100\,(1-\alpha)$ percent confidence interval of parameter estimate i can be calculated as

$$\sqrt{\boldsymbol{\Phi}(i,i)}\,t_{N-n_{\mathrm{p}}}^{\alpha/2} \tag{2.29}$$

where N represents the total number of data points, n_{p} the number of calibrated parameters using these data, and $t_{N-n_{\mathrm{p}}}^{\alpha/2}$ represents the upper $\alpha/2$ quantile of the Student's t distribution for the given confidence level α and $N-n_{\mathrm{p}}$ degrees of freedom. To estimate the parameter confidence intervals, only the diagonal elements of the parameter estimation error covariance matrix are considered, thereby ignoring the covariance between the parameter estimates.

2.2.7 Model prediction uncertainty

Since the parameter estimates are uncertain, the model predictions will consequently also be uncertain. Therefore, also a covariance matrix is used to quantify the uncertainty of the model predictions. The model prediction error covariance matrix $\boldsymbol{\Omega}$ is given by Equation 2.30 (Omlin and Reichert, 1999).

$$\boldsymbol{\Omega}(t) = \left(\left.\frac{\partial\hat{\mathbf{y}}(\boldsymbol{\theta},t)}{\partial\boldsymbol{\theta}}\right|_{\hat{\boldsymbol{\theta}}}\right)\boldsymbol{\Phi}\left(\left.\frac{\partial\hat{\mathbf{y}}(\boldsymbol{\theta},t)}{\partial\boldsymbol{\theta}}\right|_{\hat{\boldsymbol{\theta}}}\right)^{\mathsf{T}} \tag{2.30}$$

where $\boldsymbol{\Phi}$ represents the parameter estimation error covariance matrix, which was calculated earlier. The calculation of the model prediction correlations and confidence intervals are similar to those of the parameter estimates and are respectively given by Equations 2.31 and 2.32.

$$\rho_{\mathbf{\Omega}}(i,j) = \frac{\mathbf{\Omega}(i,j)}{\sqrt{\mathbf{\Omega}(i,i)\,\mathbf{\Omega}(j,j)}} \tag{2.31}$$

$$\sqrt{\mathbf{\Omega}(i,i)}\,t_{N-n_{\mathrm{p}}}^{\alpha/2} \tag{2.32}$$

where N represents the total number of data points, n_{p} the number of calibrated parameters using these data, and $t_{N-n_{\mathrm{p}}}^{\alpha/2}$ represents the upper $\alpha/2$ quantile of the Student's t distribution for the given confidence level α and $N - n_{\mathrm{p}}$ degrees of freedom.

2.2.8 Optimal Experimental Design

The aim of optimal experimental design (OED) is to design experiments which are highly informative with respect to a certain goal. Generally, two major types of OED can be distinguished, i.e. OED for parameter estimation (OED/PE) and OED for model discrimination (OED/MD) (De Pauw, 2005; Donckels, 2009). For the latter, one has multiple candidate models which can eventually be used to describe the experimental data. However, every model is in fact only a mathematical representation of the hypotheses of the underlying processes and mechanisms. For example, the ping-pong bi-bi mechanism consists of multiple hypotheses/assumptions: two stable enzyme forms, substrate A is being converted to product P before substrate B is able to bind to the enzyme form F,... This set of hypotheses needs to be confirmed or rejected by the collected experimental data. However, it is more likely that based on previous knowledge already a set of models was selected which potentially can describe the process under study. The idea of OED/MD is to perform experiments at conditions where the behaviour of the models differs significantly, since this allows to select the subset of models which is able to describe the experimental data.

On the other hand, the aim of OED/PE is to perform experiments which lead to highly confident parameter estimates with minimal experimental effort. In other words, a small change in parameter value should result in a large difference of the value of the objective function J (Donckels, 2009). A clearly defined minimum for J, can be achieved by maximising the difference between $J(\boldsymbol{\theta})$ and $J(\hat{\boldsymbol{\theta}})$. If this is the case, the minimum will be located in a deep "pit" rather than a small depression on a flat objective function plane (De Pauw, 2005). Maximising the difference between $J(\boldsymbol{\theta})$ and $J(\hat{\boldsymbol{\theta}})$ can be realised by maximising the **FIM**. This makes sense, since the inverse of the **FIM** represents the lower bound of the parameter estimates uncertainty covariance matrix $\mathbf{\Phi}$. By maximising the **FIM**, the parameter uncertainties in $\boldsymbol{\Phi}$ are minimised. However, the **FIM** needs to be reduced to a scalar metric in order to allow maximisation by an optimisation algorithm. Various real-valued functions are suggested as metrics and are shown in Table 2.3.

The D-criterion is most commonly used and will also be used in this dissertation. By maximising the determinant of the **FIM** the overall volume of the confidence region is reduced. D-optimal experiments possess the attractive property, as opposed to the other design criteria, of being invariant with respect to any rescaling of the parameter units. Although the value of the criterion changes as function of the parameter units, the optimal experiment remains the same (Petersen, 2000).

Table 2.3: The different "alphabetic" optimal design criteria based on the **FIM** properties (Fedorov and Hackl, 1997; Walter and Pronzato, 1997; De Pauw, 2005).

Design Name	Criterion
A-optimal	$\min\{\text{tr}(\mathbf{FIM}^{-1})\}$
Modified A-optimal	$\max\{\text{tr}(\mathbf{FIM})\}$
D-optimal	$\max\{\det(\mathbf{FIM})\}$
E-optimal	$\max\{\lambda_{\min}(\mathbf{FIM})\}$
Modified E-optimal	$\min\{\lambda_{\max}(\mathbf{FIM})/\lambda_{\min}(\mathbf{FIM})\}$

tr(): sum of eigenvalues; det(): product of eigenvalues

Mathematically the optimal experiment, using the D-criterion, is given by Equation 2.33.

$$\boldsymbol{\psi}_{\mathrm{D}} = \arg\left\{\max_{\boldsymbol{\psi}\in\boldsymbol{\Psi}}\left[\det[\mathbf{FIM}(\boldsymbol{\theta},\boldsymbol{\psi})]\right]\right\} \tag{2.33}$$

where $\boldsymbol{\Psi}$ represents the experimental design space and $\boldsymbol{\psi}_{\mathrm{D}}$ the optimal experiment for a specific parameter set $\boldsymbol{\theta}$ using the D-criterion. The experimental design $\boldsymbol{\psi}$ potentially consists of all the process settings which can be varied, e.g. the initial concentrations of the different substrates and products, the sampling times, pumping rate,...

In this dissertation, the focus lies entirely on the OED/PE, since it is widely accepted that the ω-transaminase follows the ping-pong bi-bi mechanism. However, in reality it is likely that both the model structure needs to be selected and the parameters need to be uniquely estimated. Many approaches in literature first select the appropriate model structure before starting the parameter estimation. Donckels (2009) integrated both approaches (i.e. OED/MD+PE), since the sequential approach generally requires more experiments and can thus be regarded as less efficient.

2.2.9 pyIDEAS

The methodologies discussed above have been implemented in a Python package called pyIDEAS (Van Daele et al., 2015). The pyIDEAS package allows novice and experienced modellers to execute basic and more advanced techniques by executing just a few lines of code. pyIDEAS is open source and well-documented so that everybody is able to use it and has the ability of extending or adding functionalities. Such an integrated and flexible modelling package, providing access to optimal experimental design techniques, is not yet available to our knowledge and could improve overall access to this kind of tools and, hence, the quality of many modelling studies which often ignore issues related to model parameter identifiability and the like. Moreover, it allows modelling experts to verify current implementations and to debug them, something which is not possible for closed software packages. Therefore, this integrated package is made available online at `https://github.com/TimothyVD` and some examples have been included in the Appendix A.

2.3 Conclusions

The application and modelling of biocatalytic microreactors was briefly introduced. It was shown that the Navier-Stokes equations are applicable for describing flow in microreactors, which will be exploited in Chapters 5 and 6. Afterwards, the general model presentation and the Michaelis-Menten and ping-pong bi-bi model were introduced. Finally, different modelling concepts like the parameter estimation, local sensitivity analysis, and optimal experimental design, were explained in detail and will be intensively used in the following chapters.

CHAPTER 3

A NUMERICAL PROCEDURE FOR MODEL IDENTIFIABILITY ANALYSIS APPLIED TO ENZYME KINETICS

Partially redrafted from

Van Daele, T., Van Hoey, S., Gernaey, K.V., Krühne, U., Nopens, I. (2015) A numerical procedure for model identifiability analysis applied to enzyme kinetics, *Comput Aided Chem Eng*, 37, p575-580, doi:10.1016/B978-0-444-63578-5.50091-8

Abstract

The proper calibration of models describing enzyme kinetics can be quite challenging. In the literature, different procedures are available to calibrate enzymatic models in an efficient way (Shin and Kim, 1998; Chen et al., 2008; Al-Haque et al., 2012). However, in most cases the model structure is already decided on prior to the actual calibration exercise, thereby bypassing the challenging task of model structure determination and identification. Parameter identifiability problems can thus lead to ill-calibrated models with low predictive power and large model uncertainty. Every calibration exercise should therefore be preceded by a proper model structure evaluation by assessing the local identifiability characteristics of the parameters. Moreover, such a procedure should be generic to make sure it can be applied independently from the structure of the model.

A numerical identifiability approach, based on the work of Walter and Pronzato (1997), is applied and can be easily set up for any type of model. In this chapter the proposed approach is applied to the plain ping-pong bi-bi kinetics. Structural identifiability analysis showed that no local structural model problems were occurring. In contrast, the practical identifiability analysis revealed that not all parameters were practically identifiable. At higher measurement uncertainties, the parameters became practically unidentifiable. By using the presented approach it

is possible to detect potential identifiability problems and avoid pointless calibration (and experimental) effort. Moreover, the performance of the optimisation algorithm can be assessed as well.

3.1 Introduction

Nowadays, mathematical models are often used to describe enzymatic reactions, because in that way it is possible to gain information about the underlying kinetics (i.e. parameter values) and optimise overall performance of these reactions. By improving the performance, enzymatic reactions can become competitive with the chemical synthesis and yield a greener process. This is also the case for the production of chiral amines, for which transaminases can provide an interesting alternative for current chemical production (Tufvesson et al., 2011). In this respect, Shin and Kim (1998) presented a ping-pong bi-bi model to describe the enzymatic kinetic resolution of α-methylbenzylamine by ω-transaminase. Shin and Kim (1998) successfully performed a parameter estimation, but did not perform an identifiability analysis. As already introduced in Chapter 2, identifiability is an important model characteristic and can be defined as the existence of a unique combination of parameter values describing the system's behaviour. Two major types of identifiability problems exist: structural and practical. In a structural identifiability problem, the model parameters cannot be identified from noise-free data and any arbitrary chosen input/output measurements because multiple parameter sets yield the same input/output model predictions because of their correlation in the model structure.. Practical identifiability extends the problem by including the quality and availability of data. The latter provides an answer to the question: are the available data sufficiently informative to allow finding this unique parameter set (given structural identifiability)?

To allow the assessment of both identifiability types, the original numerical local identifiability approach of Walter and Pronzato (1997) is extended. The original technique consists of two steps: first the nominal parameter values are selected and the model under investigation is used to generate a lot of high quality, but fictitious data. Second, the aim is to estimate the parameters from these data by minimising an objective function. The minimisation is started at the nominal parameter values, so if the parameter set remains stable the solution is structurally locally identifiable, otherwise it is structurally unidentifiable. This procedure needs to be repeated for different nominal values before drawing conclusions about the model identifiability (Walter and Pronzato, 1997). The extended identifiability procedure presented in this chapter is developed to cope with both structural and practical identifiability analyses. The plain ping-pong bi-bi model (Equation 2.16) is used to illustrate the advantages of the proposed technique. It must be noticed that in any identifiability analysis, it is assumed that the model structure is error-free.

3.2 Methods

3.2.1 Parameter estimation procedure of the ping-pong bi-bi model

The structural and practical identifiability of the plain ping-pong bi-bi model will be assessed in this chapter. This model was already introduced in section 2.2.2 and is given in Equation 3.1.

$$\frac{v}{[E]_t} = \frac{V_\mathrm{f} V_\mathrm{r}\left([A][B] - \frac{[P][Q]}{K_\mathrm{eq}}\right)}{\begin{array}{l} V_\mathrm{r} K_{\mathrm{m_B}}[A] + V_\mathrm{r} K_{\mathrm{m_A}}[B] + V_\mathrm{r}[A][B] + \dfrac{V_\mathrm{f} K_{\mathrm{m_Q}}[P]}{K_\mathrm{eq}} + \dfrac{V_\mathrm{f} K_{\mathrm{m_P}}[Q]}{K_\mathrm{eq}} \\ \quad + \dfrac{V_\mathrm{f}[P][Q]}{K_\mathrm{eq}} + \dfrac{V_\mathrm{f} K_{\mathrm{m_Q}}[A][P]}{K_\mathrm{eq} K_\mathrm{ia}} + \dfrac{V_\mathrm{r} K_{\mathrm{m_A}}[B][Q]}{K_\mathrm{iq}} \end{array}} \tag{3.1}$$

where V_f and V_r represent the maximum velocity of the forward and backward reaction, $K_{\mathrm{m_A}}$, $K_{\mathrm{m_B}}$, $K_{\mathrm{m_P}}$, and $K_{\mathrm{m_Q}}$ the Michaelis constants, K_ia and K_iq the dissociation constants, and K_eq the equilibrium constant (Segel, 1975). However, to estimate the values of the different parameters the model complexity is typically reduced by splitting the model into different submodels, i.e. the forward initial reaction rate and the backward initial reaction rate (Shin and Kim, 1998; Al-Haque et al., 2012). By setting all the product concentration related variables (i.e. $[P]$ and $[Q]$) to zero, the forward initial reaction rate is obtained (Equation 3.2).

$$\frac{v_\mathrm{forw}}{[E]_t} = \frac{V_\mathrm{f}[A][B]}{K_{\mathrm{m_B}}[A] + K_{\mathrm{m_A}}[B] + [A][B]} \tag{3.2}$$

To obtain the backward initial reaction rate, the substrate concentrations $[A]$ and $[B]$ are set to zero, yielding Equation 3.3.

$$\frac{v_\mathrm{back}}{[E]_t} = \frac{V_\mathrm{r}[P][Q]}{K_{\mathrm{m_Q}}[P] + K_{\mathrm{m_P}}[Q] + [P][Q]} \tag{3.3}$$

When the forward initial reaction rate (Equation 3.2) and the backward initial reaction rate (Equation 3.3) are calibrated, only three more parameters need to be estimated: K_{eq}, K_{ia}, and K_{iq}. K_{eq} can be calculated using the Haldane relationship shown in Table 2.2. The two dissociation parameters K_{ia} and K_{iq} are estimated using the initial rate approach, i.e. by varying the concentrations of both the substrates and the products, these parameter values can be estimated. This approach was used by Shin and Kim (1998) to calibrate the ping-pong bi-bi model. The experimental designs, used by Shin and Kim (1998) to estimate the kinetic parameter values, are described in detail in Section 3.3).

3.2.2 Extended numerical identifiability analysis approach

To assess whether a model is both structurally and practically (locally) identifiable, the structural numerical local approach of Walter and Pronzato (1997) was adapted with respect to two major points. First, instead of starting the identifiability procedure at the real parameter values, the procedure is started at a random point in the parameter space $\mathbf{\Theta}$. This strategy allows to detect any optimisation problems related to the optimisation algorithm or objective function. Second, in case of practical identifiability, noise is added to the model output to mimic the behaviour of real-life experimental data.

The developed numerical identifiability procedure can be divided in three parts: 1) preparative part, 2) actual identifiability part and 3) postprocessing part (Figure 3.1).

Part 1: Preparative part

The first step in the preparative part is to select a model structure to perform the numerical identifiability analysis on. However, one needs to keep in mind that the model complexity should always be related with the available data. A high measurement error and/or low data availability will typically lead to a decrease of the practical identifiability, and thus a lower amount of parameters which can be estimated reliably. Therefore, it is important to balance the model complexity with the expected data quality and quantity. If this experimental information is not known (*a priori*), the identifiability procedure can help to determine minimum requirements of lab equipment to ensure the identifiability of the model. Second, the initial parameter values need to be chosen based on preliminary data or on expert knowledge.

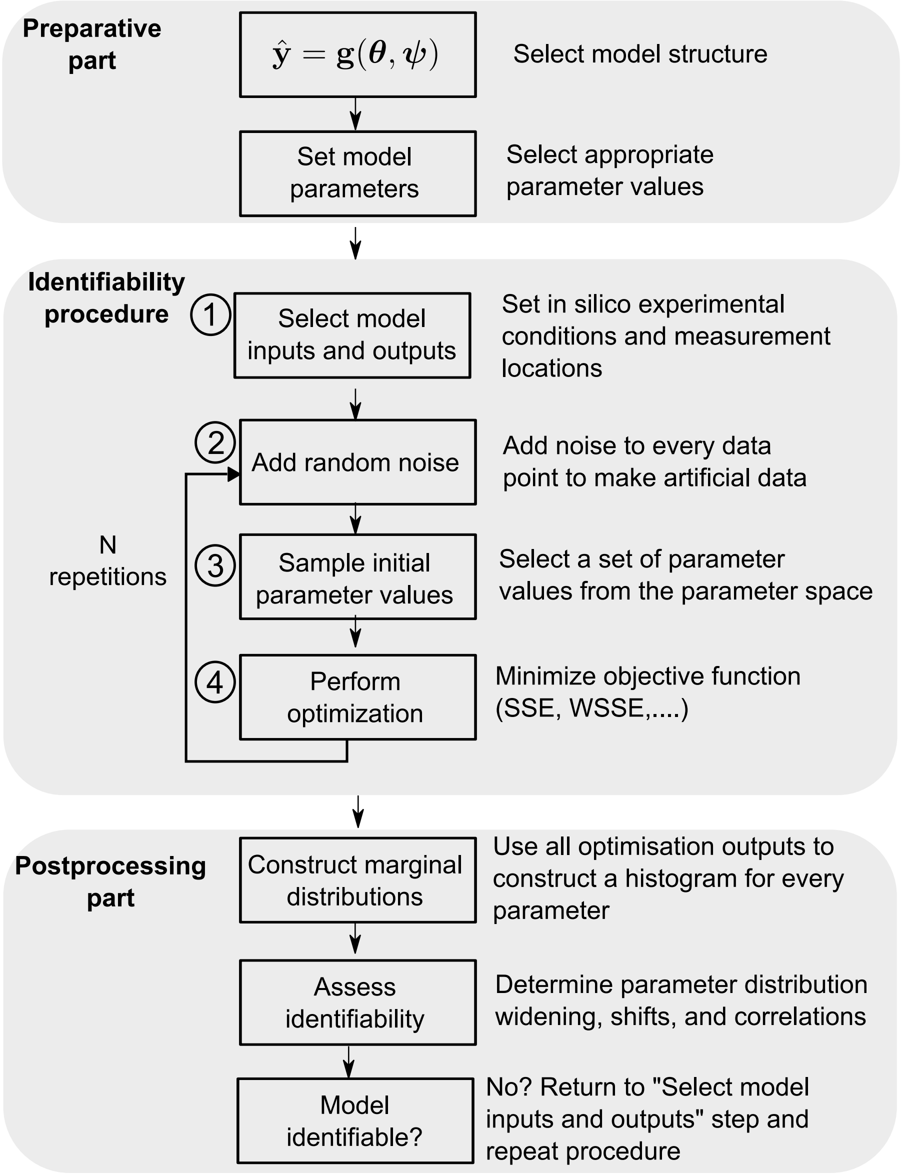

Figure 3.1: Schematic overview of the proposed numerical procedure for assessing structural and practical identifiability of (simple) models.

Part 2: Identifiability procedure

The first step of the actual identifiability procedure, is to select the model inputs and outputs (①). Model inputs comprise of all the variables which can be altered by the experimentalist, e.g. the initial conditions, substrate and product concentrations, feeding strategy (e.g. quenching of substrate or product),. . . The model outputs consist of all the process variables which can be potentially be measured. For a structural identifiability approach, all model outputs are measurable and the number of data points is unlimited. However, when assessing practical (local) identifiability, the actual experimental facilities and the type and number of experiments should reflect what is feasible in practice. The following step is to add noise to the model outputs. When structural identifiability is the aim, this step (②) may be ignored. For assessing practical identifiability, random noise should be added to each data point (②). The noise level and distribution can be chosen freely, however, in most cases the normal distribution with zero mean (i.e. Gaussian white noise) is most logical to choose. Moreover, the higher the noise levels the less likely it will be that the model will be practically identifiable. Noise levels should therefore be chosen realistically and if possible based on prior experiments or knowledge. Third (③), one should sample an initial parameter set from the parameter space $\boldsymbol{\Theta}$ according to the underlying marginal distribution of every parameter. The final step (④) in the identifiability procedure is to perform the optimisation, thus minimising the objective function based on the difference between the model and the *in silico* data. For white noise, objective functions like the sum of squared errors (SSE) or the weighted sum of squared errors (WSSE) are logical choices. However, the choice of the objective function should be related with the noise distribution which was selected. The identifiability procedure is then repeated N times to cover the entire parameter space. N should be sufficiently large to ensure that the (marginal) parameter distribution is correctly reproduced and the mean parameter estimate coincides with the true (nominal) parameter value. Moreover, the number of repetitions should be based on the dimensionality of the problem. In this respect, a good guideline to decide whether the number of samples is sufficiently large, is that the *posterior* parameter distribution does not change when adding more samples.

Part 3: Postprocessing

The postprocessing part consist of three steps: First from the N repetitions of the identifiability procedure, one gets N optimised parameter sets. For each individual parameter a marginal distribution can therefore be constructed. However, the use of scatter plots is strongly encouraged, since these plots allow to detect correlations between parameters. A strong correlation between two parameters can already indicate that identifying these parameters will be challenging (and maybe impossible). The second step is to derive characteristics from these distributions (e.g. percent deviation form the mean expected value) and detect whether identifiability problems are occurring or not. The final postprocessing step is to decide whether the model is identifiable based on the characteristics and/or scatter plots. If the model identifiability cannot be proven, it is possible that the information contained in the *in silico* is not sufficiently informative. In this case, one should return to the first step of the identifiability procedure in order to retrieve conditions under which model identifiability can be proven.

3.2.3 Implementations

The approach described above was implemented using the IPython Notebook environment (Pérez and Granger, 2007). This environment was selected because of the availability of the so-called magic functions, which drastically reduced the effort to use multiple cores of the calculation cluster. In order to perform the necessary optimisations, the optimisation module of the Scipy package was used and gave access to the minimise function (Jones et al., 2001). This function gives access to different local (and global) minimisation approaches. In this chapter the Nelder-Mead minimisation is used, which is a local optimisation method (Nelder and Mead, 1965). The plotting of the histograms was done by using the hist function in matplotlib.pyplot (Hunter, 2007).

3.3 Results and Discussion

The presented methodology is applied to the plain ping-pong bi-bi kinetics to examine whether the model structure (Equation 3.1) is at least locally identifiable. The local identifiability is assessed for the parameter values (Table 3.1) and experimental conditions (i.e. substrate and product concentrations) reported by Shin and Kim (1998). To assess the structural and practical identifiability, the model is also split into different submodels, since this is also the approach which was used by Shin and Kim (1998) to calibrate the model. For each of the submodels both structural local identifiability (i.e. sufficient and noise-free data) and practical local identifiability (i.e. experimental limited and noisy data) were investigated. In both cases, the chosen objective function was the weighted sum of squared errors (WSSE) (Equation 3.4).

$$J(\boldsymbol{\theta}) = \sum_{i=1}^{N} \frac{(y_i - \hat{y}(\boldsymbol{\theta}, \boldsymbol{\psi}_i))^2)}{\sigma_i} \tag{3.4}$$

where y_i represents the *in silico* data points, $\hat{y}(\boldsymbol{\theta}, \boldsymbol{\psi}_i)$ the model output for a specific parameter set $\boldsymbol{\theta}$ and experimental conditions $\boldsymbol{\psi}_i$, and σ_i the measurement standard deviation.

Table 3.1: The different kinetic parameter values of the plain ping-pong bi-bi mechanism, which were calibrated for ω-transaminase by Shin and Kim (1998).

Kinetic parameters	Value
V_f	$0.42\,\mathrm{mM/min}$
V_r	$5.18 \times 10^{-4}\,\mathrm{mM/min}$
$K_{\mathrm{m_A}}$	$35.03\,\mathrm{mM}$
$K_{\mathrm{m_B}}$	$9.58\,\mathrm{mM}$
$K_{\mathrm{m_P}}$	$1.07\,\mathrm{mM}$
$K_{\mathrm{m_Q}}$	$0.54\,\mathrm{mM}$
K_ia	$1.02 \times 10^{-2}\,\mathrm{mM}$
K_iq	$2.85\,\mathrm{mM}$
K_eq	$0.42\,\mathrm{mM}$

3.3.1 Structural local identifiability

To assess the structural local identifiability of the different submodels, the experimental conditions used by Shin and Kim (1998) are used as model inputs (Step ① of the identifiability procedure). For each of the individual submodels, the corresponding model inputs will be discussed in more detail. To obtain the posterior parameter distributions, 15 000 repetitions (N) of the identifiability procedure are executed by using noise-free data.

Forward initial reaction rate parameters

In order to calibrate the forward initial reaction rate, Shin and Kim (1998) performed experiments at different concentrations of the two substrates. More specific, at fixed experimental concentrations of the pro-chiral amine donor $[A]$ (10, 30, 50, 70 and 100 mM), the ketone substrate $[B]$ ranged from 10 and 300 mM (i.e. 10, 30, 50, 100 and 300 mM). Shin and Kim (1998) performed every experiment twice, yielding a total of *in silico* 50 experiments. These experimental conditions are used as model inputs to calculate the forward initial reaction rate. The structural identifiability procedure yielded the marginal distributions of the forward initial rate parameters (i.e. V_f, $K_{\mathrm{m}_\mathrm{A}}$, and $K_{\mathrm{m}_\mathrm{B}}$) given in Figure 3.2. From this figure, it can be seen that the original parameter values are not retrieved in all cases, since only about 12 000 out of 15 000 end up in the expected parameter value. For a structural identifiability analysis, it is expected that the objective function approaches zero when moving to the real parameter values. Since all the "bad" parameter sets yield a high objective function value ($J(\hat{\boldsymbol{\theta}}) > 10$) (Figure 3.2), it can be concluded that the problem is related with the optimisation algorithm.

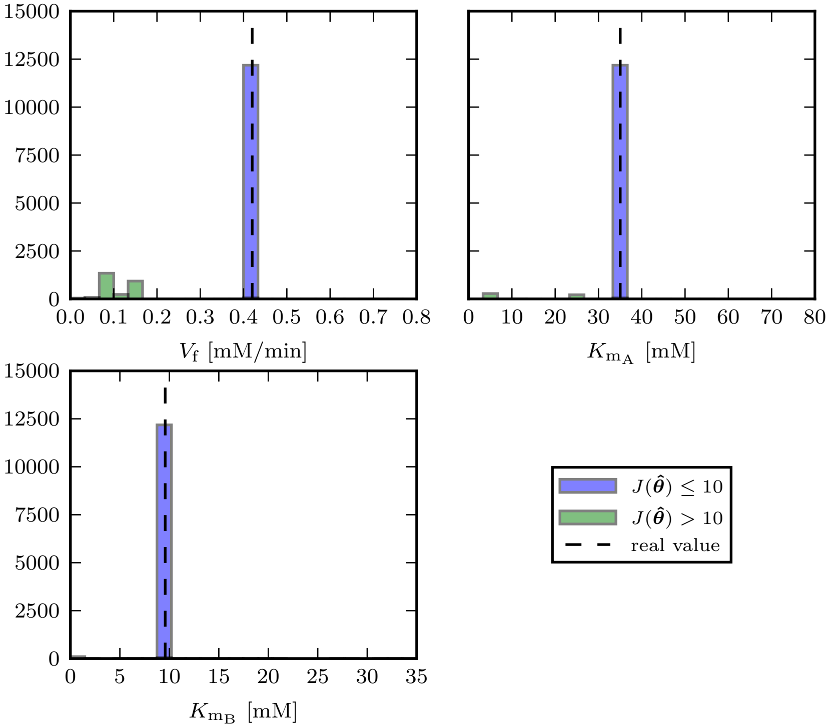

Figure 3.2: Marginal distributions for the three forward parameters. 15 000 initial parameter samples were locally optimised using the *in silico* data.

To illustrate that other optimisation methods might be more appropriate, 5000 optimisations were performed using the basin-hopping algorithm which is a global optimisation algorithm (Wales and Doye, 1998). This algorithm consists of three different steps which are iteratively repeated: first the parameter values are randomly perturbated, next a local optimisation is performed, finally the obtained parameter values are accepted or rejected based on the value of the objective function. The application of this global algorithm yields more robust minimisations , since in 90 % of the optimisations it retrieves the original parameter set (Figure 3.3). This is an improvement of 10 % compared to the local optimisation approaches. However, the local optimisation algorithm from Nelder-Mead is used throughout this chapter, since it can be easily decided whether the algorithm successfully finished its search by comparing the objective function value. Moreover, Al-Haque et al. (2012) (and probably also Shin and Kim (1998), but they provided no detailed information) used the Nelder-Mead simplex algorithm to perform a minimisation. As such, the robustness of this approach can be assessed.

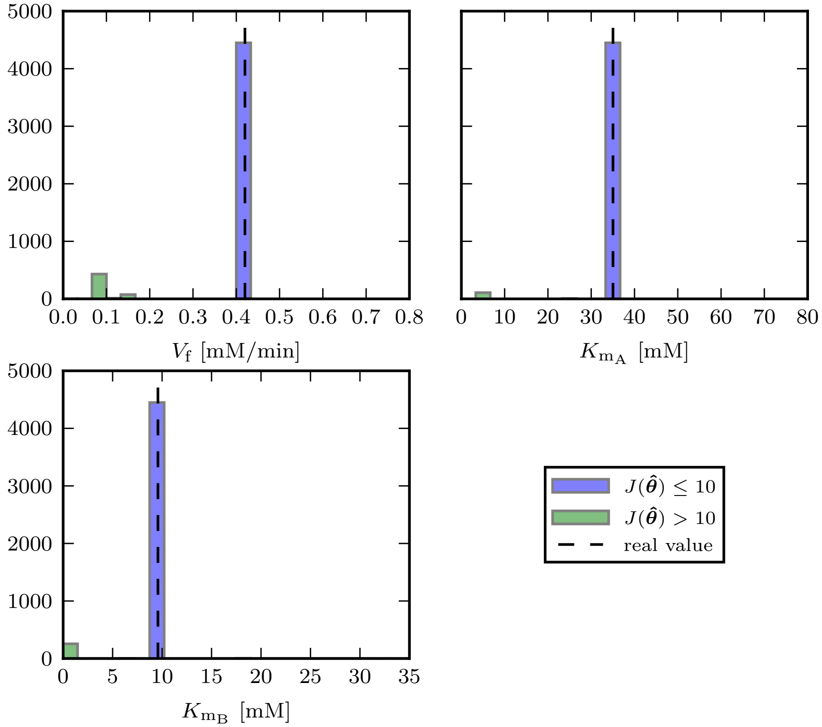

Figure 3.3: Marginal distributions for the three forward parameters when using a the global basin-hopping algorithm. 5000 initial parameter samples were globally optimised using the *in silico* data.

Backward initial reaction rate parameters

To assess the structural identifiability of the backward initial reaction rate (Equation 3.3), the experimental conditions used by Shin and Kim (1998) are used. At fixed experimental concentrations of the coproduct ketone $[P]$ (1, 2, 3, 5 and 10 mM), the chiral amine product $[Q]$ ranged from 10 to 50 mM (i.e. 10, 20, 30, 40 and 50 mM). Every experiment is performed twice, yielding a total of *in silico* experiments. These experimental conditions were used as model inputs for the backward initial reaction rate. The structural local identifiability analysis (Figure 3.4) yields comparable results as the forward initial reaction rate, i.e. all backward parameters are structural identifiable and the Nelder-Mead algorithm is unable to retrieve the "real" parameter values for all optimisations (only about 80 % of the optimisations find the minimum).

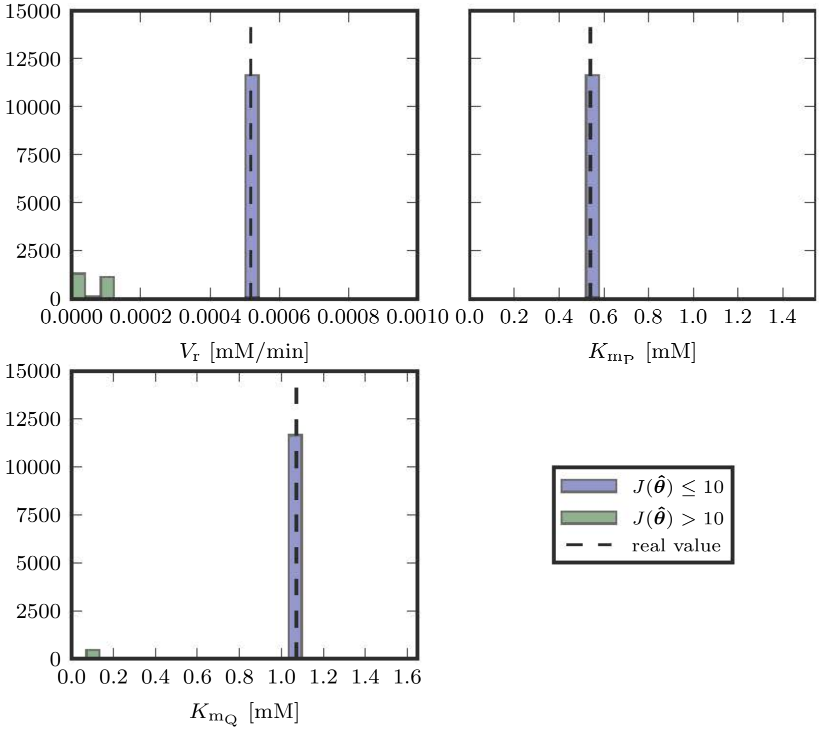

Figure 3.4: Marginal distributions for the three backward parameters. 15 000 initial parameter samples were locally optimised using the *in silico* data.

Dissociation constants

To obtain the parameter values of the dissociation constants K_ia and K_iq, Shin and Kim (1998) performed experiments at different substrate and product concentrations. The substrate concentrations of the pro-chiral amine donor $[A]$ and the ketone substrate $[B]$ are both set to 20, 30 and 50 mM. The product concentrations of the coproduct ketone $[P]$ and the chiral amine product $[Q]$ are set to 1, 2, 3, 5 and 10 mM and 10, 20, 30, 40 and 50 mM respectively. These experiments are also repeated twice, yielding a total of *in silico* experiments. The number of *in silico*experiments is much larger compared to the forward and backward initial reaction rate, but in the original article two additional inhibition parameters had to be calibrated which are not considered in this chapter. However, these 150 experiments will be used as model inputs for the plain ping-pong bi-bi model in Equation 4.2. In Figure 3.5, the results of the structural identifiability analysis are shown for both dissociation constants. In contrast to the results of the forward and backward initial reaction rates, all local optimisations yield the “real” parameter values independent from the initial parameter guesses. This observation indicates that both dissociation constants can be considered as (at least locally) structurally identifiable.

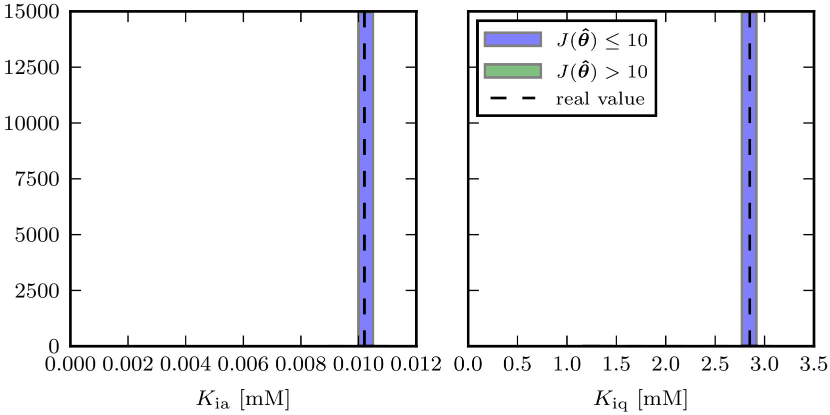

Figure 3.5: Marginal distributions for the two dissociation constants. 15 000 initial parameter samples were locally optimised using the *in silico* data.

3.3.2 Practical local identifiability

After checking the structural local identifiability, a practical identifiability analysis was performed. This procedure was performed for each submodel for 3 different noise levels: a relative Gaussian white noise with a standard deviation of 1, 2.5 and 5 % respectively. In this way higher values of v can have a larger absolute noise compared to lower v values. The model inputs used for the practical local identifiability are equal to those of the theoretical local identifiability.

Forward initial reaction rate parameters

From the results in Figure 3.6, it can be seen that the parameters are practically identifiable at a low measurement noise (i.e. maximum standard deviation of 2.5 %). At higher noise levels, the parameters can no longer be uniquely identified. This valuable information can be used to set minimum requirements with respect to the experimental equipment and/or measurement procedure to assure the practical identifiability of all parameters. It can also been observed that the marginal parameter distribution tend to skew to lower parameter estimates at higher noise levels. This skew is a result of the (high) correlations between the different parameters, and is typical for nonlinear models. At high parameter correlations, a change of the value of one parameter can be (partially) compensated by changing another parameter value. As a consequence, a reliable estimation of kinetic parameter values at high noise levels becomes a challenging task.

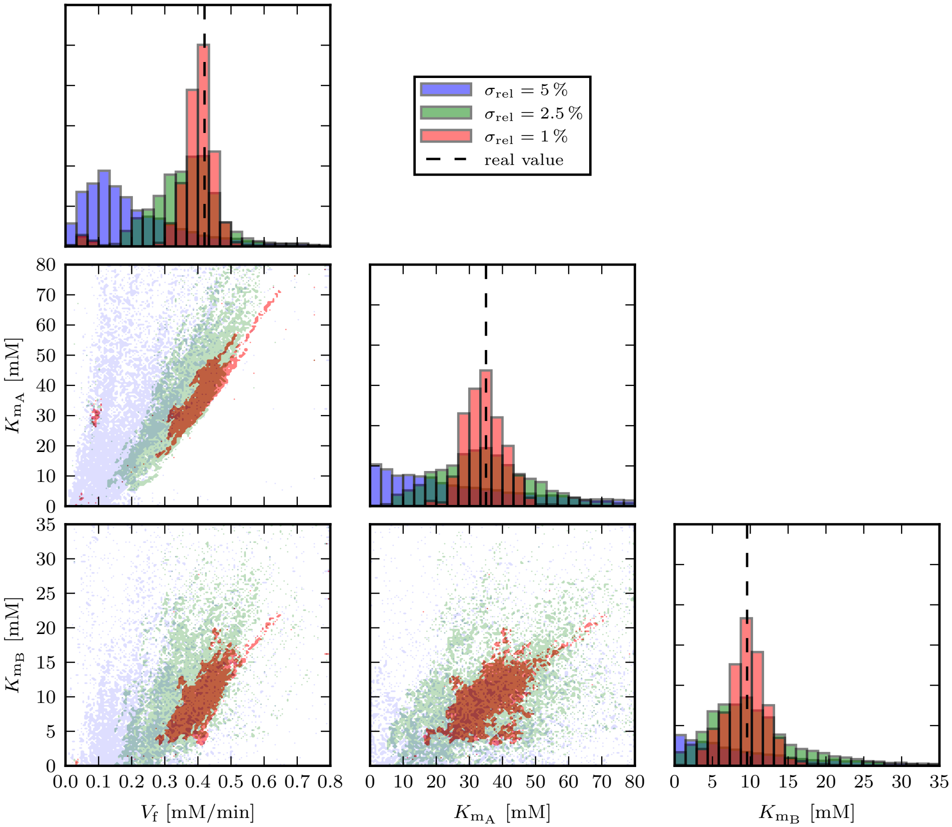

Figure 3.6: Scatter plot of the practical identifiability study for the three forward parameters.

Backward initial reaction rate parameters

The backward initial rate shows comparable results as the forward reaction rate regarding the practical identifiability, since the parameters become structurally unidentifiable at higher measurement errors. This conclusion is only valid for parameters V_r and $K_{\mathrm{m_P}}$ (Figure 3.7), since $K_{\mathrm{m_Q}}$ is practically unidentifiable for all measurement errors. Even for the optimistically low measurement error with a standard deviation of 1 % (i.e. 95 % of the measurements have a measurement error smaller or equal to 2 %), the parameter is unidentifiable. Therefore, it can be concluded that the value of $K_{\mathrm{m_Q}}$ reported by Shin and Kim (1998) is uncertain and thus more informative *in silico* experiments need to be designed to allow its proper estimation. Both $K_{\mathrm{m_P}}$ and $K_{\mathrm{m_Q}}$ have comparable parameter estimate values and were found to be (at least locally) theoretically identifiable. However, the experimental design differs significantly between P and Q: P is varied between 1 and 5 mM while Q is being varied between 10 and 50 mM. Therefore, it is expected that $K_{\mathrm{m_Q}}$ will become practically identifiable at low concentrations of Q.

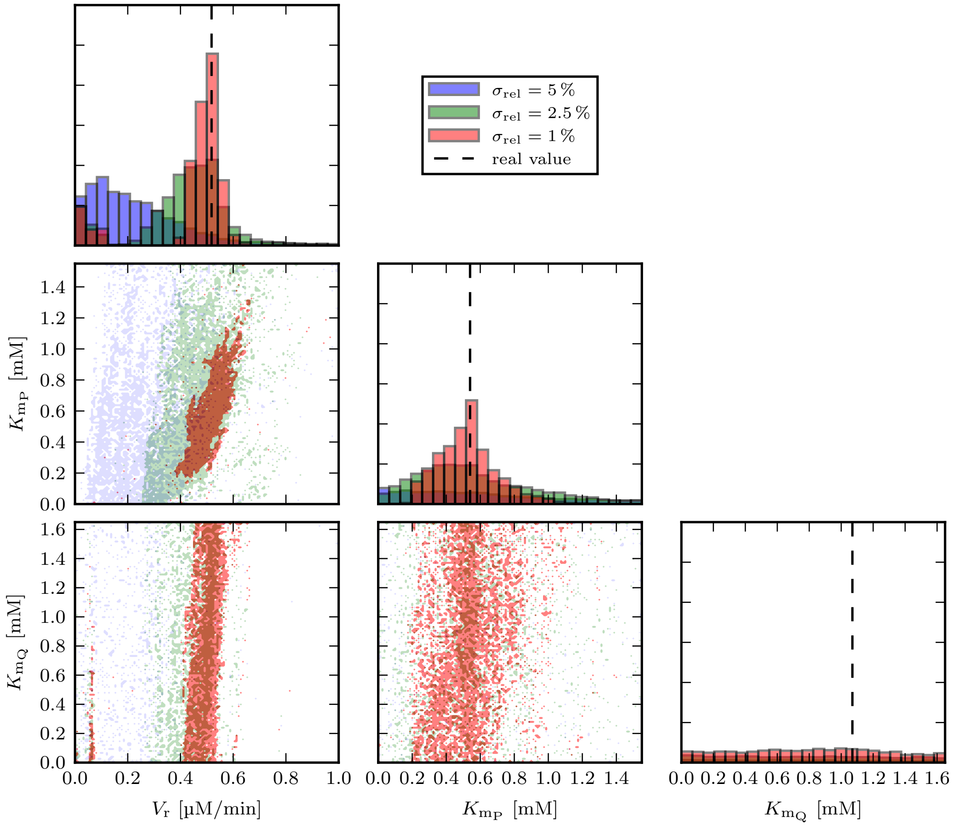

Figure 3.7: Scatter plot of the practical identifiability study for the three backward parameters.

Dissociation constants

The practical identifiability of both dissociation constants is shown in Figure 3.8. From this figure, it can be derived that the parameters are practically identifiable when the measurement error is low. The dissociation constants become already practical unidentifiable at a standard deviation of measurement of 2.5 %.

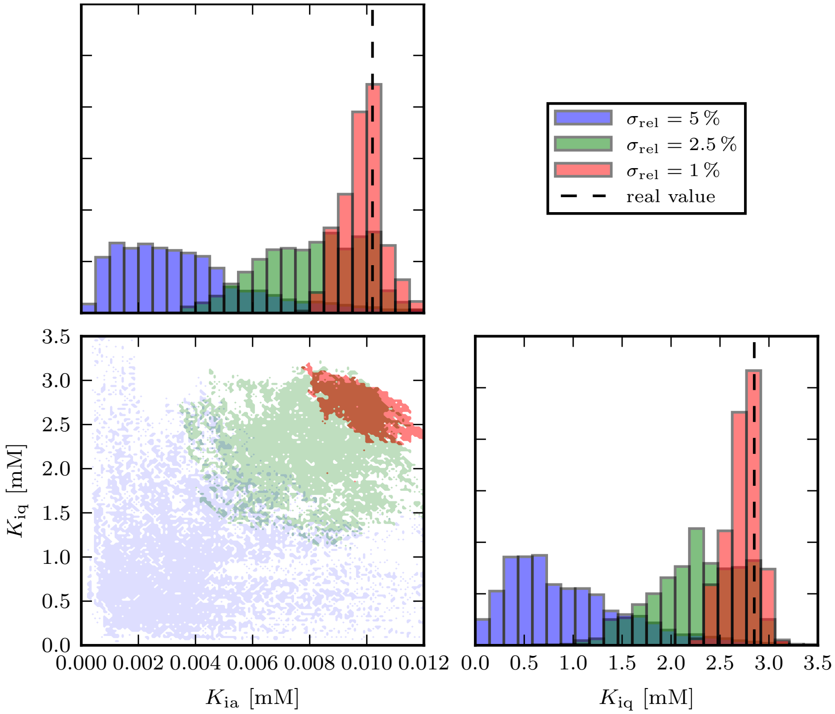

Figure 3.8: Scatter plot of the practical identifiability study for the two dissociation constants.

3.4 Conclusions

A conceptually simple yet powerful technique to assess the structural and practical local identifiability was presented. The identifiability technique of Walter and Pronzato (1997) was extended and is now also applicable to perform a practical identifiability analysis. Moreover, it also allows to assess the performance of the optimisation procedure in order to improve the robustness of the parameter estimation. The technique allows the model user who wants to perform modelling and calibration to verify whether the model under study is (at least locally) identifiable. The technique requires the use of a considerable amount of computational power, however this requirement depends on the desired accuracy and the complexity of the model. For simple models one can obtain high accuracy at a reasonable cost. The ping-pong bi-bi model was found to be structurally identifiable. However, using the experimental conditions used by Shin and Kim (1998), most parameters were found to be only practically identifiable at low measurement uncertainties. One Michaelis constant of the backward initial reaction rate was found to be unidentifiable for the current experimental design, stressing the importance of a proper experimental design for an accurate and precise parameter estimation.

CHAPTER 4

APPLICATION OF ITERATIVE ROBUST MODEL-BASED OPTIMAL EXPERIMENTAL DESIGN FOR THE CALIBRATION OF BIOCATALYTIC MODELS

Abstract

The aim of model calibration is to estimate unique parameter values from available experimental data. The traditional approach of first gathering a multitude of data followed by performing a model calibration is inefficient, since the information gathered during experimentation is not used to optimise the experimental design. By applying an iterative model-based optimal experimental design algorithm, the limited amount of data collected is used to design additional informative experiments. The application of this algorithm allows to estimate the kinetic parameters of an ω-transaminase catalysed reaction in a more accurate way. The parameter confidence region estimated from the Fisher information matrix is compared with the likelihood confidence region, which is a more accurate, but also a computationally more expensive method. As a result, an important deviation between both approaches is found, confirming that linearisation methods should be applied with care for nonlinear models.

4.1 Introduction

The rate at which a biocatalyst converts substrates into products, depends on the availability of these molecules in the direct neighbourhood of such a biocatalyst.The relation between the reaction rate and the local environmental conditions can be formalised in a mathematical model. A well-known and widely used mathematical model is the Michaelis-Menten model (Equation 4.1), which describes the irreversible conversion of a substrate in a product by a biocatalyst.

$$v = \frac{V_{\mathrm{max}}[S]}{K_{\mathrm{m}} + [S]} \tag{4.1}$$

where v denotes the reaction rate, $[S]$ the substrate concentration, V_{max} the maximum reaction rate, K_{m} the Michaelis constant. If $[S] = K_{\mathrm{m}}$, the reaction rate v equals half of the maximum reaction rate V_{max}. The two parameters describing the relation between the reaction rate and the substrate concentration (V_{max} and K_{m}) depend on the substrate and enzyme used, but also on conditions such as the temperature and the pH. Consequently, these parameters need to be "updated" for each specific case. In most cases, experimental data are collected at certain conditions allowing to estimate the actual parameter values. In Chapter 2, the two major classes of methods were already introduced, i.e. the linear plotting and nonlinear optimisation. Since the linear plotting methods are inferior compared to the nonlinear optimisation methods, this latter will be the followed approach within this chapter and dissertation. However, this is only one step in the entire parameter estimation approach. The experiments, which were designed to gather the necessary data, had to be designed first. Traditionally, first all the experimental data are gathered before starting the parameter estimation exercise, whereby the gathered information is not used during the experimentation phase to adjust experimental conditions (i.e. experimentation and model calibration are conducted sequentially) (Lineweaver and Burk, 1934; Shin and Kim, 1998; Chen et al., 2008; Presečki and Vasić-Rački, 2009; Al-Haque et al., 2012; Verbruggen et al., 2016). This seems abstract, but can be easily illustrated using the Michaelis-Menten model (Equation 4.1). Let us assume, that initially no information is available about the parameter values, and thus a proper experimental design cannot be set up. Therefore, the experimentalist first has to perform experiments before trying to estimate the parameter values. However, if all experiments are designed in the region where $[S] \ll K_{\mathrm{m}}$, Equation 4.1 reduces to $v = V_{\mathrm{max}}[S]/K_{\mathrm{m}}$. In this way, only the ratio between the two parameters can be estimated, and thus more experiments need to be performed at concentrations well above K_{m} in order to estimate both parameters in a reliable way. To avoid this kind of problems, i.e. lack of informative data, it may be much more interesting to use an iterative approach as depicted in Figure 4.1.

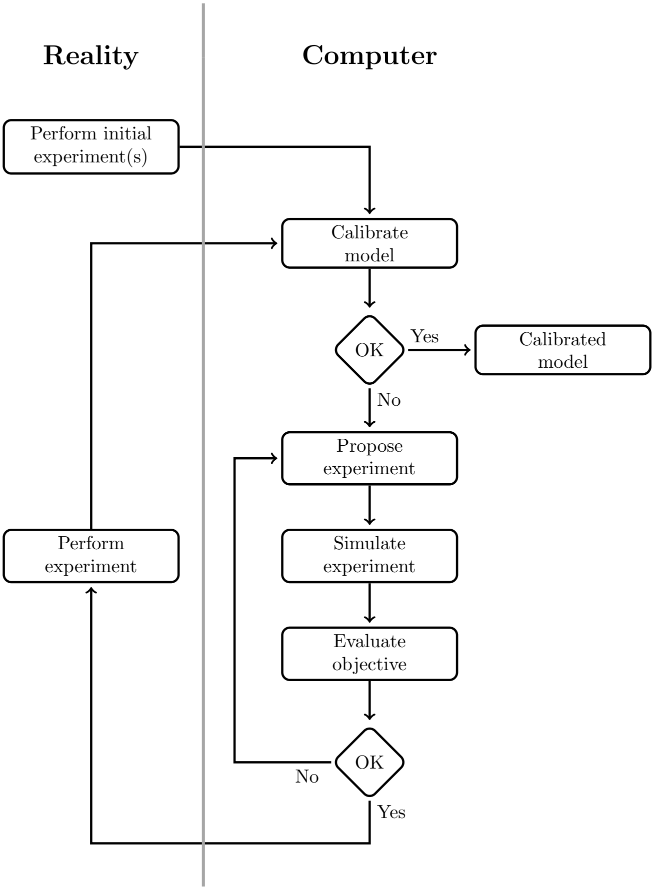

Figure 4.1: Schematic overview of the iterative optimal experimental design procedure (Dochain and Vanrolleghem, 2001; De Pauw, 2005).

Dochain and Vanrolleghem (2001), De Pauw (2005) and Donckels (2009) proposed this procedure in order to optimise the experimental conditions. First, some preliminary experiments are conducted, which can afterwards be used to perform an initial parameter estimation. Next, one needs to assess whether the reliability of the parameter estimates is sufficiently high. If not, new informative experiments need to be conducted to gain additional information. Using the model, regions with high information content for specific model parameters can be detected and new experiments will be designed taking this information into account. These new experiments are then executed, and afterwards this new information is again added and used for improving the quality of the parameter estimates. Application of this strategy is powerful and is often referred to as iterative Optimal Experimental Design (OED) (De Pauw, 2005; Goujot et al., 2012). Despite the availability of the theoretical framework for several decades, most of the available literature focusses on *in silico* studies. Due to the computational burden, the real-life application of these methods is fairly limited (e.g. Franceschini and Macchietto (2007) and Goujot et al. (2012)), and seldom applied to biocatalytic processes (Goujot et al., 2012). The aim of this chapter is to apply robust OED to a biocatalytic process in real life to illustrate its merit.

In the following sections, the parameter estimation procedure for ping-pong bi-bi kinetics (Equation 2.16) is introduced. Next, some theoretical background will be given about parameter confidence estimation, and how this can be used to design informative experiments. Next, a robust OED procedure is applied for this specific case. Finally, the confidence region of the parameter estimates is calculated using the traditional approach of the Fisher information matrix and compared with the likelihood method, which is a more accurate, but computationally more expensive approach.

4.2 Theoretical background

4.2.1 Reaction

The reaction under study is the synthesis of acetone (ACE) and (S)-1-methyl-3-phenylpropylamine (MPPA) from isopropylamine (IPA) and benzylacetone (BA) by means of a (S)-selective ω-transaminase ((S)-ω-TA). By using ω-transaminase (EC 2.6.1.X), optically pure chiral amines are produced by transferring the amine group from an amine donor, to a pro-chiral acceptor ketone, yielding a chiral amine and a ketone as co-product (Figure 4.2). The enzyme requires pyridoxal 5'-phosphate (PLP) as a cofactor to act as a shuttle to transfer the amine moiety between the molecules (Al-Haque et al., 2012; Hwang et al., 2005). In this dissertation, only the (S)-selective ω-transaminase is considered. It should be noted that in order to produce (R)-amines, (R)-selective transaminase are also available. However, these (R)-selective transaminases are generally less abundant in nature (Łyskowski et al., 2014).

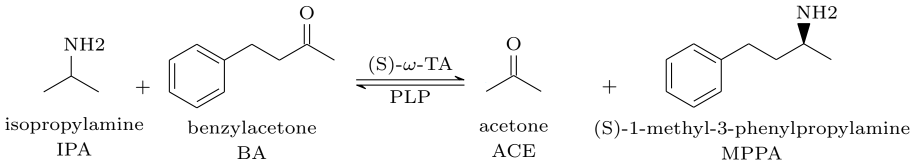

Figure 4.2: Conversion of isopropylamine and benzylacetone to acetone and (S)-1-methyl-3-phenylpropylamine by a (S)-selective ω-transaminase ((S)-ω-TA) in presence of coenzyme pyridoxal-5'-phosphate (PLP).

4.2.2 Kinetic Model

Since the reaction in Figure 4.2 is an asymmetric synthesis reaction catalysed by a (S)-selective ω-transaminase, it also obeys the ping-pong bi-bi mechanism (also known as substituted-enzyme mechanism) (Cornish-Bowden, 2004). The quasi steady-state model of the plain ping-pong bi-bi mechanism, i.e. without substrate or product inhibition, is given in Equation 4.2 (Segel, 1975). The model structure of this equation is similar to that of Equation 2.16, but the kinetic constants and degrees of freedom have been renamed for clarification and will also be used throughout this chapter.

$$\frac{v}{[E]_\mathrm{t}} = \frac{V_\mathrm{f}V_\mathrm{r}\left([IPA][BA] - \frac{[ACE][MPPA]}{K_\mathrm{eq}}\right)}{\begin{array}{l} V_\mathrm{r}K_\mathrm{BA}[IPA] + V_\mathrm{r}K_\mathrm{IPA}[BA] + V_\mathrm{r}[IPA][BA] + \dfrac{V_\mathrm{f}K_\mathrm{MPPA}[ACE]}{K_\mathrm{eq}} + \dfrac{V_\mathrm{f}K_\mathrm{ACE}[MPPA]}{K_\mathrm{eq}} \\ + \dfrac{V_\mathrm{f}[ACE][MPPA]}{K_\mathrm{eq}} + \dfrac{V_\mathrm{f}K_\mathrm{MPPA}[IPA][ACE]}{K_\mathrm{eq}K_\mathrm{iIPA}} + \dfrac{V_\mathrm{r}K_\mathrm{IPA}[BA][MPPA]}{K_\mathrm{iMPPA}} \end{array}} \tag{4.2}$$

where IPA, BA, ACE, and MPPA represent the substrate/product concentrations [mM], V_f, and V_r the maximum forward and backward reaction rate [nmol/(Umin)], and K_BA, K_IPA, K_MPPA, K_ACE the Michaelis constants [mM]. K_eq represents the equilibrium constant [-] and K_iIPA and K_iMPPA represent the dissociation constants [mM] (Cornish-Bowden, 2004; Segel, 1975). Equation 4.2 contains 9 kinetic parameters, which all have to be estimated from experimental data. However, by using the Haldane relationship, K_eq can be estimated from the other parameter values. The Haldane relationship for a plain ping-pong bi-bi mechanism is given in Equation 4.3 (Segel, 1975; Shin and Kim, 1998).

$$K_\mathrm{eq} = \left(\frac{V_\mathrm{f}}{V_\mathrm{r}}\right)^2 \frac{K_\mathrm{ACE}K_\mathrm{MPPA}}{K_\mathrm{IPA}K_\mathrm{BA}} \tag{4.3}$$

By using this relationship, the total number of kinetic parameters which need to be estimated is reduced to 8, and thus the difficulty of the model calibration is slightly but not substantially reduced.

4.2.3 Parameter estimation procedure of ping-pong bi-bi constants

As previously discussed, different approaches exist to estimate the kinetic parameter values of a model. However in this case, it can be challenging to calibrate all eight parameters of Equation 4.2. To reduce the model complexity the same procedure will be followed as in Chapter 3, i.e. reduce the number of parameters which need to be estimated simultaneously by reducing the full model to several simpler initial rate models. At very low product concentrations (i.e. typically during the first minutes of the reaction when $[MPPA]$ and $[ACE]$ are close to zero), Equation 4.2 can be reduced to the initial forward reaction rate v_{forw} in Equation 4.4. In this way, only three parameters need to be estimated simultaneously under these conditions.

$$\frac{v_{\mathrm{forw}}}{[E]_{\mathrm{t}}} = \frac{V_{\mathrm{f}}[IPA][BA]}{K_{\mathrm{BA}}[IPA] + K_{\mathrm{IPA}}[BA] + [IPA][BA]} \tag{4.4}$$

Similarly, at very low substrate concentrations (i.e. when $[IPA]$ and $[BA]$ are close to zero), Equation 4.2 can be reduced to the initial backward reaction rate v_{back} (Equation 4.5).

$$\frac{v_{\mathrm{back}}}{[E]_{\mathrm{t}}} = \frac{V_{\mathrm{r}}[MPPA][ACE]}{K_{\mathrm{ACE}}[MPPA] + K_{\mathrm{MPPA}}[ACE] + [MPPA][ACE]} \tag{4.5}$$

After calibrating both Equations 4.4 and 4.5, only two parameters remain to be calibrated in the original rate Equation 4.2, i.e. both dissociation constants K_{iIPA} and K_{iMPPA}. Al-Haque et al. (2012) proposed to use progress curves, which typically consists of the measurement and calibration of the time-dependent evolution of the different substrate and/or product concentrations. This analysis was performed at different substrate and product concentrations to estimate the dissociation constants and K_{eq}. However, in this chapter the initial rate approach used by Shin and Kim (1998), will be used to calibrate the dissociation constants since these data was already available. To ensure that the parameter estimates are suitable, progress curve analysis will be used to validate the full model under different conditions.

In this chapter, the parameter estimation is performed using the WSSE using the downhill simplex algorithm (Nelder and Mead, 1965), which is a local optimisation method. However, the downhill simplex algorithm was repeated a number of times for different initial parameter guesses to avoid ending up in a local minimum.

4.2.4 Confidence regions of parameter estimates

After finishing a (preliminary) model calibration, there is still the need to assess the quality of the obtained parameter estimates, an often forgotten or ignored step in parameter estimation. Some parameters might have little or no influence on the model output, and therefore the estimated parameter value will be meaningless. In this context, it was already stated in Chapter 2 that parameter values always need to be accompanied by a confidence region in order to be meaningful (De Pauw, 2005). The confidence region is the region in which it can be expected that, with a certain probability, the true parameters will lie (De Pauw, 2005). An “exact” confidence region, in the sense that it is not based on any approximations, is given by Equation 4.6 (Seber and Wild, 1989):

$$\left\{\boldsymbol{\theta} : J(\boldsymbol{\theta}) \leq c\, J(\hat{\boldsymbol{\theta}})\right\}, \tag{4.6}$$

where $c > 1$. The constant c is generally unknown, but can be approximated for a sufficiently large number of data points N (Beale, 1960; Seber and Wild, 1989):

$$\left\{\boldsymbol{\theta} : J(\boldsymbol{\theta}) \leq \left(1 + \frac{n_\mathrm{p}}{N - n_\mathrm{p}} F^{\alpha}_{n_\mathrm{p}, N-n_\mathrm{p}}\right) J(\hat{\boldsymbol{\theta}})\right\}, \tag{4.7}$$

where $F^{\alpha}_{n_\mathrm{p}, N-n_\mathrm{p}}$ is the upper α critical level of the F-distribution with n_p (number of estimated parameters) and $N - n_\mathrm{p}$ degrees of freedom. The confidence region produced by Equation 4.7, is generally referred to as the likelihood confidence region. The expectation surface of the objective function is planar if there exists a reparametrisation of $\hat{\mathbf{y}}(\boldsymbol{\psi}, \boldsymbol{\theta})$ that makes the function linear in the n_p parameters (Donaldson and Schnabel, 1987). If this is the case, the confidence regions constructed by the likelihood method are exact. One advantage of using the likelihood method is that the confidence region is not affected by any reparametrisation of the function $\hat{\mathbf{y}}$. However, to obtain the likelihood confidence region, a lot of calculations need to be performed since J needs to be evaluated at a sufficient number of points to produce a contour (Donaldson and Schnabel, 1987). To overcome this computational burden, most often linear approximations of the objective function J are used to construct the confidence region. The objective function $J(\boldsymbol{\theta})$ (Equation 2.19) can be approximated by a second order Taylor series:

$$J(\boldsymbol{\theta}) \approx J(\hat{\boldsymbol{\theta}}) + \frac{\partial J(\hat{\boldsymbol{\theta}})}{\partial \boldsymbol{\theta}} (\boldsymbol{\theta} - \hat{\boldsymbol{\theta}}) + \frac{1}{2} \left[(\boldsymbol{\theta} - \hat{\boldsymbol{\theta}})^{\mathsf{T}} \frac{\partial^2 J(\hat{\boldsymbol{\theta}})}{\partial \boldsymbol{\theta}\, \partial \boldsymbol{\theta}^{\mathsf{T}}} (\boldsymbol{\theta} - \hat{\boldsymbol{\theta}}) \right] \tag{4.8}$$

In a (global) minimum, the first derivative of the objective function J equals zero, reducing Equation 4.8 to Equation 4.9.

$$J(\boldsymbol{\theta}) \approx J(\hat{\boldsymbol{\theta}}) + \frac{1}{2} \left[(\boldsymbol{\theta} - \hat{\boldsymbol{\theta}})^{\mathsf{T}} \frac{\partial^2 J(\hat{\boldsymbol{\theta}})}{\partial \boldsymbol{\theta}\, \partial \boldsymbol{\theta}^{\mathsf{T}}} (\boldsymbol{\theta} - \hat{\boldsymbol{\theta}}) \right] \tag{4.9}$$

Substituting Equation 4.9 in Equation 4.7 yields a new expression for the confidence region:

$$(\boldsymbol{\theta} - \hat{\boldsymbol{\theta}})^{\mathsf{T}}\, \boldsymbol{\Phi}^{-1}(\hat{\boldsymbol{\theta}})\, (\boldsymbol{\theta} - \hat{\boldsymbol{\theta}}) \leq n_{\mathrm{p}}\, F^{\alpha}_{n_{\mathrm{p}}, N-n_{\mathrm{p}}} \tag{4.10}$$

where $\boldsymbol{\Phi}^{-1}(\hat{\boldsymbol{\theta}})$ is the inverse of the parameter estimation error covariance matrix defined by (De Pauw, 2005):

$$\boldsymbol{\Phi}(\hat{\boldsymbol{\theta}}) = 2 \frac{J(\hat{\boldsymbol{\theta}})}{N - n_{\mathrm{p}}}\, \mathbf{H}^{-1}(\hat{\boldsymbol{\theta}}) \tag{4.11}$$

where $J(\hat{\boldsymbol{\theta}})/(N - n_{\mathrm{p}})$ is an approximation of the residual variance s^2. For a sufficiently large number of samples and in case of a perfect model fit, s^2 will approximate the real variance σ^2 of the normal error distribution. This approximation is based on the fact that, assuming the model is correct, the residuals will be random errors and the average of these squared residuals is an estimate of the error variance. In the above equation, $\mathbf{H}^{-1}(\hat{\boldsymbol{\theta}})$ is the inverse Hessian matrix defined by:

$$\mathbf{H} = \left. \frac{\partial^2 J}{\partial \boldsymbol{\theta}\, \partial \boldsymbol{\theta}^{\mathsf{T}}} \right|_{\hat{\boldsymbol{\theta}}} \tag{4.12}$$

According to the Cramér-Rao inequality (Ljung, 1999), the inverse of the $\mathbf{H}$ is equal to the lower bound of the parameter estimation error covariance matrix $\boldsymbol{\Phi}$ if the measurement errors are independent samples taken from a normal distribution with zero mean.

4.2.5 Relation between Hessian matrix and Fisher information matrix

As stated in Equation 4.11, the parameter estimation error covariance matrix $\boldsymbol{\Phi}$ can be related to the Hessian matrix $\mathbf{H}$ in Equation 4.12. However, the parameter estimation error covariance matrix $\boldsymbol{\Phi}$ is most often calculated from the so-called Fisher information matrix (**FIM**), which was already introduced in Equation 2.26. However, the **FIM** is only an approximation of the Hessian matrix $\mathbf{H}$, and the relation between both matrices is given by (Press et al., 1992; Dochain and Vanrolleghem, 2001; Marsili-Libelli et al., 2003; De Pauw, 2005):

$$\begin{aligned}
\mathbf{H} &= \left.\frac{\partial^2 J}{\partial \boldsymbol{\theta}\,\partial \boldsymbol{\theta}^{\mathsf{T}}}\right|_{\hat{\boldsymbol{\theta}}} \\
&= \frac{\partial}{\partial \boldsymbol{\theta}}\frac{\partial}{\partial \boldsymbol{\theta}^{\mathsf{T}}}\left[\sum_{i=1}^{N}(\mathbf{y}_i - \hat{\mathbf{y}}(\boldsymbol{\psi}_i,\boldsymbol{\theta}))^{\mathsf{T}} \cdot \boldsymbol{\Sigma}_i^{-1} \cdot (\mathbf{y}_i - \hat{\mathbf{y}}(\boldsymbol{\psi}_i,\boldsymbol{\theta}))\right] \\
&= 2\sum_{i=1}^{N}\left[\left(\left.\frac{\partial \hat{\mathbf{y}}(\boldsymbol{\psi}_i,\boldsymbol{\theta})}{\partial \boldsymbol{\theta}}\right|_{\hat{\boldsymbol{\theta}}}\right)^{\mathsf{T}} \cdot \boldsymbol{\Sigma}_i^{-1} \cdot \left(\left.\frac{\partial \hat{\mathbf{y}}(\boldsymbol{\psi}_i,\boldsymbol{\theta})}{\partial \boldsymbol{\theta}}\right|_{\hat{\boldsymbol{\theta}}}\right)\right. \\
&\qquad\qquad \left. - (\mathbf{y}_i - \hat{\mathbf{y}}(\boldsymbol{\psi}_i,\boldsymbol{\theta}))^{\mathsf{T}} \cdot \boldsymbol{\Sigma}_i^{-1}\left(\left.\frac{\partial^2 \hat{\mathbf{y}}(\boldsymbol{\psi}_i,\boldsymbol{\theta})}{\partial \boldsymbol{\theta}\,\partial \boldsymbol{\theta}^{\mathsf{T}}}\right|_{\hat{\boldsymbol{\theta}}}\right)\right] \\
&= 2\sum_{i=1}^{N}\left[\left(\left.\frac{\partial \hat{\mathbf{y}}(\boldsymbol{\psi}_i,\boldsymbol{\theta})}{\partial \boldsymbol{\theta}}\right|_{\hat{\boldsymbol{\theta}}}\right)^{\mathsf{T}} \cdot \boldsymbol{\Sigma}_i^{-1} \cdot \left(\left.\frac{\partial \hat{\mathbf{y}}(\boldsymbol{\psi}_i,\boldsymbol{\theta})}{\partial \boldsymbol{\theta}}\right|_{\hat{\boldsymbol{\theta}}}\right)\right] \\
&\qquad - 2\sum_{i=1}^{N}\left[(\mathbf{y}_i - \hat{\mathbf{y}}(\boldsymbol{\psi}_i,\boldsymbol{\theta}))^{\mathsf{T}} \cdot \boldsymbol{\Sigma}_i^{-1}\left(\left.\frac{\partial^2 \hat{\mathbf{y}}(\boldsymbol{\psi}_i,\boldsymbol{\theta})}{\partial \boldsymbol{\theta}\,\partial \boldsymbol{\theta}^{\mathsf{T}}}\right|_{\hat{\boldsymbol{\theta}}}\right)\right]
\end{aligned} \tag{4.13}$$

Based on Equations 2.26 and 4.13, the Hessian matrix $\mathbf{H}$ can thus be rewritten as follows:

$$\mathbf{H} = 2\,\mathbf{FIM} - 2\sum_{i=1}^{N}\left[(\mathbf{y}_i - \hat{\mathbf{y}}(\boldsymbol{\psi}_i,\boldsymbol{\theta}))^{\mathsf{T}}\ \boldsymbol{\Sigma}_i^{-1}\left(\left.\frac{\partial^2 \hat{\mathbf{y}}(\boldsymbol{\psi}_i,\boldsymbol{\theta})}{\partial \boldsymbol{\theta}\,\partial \boldsymbol{\theta}^{\mathsf{T}}}\right|_{\hat{\boldsymbol{\theta}}}\right)\right] \tag{4.14}$$

The relation between the Hessian $\mathbf{H}$ and the **FIM** is given in Equation 4.14, and from this equation it can be seen that they differ by the term:

$$2\sum_{i=1}^{N}\left[(\mathbf{y}_i - \hat{\mathbf{y}}(\boldsymbol{\psi}_i,\boldsymbol{\theta}))^{\mathsf{T}}\ \boldsymbol{\Sigma}_i^{-1}\left(\left.\frac{\partial^2 \hat{\mathbf{y}}(\boldsymbol{\psi}_i,\boldsymbol{\theta})}{\partial \boldsymbol{\theta}\,\partial \boldsymbol{\theta}^{\mathsf{T}}}\right|_{\hat{\boldsymbol{\theta}}}\right)\right] \tag{4.15}$$

The term consists of three components: the estimation error $(\mathbf{y}_i - \hat{\mathbf{y}}(\boldsymbol{\psi}_i,\boldsymbol{\theta}))$, the inverse measurement error covariance matrix $\boldsymbol{\Sigma}_i^{-1}$, and the second derivatives of

$\hat{\mathbf{y}}$ to the parameters, also known as the “curvature”. For a model which has successfully been calibrated using the available data, the estimation error should be the random (i.e. normally distributed with mean 0 and σ^2) measurement error of each point. Therefore, the second derivative terms tend to cancel out when summed over all points i (De Pauw, 2005), and thus Equation 4.9 can be reduced to

$$J(\boldsymbol{\theta}) \approx J(\hat{\boldsymbol{\theta}}) + (\boldsymbol{\theta} - \hat{\boldsymbol{\theta}})^{\mathsf{T}}\, \mathbf{FIM}\, (\boldsymbol{\theta} - \hat{\boldsymbol{\theta}}) \tag{4.16}$$

As stated before, this is only true for linear models and when the model fits the data perfectly, i.e. the model structure is correct and the global minimum is found (De Pauw, 2005). Marsili-Libelli et al. (2003) proposed to use the conceptual difference between the Hessian matrix **H** and the **FIM** to detect inaccurate parameter results because the optimisation algorithm will be terminating far from the optimum. This method was successfully applied to two simple ecological models using *in silico* generated data. However, De Pauw (2005) pointed out that also other factors beside the premature convergence might influence the difference between the Hessian matrix **H** and the **FIM**. First, the model could be inadequate. Second, by fixing some parameters at specified values, an unsatisfactory model fit might be obtained (although being the global optimum for the selected parameter subset). Therefore, the difference between the Hessian matrix and the **FIM** can be used as an indicator for model inadequacies, local minima and/or non-normally distributed residuals (De Pauw, 2005). In this chapter, both the Hessian matrix **H** and the **FIM** will be used to calculate the confidence regions, since this will allow to determine whether the model is calibrated properly.

4.2.6 Optimal Experimental Design for parameter estimation

As introduced in Chapter 2, the aim of optimal experimental design for parameter estimation (OED/PE) is to perform experiments which lead to highly confident parameter estimates with minimal experimental effort. However, the optimal experiment designed by using Equation 2.33 is only optimal for the parameter set it was designed for. The **FIM** is calculated from the local sensitivity functions (see Equation 2.26), and for nonlinear models the **FIM** is directly influenced by the parameter values themselves. Therefore, all designs based on the **FIM** properties are called local designs (De Pauw, 2005). Prior to a model calibration no detailed knowledge is available about the actual parameter values, but this knowledge is important since it will determine the effectiveness of the experimental design.

To overcome this problem, more robust model-based optimal experimental design (rMbOED) methods have been proposed in literature which are insensitive (or at least less sensitive) to the starting values of the different parameters (Pronzato and Walter, 1988; Asprey and Macchietto, 2002). The use of rMbOED is therefore more suitable for parameter estimation, and will be used in this chapter.

The aim of robust OED is to design experiments which are suitable for an entire parameter space $\boldsymbol{\Theta}$ and not just for one parameter set $\boldsymbol{\theta}$. Different rMbOED methodologies exist in literature (Pronzato and Walter, 1988; Asprey and Macchietto, 2002; De Pauw, 2005). In this chapter the focus will be on the implementation and use of the maximin approach, since it was shown that this approach is superior compared to other robust methodologies (Asprey and Macchietto, 2002; De Pauw, 2005).

Maximin approach

The maximin approach, also known as the worst-case approach, aims to optimise the experiment design for any $\boldsymbol{\theta} \in \boldsymbol{\Theta}$ (Asprey and Macchietto, 2002). By searching for the experimental design $\boldsymbol{\psi}$ which maximises the information for the worst performing parameter set, this approach tries to find an acceptable performance for all parameter sets $\boldsymbol{\theta}$ in the parameter design space $\boldsymbol{\Theta}$. This results in a robust design $\boldsymbol{\psi}_{\mathrm{MMD}}$, which is given by Equation 4.17.

$$\boldsymbol{\psi}_{\mathrm{MMD}} = \arg\left\{ \max_{\boldsymbol{\psi}\in\boldsymbol{\Psi}} \left[\min_{\boldsymbol{\theta}\in\boldsymbol{\Theta}} \left[\det(\mathbf{FIM}[\boldsymbol{\theta},\boldsymbol{\psi}]) \right] \right] \right\} \tag{4.17}$$

Asprey and Macchietto (2002) stated that Equation 4.17 can also be written as an infinite dimensional problem, as the constraints must be satisfied for *all* values of $\boldsymbol{\theta}$ within the infinite parameter space $\boldsymbol{\Theta}$ (Equation 4.18).

$$\begin{gathered}\boldsymbol{\psi}_{\mathrm{MMD}} = \arg\left\{ \max_{\boldsymbol{\psi}\in\boldsymbol{\Psi},\boldsymbol{\theta}\in\boldsymbol{\Theta}} \Psi \right\} \\ \text{s.t. } \Psi \leq \det(\mathbf{FIM}[\boldsymbol{\theta},\boldsymbol{\psi}]), \quad \forall\boldsymbol{\theta} \in \boldsymbol{\Theta}\end{gathered} \tag{4.18}$$

Equation 4.18 represents an infinite dimensional problem, as the constraint must be satisfied for *all* values of $\boldsymbol{\theta}$ within the infinite set $\boldsymbol{\Theta}$ (Asprey and Macchietto, 2002). Gustafson (1983) suggested a general algorithm to solve such problems for constrained nonlinear optimisation under uncertainty. Instead of calculating the nested optimisation directly, the general algorithm allows to solve the optimisation in two separate steps: First, the experimental design $\boldsymbol{\psi}$ is optimised for the worst performing parameter set in a list of parameter sets with unacceptably low performance. Initially, this list only contains the initial parameter guess, but gradually expands during the iterations. Second, for the current design $\boldsymbol{\psi}$ the worst performing parameter set $\boldsymbol{\theta}$ within the parameter space $\boldsymbol{\Theta}$ is searched for. If a new parameter set is found which performs worse for the current optimal design, the parameter set is added to the list of parameter sets with low performance and the procedure is repeated. Otherwise it can be concluded that the current optimal design is robust for the parameter space $\boldsymbol{\Theta}$ (Asprey and Macchietto, 2002). The practical implementation of the algorithm is discussed in more detail by Asprey and Macchietto (2002). The maximin optimisation is performed using the particle swarm optimisation (PSO) algorithm, a global optimisation method which is informally explained here. PSO makes use of a population of particles (a so-called “swarm”) which is moving through the experimental design space. Every particle consists of its current position in the design space, its fitness value at this position, the displacement vector which will be used to compute the next position, its previous best position and the corresponding fitness. Within this swarm, a network exists in which the information about the best position and fitness is exchanged. Each particle recieves this information from a limited number of particles (i.e. a neighbourhood), and hence this information is used to calculate the following displacement vector which is likely to direct to a region with a more optimal fitnes. By incorporating this approach in an iterative procedure, it has been shown in literature that this approach is powerful to find global optima (Kennedy and Eberhart, 1995; Poli, 2008).

4.2.7 Curvature measures of nonlinearity

The linear approximation of the confidence region (Equation 4.10) is only exact for linear models. Only in this case the objective function contours are of a quadratic form, meaning that the two-dimensional confidence regions are ellipses and the three-dimensional confidence regions are ellipsoids. However, for nonlinear models Equation 2.19 is not exactly quadratic, and as a result the linear approximation of Equation 4.10 is only appropriate if the curvature of the model (i.e. second derivative of $\hat{\mathbf{y}}$ to the parameters $\boldsymbol{\theta}$) is sufficiently small. In much of the applied literature (De Pauw, 2005; Donckels, 2009; Al-Haque et al., 2012), the importance of the curvature is ignored. Bates and Watts (1988) proposed relative curvature measures which allow to determine whether the model nonlinearity is important. These curvature measures can be divided in two kinds of curvatures, i.e. the *intrinsic* curvature and the *parameter-effects* curvature. The *intrinsic* curvature measures how much the expectation surface deviates from a plane (Benabbas et al., 2005). The *parameter-effects* curvature represents the degree of curvature induced by the choice of the parameters and its parametrisation. Bates and Watts (1980) found that the nonlinearity induced by the parametrisation is generally greater than the intrinsic nonlinearity of the model. Donaldson and Schnabel (1987) confirmed that the *parameter-effects* curvature provides an excellent indication when the linearisation method may produce less satisfactory results. Therefore, these relative curvature measures will be used to determine whether the linear approximation of the confidence region can be regarded as reliable. The calculation of the *intrinsic* and *parameter-effects* curvature is briefly introduced below.

Since the second and higher order derivatives of a linear function with respect to the parameters are zero, Bates and Watts (1988) used second order derivatives of the expectation function to measure the nonlinearity of a model. They introduced a $N \times n_\mathrm{p}$ derivative matrix $\dot{\mathbf{V}}$, where each row contains the gradient of $\hat{\mathbf{y}}$ at a specific sample point $\boldsymbol{\psi}_i$ to the n_p parameters $\boldsymbol{\theta}$

$$\dot{\mathbf{V}} = \frac{\partial \hat{\mathbf{y}}(\boldsymbol{\psi}, \boldsymbol{\theta})}{\partial \boldsymbol{\theta}} \tag{4.19}$$

and a $N \times n_\mathrm{p} \times n_\mathrm{p}$ second order derivative matrix $\ddot{\mathbf{V}}$

$$\ddot{\mathbf{V}} = \frac{\partial^2 \hat{\mathbf{y}}(\boldsymbol{\psi}, \boldsymbol{\theta})}{\partial \boldsymbol{\theta}\, \partial \boldsymbol{\theta}^\mathsf{T}} \tag{4.20}$$

where each face of $\ddot{\mathbf{V}}_i$ of $\ddot{\mathbf{V}}$ is a complete $n_\mathrm{p} \times n_\mathrm{p}$ second derivative matrix, or Hessian. From $\ddot{\mathbf{V}}$ the $n_\mathrm{p}(n_\mathrm{p}+1)/2$ nonredundant acceleration vectors can be easily extracted to construct a matrix $\ddot{\mathbf{W}}$ and be combined with the tangent vectors in $\dot{\mathbf{V}}$ to give

$$\mathbf{D} = \left(\dot{\mathbf{V}}, \ddot{\mathbf{W}}\right). \tag{4.21}$$

Matrix $\mathbf{D}$ can be uniquely decomposed into two matrices by using the QR decomposition. This decomposition yields an ortogonal matrix $\mathbf{Q}$ and an upper triangular matrix $\mathbf{R}$. By performing a QR decomposition on $\mathbf{D}$, the different acceleration vectors are projected into the tangent plane and into the space normal to the tangent plane but spanned by the acceleration vectors.

$$\mathbf{D} = \mathbf{QR} = [\mathbf{Q}_1|\mathbf{Q}_1^{\mathsf{T}}|\mathbf{Q}_2] \cdot \begin{bmatrix} \mathbf{R_{11}} & \mathbf{A}^{\boldsymbol{\theta}} \\ \mathbf{0} & \mathbf{A}^{i} \\ \mathbf{0} & \mathbf{0} \end{bmatrix} \tag{4.22}$$

where $\mathbf{R_{11}}$ is a $n_{\mathrm{p}} \times n_{\mathrm{p}}$ upper-left triangular matrix, which equals the full R matrix when performing a QR decomposition only on $\dot{\mathbf{V}}$. The matrices $\mathbf{A}^{\boldsymbol{\theta}}$ and $\mathbf{A}^{i}$ have dimensions $n_{\mathrm{p}} \times n_{\mathrm{p}}(n_{\mathrm{p}}+1)/2$ and $n_{\mathrm{p'}} \times n_{\mathrm{p}}(n_{\mathrm{p}}+1)/2$ respectively, and are used to form the parameter effects and intrinsic components of the curvature or acceleration array $\ddot{\mathbf{A}}$. The tangential components of the acceleration vectors are contained in $\mathbf{A}^{\boldsymbol{\theta}}$, while the normal components are contained in $\mathbf{A}^{i}$. The extent to which the acceleration vectors lie outside the tangent plane provides a measure of how much the expectation surface deviates from a plane, which is called the *intrinsic nonlinearity* since it does not depend on the parametrisation chosen for the expectation function, but only on the experimental design and the expression of the expectation function. However, the projections of the acceleration vectors in the tangential plane depend on the parametrisation of the model, and measure the nonuniformity of the parameter lines on the tangent plane, which is called the *parameter-effects nonlinearity* (Bates and Watts, 1988).

Bates and Watts (1988) pointed out that the curvatures, are measured in units of 1/response, and thus the values depend on the scaling of the data. To remove this dependence, a $(n_{\mathrm{p}} + n_{\mathrm{p'}}) \times n_{\mathrm{p}} \times n_{\mathrm{p}}$ *relative curvature array* can be calculated (Equation 4.23).

$$\mathbf{C} = \mathbf{R}_{11}^{-\mathsf{T}} \ddot{\mathbf{A}} \mathbf{R}_{11}^{-1} s\sqrt{n_{\mathrm{p}}} \tag{4.23}$$

where s represents $\sqrt{SSE/(N - n_{\mathrm{p}})}$. For data analysis, a simple overall measure of the nonlinearity is needed to assess the quality of a linear approximation. Bates and Watts (1988) proposed a simple overall scalar measure, i.e. root mean square (RMS) curvature measure, which is the square root of the average over all directions of the squared curvature (Benabbas et al., 2005), calculated by

$$c^2 = \frac{1}{n_{\mathrm{p}}(n_{\mathrm{p}}+2)} \sum_{n} \left[2 \sum_{p=1}^{n_{\mathrm{p}}} \sum_{q=1}^{n_{\mathrm{p}}} C_{npq}^2 + \left(\sum_{p=1}^{n_{\mathrm{p}}} C_{npp} \right)^2 \right]. \tag{4.24}$$

where index n goes from 1 to n_{p} for $c^{\boldsymbol{\theta}}$ and from $n_{\mathrm{p}} + 1$ to $n_{\mathrm{p}} + n_{\mathrm{p'}}$ for c^{i}.

4.3 Materials and methods

4.3.1 Experimental Approach

Stock solutions

For performing the different experiments, different stock solutions were prepared. First, a 20 mM KH_2PO_4 /K_2HPO_4 buffer was prepared at pH 8. From this buffer solution, a stock solution containing 0.1 mM pyridoxal-5'-phosphate (PLP) was prepared which was used to prepare the 500 mM ACE and 40 mM MPPA stock solutions. For all the stock solutions, the pH was measured and adjusted to obtain the required pH 8. All stock solutions were contained in the fridge to avoid concentration losses due to evaporation. The enzyme solution was prepared daily, using the buffer stock solution without PLP. The enzyme solution was prepared using ω-transaminase (ATA-wt) crude enzyme powder and freeze-dried cells with a specific activity varying between 1.56 and 1.58 U/mg and was provided by c-LEcta GmbH, Leipzig, Germany. The production host was *E. coli* BL21(DE3) and expression of ATA-wt (pLE1A17-ATA-50) was directed from a plasmid containing a strong T7 promotor by IPTG induction.

Experiments

The proper amount of buffer with PLP, ACE and MPPA were injected in a 4.5 mL glass vial. These vials were sealed using a lid with a septum and placed in a thermoshaker which was operated at an orbital agitation of 400 rpm and at a temperature of 30 °C. The sealing was performed to minimise the losses of substrate and products. After heating the solution for about 20 min, the reaction was started by injecting the enzyme solution. The injection time of the enzyme was considered as time zero, and samples were taken after 0.5, 15, 30, 45 and 60 min. Using a manual high-performance liquid chromatography (HPLC) syringe of 25 µL, 20 µL samples were taken from the vials and injected in a small HPLC vial containing 180 µL of 1 M NaOH in order to quench the reaction.

HPLC

The samples were analysed *ex situ* with a reversed-phase chromatography on an Ultimate 3000 HPLC (Dionex, Sunnyvale, CA, USA) equipped with a UV detector.

The column was a Gemini® 3 µm NX-C18 110 Å, 100 x 2.0 mm (Phenomenex, Torrance, CA, USA), and the analytes were eluted at a flow rate of 0.450 mL/min in isocratic mode using a mobile phase composition of 65 % Milli-Q aqueous phase pH 11 (adjusted with NaOH) and 35 % acetonitrile.

4.4 Results & Discussion

First, the model parameters of Equation 4.5 (V_r, K_ACE, and K_MPPA) are estimated using the iterative rMbOED approach. Next, the estimation of the 95 % confidence region is compared with the more accurate likelihood method. Afterwards, the rMbOED strategy is compared with a straightforward uniform design strategy to illustrate the merit of using rMbOED. Finally, the parameter estimation of the remaining model parameters (V_f, K_IPA, K_BA, K_iIPA, and K_iMPPA) is shown, but since the corresponding data were already collected earlier, no rMbOED was performed for these model parts.

4.4.1 Parameter estimation of backward initial reaction rate using iterative rMbOED

To retrieve the intrinsic parameter values of the backward initial reaction rate, experiments need to be performed at conditions which are most informative. The corresponding degrees of freedom for the experimental design are the concentrations of ACE and $MPPA$.

Preliminary expert-based experiments

Before starting the actual rMbOED, some preliminary experiments needed to be performed. By gathering such preliminary data, a very rough estimation of the different parameter values can be made. Initially, the experimental design ranges of $[ACE]$ and $[MPPA]$ were limited between 25 and 100 mM and 2.5 and 10 mM respectively. These small concentration ranges were considered to avoid inhibition, and were based on expert knowledge. The preliminary experiments are shown in Figure 4.3. For every experiment four to five reliable samples were collected (one sample every 15 min), which are afterwards being analysed by the HPLC in order to obtain the concentration of BA in the sample. The initial sample (after 0.5 min) is used to determine whether the samples showed an initial deviation with respect to the concentration. In case a major deviation from zero is found initially, the obtained data needs to be rescaled in order to obtain accurate reaction rate estimations. However, for none of the experiments such a major deviation is found. Once the data quality has been assessed, the initial reaction rate can be estimated using a linear regression ($y = a\,x$). Since all experiments showed a linear increase as a function of time, no samples were omitted for the linear regression. It is important only to use the linear part of the initial reaction experiments, otherwise the initial reaction rate assumption (i.e. the reaction is initially irreversible), does not longer hold true. The estimated initial reaction rates are also shown in Figure 4.3.

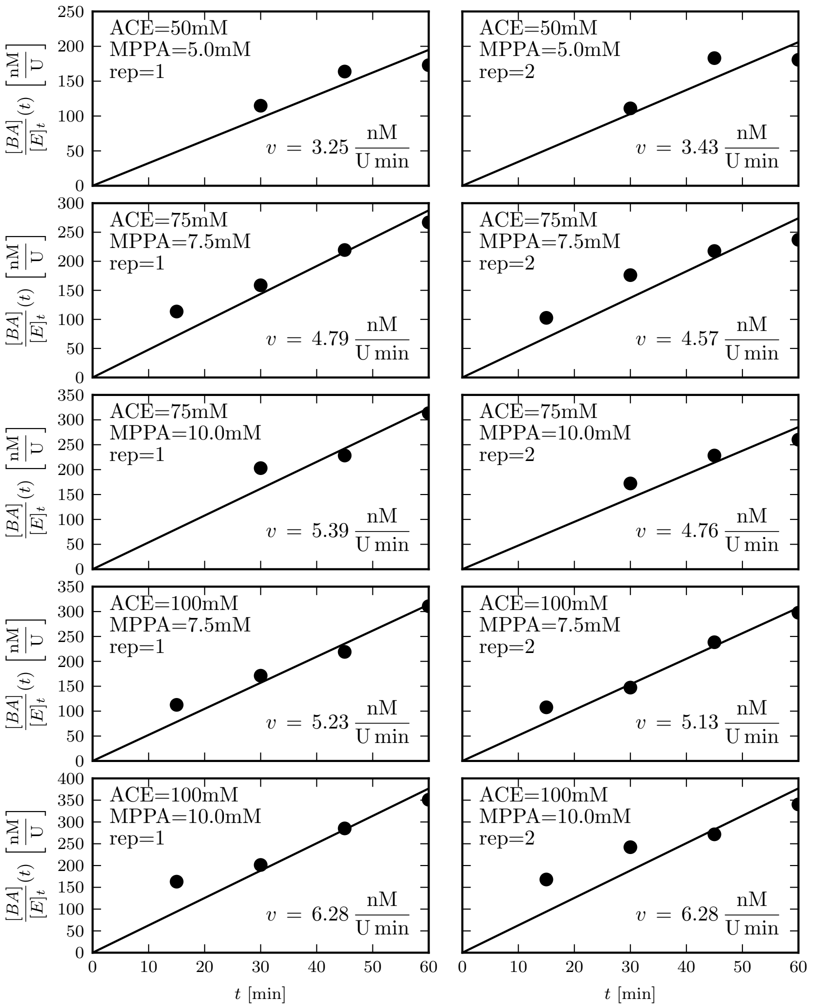

Figure 4.3: The initial reaction rate experiments of the preliminary expert-based design are estimated using a linear regression.

Using these preliminary expert-based experiments, a preliminary parameter estimation of the backward initial rate (Equation 4.5) can be performed. The corresponding parameter estimates and uncertainties are provided in Table 4.1. Since the 95 % confidence interval is much larger compared to the estimated parameter values, it is obvious that more informative experiments need to be conducted. Therefore, the rMbOED approach was used to design five new experiments with two repetitions each (total of 10 experiments). All newly designed experiments seem to be located at a concentration of 100 mM of *ACE*, indicating that more information can potentially be found at higher *ACE* concentrations. As shown in Table 4.1, the preliminary estimate of K_{ACE} is 263 mM which indicates that experiments need to be performed at higher *ACE* concentrations and is confirmed by Figure 4.4. Since parameter relative sensitivities are used in Figure 4.4, the sensitivity of the different parameters can be directly compared, yielding that V_{r} is the most sensitive parameter, followed by K_{MPPA} and K_{ACE}. It is interesting that the region where the parameters are most sensitive are quite different (indicated in grey), which allows to reduce correlation between the parameters. The sign of the local parameter relative sensitivity of V_{r} is positive, which indicates that an increase of V_{r} will lead to an increase of the v_{back} and *vice versa*. For the other two parameters (K_{MPPA} and K_{ACE}), the sign is negative, indicating that an increase in parameter value will lead to a decrease of v_{back}.

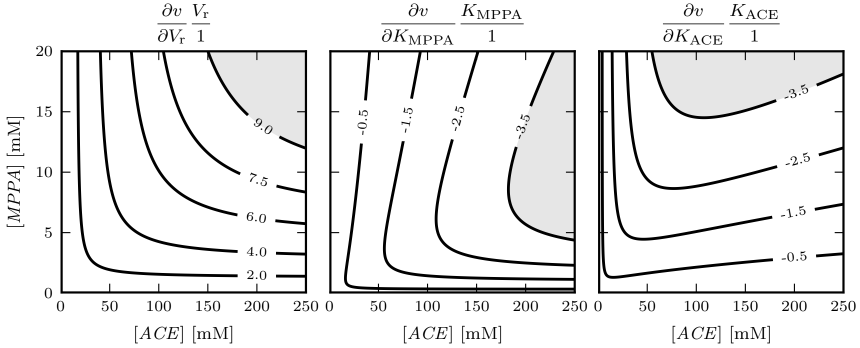

Figure 4.4: Local parameter relative sensitivity for the different parameters of the backward initial reaction rate for the estimated parameter values of the preliminary expert-based design iteration ($V_{\mathrm{r}} = 34\,\mathrm{nmol/(Umin)}$, $K_{\mathrm{MPPA}} = 21\,\mathrm{mM}$ and $K_{\mathrm{ACE}} = 263\,\mathrm{mM}$). Higher absolute values, i.e. larger deviation from zero, means that the parameter has more influence. The region where the parameter is most influential is indicated in grey.

Table 4.1: Experiments conducted for the first two iterative steps of the rMbOED. The parameter estimates and uncertainties are always based on the cumulative dataset, i.e. the parameter estimation of iteration $i+1$ also takes into account the data gathered in iterations i, $i-1$, …, 0.

Iteration	**Experiment**	**Conditions**		**Measurements**		**Estimated parameter**			
	nr.	$[ACE]$	$[MPPA]$	$v_{\mathrm{rep},1}$	$v_{\mathrm{rep},2}$		value	95 % CI	(SD)
preliminary expert-based design	1	50	5	3.25	3.43				
	2	75	7.5	4.79	4.57	K_{ACE}	= 263	±798	(337)
	3	75	10	5.39	4.76	K_{MPPA}	= 21	± 68	(28)
	4	100	7.5	5.23	5.13	V_{r}	= 34	± 86	(36)
	5	100	10	6.28	6.28				
1	6	35	10	2.93	2.77				
	7	115	20	8.04	8.09	K_{ACE}	= 263	±161	(76)
	8	200	2.5	6.86	6.89	K_{MPPA}	= 3.4	± 3.2	(1.5)
	9	200	7.5	8.47	8.21	V_{r}	= 24	± 12	(5.5)
	10	200	15	9.86	8.96				

Iteration 1 of rMbOED

Since no inhibition was observed in the preliminary expert-based experiments, the maximum allowed concentrations of $[ACE]$ and $[MPPA]$ were doubled to 200 and 20 mM respectively. It is expected that the extended range will yield more information for the parameter calibration, since the parameters are more sensitive at higher concentrations. The newly designed experiments are given in Table 4.1: iteration 1. For the current and the following iterations, the experiments proposed by the rMbOED algorithm were rounded to concentrations and volumes which were easy to handle in practice. Performing these experiments, 10 additional data points were generated, yielding a total of 20 data points (10 from iteration 0 and 10 from iteration 1) which were used to calibrate Equation 4.5. By comparing the estimated parameter values preliminary expert-based design and iteration 1, some changes were noticed. First, the K_{MPPA} value decreased from 21 mM to 3.4 mM and V_{r} decreased from 34 nmol/(Umin) to 24 nmol/(Umin).

Moreover, the standard deviations (SDs) of all parameters dropped with at least a factor 5, indicating that the experiments in iteration 1 were informative. A similar trend was observed for the 95 % confidence intervals (CIs), leading to the fact that for all parameters 0 was no longer within the 95 % CI. This might seem unimportant, but as long as 0 is part of the 95 % CI, the parameter has no significant added value for the model and thus may as well be omitted. In order to evaluate the effectivity of the rMbOED approach, the standard deviations between the different iteration need to be compared. The 95 % CIs are dependent on the number of experiments (see Equation 2.29), and thus make a fair comparison between the different iterations impossible as the 95 % CI decreases as the number of experiments increases.

Iteration 2 of rMbOED

Since no inhibition was observed in the previous iteration too, the maximum allowed concentration of $[ACE]$ was further increased to 300 mM (Table 4.2: iteration 2). Since K_{MPPA} is low $(3.4 \pm 3.2\,\mathrm{mM})$, it was decided to reduce the maximum $[MPPA]$ concentration to 16 mM. The stepwise increase/decrease of the maximum concentrations can look inefficient, however this approach has some advantages: The product concentrations in the current experimental setups are always well below 10 mM, so the current range is already high compared to the experiments. Moreover, the model structure is limited to only three parameters instead of requiring two additional parameters to describe the inhibition. More complex models are harder to calibrate and also require more data to estimate the parameters in a reliable way. The estimated parameter values in this iteration remained fairly constant (small decreases for all parameter values), but the standard deviations and 95 % uncertainty were further reduced by more than 30 % for all parameters.

Iteration 3 of rMbOED

Based on the parameter values of iteration 2, the maximum concentration of $[MPPA]$ was reduced to 10 mM since the estimated K_{MPPA} value was around 2.7 mM in the previous iteration, and thus will be most sensitive at values below 10 mM. The experiments proposed by the rMbOED algorithm were mainly located at the maximum concentration for both ACE and $MPPA$ (Table 4.2: iteration 3). Therefore, three out of five newly designed experiments are located at an ACE concentration of 250 mM and a $MPPA$ concentration of 10 mM. The newly gathered data allowed to perform a third calibration and uncertainty calculation. Like in previous iterations, the standard deviations (SD) for the different parameters further decreased, and it was decided that given the experimental uncertainty, the parameter values and confidence intervals were now sufficiently accurate. The local parameter relative sensitivities for the final iteration are given in Figure 4.5. Compared to the preliminary expert-based design (Figure 4.4), the sensitivities have changed (most pronounced for K_{MPPA}), stressing the importance of the parameter value on the local sensitivity and hence on the experimental design. This comparison yields that the parameter relative sensitivity of both Michaelis constants (i.e. K_{MPPA} and K_{ACE}) has decreased. Moreover, the correlation between the different parameters has changed, since the different regions of maximum sensitivity are relocated compared to the preliminary iteration. This last observation is discussed in the following section.

4.4.2 Parameter correlation

The parameter correlations for the different iterations can be calculated based on Equation 2.28 and are listed in Table 4.3. The correlation between the different parameters is high, especially between parameters V_{r} and K_{ACE}. From the local parameter relative sensitivities in Figure 4.5, it can be seen that the absolute value of the local parameter relative sensitivities increases when increasing both $[ACE]$ and $[MPPA]$, making it difficult to decouple the effect of both parameters. The parameter correlations can be reduced by increasing the maximum ACE concentration to about 500 mM, since the K_{ACE} will show a decreasing sensitivity at higher

Table 4.2: Experiments conducted for the final two iterative steps of the rMbOED. The parameter estimates and uncertainties are always based on the cumulative dataset, i.e. the parameter estimation of iteration $i+1$ also takes into account the data gathered in iterations i, $i-1$, …, 0. Therefore, the gathered information of Table 4.1 is also taken into account.

Iteration	**Experiment**	**Conditions**		**Measurements**		**Estimated parameter**				
	nr.	$[ACE]$	$[MPPA]$	$v_{\mathrm{rep},1}$	$v_{\mathrm{rep},2}$			value	95 % CI	(SD)
	11	50	12	3.39	3.73					
	12	105	2.5	4.61	4.55	K_{ACE}	=	262	±111	(54)
2	13	185	16	8.08	8.62	K_{MPPA}	=	2.7	± 1.8	(0.87)
	14	250	10	10.19	10.01	V_{r}	=	23.1	± 7.6	(3.7)
	15	300	2.5	8.59	8.84					
	16	50	10	2.74	2.99					
	17	190	2.5	5.15	5.57	K_{ACE}	=	250	± 81	(40)
3	18	250	10	8.40	8.74	K_{MPPA}	=	2.96	± 1.48	(0.73)
	19	250	10	9.74	8.72	V_{r}	=	21.7	± 5.3	(2.6)
	20	250	10	9.11	8.49					

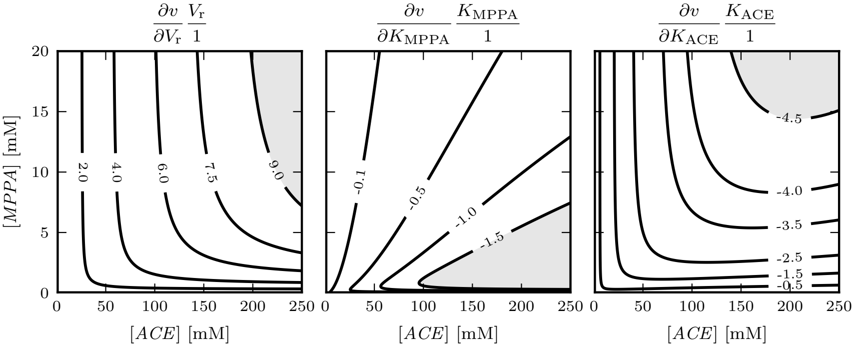

Figure 4.5: Local parameter relative sensitivity for the different parameters of the backward initial reaction rate for the estimated parameter values of the third/final iteration ($V_r = 21.7\,\text{nmol/(Umin)}$, $K_{MPPA} = 2.96\,\text{mM}$ and $K_{ACE} = 250\,\text{mM}$). The region where the parameter is most influential is indicated in grey.

concentrations (Figure 4.6). Another way to reduce the parameter correlations, is to design experiments using the modified E-optimal criterion instead of the the D-optimal criterion (Table 2.3) (De Pauw and Vanrolleghem, 2006b). However, the modified E-optimal criterion does only reduce the parameter correlations, not necessarily the parameter uncertainties. Therefore, the modified E-optimal criterion may yield uncorrelated, but uncertain parameter estimates (Dochain and Vanrolleghem, 2001). To overcome this problem, Franceschini and Macchietto (2008) proposed different novel criteria which ensure the simultaneous reduction of parameter uncertainties and correlations.

Table 4.3: Parameter correlation coefficients for the different iterations.

Iteration	V_r vs K_{MPPA}	V_r vs K_{ACE}	K_{MPPA} vs K_{ACE}
0	0.933	0.953	0.783
1	0.876	0.986	0.816
2	0.878	0.983	0.808
3	0.868	0.975	0.776

4.4.3 Measurement uncertainty

For the forward initial reaction rate a measurement uncertainty analysis had already been carried out. This measurement uncertainty analysis yielded that the

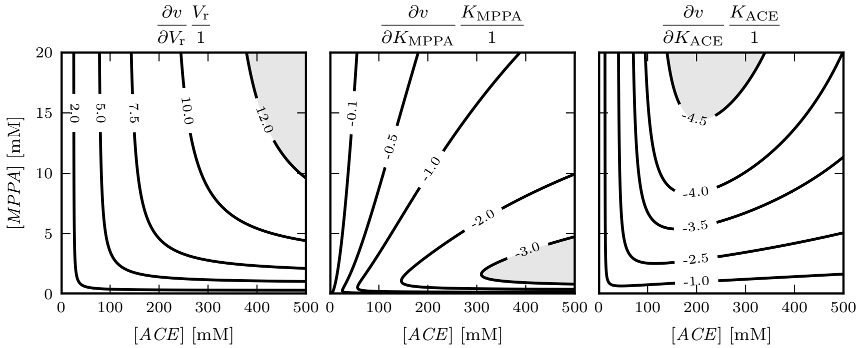

Figure 4.6: Local parameter relative sensitivity for the different parameters of the backward initial reaction rate for the estimated parameter values of the third/final iteration for an extended experimental design space of ACE. The region where the parameter is most influential is indicated in grey.

measurement uncertainty relative to the reaction rate, was following a normal distribution ($\mu = 0$ and $\sigma(v) = 0.10\,v$).

Therefore, for the backward reaction rate the same uncertainty was assumed and used to perform the rMbOED, since the same equipment and solutions were used. It would be possible to estimate the uncertainty during the actual experimentation, but this would require at least three repetitions for each experiment, which would increase the experimental effort considerably. Otherwise, estimating the uncertainty from the deviation between the data and model is only reasonable when a sufficiently high number of experimental data points have been collected, and thus is preferably done after the data collection. However, now it is verified whether the use of the relative error of the forward initial reaction rate is also valid for the backward initial reaction rate. The relative error $\epsilon_{\mathrm{rel},i}$ is given in Equation 4.25 and the corresponding histogram for the gathered data and calibrated model is given in Figure 4.7.

$$\epsilon_{\mathrm{rel},i} = \frac{\mathbf{y}_i - \hat{\mathbf{y}}_i(\boldsymbol{\theta}, \boldsymbol{\psi})}{\mathbf{y}_i} \tag{4.25}$$

The null hypothesis was that the relative measurement uncertainty ($\epsilon_{\mathrm{rel},i}$) was indeed following a normal distribution. This null hypothesis was tested using an omnibus test of normality proposed by D'Agostino (1971), and is appropriate to detect deviations from normality due to either skewness or kurtosis (D'Agostino and Pearson, 1973). This normality test is available in the scipy package (scipy.stats.normaltest) (Jones et al., 2001), and returns a two-sided χ^2 probability for the hypothesis test. The test yielded a p-value of 0.595, and

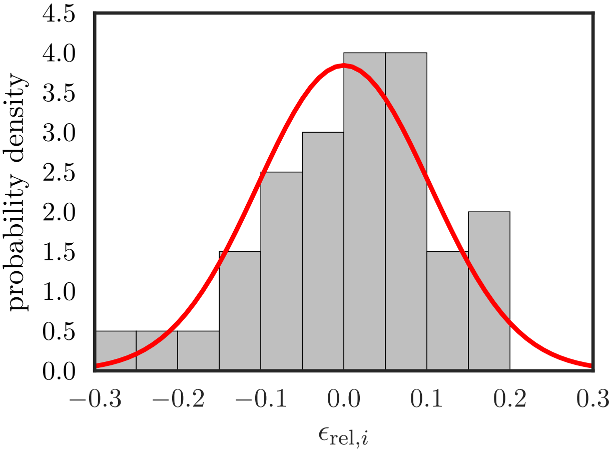

Figure 4.7: Histogram of the relative error $\epsilon_{\mathrm{rel},i}$ (Equation 4.25). The red line represents a normal probability density function with mean μ and standard deviation σ equal to 0 and 0.104 respectively.

thus the null hypothesis could not be rejected. Therefore it was concluded that the relative measurement uncertainty was following a normal distribution with $\sigma(v_{\mathrm{back}}) = 0.104\, v_{\mathrm{back}}$. The approach of estimating the measurement error by evaluating the difference between the model prediction and measurements is only valid if the model in Equation 4.5 represents the true model. The measurements of Tables 4.1 and 4.2 and the model prediction using the parameter values and covariance matrix obtained in the third iteration are shown in Figure 4.8. From this figure, it can be observed that the measurement uncertainty (which is calculated by using Equation 4.25, and thus only provides an estimate of the real error) is much larger compared to the predicted 95 % model confidence interval. Moreover, it can be noticed that the measurements performed in iteration 3 are overpredicted by the model. The enzyme used for this iteration was from a different batch, probably increasing the overall uncertainty of the parameter estimates. However, in this way the potential deviations between the batches originating from the enzyme production are also incorporated in the parameter uncertainty.

4.4.4 Difference between FIM and Hessian matrix H

In the previous calculations, the $\mathbf{FIM}^{-1}$ was used to estimate the covariance matrix. However, the $\mathbf{FIM}$ is only a good estimate of the Hessian $\mathbf{H}$ if no important deviation exists between the model and the data (Equation 4.15). Since the model under study is an algebraic model, it is straightforward to calculate the second

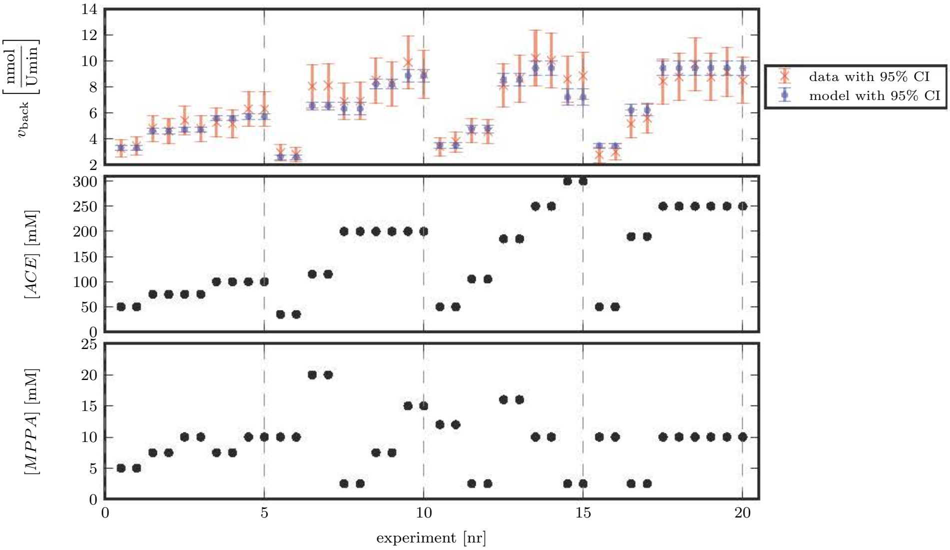

Figure 4.8: The model prediction v_{back} is shown for the different experiments shown in Table 4.1. The measurement uncertainty depicted is twice the standard deviation shown in Figure 4.7, and thus is only an estimate of the actual measurement error.

derivatives of $\hat{\mathbf{y}}$ to the parameters. The $\mathbf{H}-2\,\mathbf{FIM}$ is given in Equation 4.26 and is very small compared to the $\mathbf{H}$, since the maximum relative deviation between the different terms (i.e. $(\mathbf{H}_{ij}-2\,\mathbf{FIM}_{ij})/\mathbf{H}_{ij})$) is smaller than 2 %). Therefore based on Marsili-Libelli et al. (2003), it is concluded that the model is calibrated properly.

$$\mathbf{H}-2\,\mathbf{FIM}=\begin{bmatrix} 0.00\times10^{0} & -4.66\times10^{-4} & -1.05\times10^{-5}\\ -4.66\times10^{-4} & 2.45\times10^{-1} & -3.56\times10^{-3}\\ -1.05\times10^{-5} & -3.56\times10^{-3} & 3.00\times10^{-5}\end{bmatrix} \tag{4.26}$$

4.4.5 Importance of curvature for parameter confidence estimation

Using the procedure proposed by Bates and Watts (1988) (section 4.2.7), the importance of the curvature of the objective function J can be assessed. It is found that the relative *intrinsic* curvature c^{i} is equal to 0.034 and the relative *parameter-effect* curvature $c^{\boldsymbol{\theta}}$ is equal to 0.296. From these results, it can already be concluded that the intrinsic curvature is much less important compared to the parameter-effects curvature, which is in accordance with previous observations of

Bates and Watts (1980) and Donaldson and Schnabel (1987). In order to provide a sufficiently low deviation from the tangent plane at a distance $\sqrt{F}$ from the tangent point, $c\sqrt{F}$ needs to be (much) smaller than 1, where F represents the value of the F-distribution. The square root of the critical F-value ($F(N, N-n_{\mathrm{p}}, 0.95)$) here found is equal to 1.70. Bates and Watts (1988) stated that $c\sqrt{F}$ should be lower than 0.3, to have deviations lower than 15 %. Since $c^{\boldsymbol{\theta}}\sqrt{F}$ is equal to 0.503, it is expected that the *parameter-effects* curvature is important and thus the **FIM** and **H** will not provide proper estimates of the parameter confidence intervals. To determine how close the current confidence region prediction is compared to reality, independent samples were taken to estimate the likelihood confidence region (Equation 4.7). The likelihood method is suitable to estimate the confidence region, since the intrinsic curvature is very low and thus will provide a good approximation of the confidence regions. 1 000 000 random parameter samples are taken from uniform distributions, for which the ranges are given in Table 4.4.

Table 4.4: Parameter ranges used to estimate the likelihood confidence region.

Parameter	**Minimum**	**Maximum**	**Units**
V_{r}	10	40	nmol/(Umin)
K_{ACE}	100	500	mM
K_{MPPA}	0.5	6.5	mM

Only 14 876 samples were found to be located within the 95 % likelihood confidence region. The approximated confidence regions for the different methods are shown in Figure 4.9. From this figure, it is clear that the use of the **FIM** and Hessian matrix **H** to construct the confidence ellipses, yield the same result. However, these linear approximations differ considerably from the likelihood confidence region, and thus it can be concluded that it is important to determine the curvature of the objective function, in order to assess whether the linear approximation methods yield reliable results. In this case, the confidence intervals are overpredicted for low parameter values, and underpredicted for high parameter values. These asymmetric confidence intervals are typical for nonlinear models, since only linear models will yield a symmetric, ellipsoidal confidence region around the optimal parameter estimate (Donaldson and Schnabel, 1987).

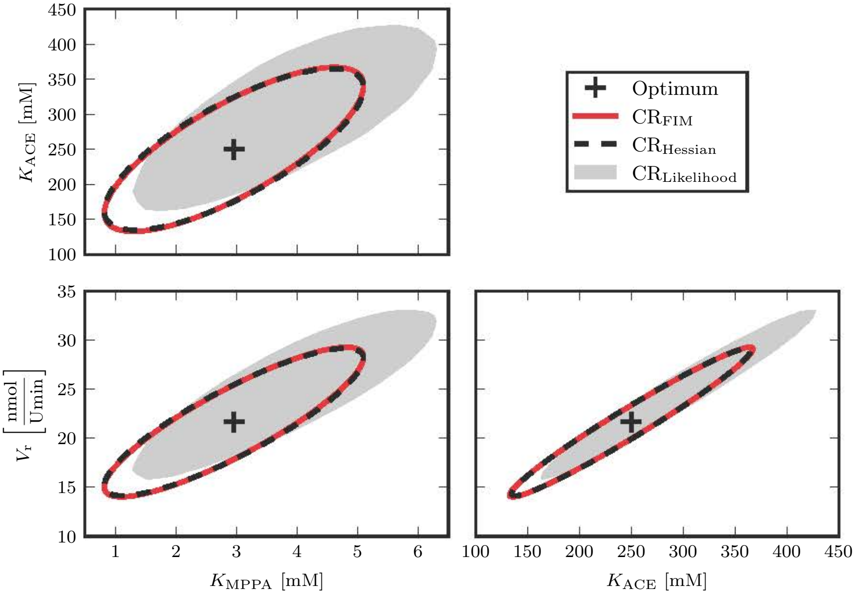

Figure 4.9: The confidence regions are shown for the three backward initial reaction rate parameters. These regions are calculated using two linear approximation methods ($\mathrm{CR}_{\mathrm{FIM}}$ and $\mathrm{CR}_{\mathrm{Hessian}}$) and a more accurate approximation, i.e. the likelihood confidence region ($\mathrm{CR}_{\mathrm{Likelihood}}$).

4.4.6 Uniform design approach

To illustrate the added value of the iterative rMbOED strategy, the results are compared with a traditional uniform design based on the initial ranges of the independent variables ($[ACE]$ and $[MPPA]$). For the rMbOED, 20 experiments were conducted with two repetitions for each experiment. To allow comparison, the same number of *in silico* experiments is used for the uniform design. Both design strategies are shown in Figure 4.10, and as expected the design space for the uniform design is much smaller since it uses the initial product ranges.

Assuming that the calibrated parameter values and the measurement error calculated earlier ($\sigma(v_{\mathrm{back}}) = 0.104\, v_{\mathrm{back}}$) are correct, the parameter confidence levels for the uniform design of Figure 4.10 can be calculated. The 95 % confidence intervals (CI) for the uniform design strategy are given in Table 4.5. Compared to the iterative rMbOED strategy, the information content is much lower for the uniform design strategy since the det[**FIM**] is about ten times lower. This also results in confidence intervals which are two times larger for the same experimental effort, since the knowledge gained during the experimentation is not used to optimise

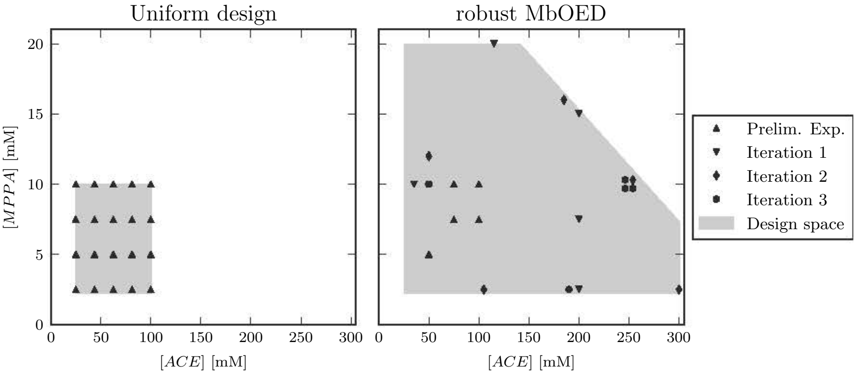

Figure 4.10: The experimental design strategies for the uniform design and robust model-based optimal experimental design (rMbOED). The gray areas show the design space, i.e. the ranges in which an experiment could be designed. The maximum design space is shown for the rMbOED, since it was gradually expanded during the rMbOED iterations.

Table 4.5: Parameter 95 % confidence intervals (CI) when using the uniform design strategy of Figure 4.10. The parameter 95 % CIs for the iterative rMbOED are shown in the last column (Table 4.1).

Parameter	**Value**		**95 % CI Uniform**	**95 % CI rMbOED**	**Units**
V_r	21.7	±	11.6	5.2	nmol/(Umin)
K_ACE	250	±	155	80	mM
K_MPPA	2.96	±	2.92	1.49	mM

the experimental design. This shows that the application of an iterative design approach, allows identifying experimental conditions which yield more information with regard to the parameter estimation.. This is especially true when the *a priori* knowledge about the parameter values is low and/or the model is highly nonlinear. In these cases, it is impossible to come up with an experimental design which is informative and efficient. In contrast, an iterative procedure allows to update the parameter values and uncertainties during the experimentation, and allows to identify and narrow the experimental regions of interest. In Figure 4.10, only a uniform design for the initial design space is considered, which might seem unfair to be used for a comparison. However, initially only a limited amount of information is available about the design space, and thus in practice this small design space would be used to design the experiments. If the maximum design space of the rMbOED would be used for the uniform design, the parameter uncertainties would be close to those of the rMbOED, but still be higher (about 2%). However, this small difference raises the question to what extent an optimal experimental design approach will outweigh an intuitive planning based on the experimental interpretation of the results. Bauer et al. (2000) performed such a comparison, and found that the standard deviations of an intuitive design by an experienced experimentalist were about 30 % higher compared to the model-based design. This illustrates that the use of MbOED is generally superior, and yields more accurate parameter estimations.

4.5 Parameter estimation remaining model parts

The data for the forward initial reaction rate and the dissociation parameters were gathered separately, and thus the presented rMbOED methodology was not applied for the model calibration of the remaining model parts. All parameter estimates, uncertainties and correlation derived from the **FIM** are given in Tables 4.6 and 4.7.

4.5.1 Forward initial reaction rate

The forward initial reaction rate in Equation 4.4 contains three parameters, i.e. V_{f}, K_{IPA}, and K_{BA}. In order to estimate the parameter values 54 experiments were conducted, for which the substrate concentrations were varied between 20 and 800 mM for *IPA* and between 0.5 and 10 mM for *BA*. The initial product concentrations for $[MPPA]$ and $[ACE]$ were equal to 0 mM. After the data collection, the model was calibrated using two different error distributions, i.e. the absolute constant error and the relative error. It was found that the absolute constant error distribution was no suitable error distribution (p-value of 0.00715), and thus was rejected. The relative error distribution seemed to represent the error distribution well, for $\mu = 0$ and $\sigma(v) = 0.10\,v$. The calibrated parameter values and 95 % CIs are given in Table 4.6. The gathered forward initial reaction rate data and calibrated model are shown in Figure 4.11.

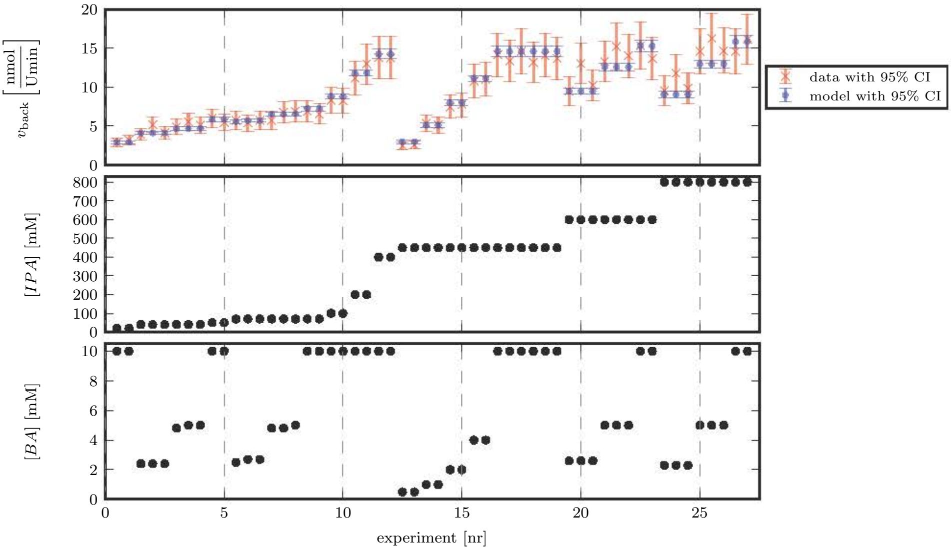

Figure 4.11: The model prediction v_{forw} and corresponding experimental data are shown for different concentrations of IPA and BA.

From Figure 4.11 it is clear that the model is able to predict the data well. However, at high concentrations of *IPA*, the measurement uncertainty is higher. This is probably related to the operational instability of the enzyme at high amine donor-to-acceptor ratios.

4.5.2 Dissociation parameters

After estimating the parameters of both the forward and backward initial reaction rate, three parameters remained to be calibrated: K_{eq}, K_{iIPA}, and K_{iMPPA}. Using the Haldane relationship from Equation 4.3, K_{eq} could already be estimated (Segel, 1975). To estimate the other two parameters, additional initial rate experiments were performed. The substrate concentrations for $[IPA]$ and $[BA]$ were fixed to 450 and 10 mM respectively. The product concentration of $[ACE]$ was varied between 0 and 100 mM and that of $[MPPA]$ was varied between 0 and 20 mM, and is shown in Figure 4.12. Twelve experiments were carried out, allowing to calibrate the two remaining parameters (Table 4.6).

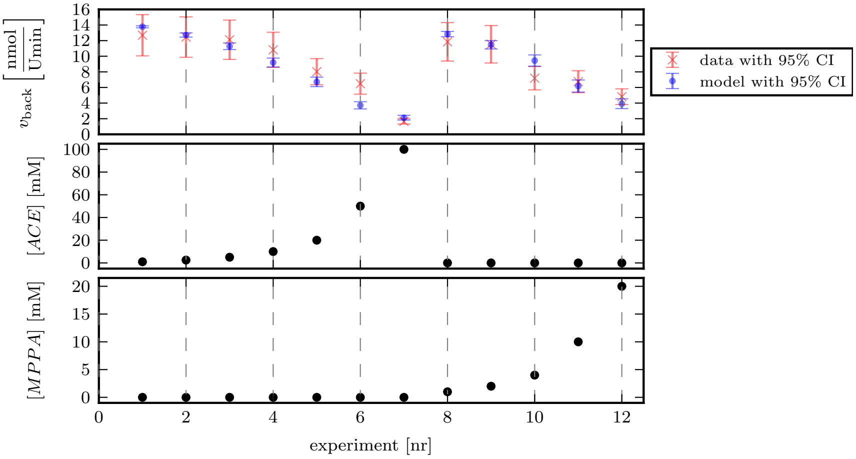

Figure 4.12: The experiments to estimate the dissociation parameters were performed at varying product concentrations ($[ACE]$ and $[MPPA]$) and constant substrate concentrations ($[IPA] = 450\,\text{mM}$ and $[BA] = 10\,\text{mM}$).

4.5.3 Model validation

A model validation was performed at different initial conditions and it was found that the model prediction showed a good correspondence with the experiments at low reaction times ($< 7\,\text{h}$). At higher reaction times (up to $17\,\text{h}$), $[MPPA]$ was overpredicted and $[BA]$ underpredicted. Two possible reasons can be formulated: First, the model in Equation 4.2 might be unsuitable for predicting the concentrations for high reaction times. Second, the enzyme was suffering from some stability issues and precipitation was observed, possibly influencing the reaction kinetics. To obtain a more accurate model predictions at high reaction times, an extension of the model with a suitable enzyme deactivation mechanism should be considered. Most often enzyme deactivation can be described by a first-order mechanism (Sadana, 1988), and thus model complexity is not increased considerably. As the model can be regarded as calibrated and validated for low reaction times, the final parameter values, 95 % confidence intervals and correlation are given in Table 4.6. The 95 % confidence intervals and correlations were calculated using the **FIM** (Table 4.7), and since the model in Equation 4.2 is nonlinear, this is only a rough approximation (see section 4.4.5).

Table 4.6: Calibrated parameter values and corresponding 95 % confidence intervals for the model in Equation 4.2.

Parameter type	Parameter	Value	95 % CI		(SD)	Units
Forward	V_f	24.0	±	2.5	(1.3)	$\frac{\text{nmol}}{\text{Umin}}$
	K_BA	3.39	±	0.67	(0.33)	mM
	K_IPA	138	±	22	(11)	mM
Backward	V_r	21.7	±	5.3	(2.6)	$\frac{\text{nmol}}{\text{Umin}}$
	K_MPPA	2.96	±	1.48	(0.73)	mM
	K_ACE	250	±	81	(40)	mM
Dissociation	K_iIPA	1.76	±	0.29	(0.13)	mM
	K_iMPPA	1.60	±	0.40	(0.18)	mM
Equilibrium	K_eq	1.94	±	0.65*	(0.32)	–

* Using Equation 4.3, the uncertainty of K_eq was estimated directly from the uncertainties of the other parameters, taking into account the correlation between the different parameters.

Table 4.7: The correlation matrix for all the parameters from Equation 4.2. It can be seen that the correlation between parameters which are estimated simultaneously is high. Parameter estimates which have been estimated separately have no correlation (since they were estimated from different data sets), and are therefore set to zero.

$$\begin{array}{l|ccccccccc|}
 & V_\mathrm{f} & K_\mathrm{BA} & K_\mathrm{IPA} & V_\mathrm{r} & K_\mathrm{MPPA} & K_\mathrm{ACE} & K_\mathrm{iIPA} & K_\mathrm{iMPPA} & K_\mathrm{eq} \\
V_\mathrm{f} & 1 & 0.88 & 0.91 & 0 & 0 & 0 & 0 & 0 & -0.33 \\
K_\mathrm{BA} & - & 1 & 0.71 & 0 & 0 & 0 & 0 & 0 & -0.38 \\
K_\mathrm{IPA} & - & - & 1 & 0 & 0 & 0 & 0 & 0 & -0.33 \\
V_\mathrm{r} & - & - & - & 1 & 0.98 & 0.87 & 0 & 0 & 0.85 \\
K_\mathrm{MPPA} & - & - & - & - & 1 & 0.78 & 0 & 0 & 0.82 \\
K_\mathrm{ACE} & - & - & - & - & - & 1 & 0 & 0 & 0.87 \\
K_\mathrm{iIPA} & - & - & - & - & - & - & 1 & 0 & 0 \\
K_\mathrm{iMPPA} & - & - & - & - & - & - & - & 1 & 0 \\
K_\mathrm{eq} & - & - & - & - & - & - & - & - & 1
\end{array}$$

4.6 Conclusions

The iterative robust model-based optimal experimental design (rMbOED) strategy was applied to the backward initial reaction rate (i.e. a submodel of the plain ping-pong bi-bi model), and proved to be powerful and superior to the uniform design strategy. By using rMbOED, parameter confidence intervals can be reduced efficiently and the experimental region of interest can be identified. This is important for experimentalists, since it allows to identify opportunities already during the experimentations, allowing them to extract more informative data. During the iterative rMbOED, the experimental design space $\boldsymbol{\Psi}$ was gradually expanded to include informative design regions. Since no detailed information was available prior to the experimentation a suitable experimental design range was unknown, and thus a conservative design space was considered initially. Using data collected earlier, the remaining model parameters were successfully calibrated, and the full model in Equation 4.2 was validated for short term experiments ($< 7\,\mathrm{h}$). However, large deviations between the data and model predictions were found at long reaction times. This is probably related to enzyme instability and/or precipitation.

The use of linearisation techniques like the Fisher information matrix (**FIM**) to approximate the confidence region of the parameters, was found to deviate significantly from the likelihood confidence region. It was found that the confidence region predicted by the **FIM** overpredicted the lower 95 % confidence interval boundary, but underpredicted the upper 95 % confidence interval boundary. The relative curvature measures proposed by Bates and Watts (1988), allowed to determine whether the **FIM** is appropriate to approximate the confidence region, and thus should be always calculated when using the **FIM** for nonlinear models.

CHAPTER 5

A GENERIC METHODOLOGY FOR QUANTIFYING MASS TRANSFER LIMITATIONS IN MICROREACTORS

Published as

Van Daele, T., Fernandes del Pozo, D., Van Hauwermeiren, D., Gernaey, K.V., Wohlgemuth, R., Nopens, I. (2016) A generic model-based methodology for quantification of mass transfer limitations in microreactors, *Chem Eng J*, 300, p193-208, doi:10.1016/j.cej.2016.04.117

Abstract

As already stated in the introductory chapter, microreactors are becoming more popular in the biocatalytic field since they provide better controllability compared to conventional batch reactors and allow to achieve process intensification by speeding up reactions. However, even these small-scale reactors can suffer from mass transfer limitations. Traditionally, dimensionless numbers such as the second Damköhler number are used to determine whether the reaction is either kinetically or mass transfer limited. However, these dimensionless numbers only give a qualitative measure of the extent of the mass transfer limitation, and are only applicable to simple reactor configurations. In practice, this makes it difficult to rapidly quantify the importance of such mass transfer limitations and compare different reactor configurations. This chapter presents a novel generic methodology to quantify mass transfer limitations. It is applied to two microreactor configurations: a microreactor with immobilised enzyme at the wall and a Y-shaped microreactor with one inlet stream containing enzyme and the other containing substrate. The results of the immobilised enzyme microreactor correspond very well with the traditional approach of using the second Damköhler number ($\mathrm{Da}_{\mathrm{II}}$). However, the results of the Y-shaped microreactor showed that the second Damköhler number is not applicable in this case, indicating that dimensionless numbers should be

applied with care. For both configurations, the mass transfer limitations could be quantified and linked with appropriate dimensionless numbers, illustrating the power of the proposed methodology.

5.1 Introduction

Microreactors have received considerable interest in the (bio)chemical field, especially due to their versatility and improved controllability of the process. Indeed, they can be operated in batch or in continuous mode, they consume only limited amounts of chemicals per experiment, which gives them a competitive advantage over conventional lab-scale batch reactors when used for process screening, for biocatalyst screening or for kinetic characterisation of the biocatalyst. These microreactors have small channels with dimensions below 1 mm, which enhances transfer rates for both mass and heat (Walter et al., 2005; Tušek et al., 2012). By reducing the distance between reactants, mass transfer limitations are reduced in a microreactor (Swarts et al., 2010). However, even at such small dimensions, mass transfer limitations can still occur and have an important impact. That is why in the literature the importance of mass transfer limitations in microreactors is discussed frequently (Kockmann et al., 2004; Walter et al., 2005; Swarts et al., 2010). Mass transfer limitations lead to a reduced volumetric productivity (Lee, 1989), but also obscure the underlying kinetic model parameter values (Kerby et al., 2006). Kinetic model parameter values which are estimated based on mass transfer limited measurements, yield apparent parameter values which represent the combined effect of both mass transfer limitations and kinetics (Kheirolomoom et al., 2002). In order to retrieve the underlying or so-called intrinsic parameter values, these mass transfer limitations need to be excluded by improving the internal mixing and/or optimising the geometry of the reactor. Given this relevance, it is important to identify whether mass transfer limitations are occurring. Traditionally, dimensionless numbers such as the second Damköhler number ($\mathrm{Da_{II}}$) are used to determine the occurrence of mass transfer limitations (Equation 5.1).

$$\mathrm{Da_{II}} = \frac{\text{Reaction rate}}{\text{Diffusion rate}} = \frac{\text{Diffusion time}}{\text{Reaction time}} \tag{5.1}$$

The second Damköhler number ($\mathrm{Da_{II}}$) represents the ratio between the reaction rate and the diffusion rate. However, in many cases it is also represented as the ratio of the diffusion time and reaction time (Kockmann et al., 2004). The diffusion time can be calculated by the Einstein equation for the Brownian motion of a particle or molecule suspended in a fluid (Equation 5.2) (Einstein, 1956).

$$\overline{x^2} = 2Dt \tag{5.2}$$

where $\overline{x^2}$ represents the mean quadratic displacement of the molecule under study, D the diffusion coefficient of the molecule and t the time the molecule could diffuse. From Equation 5.2, the diffusion time needed by the molecule to reach distance x can be calculated (Kockmann et al., 2004). To extract the reaction time, different definitions of reaction time are available in the literature: Kockmann et al. (2004) and Roberge et al. (2005) use the half-life time of the reaction to characterise reactions, while Swarts et al. (2010) use the time at which 95% conversion is reached. A reaction time yielding 100% conversion cannot be used in most cases, since for many kinetic models the reaction rate approaches zero at very low substrate concentrations, yielding an infinite reaction time (Swarts et al., 2010).

In channel-like microreactors, the second Damköhler number $\mathrm{Da_{II}}$ can be easily applied to determine whether a reaction is mass transfer limited or kinetically limited. However, this comes with some limitations. A first drawback of this dimensionless approach is that it only gives a qualitative estimate of the mass transfer limitation. For instance, when $\mathrm{Da_{II}}$ is high ($\gg 1$), the reaction is said to be mass transfer limited and when it is low ($\ll 1$), the reaction is kinetically limited. However, for most cases no quantification of the level of mass transfer limitations can be directly extracted. In the literature, the value of the second Damköhler number at which a reaction is changing from mass transfer limited to kinetically limited is around one (Gervais and Jensen, 2006). Walter et al. (2005) state that in the case of circular channels with plug flow, a $\mathrm{Da_{II}}$ below 0.1 represents the kinetically limited region, whereas for $\mathrm{Da_{II}}$ values above 100 the reaction is mass transfer limited. A $\mathrm{Da_{II}}$ value between 0.1 and 100 represents a so-called transient region. Information about the transition of mass transfer limited to kinetically limited conditions is not always available and is only valid for that particular microreactor configuration. Secondly, no quantitative information is given about the reduction in productivity, making it almost impossible to determine whether mass transfer limitations are important in terms of process efficiency.

Next to $\mathrm{Da_{II}}$, which is used to identify mass transfer limitations, the first Damköhler number ($\mathrm{Da_{I}}$) represents the ratio between the residence time of the solution in the reactor and the reaction time (Equation 5.3). The same difficulties arise with the definition of the reaction time as with the second Damköhler number. At large values of the first Damköhler number ($\mathrm{Da_{I}} \gg 1$), the reaction has sufficient time to complete. At small $\mathrm{Da_{I}}$ values ($\mathrm{Da_{I}} \ll 1$), the reaction does not have sufficient time to reach full conversion.

$$\mathrm{Da_I} = \frac{\text{Residence time}}{\text{Reaction time}} \tag{5.3}$$

Despite the fact that these dimensionless numbers are widely used in the chemical engineering field, not everyone is familiar with these dimensionless numbers and therefore one sometimes even starts developing "new" but redundant dimensionless numbers. E.g. Kerby et al. (2006) propose a criterion λ which represents the ratio of reaction rate to mass transfer rate, and they state that it "*was developed to evaluate the importance of flow-dependent, mass-transfer resistances in predicting kinetic rate constants*". In fact, the proposed λ criterion is just another representation of the second Damköhler number ($\mathrm{Da_{II}}$).

The use of $\mathrm{Da_{II}}$ is not very straightforward, not usable for more complex reactor configurations and, most importantly, does not provide quantitative information about mass transfer limitations (except in some simplified cases (Loffler and Schmidt, 1975)). As there is currently no good and easy method to decide on the appearance, let be quantifying mass transfer limitations, this chapter presents a novel generic methodology to determine whether a system is kinetically or mass transfer limited. It is based on the comparison of the outcome of a rigorous Computational Fluid Dynamics (CFD) model simulation and predictions from an ideal reactor model for the assessment of mass transfer limitations. The methodology is subsequently applied to two types of microreactor setups that are studied in this dissertation: a microreactor with immobilised enzyme at the wall and a Y-shaped microreactor with one inlet flow containing the enzyme and the other inlet flow containing the substrate. Finally, the presented generic methodology is compared with the traditional approach using dimensionless numbers.

5.2 Theoretical background

5.2.1 Dimensionless numbers

Two dimensionless numbers have already been introduced in this chapter, i.e. the first ($\mathrm{Da_I}$) and second Damköhler number ($\mathrm{Da_{II}}$). However, more dimensionless numbers are considered to be important in the context of microreactors. The Péclet number (Pe) describes the ratio of convection to diffusion (Equation 5.4).

$$\mathrm{Pe} = \frac{\bar{u}_\mathrm{x} W}{2D} \tag{5.4}$$

where $\bar{u}_\mathrm{x}$ is the average flow velocity in the x-direction (i.e. direction of flow), W the microreactor width and D the diffusion coefficient of the solute. If Pe is large, convective transport dominates over diffusive transport in the direction of flow. In this case, it is valid to assume that the upstream concentrations do not depend on the downstream concentrations. This assumption is valid for most microfluidic conditions (Ristenpart et al., 2008; Vrentas and Vrentas, 2013).

Another important dimensionless number is the Reynolds number (Re), which is defined as the ratio between inertial and viscous forces. For small and long channels, Re can be calculated by Equation 5.5 (Kockmann, 2008):

$$\mathrm{Re} = \frac{\rho \bar{u}_\mathrm{x} W}{2\mu} \tag{5.5}$$

with ρ the density of the fluid and μ the dynamic viscosity of the fluid. At low Re values, the viscous forces are dominant and the flow is well-structured and laminar. However, at high Re values, instabilities start to occur and the fluid flow starts to become turbulent (Kockmann et al., 2004). Most of small-scale liquid-phase flow systems have Reynolds numbers significantly less than 2000, which means these systems exhibit laminar flow and thus have a parabolic flow profile (Nagy et al., 2012). As a consequence, the fluid in the center spends only half as much time in the reactor compared to fluid at the walls, yet microreactors are frequently described as displaying plug flow behaviour (Nagy et al., 2012). To evaluate whether this plug flow assumption holds true, the Bodenstein number Bo can be used. Bo describes the ratio of the convection to dispersion to estimate the deviation from plug flow (Equation 5.6).

$$\mathrm{Bo} = \frac{\bar{u}_\mathrm{x} L}{\mathbf{D}} \tag{5.6}$$

where L is the length of the microreactor and $\mathbf{D}$ the Taylor dispersion coefficient. The Taylor dispersion coefficient $\mathbf{D}$ is defined as follows (Equation 5.7):

$$\mathbf{D} = D + \frac{\bar{u}_\mathrm{x}^2 W^2}{4\beta D} \tag{5.7}$$

where D is the diffusion coefficient of the solute and β is a parameter depending on the channel geometry: It is 48 for circular tubes and approximately 30 for square channels (Datta and Ghosal, 2009).

In the case of plug flow behaviour, it is expected that a pulse of a certain solute at the inlet of the reactor leads to a pulse at the outlet after a certain residence time. However, at low Bodenstein numbers (< 100) large deviations from plug flow behaviour appear since the dispersion phenomenon becomes important. In this case, a pulse of a certain solute at the inlet of the reactor will lead to a broad peak at the outlet. In order to successfully predict the behaviour of solutes at low Bo numbers, the dispersion model derived by Taylor and Aris needs to be used (Taylor, 1953; Aris, 1956).

The application of dimensionless numbers can yield interesting information, but a dimensionless analysis does not unravel the underlying physics or the nature of a physical phenomenon (Sablani et al., 2006). Moreover, dimensionless numbers rely on strong simplifications: idealised geometries, simplified chemistry, etc. Attempts to more realistically include non-idealities soon lead to extremely complex analytical models (Van Sark et al., 1990). Therefore, in order to include multidimensional effects in real-life geometries, realistic chemistry, etc. one has to resort to numerical models (Kleijn, 2012). In order to obtain a more fundamental understanding of the underlying processes taking place, a more advanced study should be performed.

5.2.2 Enzymatic process and kinetic model

Next to fluid flow, a reaction needs to be considered. In this and the following chapter a simple enzymatic reaction was selected for this study. The enzymatic process that was studied, is given in Equation 5.8.

$$E + S \xrightarrow{k_{\text{cat}}} E + P \tag{5.8}$$

with enzyme E [g/L], substrate S [mM], product P [mM]. k_{cat} [L/(g · s)] represents the turnover number of the enzyme. This reaction follows a second-order reaction mechanism (Equation 5.9). The average enzyme concentration was kept constant at 0.0454 g/L for the different reactors in this chapter, reducing the enzymatic model to pseudo first-order kinetics.

$$\frac{\mathrm{d}[P]}{\mathrm{d}t} = \frac{-\mathrm{d}[S]}{\mathrm{d}t} = r_{\text{S}} = k_{\text{cat}}[E][S] = \frac{r_{\max}}{[S]_0}[S] \tag{5.9}$$

with $r_{\max}$ [mM/s] the maximum reaction rate (which is equal to $k_{\text{cat}}[E][S]_0$) and r_{S} the substrate consumption rate [mM/s].

5.2.3 Plug flow reactor

A plug flow reactor provides the highest theoretically possible productivity, since the flow of fluid through the reactor is orderly with no element overtaking or mixing with any other element ahead or behind (Levenspiel, 1972). As a consequence, only lateral mixing can be present and the residence time of all elements of fluid is the same (Levenspiel, 1972). The aim of using a microreactor is to approximate this interesting ideal behaviour as closely as possible. The equation describing the concentration profile of the different solutes in a plug flow reactor with a constant-density fluid is given by Equation 5.10 (Levenspiel, 1972).

$$\tau = \int_{[S]}^{[S]_0} \frac{\mathrm{d}[S]}{-r_\mathrm{S}} \tag{5.10}$$

where τ [min] is the residence time, $[S]$ [mM] is the concentration of substrate S, and r_S [mM/s] is the substrate consumption rate. By inserting the kinetic expression for r_S and integrating Equation 5.10, the evolution of $[S]$ in function of the residence time τ can be easily obtained. However, the plug flow approximation is only valid in case no mass transfer limitations occur and dispersion is fairly low compared to convection (Nagy et al., 2012).

5.2.4 Advection-diffusion-reaction in a microreactor

If the mass transfer limitations are not negligible, the advection-diffusion-reaction equation has to be used in order to accurately predict time- and location-dependent substrate and product concentrations in the microreactor. The general steady-state equation for advection-diffusion-reaction is given in Equation 5.11:

$$\frac{\partial c_i}{\partial t} = \nabla \cdot (D_i \nabla c_i) - \nabla \cdot (\mathbf{u} c_i) + r_i(\{c_j\}) \tag{5.11}$$

where $\mathbf{u}$ is the velocity field, D_i is the diffusion coefficient of species i, and $r_i(\{c_j\})$ the rate of production or consumption of species i, which in general can depend on all the concentrations of the available species ($\forall j \in 1, \ldots, n$) in a nonlinear fashion (Ristenpart and Stone, 2012). In case of steady-state simulations, the term $\partial c_i / \partial t$ vanishes. In this dissertation, it is generally assumed that the diffusion coefficient D is constant and the fluid is incompressible, thereby simplifying Equation 5.11 to Equation 5.12:

$$\mathbf{u} \cdot \nabla c_i = D_i \nabla^2 c_i + r_i(\{c_j\}) \tag{5.12}$$

This equation is numerically approximated (in 2D, the microreactor height H is ignored) in the following, and compared to the ideal plug flow model predictions in order to quantify the mass transfer limitations. However, by making proper assumptions, Equation 5.12 can also be simplified to derive two dimensionless numbers which can give a qualitative estimate of the importance of mass transfer limitations. This allows to compare the generic methodology discussed later in this chapter with the traditional approach of using dimensionless numbers. For the derivation, it is assumed that the convective transport by means of a mean fluid velocity dominates over axial diffusive transport in the downstream x-direction. This assumption can be made in most microfluidic conditions because the Péclet number is sufficiently large (Ristenpart et al., 2008). Diffusion is of major importance perpendicular to the x-direction. The equation for the substrate at steady-state involving the enzymatic reaction is given by Equation 5.13.

$$u_{\mathrm{x}} \frac{\partial c_i}{\partial x} = D_i \frac{\partial^2 c_i}{\partial y^2} + r_i(\{c_j\}) \tag{5.13}$$

where u_{x} is the velocity in the x-direction. If Equation 5.13 is applied to the kinetics under study, the following equation is obtained:

$$D \frac{\partial^2 [S]}{\partial y^2} = u_{\mathrm{x}} \frac{\partial [S]}{\partial x} + \frac{r_{\max}}{[S]_0} [S] \tag{5.14}$$

Recasting Equation 5.14 in dimensionless terms

$$X^* = \frac{x}{L}; \qquad Y^* = \frac{y}{W/2}; \qquad S^* = \frac{[S]}{[S]_0}$$

where $[S]_0$ is the incoming substrate concentration, W the microreactor width and L the microreactor length, yields

$$D \frac{\partial^2 ([S]_0 S^*)}{\partial ((W/2) Y^*)^2} = u_{\mathrm{x}} \frac{\partial ([S]_0 S^*)}{\partial (L X^*)} + \frac{r_{\max}}{[S]_0} ([S]_0 S^*)$$

$[S]_0$, W and L are constant, and can therefore be moved outside the partial derivatives.

$$\frac{\partial^2 S^*}{\partial {Y^*}^2} = \underbrace{\left(\frac{u_{\mathrm{x}} W^2}{4DL} \right)}_{\mathrm{Pe_{2D}}} \frac{\partial S^*}{\partial X^*} + \underbrace{\left(\frac{r_{\max} W^2}{4D[S]_0} \right)}_{\mathrm{Da_{II}}} S^* \tag{5.15}$$

Equation 5.15 yields two dimensionless numbers. The first number resembles the Péclet number (Equation 5.4) but in a slightly modified form to include both the width and length of the microreactor and will henceforth be called the two-dimensional Péclet number ($\mathrm{Pe}_{\mathrm{2D}}$) and is given by Equation 5.16. It is defined as the ratio between diffusion time along the y-axis and the residence time along the x-axis.

$$\mathrm{Pe}_{\mathrm{2D}} = \frac{u_{\mathrm{x}} W^2}{4DL} \tag{5.16}$$

At very low flow velocities ($u_{\mathrm{x}} \approx 0\,\mathrm{m/s}$), e.g. close to the microreactor wall, the $\mathrm{Pe}_{\mathrm{2D}}$ is close to zero and the first term of Equation 5.15 vanishes.

The second dimensionless number of Equation 5.15 is the second Damköhler number ($\mathrm{Da}_{\mathrm{II}}$) applied to the current case (in contrast to the conceptual introduction of $\mathrm{Da}_{\mathrm{II}}$ in Equation 5.1), which means that it is only valid for the kinetic model and reactor geometries under study. As stated earlier, at high $\mathrm{Da}_{\mathrm{II}}$ values the process is severely mass transfer limited, i.e. diffusive mass transfer is much lower than the reaction rate. By increasing the (diffusive) mass transfer, the reactor productivity can be increased in such a case.

$$\mathrm{Da}_{\mathrm{II}} = \frac{r_{\mathrm{max}} W^2}{4D[S]_0} \tag{5.17}$$

5.3 Materials and methods

5.3.1 Microreactor configurations

Two different microreactor configurations with a rectangular cross section are investigated: a microreactor in which the enzyme is immobilised at the wall (Figure 5.1) and a Y-shaped microreactor in which one of the inlets is used to supply the solution containing the substrate and the other inlet is used to supply the solution containing the enzyme (Figure 5.2). These microreactor configurations were selected since they are widely described in literature with respect to mass transfer limitations and dimensionless numbers (Swarts et al., 2010; Gervais and Jensen, 2006; Tišma et al., 2009). The length of all the microreactors under study was 10 cm and the nominal width was 200 µm. However, the width was altered in some cases to determine the effect of the microreactor width on mass transfer limitations. The height of the microreactor was assumed to be much larger compared to the microreactor width ($H \gg W$).

Microreactor with immobilised enzyme

For this microreactor configuration, it is assumed that the enzyme is attached to the microchannel wall and a single inlet stream containing substrate is fed to the microreactor. Due to the laminar flow profile, the microreactor can be considered symmetric, with a symmetry plane around the center. A schematic representation of this configuration is given in Figure 5.1.

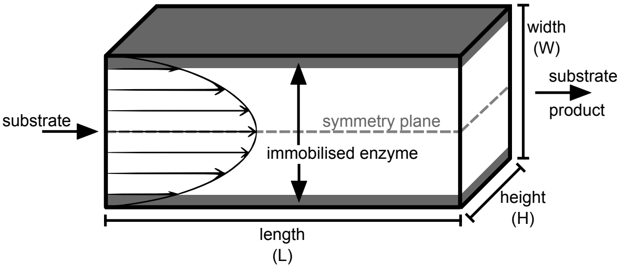

Figure 5.1: Schematic representation of an immobilised enzyme microreactor with a laminar flow profile represented as velocity vector arrows yielding a parabolic velocity profile. The top and bottom walls of the microreactor are coated with enzyme.

Y-shaped microreactor

Enzyme and substrate are fed into the microreactor by separate parallel inlet streams. A schematic representation of this configuration is represented in Figure 5.2. Since both flows exhibit a laminar flow profile, the two flows do not mix, but stay in contact with each other through an interface area in the middle of the channel through which diffusion of the solutes and enzymes can take place (Tišma et al., 2009). The dark grey area represents the area where the enzyme is available. The shape of the area depends on the inlet velocity and the diffusion coefficient of the enzyme, where higher diffusion coefficients will lead to a larger area where the enzyme is available. In Figure 5.2, the diffusion of enzyme is assumed to be negligible.

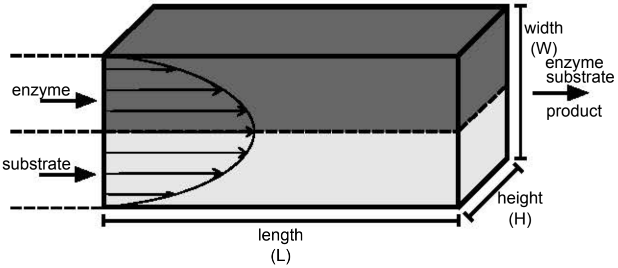

Figure 5.2: Schematic representation of the Y-shaped microreactor configuration. Substrate and enzyme are fed into the microreactor in different parallel streams. The dark grey area represents the area where the enzyme is available.

5.3.2 Modelling of microreactor configurations

Computational Fluid Dynamics (CFD) simulations can be applied rather easily to microreactors since most configurations are fairly simple and laminar flow conditions apply. Therefore, a two-dimensional CFD model is set up for both configurations in OpenFOAM, and this simplification is found to be reasonable as the relative difference between the 2D and 3D solutions is lower than 1%. For this reason the height of the microreactor is ignored. The height of the microreactor is also much larger than the width, so this simplification will have a negligible impact. Different types of OpenFOAM boundary conditions are used: the fixedValue boundary condition, the zeroGradient boundary condition, the symmetryPlane boundary condition and the empty boundary condition. In the case of a fixedValue condition, the value of the boundary condition is constant, known as a Dirichlet boundary condition. For the zeroGradient condition, the normal gradient at the boundary is kept constant at a value of zero, this is also known as a Neumann boundary condition. The symmetryPlane boundary condition can be used when a symmetry plane is present in the case under study. The empty boundary is a special boundary condition normal to the third dimension for which no solution is required. By using the symmetryPlane or empty boundary conditions the total computational effort is reduced (OpenFOAM, 2014).

Microreactor with immobilised enzyme

For the microreactor with immobilised enzyme, the computational load could be reduced by only modelling the lower part of the reactor (the part beneath the symmetry plane in Figure 5.1). In this way the number of cells in the mesh can be

Table 5.1: OpenFOAM boundary conditions for the immobilised enzyme microreactor.

Boundary	Variable	Condition	Value
inlet	$\mathbf{u}$	fixedValue	1.67×10^{-4} m/s*
	p	zeroGradient	-
	S	fixedValue	50 mM
	P	fixedValue	0 mM
	E	fixedValue	0 g/L
outlet	$\mathbf{u}$	zeroGradient	-
	p	fixedValue	0
	S	zeroGradient	-
	P	zeroGradient	-
	E	zeroGradient	-
wall	$\mathbf{u}$	fixedValue	0 m/s
	p	zeroGradient	-
	S	zeroGradient	-
	P	zeroGradient	-
	E	zeroGradient	-

* Uniform inlet velocity for $\tau = 10$ min. The parabolic laminar flow profile is already fully developed after 0.3% of the reactor length.

halved. The boundary conditions for the velocity $\mathbf{u}$, the rho-normalised pressure p, and the concentrations of the substrate S, product P and enzyme E are given in Table 5.1. The inlet concentration of the enzyme E is 0 g/L, because the enzyme is immobilised at the wall. The “computational” immobilisation of the enzyme in the CFD software is practically achieved by setting a specified enzyme concentration for all the cells adjacent to the microreactor wall. All the cells not adjacent to the wall keep the enzyme concentration of 0 g/L. For this configuration the advection-diffusion equation (Equation 5.12) is only solved for S and P and not for E, because E is immobilised at the wall, making it impossible for the enzyme to diffuse or be advected by the bulk flow. For this specific reactor configuration and (linear) reaction, a general analytical solution exists (Gervais and Jensen, 2006), which would reduce the computational requirements. However, it was decided to compute the final solution using a numerical approach since such analytical solutions only exist for simple cases. In this way, the developed methodology is also applicable to cases where no analytical solution exists.

Y-shaped microreactor

For the Y-shaped microreactor, the entire width of the microreactor has to be modelled, because the inlet is not symmetrical. Therefore, only the boundary conditions for the wall and the outlet (listed in Table 5.1) are also applicable for this configuration. The boundary conditions for both inlets for the Y-shaped microreactor are listed in Table 5.2.

Table 5.2: OpenFOAM boundary conditions for both inlets for the Y-shaped microreactor. The boundary conditions for the outlet and wall are the same as for the immobilised enzyme case (Table 5.1).

Boundary	Variable	Condition	Value
inlet-north	$\mathbf{u}$	fixedValue	$1.67 \times 10^{-4}\,\mathrm{m/s}^*$
	p	zeroGradient	-
	S	fixedValue	0 mM
	P	fixedValue	0 mM
	E	fixedValue	0.0908 g/L
inlet-south	$\mathbf{u}$	fixedValue	$1.67 \times 10^{-4}\,\mathrm{m/s}^*$
	p	zeroGradient	-
	S	fixedValue	100 mM
	P	fixedValue	0 mM
	E	fixedValue	0 g/L

* Uniform inlet velocity for $\tau = 10\,\mathrm{min}$. The parabolic laminar flow profile is already fully developed after 0.3% of the reactor length.

Since substrate molecules are much smaller compared to enzyme molecules, the substrate is therefore assumed – realistically – to diffuse faster than the enzyme (Einstein, 1956). As a consequence, the importance of the diffusivity of the enzyme will be much smaller compared to that of the substrate. It was therefore decided to ignore the diffusion of the enzyme ($D_\mathrm{E} = 0\,\mathrm{m}^2/\mathrm{s}$), i.e. only the convective flow of the enzyme is taken into account. This is a major simplification, but can be regarded as a practical solution to cope with the choice of two different diffusion values (i.e. D and D_E). As a consequence, the diffusion coefficient D will represent the combined effect of the diffusion of the solute D_S and diffusion of the enzyme D_E for all the Y-shaped microreactor simulations. However, using Equation 5.2 a simple relationship between D, D_E, and D_S can be derived. At the interface of the two parallel streams, the enzyme diffuses in the substrate stream and *vice versa*, creating an active area x_{comb} where the reaction can take place and is represented by Equation 5.18.

$$x_{\mathrm{comb}} = x_{\mathrm{S}} + x_{\mathrm{E}} \tag{5.18}$$

where x_{S} is the distance the substrate has diffused in the enzyme stream and x_{E} is the distance the enzyme has diffused in the substrate stream. Using Equation 5.2, the average distance the particles have travelled in a certain time interval t can be written as:

$$\sqrt{2Dt} = \sqrt{2D_{\mathrm{S}}t} + \sqrt{2D_{\mathrm{E}}t} \tag{5.19}$$

All terms of Equation 5.19 can be divided by $\sqrt{2t}$, leading to:

$$\sqrt{D} = \sqrt{D_{\mathrm{S}}} + \sqrt{D_{\mathrm{E}}} \tag{5.20}$$

Squaring both sides of Equation 5.20, leads to:

$$\left(\sqrt{D}\right)^2 = \left(\sqrt{D_{\mathrm{S}}} + \sqrt{D_{\mathrm{E}}}\right)^2 \tag{5.21}$$

By factorisation of the right hand side of Equation 5.21, Equation 5.23 is obtained:

$$\begin{align} D &= \left(\sqrt{D_{\mathrm{S}}}\right)^2 + \left(\sqrt{D_{\mathrm{E}}}\right)^2 + 2\sqrt{D_{\mathrm{S}}}\sqrt{D_{\mathrm{E}}} \tag{5.22} \\ &= D_{\mathrm{S}} + D_{\mathrm{E}} + 2\sqrt{D_{\mathrm{S}}D_{\mathrm{E}}} \tag{5.23} \end{align}$$

When the actual values of the diffusion coefficients of the enzyme and substrate are known, the “apparent” diffusion coefficient can be easily calculated using Equation 5.23. This approach makes that the results of the Y-shaped microreactor shown in Section 5.4.2 are applicable for a wide range of diffusion coefficient values.

5.3.3 Generic methodology to assess mass transfer limitations

To assess the mass transfer limitations of a certain reactor a generic methodology is developed which allows to determine the impact of the different degrees of freedom on the mass transfer limitation. The general overview of the methodology is given in Figure 5.3 and consists of multiple steps further discussed in this section.

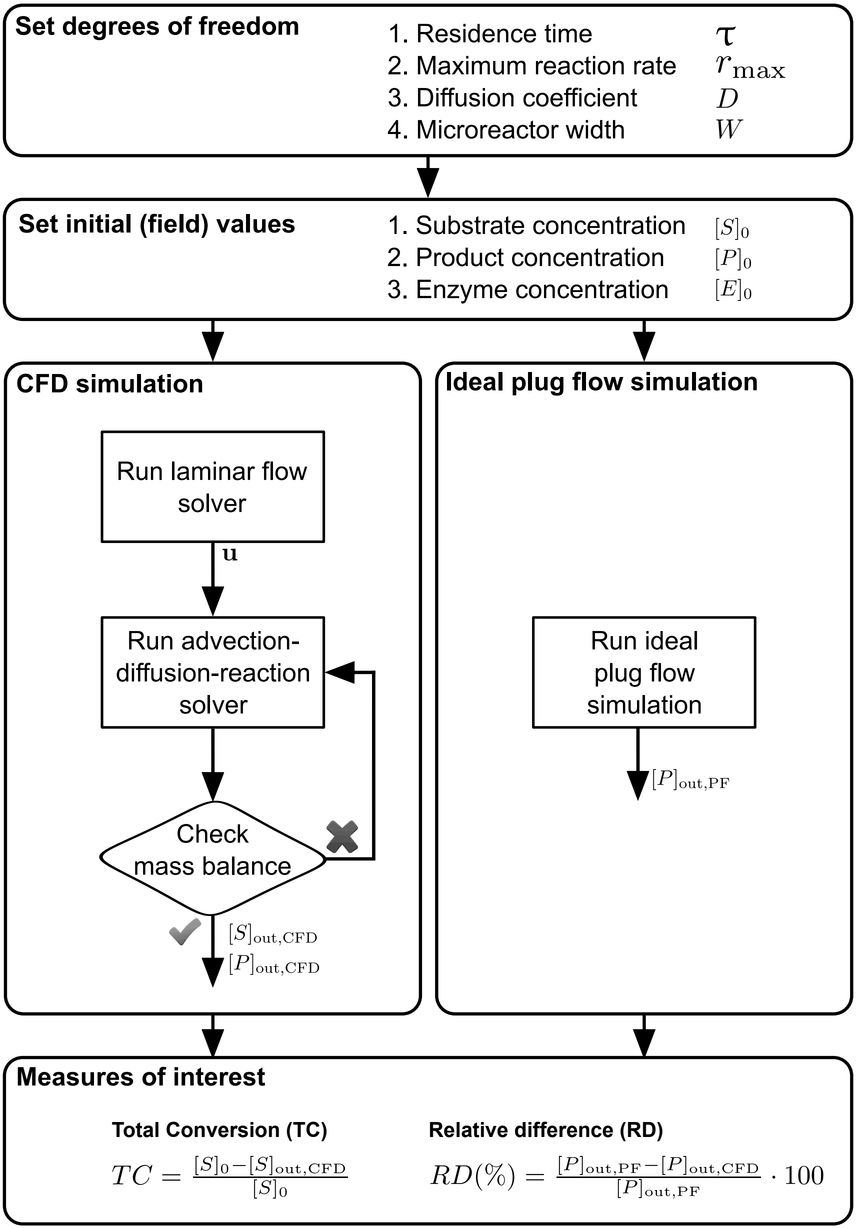

Figure 5.3: Flow chart representation of the proposed generic methodology to obtain data for the analysis of mass transfer limitations in a microreactor.

Define degrees of freedom

The different degrees of freedom need to be determined and appropriate ranges for each of these degrees of freedom should be set. In this chapter four different degrees of freedom are used.

1. **Diffusion coefficient (D)**
   The diffusion coefficient of substrate S and product P is varied between 10^{-13} and $5 \times 10^{-9}\,\mathrm{m^2/s}$, which is a broad range which also involves very small diffusion coefficients. However, this makes it possible to determine whether the results of the generic methodology relate with the traditional approach of dimensionless numbers for a broad range of diffusion values. Although D is fixed for a specific component, this also allows to investigate the effect of using substrates which differ in molecular size, and thus in diffusion coefficient. Moreover, one can judge what happens if e.g. another solvent would be used in which the component has a different D. Hence, it could assist in the choice of solvent. For every order of magnitude, samples were taken at $1 \times 10^{\mathrm{order}}$ and $5 \times 10^{\mathrm{order}}$ (with order $\in \{-9, -10, -11, -12, -13\}$), leading to 10 different D values.
2. **Microreactor width (W)**
   Three different microreactor dimensions are selected: 200 µm ($20 \times 10\,000$ cells), 400 µm ($40 \times 10\,000$ cells) and 1000 µm ($100 \times 10\,000$ cells). For the immobilised case, the number of cells to describe the microreactor can be halved by using a symmetry plane. For the 200 µm microreactor, this results in $10 \times 10\,000$ cells.
3. **Residence time (τ)**
   The study investigates three different residence times: 1, 10 and 30 min. To alter the mean residence time, the uniform inlet velocity of the fluid is changed accordingly: $u_{\mathrm{x,inlet}} = L/\tau$ where $u_{\mathrm{x,inlet}}$ is the inlet velocity in the x-direction, L the length of the microreactor and τ the mean residence time.
4. **Maximum reaction rate ($r_{\mathbf{max}}$)**
   The maximum reaction rate is varied between 1.14×10^{-4} and $2.27 \times 10^{3}\,\mathrm{mM/s}$. For every order of magnitude, samples were taken at $1.14 \times 10^{\mathrm{order}}$ and $2.27 \times 10^{\mathrm{order}}$ (with order $\in \{-4, -3, -2, -1, 0, 1, 2, 3\}$), leading to 16 different r_{max} values.

For each of the degrees of freedom, a value needs to be selected and to be fed to both the ideal reactor model and the CFD model. However, for the ideal plug flow the diffusion coefficient D and microreactor width W do not impact the simulation, since the ideal plug flow is assumed to be completely mixed in the transverse direction. The total number of CFD simulations for each microreactor configuration is 1440 simulations ([10 diffusion values]∗[3 microreactor widths]∗[3 residence times]∗[16 maximum reaction rates]).

Execute simulations

After selecting the values for the different degrees of freedom, both models are simulated.

1. **Ideal plug flow**
   The residence time τ and reaction rate r_{max} are set in the model. The model simulation is performed and the product concentration $[P]_{\mathrm{out,PF}}$ at the outlet is extracted from the simulated data.
2. **CFD**
   Depending on the selected microreactor width, the corresponding computational grid is chosen. Subsequently the initial scalar fields of substrate S, product P and enzyme E are set and a steady-state laminar flow solver is used to solve the Navier-Stokes equations and generate the steady-state flow profile. Next, this flow profile is used to calculate the solution of the advection-diffusion equations coupled with the kinetic model to generate the required steady-state output concentration of substrate $[S]_{\mathrm{out,CFD}}$ and product $[P]_{\mathrm{out,CFD}}$. The average concentration of substrates and products at the outlet is calculated as follows:

   $$C_{\mathrm{out,CFD}} = \frac{\sum_{i=0}^{n} C_i u_{\mathrm{x},i} A_i}{\sum_{i=0}^{n} u_{\mathrm{x},i} A_i} \tag{5.24}$$

   where $C_{\mathrm{out,CFD}}$ represents the average substrate or product concentration, n the number of cells at the outlet, C_i is the concentration in cell i at the outlet, $u_{\mathrm{x},i}$ the flow velocity in the x-direction in cell i and A_i the outlet area of cell i. It is always verified whether total mass is conserved in the reactor. In case mass conservation is violated, solver settings are adapted and the error-prone simulations are repeated until total mass conservation is obtained.

Mass transfer analysis

After finishing both the ideal plug flow and CFD simulations for a certain selection of degrees of freedom, the results are compared to evaluate deviations from the ideal case. Two types of measures are extracted from the simulations: the total conversion (TC) of substrate (Equation 5.25) and the relative difference (RD) in product concentration between the ideal plug flow model and the CFD model (Equation 5.26).

$$TC = \frac{[S]_0 - [S]_{\mathrm{out,CFD}}}{[S]_0} \tag{5.25}$$

$$RD\,(\%) = \frac{[P]_{\mathrm{out,PF}} - [P]_{\mathrm{out,CFD}}}{[P]_{\mathrm{out,PF}}} \cdot 100 \tag{5.26}$$

where $[P]_{\mathrm{out,PF}}$ is the outlet concentration of product calculated from the plug flow model, and $[S]_{\mathrm{out,CFD}}$ and $[P]_{\mathrm{out,CFD}}$ are respectively the average outlet concentration of substrate and product calculated from the CFD simulation (Equation 5.24). The total conversion (TC) has to be monitored, given the fact that if a reaction is completely finished ($TC \approx 1$) at the moment of comparison, no conclusions can be drawn since the relative difference RD will be close to zero. Therefore, it is important to perform measurements to quantify the conversion that has been achieved at a point where the reaction is not finished yet, because only in that case the relative difference (RD) might give a quantitative estimation of the extent of mass transfer limitations occurring in the microreactor. The validity of using the RD as a measure for mass transfer limitations, will be shown in the results section. The outlet concentrations of the CFD simulations are always compared with the outlet concentrations of the ideal plug flow simulations, even when the Bodenstein number Bo is low and ideal plug flow behaviour is violated. Like other types of mass transfer limitations, dispersion will reduce the steady-state productivity of the reactor and therefore scenarios with low Bo values will lead to increased RD values. The validity of this assumption is discussed in the results section.

5.3.4 Software

To set up the presented methodology, two open-source software packages are coupled together.

Python

Python is a high-level and open-source programming language and is used to perform the ideal plug flow calculations by using the in-house developed pyIDEAS package introduced in Chapter 2. A scenario analysis toolbox is constructed, based on the pyFoam library which allows to control OpenFOAM-runs and manipulate OpenFOAM-data (Gschaider, 2010). This toolbox is used to perform the necessary *in silico* experiments. After finishing all simulations, Python packages such as Pandas (data structures and analysis) (McKinney, 2010) and matplotlib (plotting library) (Hunter, 2007) are used to post-process the generated data.

OpenFOAM

OpenFOAM (Open source Field Operation And Manipulation) is an open-source collection of C++ class libraries developed for simulating continuum mechanics (OpenFOAM, 2014). As OpenFOAM does not have a GUI, all files and executables are called from the command line. OpenFOAM 2.2.2 is used to numerically approximate the Navier-Stokes equations for laminar flow. The OpenFOAM library contains a transient laminar flow solver icoFoam. However, transient simulations are computationally expensive and take more time to converge. Therefore, the icoFoam solver is converted into a steady-state solver, based on the implementation of the steady-state turbulent flow solver simpleFoam. This yielded a steady-state solver for laminar flow, which was used for the calculation of the flow profile in the microreactors under study. After obtaining the flow profile, the advection-diffusion-reaction equation is solved (Figure 5.3). The advection-diffusion solver for heat transfer scalarTransportFoam, is adapted and extended to include the kinetic model (Equation 5.9) based on the User Guide of OpenFOAM (OpenFOAM, 2014).

5.4 Results

The presented methodology (section 5.3.3) is applied to both microreactor configurations, i.e. the microreactor with immobilised enzyme at the wall and the Y-shaped microreactor. First, the results of the immobilised case are discussed in more detail to illustrate the presented technique. Next, the results of the Y-shaped microreactor are discussed. Both cases will also be compared with the traditional approach which relies on dimensionless numbers in order to emphasise the merit of the proposed technique.

The nominal values for the different degrees of freedom are given in Table 5.3.

Table 5.3: Nominal values for the simulations for the different degrees of freedom (DOF).

DOF	Nominal value
D	$10^{-11}\,\mathrm{m^2/s}$
$r_{\max}$	$2.271\,\mathrm{mM/s}$
W	$200\,\mu\mathrm{m}$
τ	$10\,\mathrm{min}$

5.4.1 Immobilised enzyme at the wall

First, the individual effects of different degrees of freedom, i.e. diffusion coefficient D, maximum reaction rate $r_{\max}$, residence time τ and microreactor width W, will be investigated and related to the total conversion TC and the relative difference RD. Subsequently, the combined effect of the diffusion coefficient and the maximum reaction rate is analysed. Finally, the results of the generic methodology will be compared with the second Damköhler number ($\mathrm{Da_{II}}$).

Effect of the diffusion coefficient

Figure 5.4 shows the impact of the diffusion coefficient D on the relative difference RD and the total conversion TC. It can be observed that by increasing D, TC is increasing and RD is decreasing. A higher diffusion coefficient leads to a more homogeneous concentration across the cross section of the microreactor, leading to ideal plug flow behaviour and, hence, a decrease in RD. Moreover, a high diffusion coefficient leads to higher substrate concentrations at the wall and thus also in the vicinity of the immobilised enzyme, which leads to an increase in total conversion and productivity. For the nominal values selected here, a D value higher than $5 \times 10^{-11}\,\mathrm{m^2/s}$ leads to plug flow behaviour and complete substrate conversion. These observations from the simulations are logical and fit with the theoretical understanding about this system.

Effect of maximum reaction rate

Increasing the maximum reaction rate ($r_{\max}$), which can be accomplished by means of a more active enzyme, leads to increases in both the TC and the RD (Figure 5.5). This means that higher maximum reaction rates lead to even higher

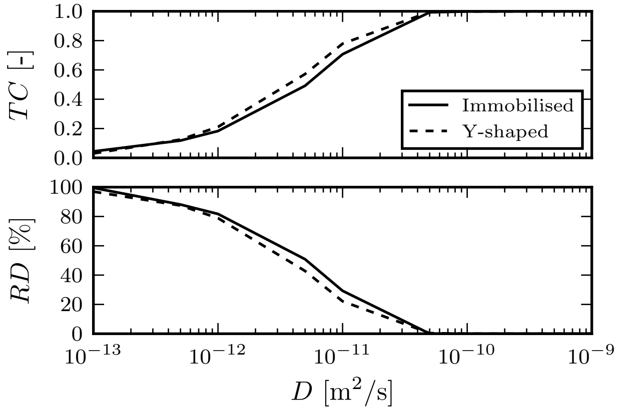

Figure 5.4: Effect of the diffusion coefficient on the total conversion (TC) and relative difference (RD) in both the enzyme immobilised microreactor and Y-shaped microreactor at $\tau = 10\,\text{min}$, $W = 200\,\mu\text{m}$ and $r_{\text{max}} = 2.271\,\text{mM/s}$.

conversions, although saturation occurs at a total conversion value of 0.7. However, this also induces mass transfer limitations as can be seen from the RD curve. For low r_{max} values ($< 0.1\,\text{mM/s}$), a monotonic increase in relative difference can be observed. By increasing the maximum reaction rate at constant diffusion rate, the CFD model reveals an increase in mass transfer limitations causing the relative difference (RD) to rise. However, at a r_{max} value of $2.27 \times 10^{-1}\,\text{mM/s}$, a maximum is observed in RD. This is caused by the fact that the ideal plug flow reactor already reaches a conversion of 99.99 % at a r_{max} value of $1.54 \times 10^{-2}\,\text{mM/s}$. Hence, the maximum conversion is reached for the ideal plug flow reactor and further increasing r_{max} no longer leads to increased conversion in the ideal plug flow. In contrast, the predicted total conversion of the CFD model does increase slightly since the substrate is locally depleted, leading to a higher driving force for the diffusive mass transfer. At r_{max} values above $10\,\text{mM/s}$, the diffusive mass transfer reaches the upper limit, leading to a constant TC and RD between the ideal reactor and the CFD simulation.

Effect of residence time

To study the effect of residence time in the immobilised microreactor, the inlet velocity is changed to the appropriate values. Table 5.4 shows that an increase in residence time leads to an increase in TC and a decrease in RD. This means that an increase in residence time positively affects the TC and the mass transfer which is expected as the substrate spends more time in the microreactor, and thus has

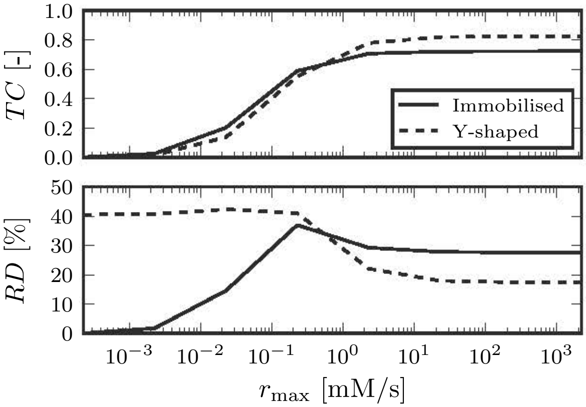

Figure 5.5: Effect of the maximum reaction rate on the total conversion (*TC*) and relative difference (*RD*) in both the enzyme immobilised microreactor and Y-shaped microreactor at $\tau = 10$ min, $W = 200$ µm, $D = 10^{-11}$ m^2/s.

more time to be converted to product. Moreover, the effect of diffusion limitations is reduced, because the substrate has more time to diffuse from the bulk of the reactor to the enzyme.

Table 5.4: Impact of the residence time on the total conversion (*TC*) and relative difference (*RD*) for both the enzyme immobilised microreactor and the Y-shaped microreactor at $W = 200$ µm, $r_{\max} = 2.271$ mM/s, $D = 10^{-11}$ m^2/s.

	Immobilised		Y-shaped	
τ [min]	*TC* [-]	*RD* [%]	*TC* [-]	*RD* [%]
1	0.173	81.46	0.033	86.25
10	0.707	29.27	0.779	22.13
30	0.969	3.07	0.988	1.22

Effect of microreactor width

The effect of changing the microreactor width is explored. In order to be able to fairly compare simulation results corresponding to different microreactor widths, kinetic conditions must remain constant. This is achieved by keeping the enzyme and substrate concentrations at the same levels in the different simulated cases. This implies that when W is doubled, the total amount of enzyme immobilised at the wall needs to be doubled in the case of a rectangular reactor (Walter et al., 2005). In this way the average enzyme concentration in the reactor is kept constant. It is assumed for the simulation that the amount of enzyme which could be immobilised at the walls is no limiting factor, even though enzymes typically have a diameter between 2 and 20 nm and thus this assumption will not be valid in reality (Chaplin and Bucke, 1990). From Table 5.5, it can be concluded that an increase in microreactor width, for a constant residence time τ, leads to lower TC and higher RD values. This implies that an increase in microreactor width negatively affects the extent of the reaction and the mass transfer. Substrate molecules need to diffuse over longer distances to reach the enzyme which is immobilised at the wall, yielding increased mass transfer limitations. Substrate molecules originating from the center of the microreactor, might in some cases even leave the microreactor without reaching the enzymes.

Table 5.5: Impact of the enzyme immobilised microreactor width on the total conversion (TC) and relative difference (RD) at $\tau = 10\,\text{min}$, $r_{\text{max}} = 2.271\,\text{mM/s}$, $D = 10^{-11}\,\text{m}^2/\text{s}$.

	Immobilised		Y-shaped	
W [µm]	TC [-]	RD [%]	TC [-]	RD [%]
200	0.707	29.27	0.779	22.13
400	0.323	67.74	0.426	57.37
1000	0.133	86.73	0.170	83

Combined effect of the diffusion coefficient and maximum reaction rate

After investigating the effects of the individual degrees of freedom, the combined influence of the diffusion and maximum reaction rate is investigated. This combined investigation yields more information about the mass transfer limitations, but also on how the proposed methodology relates with the second Damköhler number. The values of the residence time τ and microreactor width W are fixed at their nominal values (Table 5.3) for this analysis. The diffusion coefficient values and maximum reaction rate values are varied and 160 CFD simulations are carried out. Figure 5.6 shows both the TC (dashed lines) and RD (greyscale) for the different sets of diffusion coefficients and maximum reaction rates. The dashed lines in the figure represent sets of degrees of freedom with a constant conversion value, i.e. iso-conversion lines. A linear interpolation is performed between adjacent simulation values to generate continuous dashed lines.

From Figure 5.6, three different regions can be distinguished:

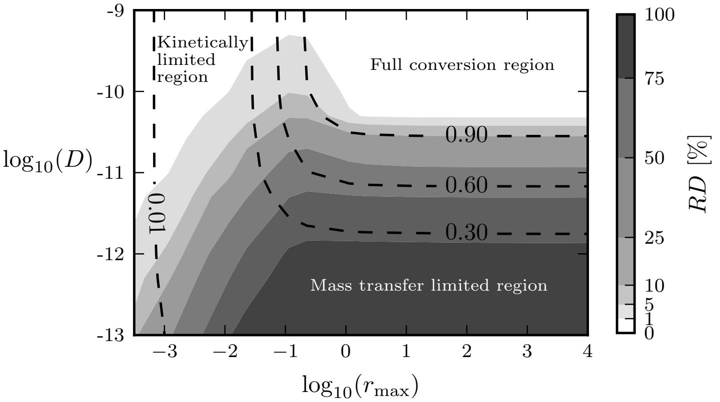

Figure 5.6: Influence of the diffusion coefficient and maximum reaction rate on conversion (dashed lines) and relative difference (grey colormap) in an immobilised enzyme microreactor at constant values of $\tau = 10\,\text{min}$ and $W = 200\,\mu\text{m}$. Dashed lines represent iso-conversion lines.

- **Mass transfer limited region**
  At high maximum reaction rates ($r_{\max} > 10^{-2}\,\text{mM/s}$) and low diffusion coefficients ($D < 10^{-11}\,\text{m}^2/\text{s}$) (bottom right in Figure 5.6), a high RD between the ideal plug flow and the CFD model prevails. The conversion of substrate to product proceeds so fast that mass transport rates govern the system because they are much slower. Since in this region the conversion only depends on the diffusion coefficient, the system is said to be mass transfer controlled.

- **Kinetically limited region**
  When the values of the diffusion coefficients are high ($D > 10^{-11}\,\text{m}^2/\text{s}$), a low RD is found, implying that under these conditions no mass transfer limitations occur independent from the value of the maximum reaction rate. However, the latter is not entirely true, since the RD can only be used as a measure for mass transfer limitation if the TC is sufficiently low (< 0.9). At high TC values, the RD automatically diminishes because the substrate is almost fully converted into product, making the RD useless as measure for mass transfer limitations. Therefore, only the region which has both a low RD and sufficiently low TC can be regarded as the kinetically limited region, which means that mass transfer limitations do not prevail and ideal plug flow models can be used to simulate the reactor behaviour, hereby avoiding the use of CFD models which are more computationally intensive. This region is found at low maximum reaction rates and high diffusion coefficients (top left region in Figure 5.6).

- **Full conversion region**
  At high maximum reaction rates ($r_{\max} > 0.1\,\mathrm{mM/s}$) as well as high diffusion coefficients ($D > 5 \times 10^{-11}\,\mathrm{m^2/s}$), the substrate is (almost) completely converted at the microreactor outlet. That is why the RD is low. However, no conclusions can be drawn about the fact whether mass transfer limitations occur under these conditions. Therefore, it is important to keep TC sufficiently low ($TC < 0.90$). By reducing the residence time, the RD can be evaluated at lower conversions and conclusions can be drawn about mass transfer limitations. This can be achieved by evaluating the current CFD simulation result at a point inside the microreactor instead of at the outlet. However, in real life, it is not always possible to have appropriate optical access to the whole flow path (Mozharov et al., 2011).

Influence of microreactor width and residence time

The importance of the microreactor width (W) can be seen in Figure 5.7. By decreasing the microreactor width, the size of the kinetically limited region and full conversion region are increased. This means that mass transfer limitations can be reduced by decreasing the maximum diffusion length of the substrate molecules to the immobilised enzymes (i.e. microreactor width W).

By increasing the residence time (τ), the size of the full conversion region is increasing. This could be expected, since the reaction has more time to complete at high residence times. The size of the kinetically limited region is fairly constant for the different residence times, however at low maximum reaction rates and low diffusion coefficients a slight increase in mass transfer limitations can be found. For high residence times, the reaction can proceed for much longer, so a small deviation between the CFD model and the ideal model will be more pronounced.

Relation with dimensionless numbers

In Figure 5.8, the RD of Figure 5.7 is plotted along with the second Damköhler number ($\mathrm{Da}_{\mathrm{II}}$). It can be observed that the iso-$\mathrm{Da}_{\mathrm{II}}$ lines correspond nicely with the transition from kinetically limited to mass transfer limited conditions. This shows that the proposed methodology is consistent with the theory behind the second Damköhler number. For this particular case, the second Damköhler number values can be related to the RD and therefore the level of mass transfer limitation, e.g. for all the simulations a $\mathrm{Da}_{\mathrm{II}}$-value of 1 corresponds with a RD of 5 to 10%. The correspondence of the $\mathrm{Da}_{\mathrm{II}}$ with the simulations also yields that both the

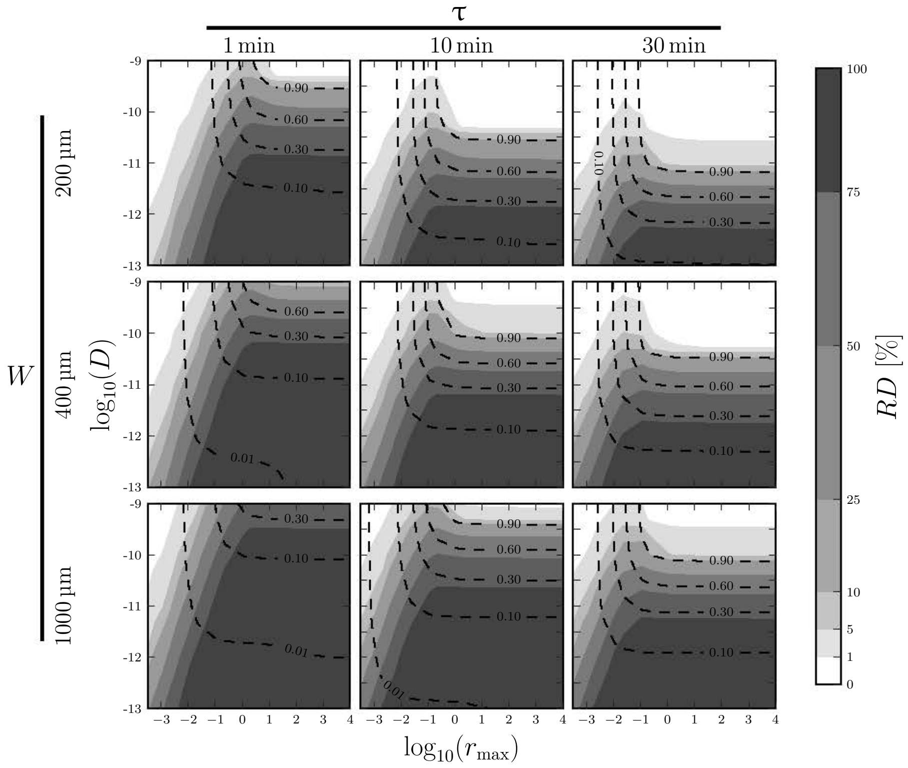

Figure 5.7: Influence of residence time and microreactor width on conversion and mass transfer limitation in an immobilised enzyme microreactor, with sets of diffusion coefficients and maximum reaction rates at $\tau = 1$, 10 and 30 min and W=200, 400 and 1000 µm. Each subplot represents RD as a grey-scale map, where iso-conversion lines are shown as dashed lines.

diffusion coefficient (D) and the maximum reaction rate (r_{max}) play an important role.

The importance of the Bodenstein number (Bo) is also assessed for the following case: a microreactor width W of 400 µm, a residence time τ of 30 min and a r_{max} value of 2.271×10^{-2} mM/s. This particular case is evaluated for two different diffusion values, i.e. 10^{-13} and 10^{-9} m^2/s. For the low diffusion case, the Bo value is equal to 0.13, indicating that a large deviation from the plug flow is expected (Nagy et al., 2012). For the high diffusion case, the corresponding Bo value is equal to 1086, indicating that this case should resemble a plug flow behaviour. The importance of the Bodenstein number is shown in Figure 5.9, which shows the product concentration $[P]$ across the cross section at the outlet of the microreactor. For the high Bo value, $[P]$ shows only a small decrease when approaching the center

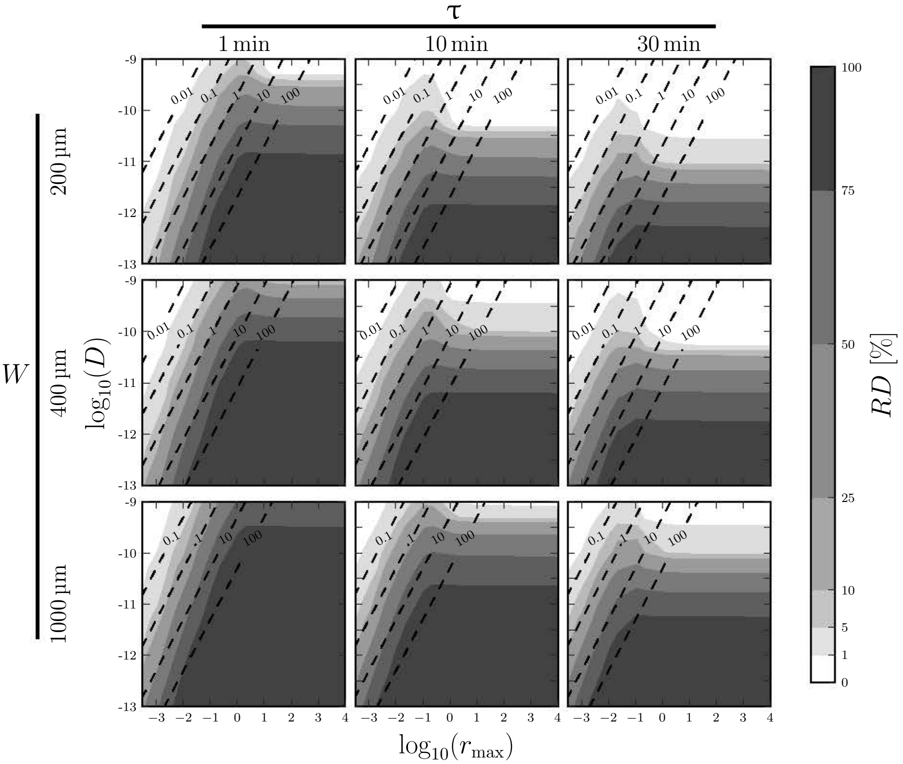

Figure 5.8: The results of the proposed methodology are compared with the second Damköhler ($\mathrm{Da}_{\mathrm{II}}$). Each subfigure represents RD as a grey-map, the iso-$\mathrm{Da}_{\mathrm{II}}$ lines are shown as dashed lines.

of the reactor (−3.4 %). However, for low Bo values a large concentration gradient exists near the reactor walls (at ±200 µm) and the concentration in the center of the reactor is close to zero. This illustrates that the dispersion phenomenon is important and can lead to a decrease in reactor productivity.

5.4.2 Y-shaped microreactor

The proposed methodology is also applied for the Y-shaped microreactor to illustrate the power and flexibility of the proposed methodology.

Effect of the diffusion coefficient

Increasing the diffusion coefficient has a positive impact on the TC and also reduces the mass transfer limitations, as evidenced in Figure 5.4. A slight improvement in

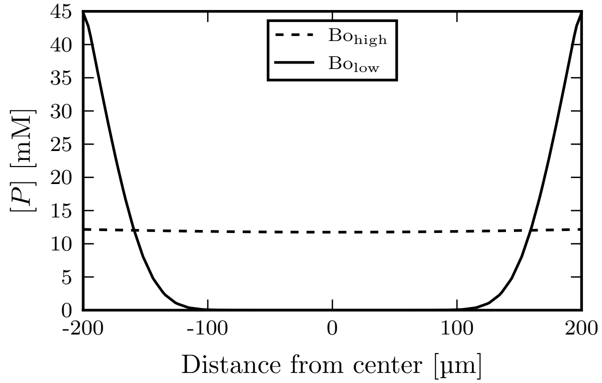

Figure 5.9: The concentration profiles of product P across the cross section of the outlet for a high Bo value (Bo = 1086) and a low Bo value (Bo = 0.13). Simulations are conducted for the immobilised enzyme microreactor for the following case: $W = 400\,\mu\text{m}$, $\tau = 30\,\text{min}$ and $r_{\text{max}} = 2.271 \times 10^{-2}\,\text{mM/s}$. The diffusion coefficients for Bo_{high} and Bo_{low} are 10^{-9} and $10^{-13}\,\text{m}^2/\text{s}$ respectively.

performance with the same sets of degrees of freedom in TC and RD can be noticed, upon comparison with data for the immobilised enzyme microreactor.

Effect of the maximum reaction rate

Increasing the maximum reaction rate has a positive influence on the total conversion (TC) and mass transfer limitation (Figure 5.5). Microreactor performance in terms of total conversion, increases when the reaction proceeds faster. Upon comparing data of the Y-shaped microreactor with the enzyme immobilised microreactor, the Y-shaped system reaches a higher TC when r_{max} reaches high values. The evolution of the relative difference (RD) of the Y-shaped reactor remains constant around 40 % at low r_{max} values ($r_{\text{max}} < 0.5\,\text{mM/s}$), while the immobilised enzyme microreactor shows a positive trend as a function of the r_{max}. This observation already indicates that the behaviour of the Y-shaped microreactor is different from the immobilised enzyme microreactor.

Effect of the residence time

By increasing the residence time τ, the TC is positively affected and the RD is reduced (Table 5.4). Comparing with the immobilised enzyme microreactor values, it can be seen that at a higher residence time, total conversion and relative difference are slightly improved in the Y-shaped microreactor.

Effect of the microreactor width

An increase in microreactor width W leads to a decrease in TC and an increase in RD (Table 5.5). This means that an increase of the microreactor width W negatively affects the performance of the Y-shaped microreactor. Comparing the RD values of the Y-shaped case with the immobilised case, it seems that the effect of changing the microreactor width is similar for both microreactor configurations.

5.4.3 Impact of the combination of the degrees of freedom

As shown with the immobilised enzyme case, the combined influence of different degrees of freedom yielded considerable additional insight and information about the conditions at which mass transfer limitations occur. To verify whether the second Damköhler number can be applied in this case, a similar analysis is performed.

Combined effect of the diffusion coefficient and maximum reaction rate

The influence of the diffusion coefficient D and maximum reaction rate $r_{\max}$ on both the TC and RD is shown in Figure 5.10. As in the previous case, three different regions can be distinguished: the mass transfer limited region, the kinetically limited region, and the full conversion region. The size and shape of the full conversion region is quite similar to the immobilised enzyme case. However, the transition from the kinetically limited region to the mass transfer limited region is totally different from the previous case. For the immobilised case, the RD increases when the maximum reaction rate $r_{\max}$ increases (at constant D). In contrast, no increase of the RD is observed at low maximum reaction rates for the Y-shaped reactor case (at constant D). This behavioural change indicates that the diffusion coefficient is primarily limiting the performance of the system under such circumstances. Moreover, it should be noticed that, in contrast to the immobilised enzyme reactor, an improvement of the reaction rate of the enzyme does not yield any productivity increase. This indicates that the transport process occurring at the interface of the two streams (i.e. the Y-shaped microreactor) is different from that occurring at the microreactor wall (i.e. the immobilised enzyme microreactor). This is also illustrated in Figure 5.11, where the second Damköhler number ($\mathrm{Da_{II}}$) is unable to describe the transition from the kinetically limited region to the mass transfer limited region..

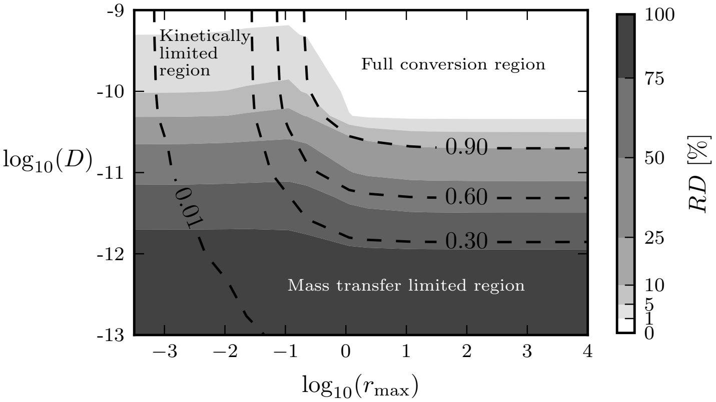

Figure 5.10: Influence of the diffusion coefficients and maximum reaction rates on conversion in a Y-shaped microreactor with constant values of $\tau = 10\,\mathrm{min}$ and $W = 200\,\mathrm{\mu m}$. The dashed lines represent the iso-conversion lines.

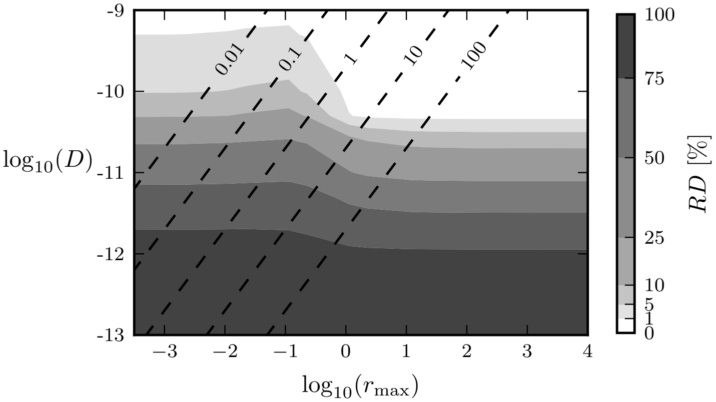

Figure 5.11: The effect of the diffusion coefficient values and the maximum reaction rates on the mass transfer limitations in a Y-shaped microreactor with constant values of $\tau = 10\,\mathrm{min}$ and $W = 200\,\mathrm{\mu m}$. The dashed lines represent the $\mathrm{Da_{II}}$ numbers.

Influence of microreactor width and residence time

The influence of residence time and microreactor width on the TC and mass transfer limitation in a Y-shaped microreactor is shown in Figure 5.12. From this figure, it can be derived that mass transfer limitation is negatively affected by an increase in microreactor width. It seems that, for a better microreactor performance, it is preferable to operate at low W, because both the kinetically limited region and full conversion region are larger. As expected, the residence time has a positive impact on the conversion, because the system has more time to react. In contrast to the immobilised enzyme case, an increased residence time also leads to a larger kinetically limited region. This supports the observation made above that another process is governing the mass transfer limitations in contrast to the findings with the immobilised enzyme case.

Relation with dimensionless numbers

As stated above, from Figure 5.12 it could be concluded that the diffusion coefficient is primarily limiting the performance of the system in the kinetically limited region. This indicates that the second Damköhler number ($\mathrm{Da_{II}}$) is not suitable to differentiate between kinetically limited and mass transfer limited conditions for this specific microreactor configuration.

This can be seen from Equation 5.15 as the largest fraction of the reaction takes place in the region where the advection cannot be ignored. This means that the term $\partial S^* / \partial X^*$ will have an important effect on the reaction rate.

It is possible that these two regions, with a constant RD, are influenced by the value of the dimensionless numbers (the two-dimensional Péclet ($\mathrm{Pe_{2D}}$) and the second Damköhler number ($\mathrm{Da_{II}}$)). Dividing both dimensionless numbers yields a new dimensionless number, which is often referred to as the first Damköhler number ($\mathrm{Da_{I}}$) and gauges the reaction rate and the convection:

$$\mathrm{Da_I} = \frac{\left(\dfrac{r_{\mathrm{max}} W^2}{4D[S]_0}\right)}{\left(\dfrac{u_{\mathrm{x}} W^2}{4DL}\right)} = \frac{r_{\mathrm{max}} L}{u_{\mathrm{x}}[S]_0} \tag{5.27}$$

Ristenpart and Stone (2012) state that neglecting the concentration term in Equation 5.15 can be assumed to be correct if the inequality ($\mathrm{Da_I} \ll 1$) is satisfied. This simplification (shown in Equation 5.28) implies that the two-dimensional Péclet

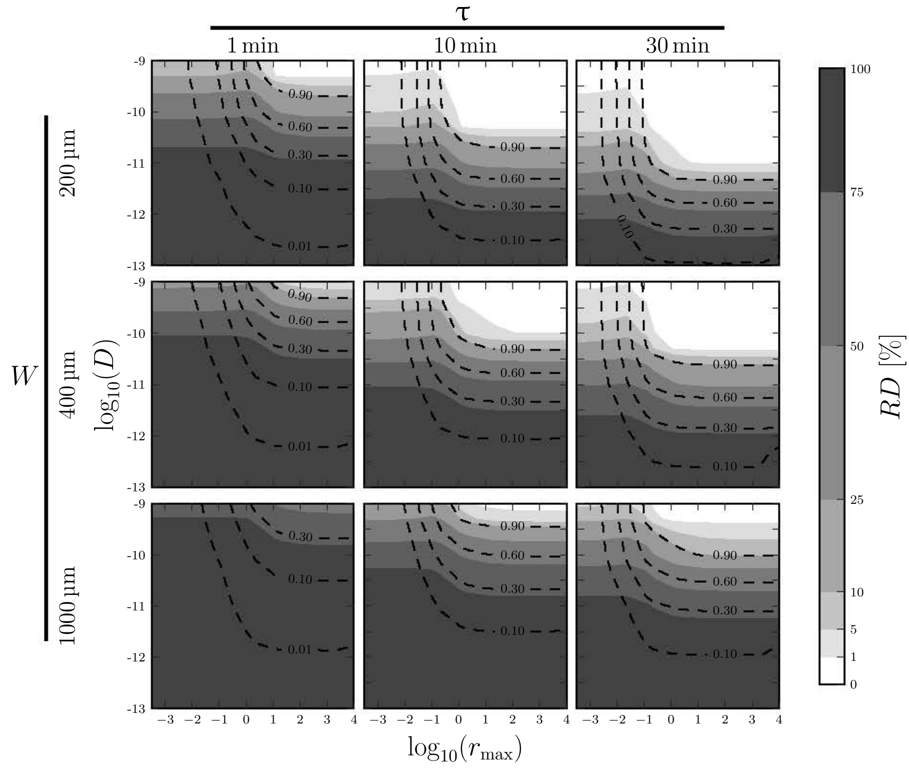

Figure 5.12: Influence of residence time and microreactor width on conversion and mass transfer limitation in a Y-shaped microreactor configuration with sets of diffusion coefficients and maximum reaction rates at $\tau = 1$, 10 and 30 min and $W = 200$, 400 and 1000 µm. Each subplot represents *RD* as a grey-scale map, and iso-conversion lines are shown as dashed lines.

number ($\mathrm{Pe}_{2\mathrm{D}}$) has a large impact on the solution of the equation, and the diffusion of substrate is mainly governed by the fluid velocity and not by the maximum reaction rate.

$$\frac{\partial^2 S^*}{\partial {Y^*}^2} \approx \left(\frac{u_\mathrm{x} W^2}{4DL}\right) \frac{\partial S^*}{\partial X^*} \tag{5.28}$$

However, at large maximum reaction rates, Da_I is near or above unity and the inequality is not satisfied and both terms contribute significantly to the solution. In Figure 5.13 the correspondence of $\mathrm{Pe}_{2\mathrm{D}}$ with the proposed methodology is shown. It is clear that the second Damköhler number is not applicable for the Y-shaped microreactor case. However, in the literature Da_II is wrongly used to describe the mass transfer limitations for this specific case (Swarts et al., 2010).

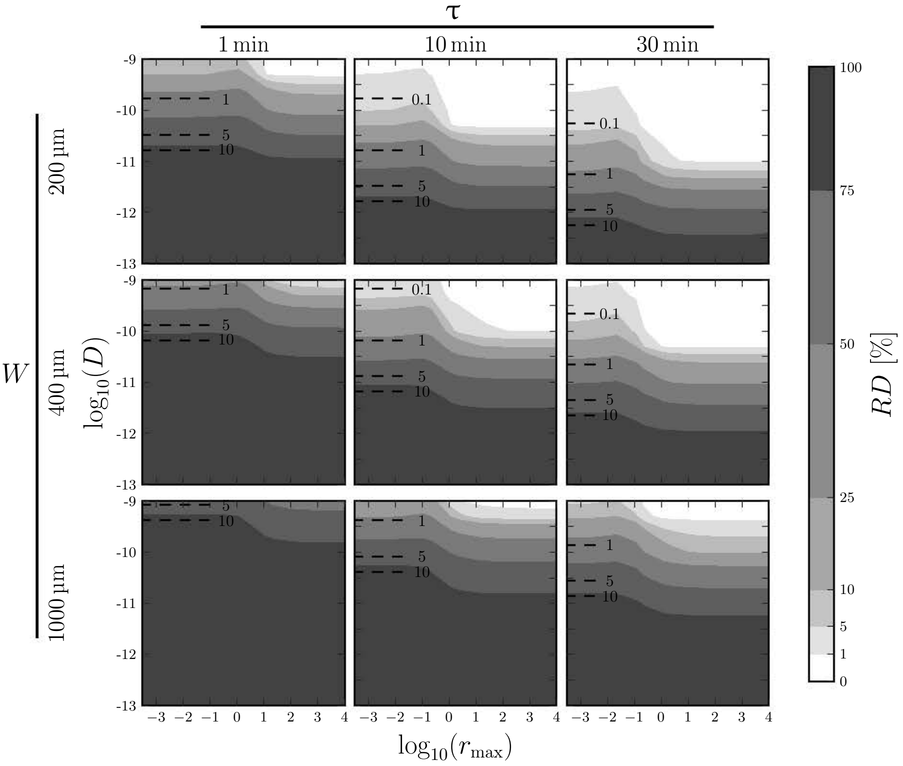

Figure 5.13: Influence of residence time and microreactor width on conversion and mass transfer limitation in a Y-shaped microreactor configuration with sets of diffusion coefficients and maximum reaction rates at $\tau = 1$, 10 and 30 min and $W = 200$, 400 and 1000 µm. Each subplot represents the RD as a grey-scale map, iso-Pe_{2D} lines are shown as dashed lines.

The Bodenstein number (Bo) is evaluated for the same DOF values as in the immobilised enzyme case, leading to the results shown in Figure 5.14. For the high Bo number, the product concentration across the cross section of the reactor is almost constant. In contrast, the concentration of the product for the low Bo case is only present in the center of the reactor, i.e. the interface between the stream containing substrate and the stream containing enzyme. This again shows, that dimensionless numbers like Bo can be powerful if applied correctly, but also that the proposed methodology can capture these effects since it will affect the RD and TC.

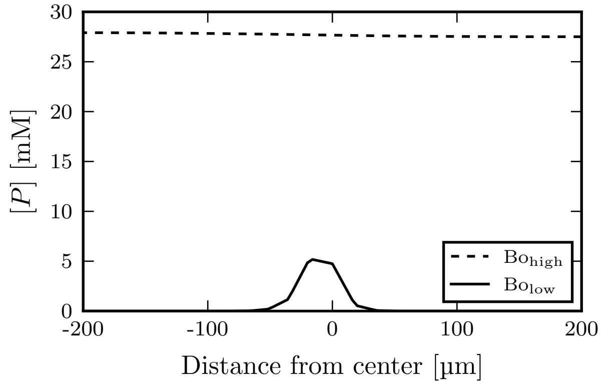

Figure 5.14: The concentration profiles of product P across the cross section of the outlet for a high Bo value ($\mathrm{Bo}_{\mathrm{high}} = 1086$) and a low Bo value ($\mathrm{Bo}_{\mathrm{low}} = 0.13$). Simulations were conducted for the Y-shaped microreactor for the following case: $W = 400\,\mu\mathrm{m}$, $\tau = 30\,\mathrm{min}$ and $r_{\max} = 2.271 \times 10^{-2}\,\mathrm{mM/s}$. The diffusion coefficients for $\mathrm{Bo}_{\mathrm{high}}$ and $\mathrm{Bo}_{\mathrm{low}}$ were 10^{-9} and $10^{-13}\,\mathrm{m^2/s}$ respectively. The stream containing enzyme is located at the left side of the outlet, as illustrated in Figure 5.2.

5.5 Discussion

A qualitative overview of the presented methodology is given in Figure 5.15. At low relative difference (RD) and low total conversion ($TC < 0.9$), the reaction is said to be kinetically limited. At low RD and high TC, the substrate is (almost) fully converted to product. At high RD and low TC, the reaction is mass transfer limited since there is a large difference between the CFD and ideal plug flow simulations. Since it is not possible to yield a high RD and high TC together, this result can never be achieved. Since a high TC indicates that the substrate concentration in the CFD simulation is low, the RD can never reach high values. This kind of approach yields some opportunities, since it allows to quantify and reduce mass transfer limitations. In this respect, it is possible to optimise the (internal) reactor geometry, e.g. by including static mixers (Yang et al., 2015). As stated before, dimensionless numbers can only be used for idealised reactor geometries and simplified kinetics (Kleijn, 2012). In this sense, dimensionless numbers are useless for advanced process optimisation.

For a real-life case, the required number of CFD simulations will depend on the case. In this chapter two configurations are investigated in more detail, so the corresponding dimensionless numbers can be used directly. For other and/or more advanced configurations, it is advisable to perform at least some CFD simulations

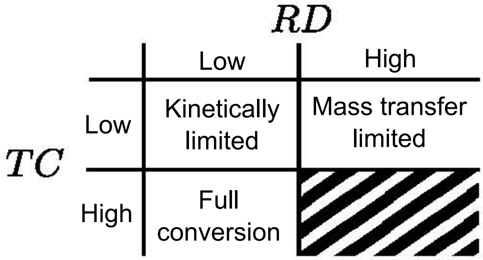

		RD	
		Low	High
TC	Low	Kinetically limited	Mass transfer limited
	High	Full conversion	▨

Figure 5.15: Based on the proposed measures of interest, i.e. the relative difference (*RD*) and the total conversion (*TC*), the three mass transfer regimes can be differentiated.

to increase the understanding about the system under study. The diffusion coefficients of the different substrates and products are typically known *a priori*, and the order of magnitude of the reaction rate can also be estimated. If the aim is to perform experiments in the kinetically limited region to estimate the reaction rate more precisely, the microreactor width is the variable which has most influence. So with only a few CFD experiments, the optimal microreactor width can be determined, keeping in mind any practical limitations. Experimental validation of the *in silico* experiments can be achieved by altering the residence times and microreactor widths (Swarts et al., 2010). However, altering diffusion coefficients and maximum reaction rates would yield some practical hurdles, since the substrate and/or enzyme need to be changed.

For the two cases considered here, mass transfer limitations could be easily related with an appropriate dimensionless number. This indicates that dimensionless numbers can be easily calculated for simple microreactor setup, and thus are certainly useful and powerful. However, the correct identification of the underlying mass transfer processes is crucial, since this will determine which dimensionless number is appropriate. In this respect, Swarts et al. (2010) used the second Damköhler number to calculate the mass transfer limitations in a Y-shaped microreactor. In this chapter, it was shown that this not correct, since $\mathrm{Da}_{\mathrm{II}}$ is only applicable for immobilised enzyme microreactors. However, based on this dimensionless number, one might wrongly conclude that improving the turnover number of the enzyme is crucial to improve the reactor productivity. Therefore, dimensionless numbers should be applied with care. For more complex reactor configurations and/or reactions, the mass transfer will be governed by a multitude of phenomena, making it difficult to directly relate the results with an appropriate dimensionless number. By using the generic methodology proposed in this chapter, it is even possible to determine and quantify mass transfer limitations for more complex reactor configurations and/or reactions.

According to Walter et al. (2005), the modified residence time should be kept constant to determine whether mass transfer limitations occur. The modified residence time (τ_{mod}) is defined as:

$$\tau_{\text{mod}} = \frac{\text{Enzyme mass}}{\text{Reactant flow}} = \frac{n_{\text{enzyme}}}{F_{\text{S}}} \tag{5.29}$$

where n_{enzyme} is the total amount of enzyme in the microreactor and F_{S} is the substrate flux at the inlet. When varying the microreactor width W and/or the residence time τ, the enzyme concentration should be adapted to keep the τ_{mod} constant. For the immobilised enzyme case, the total enzyme mass immobilised at the wall is adapted when the microreactor width is changed. For the Y-shaped microreactor, the incoming enzyme concentration is kept constant, since both the total enzyme mass and substrate mass flowing in the reactor are related proportionally to the microreactor width. So for the simulations involving different microreactor widths, the τ_{mod} requirement is met. However, for the simulations involving different residence times, no changes are done in total enzyme mass, leading to different τ_{mod} values. Walter et al. (2005) conclude that in this case, microreactor results cannot be compared to assess mass transfer limitations. However, by using the proposed methodology the microreactor (CFD) results are not compared directly with each other, but with the corresponding ideal plug flow case. As a result, the mass transfer limitations can be assessed as long as the conditions are the same for both the CFD reactor and the ideal plug flow reactor. The τ_{mod} does not have to be taken into account for the proposed method. However, for experimental approaches, in which experimental results have to be compared directly, a constant τ_{mod} remains an important requirement.

Loffler and Schmidt (1975) derived an effectiveness factor η, which was the ratio of the diffusion-limited reaction rate to the maximum reaction rate, in function of Da_{II}. In this way, reductions in productivity due to mass transfer limitations could be directly related with the Da_{II}. However, the process was only governed by diffusion and took place in a simple and repetitive geometry, making it possible to derive this analytic relationship. For more complex (nonrepetitive) geometries and/or more complex processes, it will become impossible to derive such relations (Kleijn, 2012). In this chapter, the choice for comparing simulated (outlet) concentrations instead of reaction rates, makes the proposed methodology independent of the actual reactor geometry and potentially also applicable for experimental work.

The Bodenstein number (Bo) is evaluated for different cases, and the importance of the dispersion phenomena can be directly linked with a reduced reactor productivity (increased RD). Therefore, it can be concluded that, even for low Bo values, the ideal plug flow model is the proper reference model to compare the CFD simulations with in order to assess mass transfer limitations. In this chapter this comparison is only carried out for steady-state simulations. For transient simulations, it will become much harder to compare both simulation results, since the nonideal behaviour of the real-life reactor will lead to changes in the mean residence time and residence time distribution function (Scott Fogler, 2004).

In some cases, the Y-shaped microreactor outperforms the immobilised enzyme reactor, e.g. higher TC values in Figure 5.4. However, this difference in TC should be very high to make a system relying on free enzyme economically feasible, due to the fact that the enzyme catalyst is expensive. In the immobilised reactor configuration the enzyme will be reused each time new substrate is passed over the immobilisation surface, while in the Y-shaped reactor fresh enzyme needs to be added continuously.

No explicit diffusion of the enzyme is considered here, however for enzymes which can diffuse the obtained results will be similar. In this chapter, the diffusion coefficient of the solute (D) in the Y-shaped case was in fact a lumping of both the diffusion coefficient of the solute (D_{S}) and the enzyme (D_{E}) (Equation 5.23). So by taking into account the actual diffusion value of the enzyme, the diffusion coefficient of the solute needs to be reduced (Equation 5.23) to obtain comparable mass transfer limitations. Some diffusion coefficients of enzymes in water of 25 °C are listed in Table 5.6. From this table it can be concluded that an enzyme diffusion coefficient of about $10^{-11}\,\mathrm{m^2/s}$ is more realistic for experiments in water. Since the diffusion coefficient values are particle-, solvent- and temperature-dependent, lower diffusion coefficient values are possible in other solvents or mixtures (Chirico et al., 1999).

A grid independency test was performed for both microreactor cases. Since simulations were conducted for many different conditions, the grid independency was only evaluated for a residence time τ of 10 min and a width W of 200 µm. To perform the grid independency test, three different meshes were constructed by changing the number of cells perpendicular to the flow direction to 20, 40 and 100. Using these different meshes, it was found that for the relative difference in outlet concentration of product P (Equation 5.24) between the basic mesh ($20 \times 10\,000$ cells) and refined mesh ($100 \times 10\,000$ cells), is sufficiently low ($< 5\%$). Only for conditions where both the diffusion is low ($D < 10^{-11}\,\mathrm{m^2/s}$) and the maximum reaction rate is high ($r_{\mathrm{max}} > 2.271\,\mathrm{mM/s}$), the difference between both meshes was found to be slightly higher and a more refined mesh would improve the accuracy. However, at these conditions mass transfer limitations are already severe and some

Table 5.6: Diffusion coefficients of different solutes and enzymes in water at 25 °C. (Freitas, 2003; Miložič et al., 2014; He and Niemeyer, 2003; Kremzner and Wilson, 1964)

	Particle	Mol. Wt. [g/mol]	D [m^2/s]
Solutes	NaCl	58.5	1.5×10^{-9}
	Acetophenone	120.2	7.35×10^{-10}
	Glucose	180	7.1×10^{-10}
	Citric acid	192	6.9×10^{-10}
Enzymes	Insulin	24 430	7.7×10^{-11}
	Hexokinase (yeast)	99 000	$6.0 \times 10^{-11*}$
	Glucose dehydrogenase	190 000	3.6×10^{-11}
	Acetylcholinesterase	230 000	$4.3 \times 10^{-11*}$

* Diffusion value at 20 °C.

(small) changes in productivity will have a limited impact on the mass transfer prediction. Moreover, the study was computationally very demanding and thus a trade-off was made between accuracy and computational time. On average one CFD simulation took about 36 min on eight cores, so in order to calculate all 2880 simulations about 72 days of computational time were required.

The uncertainty of the quantification of the mass transfer limitations depends on both the accuracy of the kinetic model and the CFD model. It is therefore important to determine whether kinetically limited data are used to calibrate the kinetic model parameters. Moreover, a grid independency test should be performed to make sure the CFD results are grid independent. When the accuracy of both models is known, it would be possible to calculate the uncertainty of the quantification of the mass transfer limitations. However, this is outside the scope of this chapter.

The presented methodology can be used for solvent selection, since changing the solvent will affect both the $r_{\max}$ and D. By identifying scenarios with low mass transfer limitations, it would be possible to switch to a more suitable solvent. From a theoretical point of view, this approach makes sense since changing the viscosity does not influence the velocity profile in laminar conditions of Newtonian fluids (Çengel et al., 2008). However, it should always be checked whether Re is sufficiently low (i.e. laminar flow conditions) and whether the required pressure-drop is realistic, since the Δp is proportional to the flow rate and viscosity μ. Moreover, the $r_{\max}$ and D values are only available for a limited amount of solvents (mostly water). This approach shows a lot of potential, but also comes with practical limitations since it requires a lot of information which probably needs to be gathered by performing a large-scale screening exercise.

5.6 Conclusions

A generic methodology was presented to assess mass transfer limitations. This methodology allows one to determine the importance of mass transfer limitations for a (micro)reactor configuration of interest.

- The second Damköhler number ($\mathrm{Da}_{\mathrm{II}}$) is frequently used to determine the extent of mass transfer limitations in microreactors. It was found that for the immobilised enzyme case $\mathrm{Da}_{\mathrm{II}}$ is suitable to decide on mass transfer limitations. However, from the results of the Y-shaped microreactor it could be concluded that the second Damköhler number is not always an appropriate number to assess mass transfer limitations. The two-dimensional Péclet number ($\mathrm{Pe}_{\mathrm{2D}}$) should be used in the case of the Y-shaped microreactor to determine the level of mass transfer limitation.
- The generic methodology can help researchers to build knowledge and support choosing the right dimensionless number. E.g. Swarts et al. (2010) wrongly used the second Damköhler number ($\mathrm{Da}_{\mathrm{II}}$) to study the effect of diffusion on the enzyme activity for a Y-shaped reactor. By using the generic methodology, such mistakes can be avoided and the real underlying process taking place can be identified.
- The generic methodology is computationally expensive. To construct one subfigure to illustrate the effect of the diffusion coefficient and the maximum reaction rate, 160 CFD simulations were required. However, this number does not reflect the required number of experiments in a real-life case. In real-life, the diffusion coefficient and maximum reaction rate are fixed. Only the residence time and microreactor width can be varied, and in this way the total number of required CFD simulations can be drastically reduced when specific substrates and enzymes have been identified for a reaction system.
- A simple kinetic model was selected. More research needs to be done for more complex kinetic models, but also for more complex reactor configurations. However, the developed methodology is independent of the kinetic model under study, and is therefore widely applicable.

5.7 Opportunities

This novel generic model-based methodology and the corresponding analysis is of much value for quantifying mass transfer limitations in different microreactor setups, as demonstrated here by the microreactor containing the immobilised enzyme at the wall and by a Y-shaped microreactor with one inlet stream containing enzyme and the other containing substrate. This will be also of much interest for microreactor configurations aiming at process designs which can be competitive with batch reactor configurations with complete conversion at high substrate concentrations, e.g. by retaining the enzyme in the microreactor by an ultrafiltration membrane (O'Sullivan et al., 2012) or for reaching high substrate concentrations in the multi-input reactor (MIR) (Lawrence et al., 2013). In addition to designing microreactor configurations which can achieve incremental improvements over batch reactor designs, the generic model-based methodology will be a useful tool for quantifying mass transfer limitations in novel process designs where the unique advantages of microreactors over batch reactors can be utilised (Wohlgemuth et al., 2015).

CHAPTER 6

MODEL CALIBRATION UNDER MASS TRANSFER LIMITED CONDITIONS

Abstract

The standard approach to estimate kinetic parameters consists of the use of a simple and idealised model where spatial heterogeneities are not considered, or only incorporated to a limited extent. Omitting or largely simplifying the description of spatial heterogenity in a reactor is a very common model assumption. This assumption makes that the data need to be collected at experimental conditions where the assumption is valid. However, in reality it may not be possible to meet this requirement and a more advanced calibration approach is needed. Instead of ignoring spatial heterogeneities and mass transfer limitations, these phenomena are taken into account by using a coupled CFD-kinetic model which would potentially allow to estimate the intrinsic kinetic parameters in a more reliable and accurate way. In this chapter, the immobilised enzyme microreactor and the kinetic model, which were introduced in previous chapter, are used to investigate whether the kinetic parameter is both theoretically and practically identifiable under mass transfer limited conditions. Moreover, the effect of the different degrees of freedom on the practical identifiability are investigated. This analysis yields that the experimental design remains an important factor under mass transfer limited conditions. Therefore, the results of the practical identifiability study are compared with the calculation of the Fisher Information Matrix (**FIM**) based on

the local sensitivity of the coupled CFD-kinetic model. The application of the **FIM** yielded comparable results when mass transfer limitations are not severe, but the *parameter-effects* curvature (Chapter 4) becomes important at increased mass transfer limitations. However, the application of **FIM** to perform OED under mass transfer limited conditions looks promising for future applications.

6.1 Introduction

In the previous chapter, a generic methodology was introduced which allows to differentiate between mass transfer and kinetically limited conditions by comparing CFD simulations with an ideal plug flow model. However, it was stated that the intrinsic values of the kinetic model parameters can only be estimated when no mass transfer limitations occur. Recently, Verbruggen et al. (2016) used a CFD model coupled with a Langmuir model, describing the adsorption of acetaldehyde on photocatalytic fiber filter material, to perform a parameter estimation of the Langmuir model parameters and stated that they were able to retrieve the intrinsic adsorption parameter values. The use of a CFD model allowed to take into account the spatial heterogeneities of the reactor configuration. The question now arises whether it is always possible to estimate the intrinsic parameter values when using CFD (even under mass transfer limited conditions). This question can be regarded as an identifiability question and consists of a theoretical and a practical part (Chapter 3).

In this chapter, an ideal plug flow model is used to perform a theoretical identifiability study based on mass transfer limited data. Subsequently, a CFD model is used to identify the intrinsic parameter value under different conditions using both uncorrupted and noise-corrupted data. Finally, the likelihood method used to determine the practical identifiability of the CFD model is compared with the **FIM**. The latter is a more simple measure which is generally used for performing OED, but is only exact for linear models. Therefore, it needs prior investigation whether the **FIM** is applicable for CFD models.

6.2 Case study

6.2.1 Reactor description

The immobilised enzyme microreactor introduced in chapter 5 will be used to illustrate the importance of mass transfer limitations when performing a parameter estimation. The nominal values of the CFD related parameters (D and W), and the residence time τ are given in Table 6.1. The turnover number k_{cat} is varied between 10^{-4} and $10^{4}\,\mathrm{L/(g\,s)}$. To generate the *in silico* data, 40 samples (N) are taken equidistantly over the reactor length (so one sample every 15 s). This kind of sampling can be achieved by using optical sensors which are nonintrusive (Ehgartner et al., 2016).

Table 6.1: Nominal values for the mass transfer limited identifiability study.

DOF	Nominal value
D	$10^{-10}\,\mathrm{m^2/s}$
W	$200\,\mathrm{\mu m}$
τ	$10\,\mathrm{min}$
N	40
$[E]$	$0.0454\,\mathrm{g/L}$
$[S]_{\mathrm{in}}$	$50\,\mathrm{mM}$

6.2.2 Measurement uncertainty

In chapter 5, the relative uncertainty was used as measurement error. This can pose problems at very low product concentrations, since the expected measurement uncertainty becomes very low at these concentrations. However, this behaviour is not realistic since the measurement devices will always have a limit of detection. Brik Ternbach et al. (2005) proposed a measurement uncertainty which approximates a constant error at concentrations below a certain limit and a relative error at higher concentrations (Equation 6.1).

$$\sigma\left([P]\right) = [P]\cdot\sigma_{\mathrm{rel}}\left(1+\frac{1}{\left(\frac{[P]}{lb_{[P]}}\right)^{2}+\frac{[P]}{lb_{[P]}}}\right) \tag{6.1}$$

where $[P]$ represents the product concentration [mM], σ_{rel} the relative standard deviation [−], and $lb_{[P]}$ the lower bound of the measurement error [mM]. All $[P]$ smaller than $lb_{[P]}$ will yield the same absolute measurement error, which allows to incorporate the limit of detection of that specific equipment and setup. In this chapter, the nominal values of σ_{rel} and $lb_{[P]}$ are equal to 0.05 and 4 mM respectively. The value of σ_{rel} is reasonable for microreactors with integrated optical sensors, taking into account the variation of the manufacturing process (Ehgartner et al., 2016). The standard deviation of the measurement error in function of the product concentration is given in Figure 6.1, and is represented both in an absolute (top) and a relative way (bottom). To allow comparison, the standard deviation for a typical relative error distribution is represented by the dashed line ($lb_{[P]} = 0\,\mathrm{mM}$).

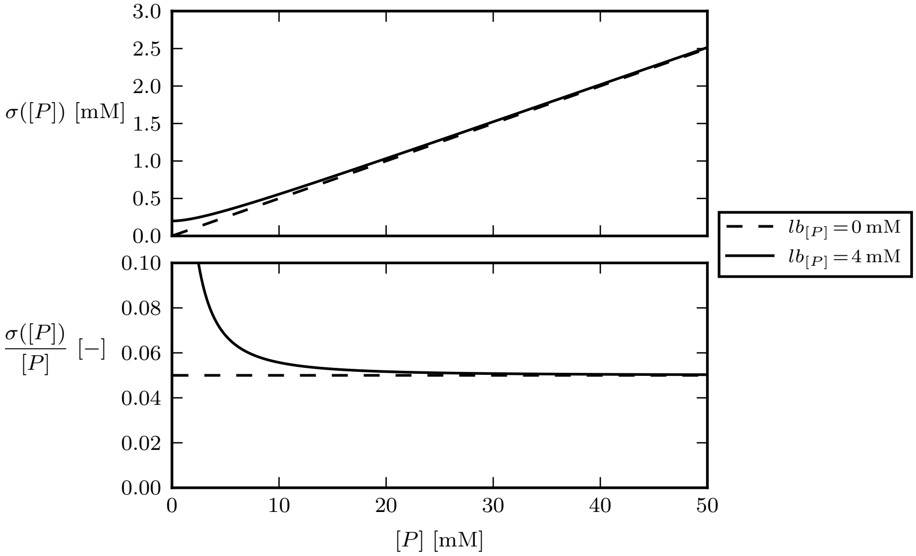

Figure 6.1: The standard deviation of the measurement error in function of the product concentration using Equation 6.1 represented in both an absolute (top) and relative way (bottom).

6.3 Parameter estimation using a plug flow model

First, a developed *in silico* approach to determine the local theoretical identifiability of k_{cat} is introduced. Next, this approach is applied to the immobilised enzyme microreactor to illustrate the importance of mass transfer limitations when performing a parameter estimation using plug flow models.

6.3.1 Methodology

To assess the local theoretical identifiability of a plug flow model using mass transfer limited data, a methodology is developed. This approach consist of multiple steps and is illustrated in Figure 6.2:

1. **Set degrees of freedom**: The values for the different degrees of freedom need to be set prior to starting the exercise. However, for this exercise the DOFs are fixed at their nominal values (Table 6.1) and only $k_{\mathrm{cat,real}}$ is chosen from the range between 10^{-4} and $10^{4}\,\mathrm{L/(g\,s)}$.

2. **Run CFD simulation**: If all the degrees of freedom have been defined, the CFD simulation can be performed for this specific set of DOFs.

3. **Sample data points**: A certain number of data points (N) can be sampled from the steady-state velocity and concentration profiles and be used as *in silico* data (y) in the optimisation. The results of the local theoretical identifiability study should be independent of the number of samples (N) taken. Therefore, N should be varied in order to assure this conditions is met.

4. **Define plug flow model**: Based on the kinetic model, the plug flow model can easily be defined using Equation 5.10.

5. **Minimise objective function**: Using the sampled data from the CFD model (y) and the plug flow model ($\hat{y}_{\mathrm{PF}}$), the objective function (Equation 6.2) can be calculated and be minimised to obtain the estimated turnover number $k_{\mathrm{cat,est}}$.

$$J_{\mathrm{PF}}(k_{\mathrm{cat}}) = \sum_{i=0}^{N} \frac{\left(y_i - \hat{y}_{\mathrm{PF}}(k_{\mathrm{cat}}, x_i)\right)^2}{\sigma_i^2} \tag{6.2}$$

   where x_i represents the ith sample in the x-direction.

6. **Determine theoretical identifiability**: When the estimated turnover number value differs from the "real" k_{cat} value defined in Step 1, k_{cat} is theoretically unidentifiable since the samples are not noise-corrupted.

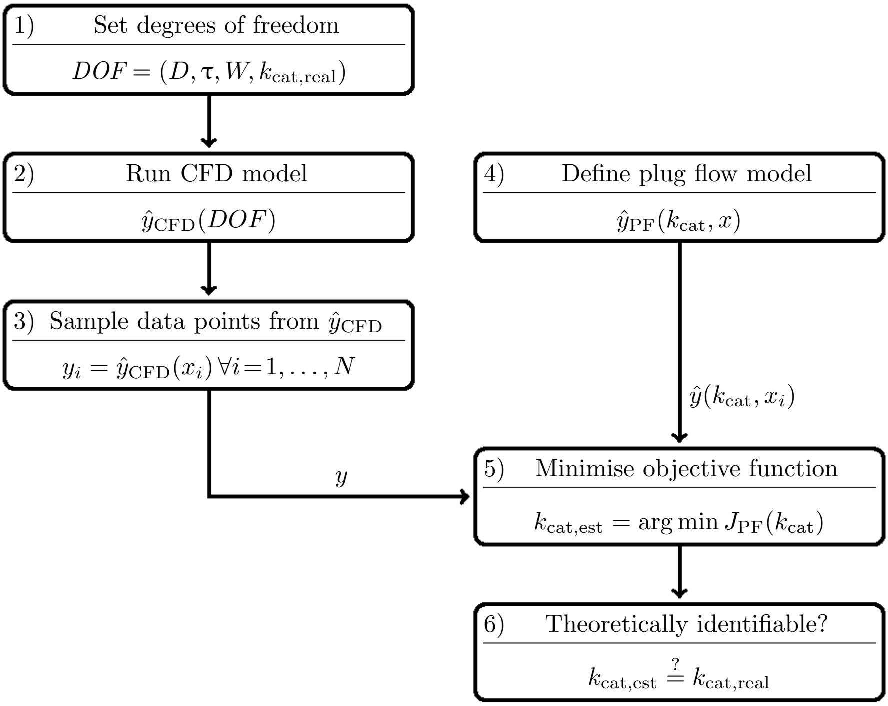

Figure 6.2: Methodology to estimate parameter values and evaluate their identifiability from *in silico* CFD-generated data, using plug flow models.

6.3.2 Local theoretical identifiability

Using the methodology proposed in Figure 6.2, it can be determined whether it is possible to estimate the intrinsic k_{cat} values properly, even under mass transfer limited conditions. In chapter 5 it was already shown that the plug flow model deviates from reality under mass transfer limited conditions, and thus the estimated parameter value will no longer reflect the intrinsic parameter values. The methodology was performed for the nominal case (Table 6.1) and for all k_{cat} values between 10^{-4} and $10^{4}\,\text{L/(g\,s)}$. The corresponding results are shown in Figure 6.3. The intrinsic k_{cat} value ($k_{\text{cat,real}}$) and the estimated k_{cat} value ($k_{\text{cat,est}}$) are given on the x-axis and y-axis respectively. The dashed line represents the ideal case in which $k_{\text{cat,est}}$ equals $k_{\text{cat,real}}$. In the most ideal case, the grey line collapses onto the dashed line. Figure 6.3 clearly shows that for low k_{cat} values ($<10^{-1}\,\text{L/(g\,s)}$), the k_{cat} values can be estimated correctly. However, at higher k_{cat} values deviations between $k_{\text{cat,real}}$ and $k_{\text{cat,est}}$ values occur, indicating that the parameter becomes unidentifiable. Since the data used are noise-free, it can be concluded that for k_{cat} values above $10^{-1}\,\mathrm{L/(g\,s)}$, the parameter is locally theoretically (and thus also practically) unidentifiable. This conclusion is only valid for the current DOF values, and it is possible that the results will be different for other DOF values. Moreover, increasing the number of samples (N) did not improve the local theoretical identifiability, indicating that all information which was available in the model output was captured.

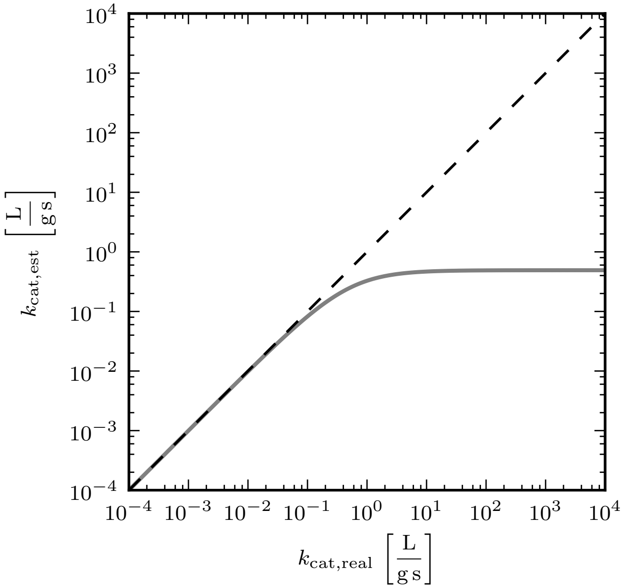

Figure 6.3: The $k_{\mathrm{cat,est}}$ values are shown in function of $k_{\mathrm{cat,real}}$ for the nominal case (grey line). At $k_{\mathrm{cat,real}}$ values above $10^{-1}\,\mathrm{L/(g\,s)}$, the grey line start to deviate from the theoretical identifiability line (dashed).

To illustrate that k_{cat} values above $10^{-1}\,\mathrm{L/(g\,s)}$ are unidentifiable, the output of the plug flow model (y_{PF}) is compared with the data sampled from the CFD simulations ($\hat{y}$) for different k_{cat} values in Figure 6.4. When $k_{\mathrm{cat,real}}$ is small ($< 10^{-1}\,\mathrm{L/(g\,s)}$), the plug flow model predictions using $k_{\mathrm{cat,real}}$ ($\hat{y}_{\mathrm{PF}}(k_{\mathrm{cat,real}})$) and $k_{\mathrm{cat,est}}$ ($\hat{y}_{\mathrm{PF}}(k_{\mathrm{cat,est}})$) both predict the data well. However, at higher values of $k_{\mathrm{cat,real}}$, the deviation between $\hat{y}_{\mathrm{PF}}(k_{\mathrm{cat,real}})$ and the *in silico* generated data y increases. This increase in deviation can be related with mass transfer limitations, as will be discussed in more detailed in the next section.

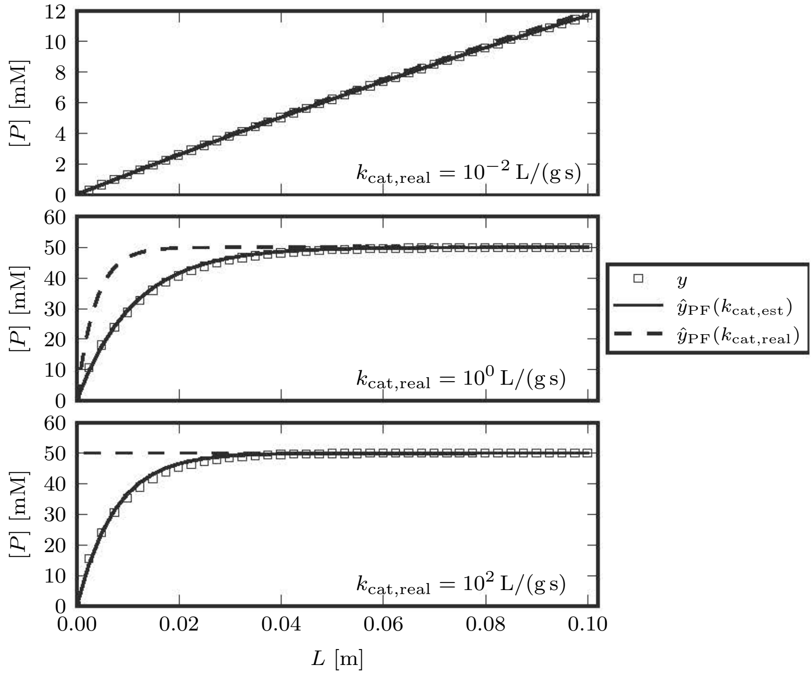

Figure 6.4: The model predictions of the plug flow model for both the intrinsic parameter value ($k_{\mathrm{cat,real}}$) and the estimated parameter value ($k_{\mathrm{cat,est}}$) are compared with the *in silico* sampled data (y). At high values of k_{cat}, mass transfer limitations obscure the intrinsic parameter values.

6.3.3 Effect of mass transfer limitations

As illustrated in the previous section, k_{cat} becomes locally unidentifiable at relatively high turnover. Since this can be related to mass transfer limitations, the immobilised enzyme case was also evaluated at a low and high diffusion coefficient of 10^{-11} and $10^{-9}\,\mathrm{m^2/s}$ respectively. From Figure 6.5 it can be seen that the high diffusion case (dotted line) is following the (dashed black) theoretical identifiability line much longer compared to that of the nominal diffusion value ($10^{-10}\,\mathrm{m^2/s}$). This leads to the conclusion that the k_{cat} parameter is locally theoretically identifiable up to $10^{0}\,\mathrm{L/(g\,s)}$ at decreased mass transfer limitations. At increased mass transfer limitations (dashed grey line), the theoretically identifiable range decreases.

Since the identifiability problem is dependent on the level of mass transfer limitation, it is expected that the dimensionless numbers introduced in chapter 5 can be related to the theoretical identifiability. For the immobilised enzyme case, it

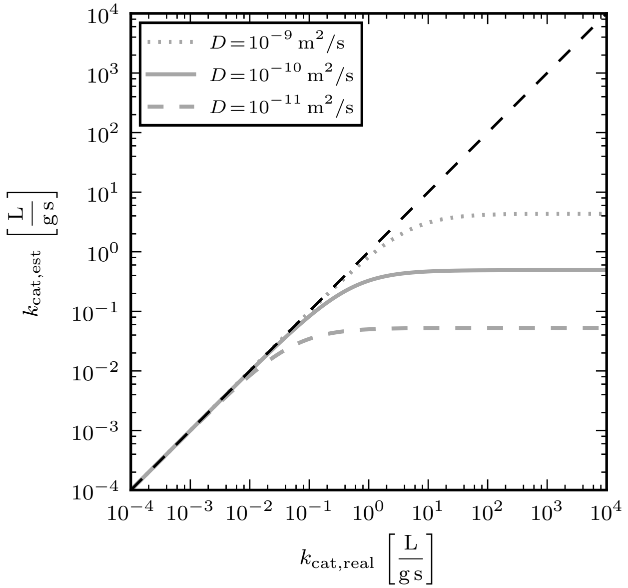

Figure 6.5: The estimated parameter values ($k_{\mathrm{cat,est}}$) are shown in function of the intrinsic parameter values ($k_{\mathrm{cat,real}}$) for three different diffusion coefficient values (10^{-9}, 10^{-10} and 10^{-11} m^2/s). At higher diffusion coefficient values, a larger range of $k_{\mathrm{cat,real}}$ values is theoretically identifiable.

was already shown that the second Damköhler number $\mathrm{Da}_{\mathrm{II}}$ (Equation 5.17) is a proper measure to determine whether a plug flow model is suitable. In this sense, it is expected that at $\mathrm{Da}_{\mathrm{II}}$ values well below 1, the plug flow model is appropriate and thus theoretically identifiable. By increasing the diffusion coefficient, it will be possible to also uniquely identify higher k_{cat} values. In Figure 6.6, the relative deviation between the estimated parameter value ($k_{\mathrm{cat,est}}$) and the intrinsic parameter value ($k_{\mathrm{cat,real}}$) is given as a function of $k_{\mathrm{cat,real}}$ for three different diffusion coefficients: 10^{-9}, 10^{-10} and 10^{-11} m^2/s. All three curves have the same sigmoidal shape, which indicates that in all three cases the diffusion is the only and most important effect playing a role. If the mass transfer limitations would be dominated by an interplay of different phenomena, the importance of the diffusion limitation would decrease at higher diffusion coefficient values and therefore changes in the location and shape of the curvature would be expected. These observations are in accordance with the results of chapter 5, and again confirm that the second Damköhler number is suitable to assess mass transfer limitations in an immobilised enzyme reactor. As indicated in Figure 6.6, the second Damköhler number is approximately 0.23 for a relative deviation of 10 % between $k_{\mathrm{cat,est}}$ and $k_{\mathrm{cat,real}}$. The exact $\mathrm{Da}_{\mathrm{II}}$ value showed limited variation between the different scenarios, and is related to the numerical errors of both the CFD simulations and the local optimisation function used.

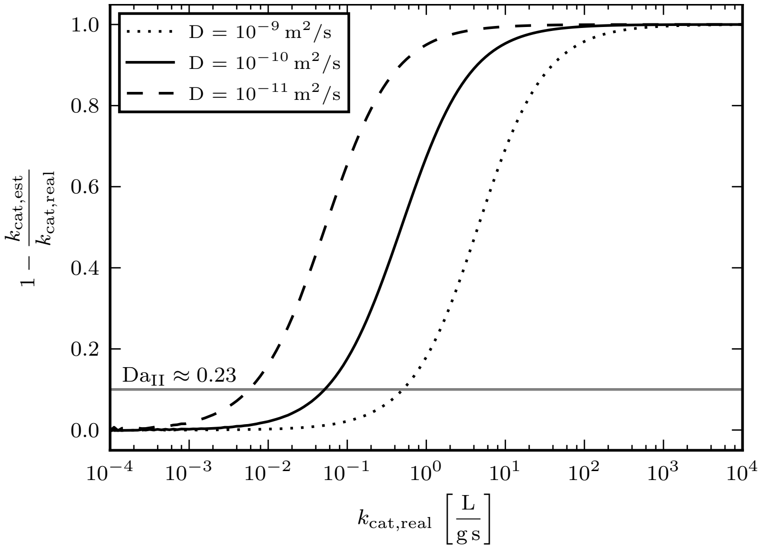

Figure 6.6: For the different diffusion coefficients the relative difference between the intrinsic parameter $k_{\mathrm{cat,real}}$ and the estimated parameter $k_{\mathrm{cat,est}}$ increases when $k_{\mathrm{cat,real}}$ increases. The horizontal line is the value of the second Damköhler number when the relative difference is 10 %, and is indifferent from the actual diffusion coefficient.

6.3.4 Conclusions

The theoretical identifiability study performed here, confirmed that the intrinsic parameter values of k_{cat} can only be estimated properly using an idealised plug flow model when the mass transfer limitations are low ($\mathrm{Da_{II}} < 0.2$). To retrieve the intrinsic parameter values, the most straightforward solution (from a theoretical point of view) is to reduce the mass transfer limitations to an acceptable level. However, in practice this is not always possible and other solutions will have to be sought.

6.4 Parameter estimation using a CFD model

The use of ideal plug flow models for the parameter estimation of kinetic parameters under mass transfer limited conditions was not successful. At $\mathrm{Da_{II}}$ values of 0.23, the deviation between the intrinsic and the estimated parameter was already 10 %. As a consequence, the data need to be free from any mass transfer limitations to ensure the estimation of the intrinsic parameter values using a plug flow model. Verbruggen et al. (2016) stated that the use of a coupled CFD-kinetic model allowed to retrieve the intrinsic adsorption parameter values by incorporating the spatial heterogeneities of the reactor. However, two important questions now arise:

1. Is it possible to estimate the intrinsic kinetic parameter values with CFD under mass transfer limited conditions?
2. How accurate and reliable are the parameter values which are estimated using CFD?

Both questions can be interpreted as an identifiability study. The first question is related to theoretical identifiability ("Is it possible to retrieve the value of $k_{\mathrm{cat,real}}$?"), while the second question relates to the practical identifiability ("If it can be estimated properly, how reliable is this estimate and does it depend on the experimental conditions?").

6.4.1 Methodology

To answer these questions, a methodology is developed which allows to assess the theoretical and practical identifiability (Figure 6.7). A parameter estimate needs to be precise, i.e. be sufficiently close to the intrinsic parameter value, and accurate, i.e. the 95 % confidence interval needs to be sufficiently small, in order to be practically identifiable.

1. **Set degrees of freedom**: The values for the different degrees of freedom need to be set prior to starting the analysis.
2. **Run CFD simulation**: If all the degrees of freedom have been defined, the CFD simulations can be performed for all k_{cat} values within the range of interest.
3. **Sample data points**: A certain number of data points (N) is sampled from the steady-state velocity and concentration profiles and is used as *in silico* data.
4. **Select $k_{\mathrm{cat,real}}$**: The intrinsic k_{cat} value is selected.
5. **Add noise to *in silico* data**: When determining the theoretical identifiability of a model, no noise is added since for a theoretical identifiability

analysis the model has access to unlimited and uncorrupted data ($\varepsilon = 0$). However, for a practical identifiability analysis the number of data points is limited and these data are noise-corrupted. In this section, the measurement uncertainty introduced by Brik Ternbach et al. (2005) is used (Equation 6.1).

6. **Calculate objective function**: After generating the data (y), these *in silico* measurements can be compared with the model predictions $\hat{y}(k_{\text{cat}}, x_i)$. As clarified in Figure 6.7, the simulations performed for all k_{cat} are compared with the "measurements" from the intrinsic kinetic value ($k_{\text{cat,real}}$). This approach yields the objective function in Equation 6.3 from which a minimum (i.e. $k_{\text{cat,est}}$) can be derived.

$$J_{\text{CFD}}(k_{\text{cat}}) = \sum_{i=0}^{N} \frac{\left(y_i - \hat{y}(k_{\text{cat}}, x_i)\right)^2}{\sigma_i^2} \tag{6.3}$$

   where σ_i^2 represents the variance of measurement i.

7. **Calculate** 95 % **confidence interval**: Using the objective function $J_{\text{CFD}}(k_{\text{cat}})$, the 95% CI can be calculated using the likelihood CI proposed by Beale (1960) and Seber and Wild (1989) (Equation 4.7). For a theoretical identifiability analysis, the only aim is to retrieve the intrinsic parameter value and the experimentalist has access to perfect data. Therefore, the calculation of the 95 % is only informative for the practical identifiability.

Step 5, 6, and 7 are repeated N times in order to converge to stable estimation of the 95 % confidence interval. Due to the noise introduced in Step 5, small skews are introduced in the estimation of the confidence intervals. In order to obtain confidence intervals which are not skewed, the three last steps are repeated 5000 times in the following sections and figures.

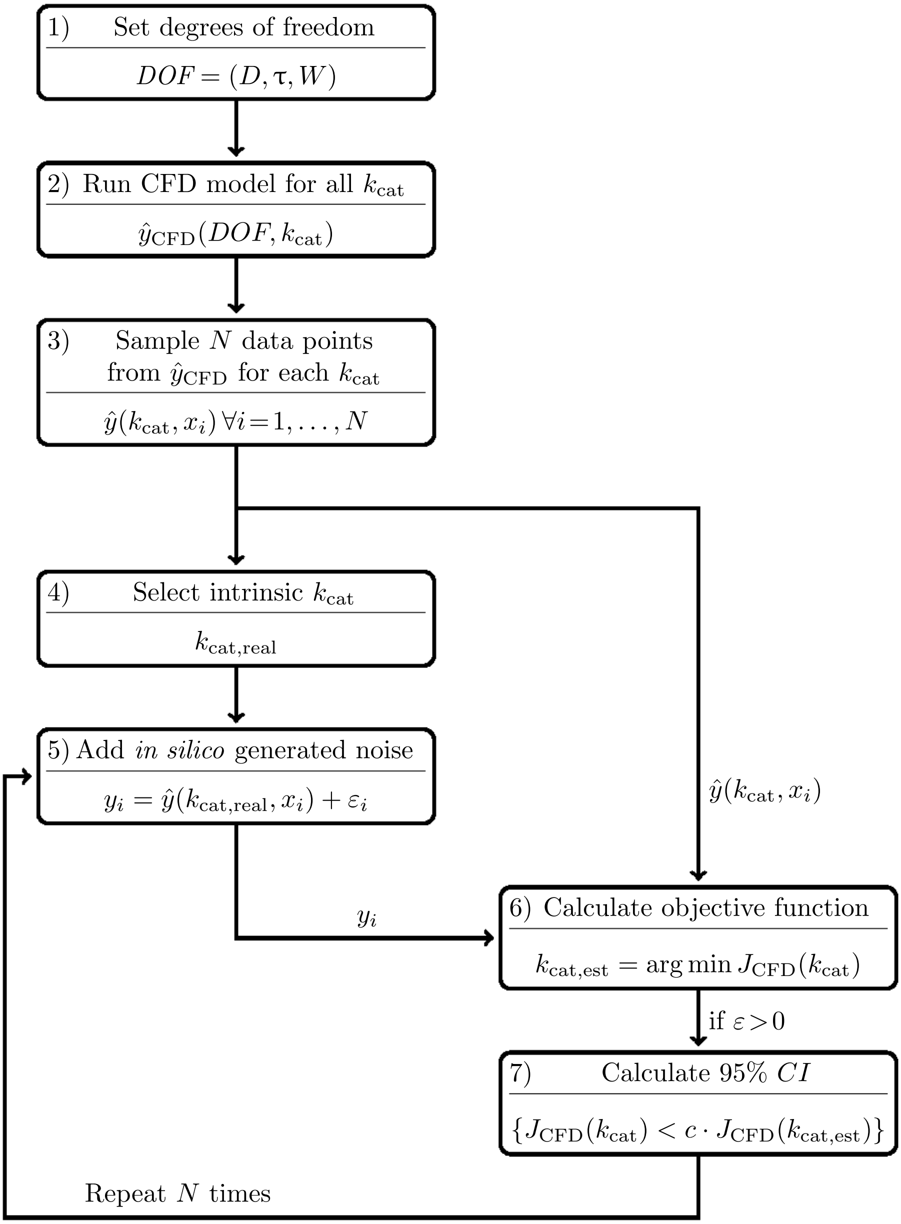

Figure 6.7: The developed methodology to determine both the theoretical (without *in silico* noise) and the practical (with *in silico* noise) parameter identifiability when performing a parameter estimation using a CFD model.

6.4.2 Background on identifiability

Using the methodology of Figure 6.7, both the local theoretical and practical identifiability can be assessed. In this section, the nominal values of the different DOFs are used.

Local theoretical identifiability

Since the theoretical identifiability is assessed, the measurement error is set to zero ($\varepsilon = 0$). The relationship between $k_{\text{cat,est}}$ and $k_{\text{cat,real}}$ is depicted in Figure 6.8. Since the relationship between $k_{\text{cat,est}}$ and $k_{\text{cat,real}}$ coincides with the theoretical identifiability line (dashed), it can be concluded that the CFD model is (at least locally) theoretically identifiable.

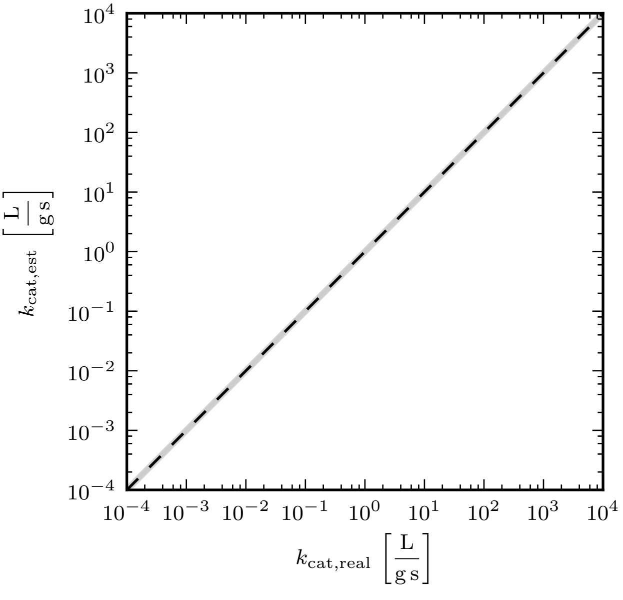

Figure 6.8: The $k_{\text{cat,est}}$ is always equal to the $k_{\text{cat,real}}$ value (grey line), and thus coincides with the theoretical identifiability line (dashed), confirming that k_{cat} is (at least locally) theoretically identifiable.

Local practical identifiability

Since k_{cat} is theoretically identifiable when using the CFD model, a practical identifiability study is performed to determine the parameter reliability under different conditions. For the nominal values described in section 6.2 and using the measurement uncertainty described in section 6.2.2, the 95 % CIs of $k_{\mathrm{cat,est}}$ as a function of $k_{\mathrm{cat,real}}$ are given as a grey colormap in Figure 6.9. This figure visualises the uncertainty as a function of the $k_{\mathrm{cat,real}}$ values, simplifying the interpretation. For example, a $k_{\mathrm{cat,real}}$ value of $10^{-1}\,\mathrm{L/(g\,s)}$ (x-axis) yields a rather narrow 95 % $\mathrm{CI}_{k_{\mathrm{cat,est}}}$ (y-axis), indicating that this $k_{\mathrm{cat,real}}$ value is practically identifiable at current conditions.

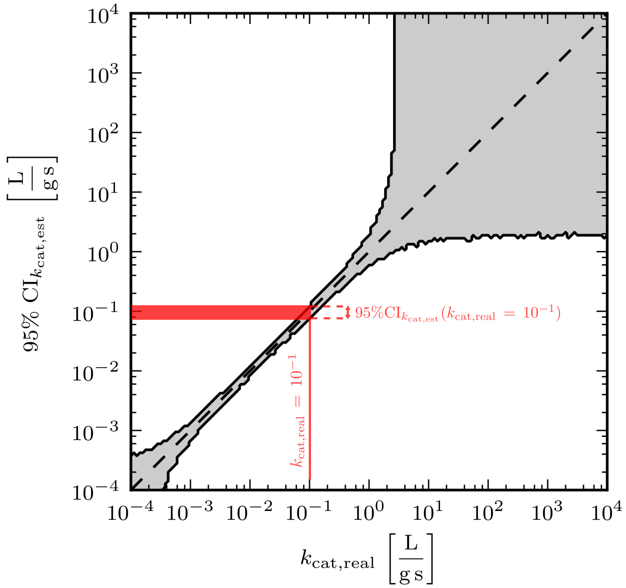

Figure 6.9: The 95 % confidence region for the nominal values (section 6.2) is given in grey. The black line enclosing this region will be used in the next sections as the nominal case.

The first important characteristic is that the theoretical identifiability line is located within the 95 % CI. This already indicates that adding randomly generated noise (using Equation 6.1) to the *in silico* generated data does not cause major skews for 95 % CI. A second characteristic is that roughly three different regions can be discriminated:

- **Lower practical unidentifiable parameter region**
  At low $k_{\mathrm{cat,real}}$ values ($< 10^{-3}\,\mathrm{L/(g\,s)}$), the 95 % CI is large compared to the intrinsic parameter value. This can be related to the measurement error introduced in section 6.2.2, because at product concentrations below 4 mM the relative error will be significantly higher than 0.05. Using the plug flow equation (Equation 5.10), the product concentration as a function of the different DOFs and k_{cat} can be derived as (Equation 6.4):

$$[P] = [S]_0 \left(1 - \exp\left(-k_{\mathrm{cat}}\,[E]\,t\right)\right) \tag{6.4}$$

For a $k_{\mathrm{cat,real}}$ of 10^{-3} L/(g s), the maximum product concentration $[P]$ at the outlet of the microreactor is only 1.34 mM, and thus well below the lower bound of the measurement error ($lb_{[P]}$). At these product concentrations, the actual relative standard deviation is 21.7 % and no accurate estimates of k_{cat} can be found. To decrease the uncertainty of the parameter estimates, two major options are possible. First, the measurement error can be reduced, but from a practical point of view this requires expensive structural changes in the equipment and measurement methods. Second, the product concentration needs to be increased, which can be achieved by increasing the residence time τ or by increasing the enzyme and/or substrate concentration.

- **Practical identifiable parameter region**
  At $k_{\mathrm{cat,real}}$ values between 10^{-3} and 10^{0} L/(g s), the 95 % CI is small, indicating that the parameter values can be estimated with low uncertainty. Interesting is that the parameter estimation uncertainty is even low when mass transfer limitations are occurring (between 10^{-1} and 10^{0} L/(g s)). As was already indicated in section 6.3.2, the plug flow model could not be used to estimate the k_{cat} value in this mass transfer limited region. In this region the second Damköhler number ($\mathrm{Da_{II}}$) is between 0.45 and 4.54, which is located in the transition region between kinetically limited and mass transfer limited (chapter 5). This observation already confirms that using a CFD model allows to estimate parameter values under mass transfer limitated conditions. However, it seems that these mass transfer limitations should not be too severe in order not to obscure the underlying parameter values.

- **Upper practical unidentifiable parameter region**
  At $k_{\mathrm{cat,real}}$ values above 10^{0} L/(g s), the $\mathrm{Da_{II}}$ is well above 4.54 and thus mass transfer limitations will be important. In contrast to the lower practical unidentifiable parameter region, the measurement error is not the major reason for the unidentifibility here. The measured product concentrations in this region are all well above $lb_{[P]}$, and thus the measurements will only experience a relative standard deviation around 5 % (Figure 6.1). However, from Figure 6.9 it can be seen that this region has a quasi-square shape. This indicates that under the current conditions and measurement error the objective function in this region is flat, which makes k_{cat} practically unidentifiable. In other words: no differentiation can be made between a $k_{\mathrm{cat,real}}$ value of 5×10^{0} and 10^{4} L/(g s). This is due to the fact that for all $k_{\mathrm{cat,real}}$ values above 2×10^{0} L/(g s), most of the substrate has been converted to

the product. Therefore, it becomes impossible to differentiate between the different $k_{\mathrm{cat,real}}$ values, i.e. practical unidentifiability.

It can thus be concluded that using the proposed methodology (Figure 6.7), allows to discriminate three different regions. In the following sections, the effect of the different DOFs on the practical identifiability of k_{cat} in the CFD model is investigated. To allow comparison with the reference case (Figure 6.9), the confidence region of this case will be shown as a black line.

6.4.3 Effect of mass transfer limitations

To evaluate the effect of the mass transfer limitations on the practical identifiability, the productivity of the immobilised enzyme microreactor was evaluated at different diffusion coefficient values (i.e. $10^{-11}\,\mathrm{m^2/s}$ and $10^{-9}\,\mathrm{m^2/s}$). Another approach to alter the mass transfer limitations, was by adapting the reactor dimensions. As shown in Chapter 5, an increase of the microreactor width of the immobilised enzyme microreactor yields the same effect as decreasing the diffusion coefficient value. The effect of these two DOFs on the mass transfer limitations is described by the second Damköhler number (Equation 5.17). Since both DOFs have a similar impact, it was decided only to change the diffusion coefficient.

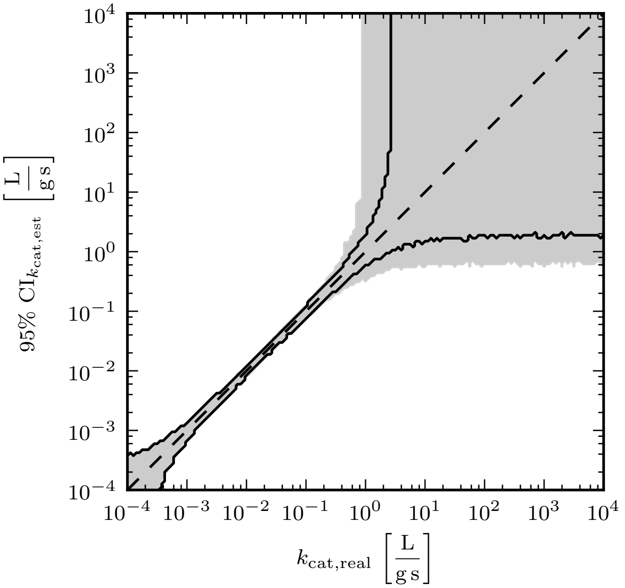

Figure 6.10: The 95 % confidence region for the low diffusion case ($D = 10^{-11}\,\mathrm{m^2/s}$) is given in grey. The nominal case is represented as a black line ($D = 10^{-10}\,\mathrm{m^2/s}$).

In Figure 6.10, all DOFs have the same values as the nominal case but only the diffusion coefficient D has been decreased to $10^{-11}\,\mathrm{m^2/s}$. The 95 % $\mathrm{CI}_{k_{\mathrm{cat,est}}}$ for the nominal case is represented by the black line. The grey region represents the 95 % $\mathrm{CI}_{k_{\mathrm{cat,est}}}$ for the current case, i.e. reduction of the diffusion coefficient to $10^{-11}\,\mathrm{m^2/s}$. From this figure, it is clear that the lower practical unidentifiable parameter region did not change. This is expected, since the major factor causing the practical unidentifiability is the measurement error and not the mass transfer limitations. The mass transfer is much higher compared to the kinetic reaction rate, thus decreasing the diffusion coefficient value has no effect. The range of the practical identifiable parameter region is decreased compared to the nominal case (black line). $k_{\mathrm{cat,real}}$ values around $10^0\,\mathrm{L/(g\,s)}$, which were practically identifiable in the nominal case, have now become unidentifiable at increased mass transfer limitation. As a consequence, the size of the upper practical unidentifiable parameter region has increased.

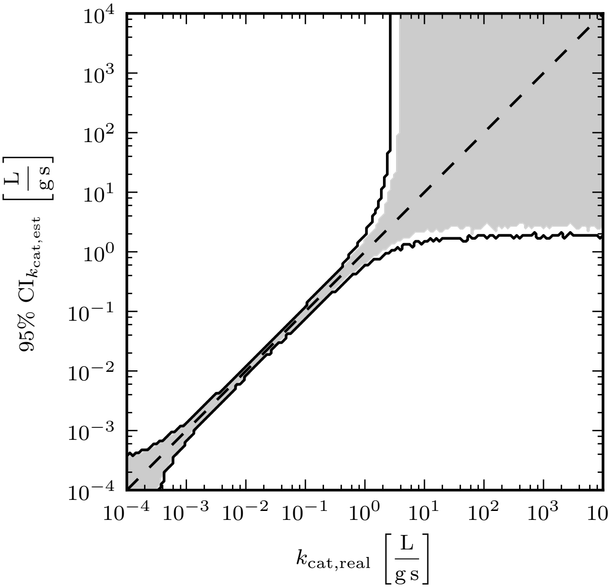

Figure 6.11: The 95 % confidence region for the high diffusion case ($D = 10^{-9}\,\mathrm{m^2/s}$) is given in grey. The nominal case is represented as a black line ($D = 10^{-10}\,\mathrm{m^2/s}$).

For the case where the diffusion coefficient has been increased to $10^{-9}\,\mathrm{m^2/s}$ (Figure 6.11), the upper practical unidentifiable parameter region is only slightly reduced in size. This limited reduction indicates that mass transfer limitations have been reduced and that the $k_{\mathrm{cat,real}}$ values around $10^0\,\mathrm{L/(g\,s)}$ can be estimated in a more reliable way. However, it seems that increasing the diffusion coefficient value only has a small positive effect on the parameter reliability. This indicates that mass transfer limitations are not the main limiting factor causing identifiability problems at $k_{\mathrm{cat,real}}$ values around 10^0 L/(g s).

6.4.4 Effect of measurement error

The nominal value of the relative standard deviation (σ_{rel}) is equal to 0.05. This means that 95 % of the samples will have an absolute error equal or smaller than 0.10. This level of noise is already sufficient to render certain ranges of $k_{\mathrm{cat,real}}$ values practically unidentifiable. Since the data used here are generated *in silico*, the measurement error can be easily changed. However, in reality the measurement error is closely related with the equipment and/or methodology used and thus the measurement error is in most cases fixed. Ehgartner et al. (2016) reported that the variation of a single sensor layer had a standard deviation of only 0.5 % (without taking into account the variation of the manufacturing process). Therefore, it seems reasonable to evaluate the practical identifiability at a low σ_{rel} value of 0.01. As a worst case scenario, the practical identifiability is evaluated at a σ_{rel} value of 0.10.

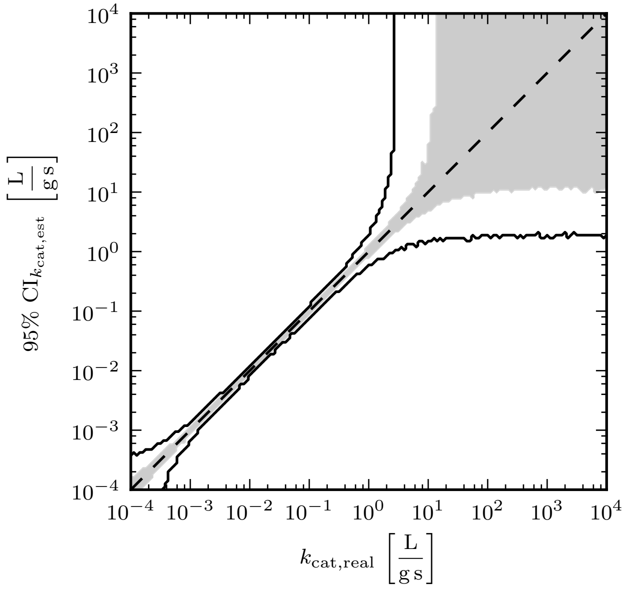

Figure 6.12: The 95 % confidence region for the low measurement error ($\sigma_{\mathrm{rel}} = 0.01$) is given in grey. The nominal case is represented as a black line ($\sigma_{\mathrm{rel}} = 0.05$).

The low measurement error case is depicted in Figure 6.12. The 95 % confidence region (grey) is significantly smaller compared to the nominal case, indicating that the parameter values will be estimated with a lower uncertainty. This (logical) result is in line with the available literature (Marsili-Libelli et al., 2014; Riedlinger et al., 2015; Docherty et al., 2011). The lower practically unidentifiable parameter region has quasi vanished, which confirms that the measurement error was an important factor for this region. The upper practically unidentifiable parameter region has decreased, allowing to estimate the $k_{\mathrm{cat,real}}$ values between 10^0 and 10^1 L/(g s) precisely and accurately.

By increasing the relative standard deviation of the measurement error to 0.10, it is expected that the practically identifiable region will decrease in size (Figure 6.13), which is indeed confirmed.

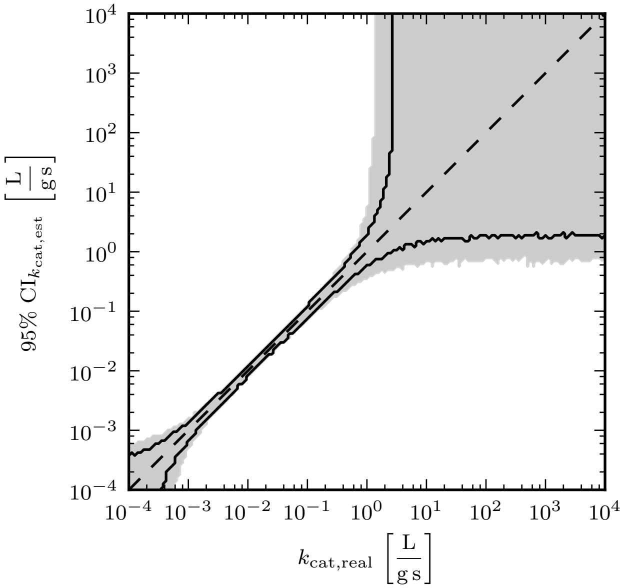

Figure 6.13: The 95 % confidence region for the high measurement error ($\sigma_{\mathrm{rel}} = 0.10$) is given in grey. The nominal case is represented as a black line ($\sigma_{\mathrm{rel}} = 0.05$).

6.4.5 Effect of the experimental design

Another factor which can be altered is the experimental design. For the microreactor setup two factors can be distinguished, i.e. the sampling frequency and the residence time. Both design variables will be altered separately to assess their individual effect.

Sampling frequency

When increasing the sampling frequency more information is gathered, and thus it is more plausible that the parameters will be estimated in a reliable way (assuming that autocorrelation is negligible). Therefore the sampling frequency was increased to 100 samples. This high number of samples can only be acquired using a nonintrusive measuring method comparable to that of Ehgartner et al. (2016) or by gathering the necessary samples during multiple experiments. The results for the increased sampling frequency are shown in Figure 6.14.

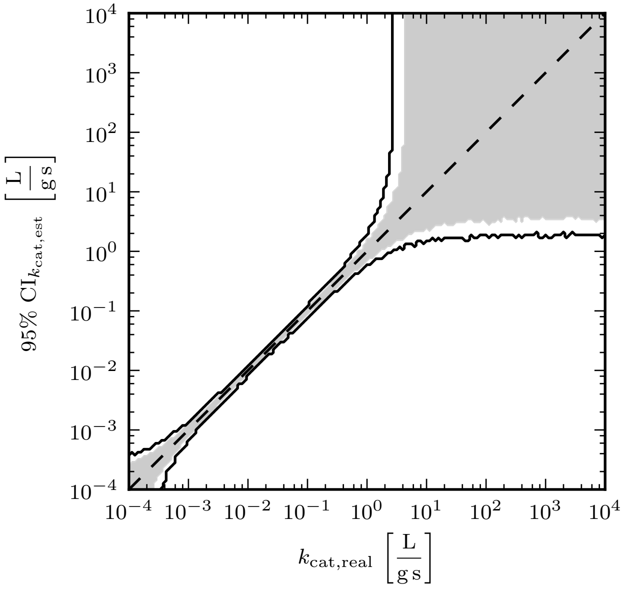

Figure 6.14: The 95 % confidence region for the intensively sampled case (100 samples) is given in grey. The nominal case is represented as a black line (40 samples).

In accordance with chapter 4, the parameter uncertainty decreases when more samples are gathered. More surprising is the fact that the upper practical unidentifiable parameter region is slightly smaller compared to that of the case with a high diffusion coefficient value (section 6.4.3). The latter indicates that in the transition zone from practical identifiable to unidentifiable (between 10^0 and 10^1 L/(g s)), the major issue is probably not related to the mass transfer limitations, but rather the lack of informative data. By increasing the sampling frequency from 40 to 100 samples, the starting point of the sampling is decreased from 2.5 mm (100 mm divided by 40 samples) to 1 mm. The improvement of the identifiability of the upper practical unidentifiable parameter region is most probably related to the shift of the first sampling point. In contrast, the identifiability improvement of the lower practical unidentifiable parameter range is only related to the increase of the number of samples. At low product concentrations (i.e. when $k_{\mathrm{cat,real}} < 10^{-3}\,\mathrm{L/(g\,s)}$), the information in the first sampling points is negligible and thus the shift of the first sampling point will not yield an increase in information. These statements are in accordance with Figure 6.15, where the normalised **FIM** values are shown as a function of the reactor location for both a low and a high $k_{\mathrm{cat,real}}$ value. Since the kinetic model in Equation 5.9 only involves one parameter (i.e. k_{cat}), the **FIM** is a Nx1x1 matrix and thus does not have to be reduced to a scalar metric, allowing its direct use as measure for uncertainty. The normalised **FIM** is plotted, since the actual **FIM** values of the two cases differ several magnitudes. The maximum **FIM** values of the low $k_{\mathrm{cat,real}}$ value ($10^{-3}\,\mathrm{L/(g\,s)}$) is about 3.7×10^{7}. This in constrast of the high $k_{\mathrm{cat,real}}$ value, where the maximum **FIM** values is only 35.5. This already indicates that the uncertainty of $k_{\mathrm{cat,est}}$ will be higher for high $k_{\mathrm{cat,real}}$ case.

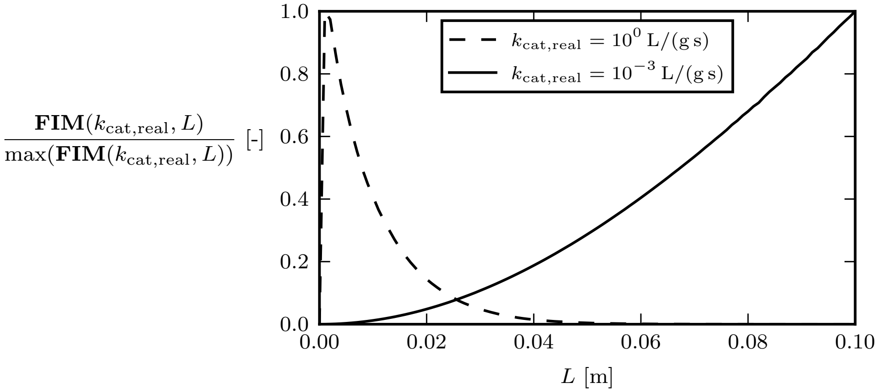

Figure 6.15: The evolution of the normalised **FIM** is given as a function of the reactor location and for two different $k_{\mathrm{cat,real}}$ values (10^{-3} and $10^{0}\,\mathrm{L/(g\,s)}$).

Residence time

As stated in previous section, the practical identifiability improvement of the $k_{\mathrm{cat,real}}$ values between 10^{0} and $10^{1}\,\mathrm{L/(g\,s)}$ was mainly due to the sampling earlier in the reactor. Therefore, the residence time of the reactor is decreased to 10 s and compared to the nominal residence time of 600 s. The sampling frequency is kept constant at its nominal value (40 samples). The result of the decrease in residence time is shown in Figure 6.16. The lower practical unidentifiable parameter region has drastically increased, and all k_{cat} values below $2 \times 10^{-2}\,\mathrm{L/(g\,s)}$ have become practically unidentifiable. By decreasing the residence time, the product concentration in the reactor drops to levels which are hard to measure for low k_{cat} values. However, the upper boundary of the practical identifiable parameter region increases from 2×10^0 to 10^1 L/(g s). A similar increase of the upper boundary was only obtained when the σ_{rel} (i.e. the relative standard deviation of the measurement error) was reduced from 0.05 to 0.01 (Figure 6.12). In this case, a decrease of the residence time from 600 to 10 s has the same negative effect (i.e. a decrease) on the parameter uncertainty as a fivefold decrease of the measurement uncertainty. This observation confirms that a proper experimental design (i.e. a suitable sampling strategy and residence time, cfr. chapter 4) is important to allow accurate parameter estimation. Moreover, it illustrates that parameter accuracy is highly dependent on the experimental design whatever the measurement accuracy of the used equipment.

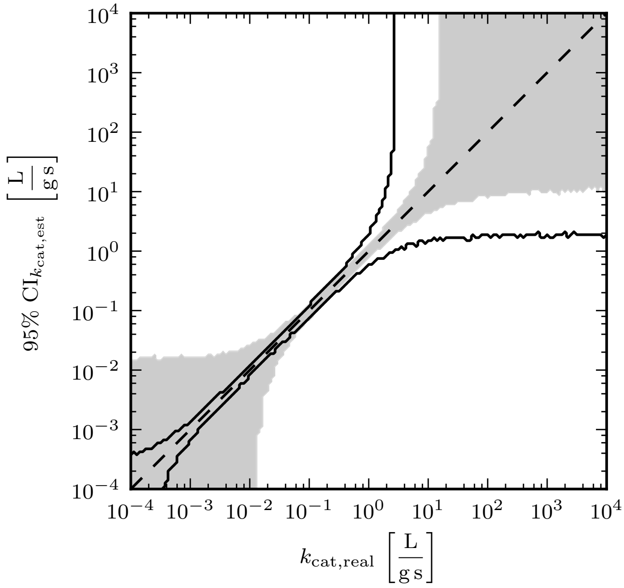

Figure 6.16: The 95 % confidence region for the low residence time ($\tau = 10$ s) is given in grey. The nominal case is represented as a black line ($\tau = 600$ s).

6.4.6 Effect of degrees of freedom at decreased residence time

The assessment of the effect of the individual degrees of freedom (i.e. the diffusion coefficient, the measurement error, the sampling frequency, and the residence time) on the practical identifiability, yielded that the upper practical unidentifiable parameter region could be reduced most effectively by decreasing the residence time or by decreasing the measurement error. However, the practical identifiability of the $k_{\mathrm{cat,real}}$ values in the range between 10^0 and $10^3\,\mathrm{L/(g\,s)}$ can probably be further improved by changing two or more degrees of freedom at a time. Since the residence time is the DOF which can be changed most easily in practice, τ will be fixed at 10 s, and the sampling frequency will be kept constant at 40 samples. The additional effect of the two other degrees of freedom (D and σ_{rel}) is investigated in the following sections.

Improved diffusion

In section 6.4.3, it was shown that increasing the diffusion coefficient value from 10^{-10} to $10^{-9}\,\mathrm{m^2/s}$ had only a minor impact on the practical identifiability, indicating that mass transfer was not the major limitation for the $k_{\mathrm{cat,real}}$ values between 10^0 and $10^1\,\mathrm{L/(g\,s)}$ at the nominal conditions. However by reducing the residence time, the $k_{\mathrm{cat,real}}$ values up to $10^{-1}\,\mathrm{L/(g\,s)}$ have become practically identifiable. At these conditions, this corresponds with a $\mathrm{Da_{II}}$ value of 45.4, which is already more than 100 times higher compared to that of the plug flow model (section 6.3.3). Since the $\mathrm{Da_{II}}$ value is very high, an increase of the diffusion coefficient value will probably improve the practical identifiability of the high-end k_{cat} values. In Figure 6.17, the effect of the high diffusion ($D = 10^{-9}\,\mathrm{m^2/s}$) at low residence times becomes clear. The upper practical unidentifiable parameter region further shrinks, allowing to accurately estimate k_{cat} values up to $4 \times 10^1\,\mathrm{L/(g\,s)}$.

Improved measurement error

Except for increasing the diffusion coefficient, the measurement error can also be decreased to allow a more accurate estimation of the parameter values. In this case the relative standard deviation σ_{rel} is decreased to 0.01 at a residence time of 10 s, which is depicted in Figure 6.18. As expected both the upper and the lower practical unidentifiable parameter regions shrink. However, for the upper region also the shape changes from square-like to a long stretched region (especially for $k_{\mathrm{cat,real}}$ values between 2×10^1 and $2 \times 10^2\,\mathrm{L/(g\,s)}$). In this stretched subregion the practical identifiability has improved, but the accuracy of the parameter estimates is still (too) low. This observation indicates that decreasing the measurement error has no longer an important impact on the practical identifiability for the parameter values above $4 \times 10^1\,\mathrm{L/(g\,s)}$. At this point, the mass transfer limitations are too severe and it becomes impossible to determine the real parameter value from the experimental data.

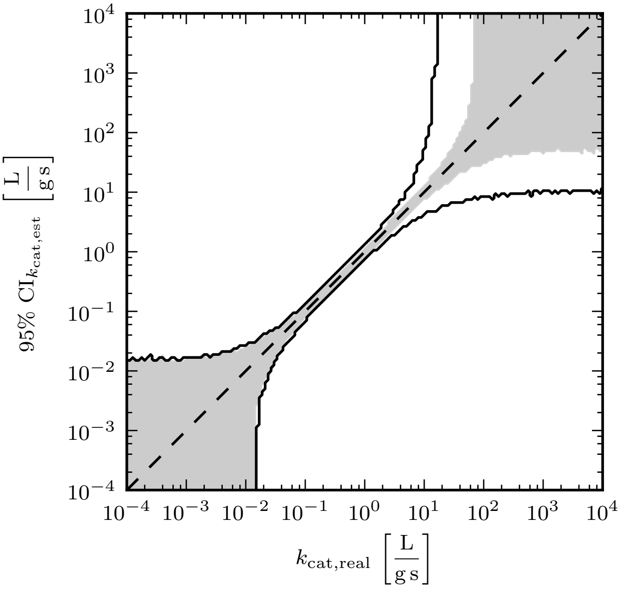

Figure 6.17: The 95 % confidence region for the increased diffusion ($D = 10^{-9}\,\mathrm{m^2/s}$) and the low residence time ($\tau = 10\,\mathrm{s}$) is given in grey. The nominal case is represented as a black line ($D = 10^{-10}\,\mathrm{m^2/s}$, $\tau = 10\,\mathrm{s}$).

Improved diffusion and measurement error

From the previous section, it was concluded that the diffusion coefficient needed to be increased in order to allow the proper estimation of k_{cat} values up to $6 \times 10^1\,\mathrm{L/(g\,s)}$. However, by further decreasing the measurement error to 0.05 it might even be possible to properly estimate higher parameter values. In Figure 6.19, the different practical identifiability regions are depicted. It is clear that the upper practical unidentifiable parameter region has further decreased in size compared to Figure 6.17, which makes it possible to estimate k_{cat} values up to $2 \times 10^2\,\mathrm{L/(g\,s)}$. As expected, the lower practical unidentifiable parameter region has the same size as in Figure 6.18. Mass transfer limitations do not occur at these conditions and thus altering the diffusion coefficient has no effect for the parameter identifiability.

6.4.7 Conclusions

The CFD model allows to estimate the intrinsic parameter values accurately even under mass transfer limited conditions. However, the qualitative analysis yields that the practical identifiability of a parameter is still highly dependent on other

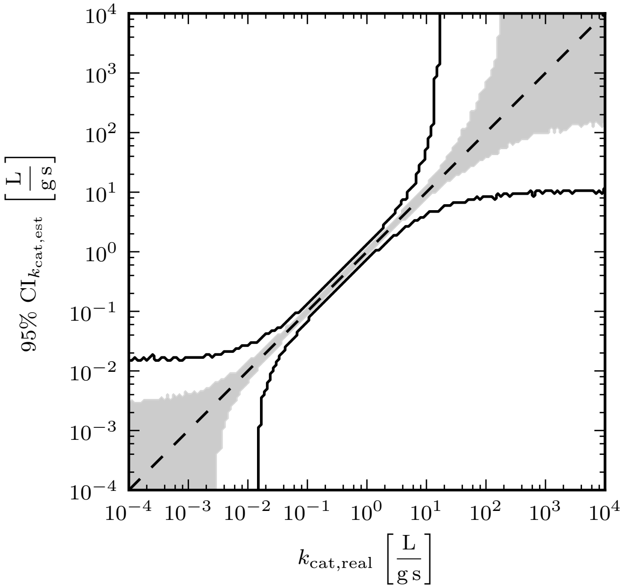

Figure 6.18: The 95 % confidence region for the decreased error ($\sigma_{\mathrm{rel}} = 0.01$) and the low residence time ($\tau = 10\,\mathrm{s}$) is given in grey. The nominal case is represented as a black line ($\sigma_{\mathrm{rel}} = 0.05$, $\tau = 10\,\mathrm{s}$).

DOFs like the residence time, the sampling frequency, and the measurement error. This confirms that the experimental design remains important, even under mass transfer limited conditions.

6.5 Applicability of the Fisher information matrix to identify optimal CFD experiments

It is clear that the intrinsic parameter values can still be estimated properly under mass transfer limited conditions. In the previous section the dependence of the practical identifiability for the different DOFs considered in this thesis was already investigated. In practice other DOFs might be considered such as the microreactor width, the solvent, the microreactor configuration. The question now arises how the most optimal measurement conditions (with respect to parameter estimation) can be identified more “easily”. In chapter 4, the Fisher information matrix (**FIM**) was used for this purpose. However, the use of the **FIM** is only accurate when the curvature of the objective function is sufficiently low. Since the initial backward reaction rate of the plain ping-pong bi-bi model (Equation 4.5) already suffered from curvature issues, it is questionable whether the **FIM** would be suitable to

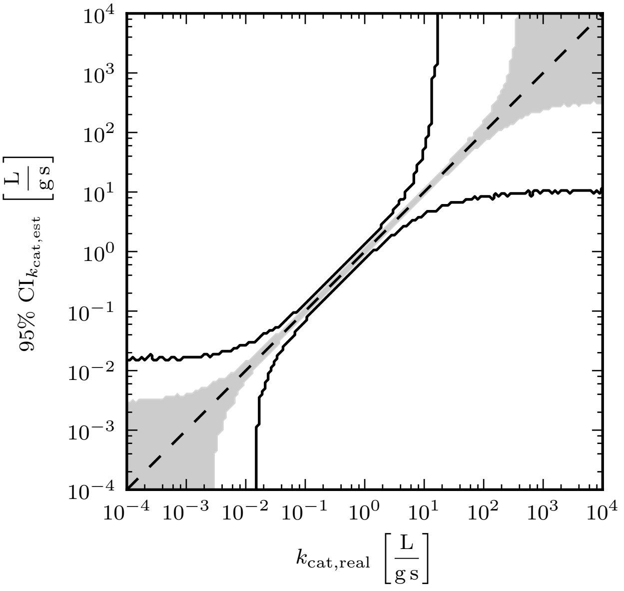

Figure 6.19: Increased D, decreased error and earlier sampling.The 95 % confidence region for the increased diffusion ($D = 10^{-9}\,\mathrm{m^2/s}$), the decreased error ($\sigma_{\mathrm{rel}} = 0.01$) and the low residence time ($\tau = 10\,\mathrm{s}$) is given in grey. The nominal case is represented as a black line ($D = 10^{-10}\,\mathrm{m^2/s}$, $\sigma_{\mathrm{rel}} = 0.05$, $\tau = 10\,\mathrm{s}$).

optimise the experimental design of a CFD model to estimate the kinetic parameter in a more reliable way.

To calculate the **FIM**, first the local sensitivity of the CFD model needs to be calculated (Equation 2.26). As discussed in Chapter 2, different approaches are available to calculate the local sensitivity. In this section, the numerical local sensitivity will be used to determine the effect of a perturbation of k_{cat} on the product concentration in the CFD simulation since it does not require the implementation of additional code in the OpenFOAM solvers. However, the use of the numerical local sensitivity requires the selection of a proper value for the perturbation factor to yield reliable local sensitivity calculations. The local sensitivity was evaluated at perturbation factors of 10^{-3}, 10^{-4} and 10^{-5}. However, the perturbation factor of 10^{-3} was found to perform better compared to the lower perturbation factors which showed a (slightly) higher uncertainty at high $k_{\mathrm{cat,real}}$. Using the **FIM**, the 95 % CI of k_{cat} can be calculated by using Equation 2.29. These results will be compared with the 95 % CIs calculated in the previous sections using the likelihood method (Equation 4.7).

In Figure 6.20, the CIs calculated from both the **FIM** (95 % $\mathrm{CI}_{\mathrm{CFD},\mathbf{FIM}}$) and the likelihood method (95 % $\mathrm{CI}_{\mathrm{CFD,likelihood}}$) are represented for the nominal case. The 95 % $\mathrm{CI}_{\mathrm{CFD},\mathbf{FIM}}$ is fairly uncertain at low $k_{\mathrm{cat,real}}$ values, but this uncertainty drops to 2 % for $k_{\mathrm{cat,real}}$ values around 2×10^{-2} L/(g s). For $k_{\mathrm{cat,real}}$ values above 2×10^{-2} L/(g s), the parameter uncertainty increases again to reach a 100 % relative uncertainty (black line) at a $k_{\mathrm{cat,real}}$ value of 6×10^{0} L/(g s). All $k_{\mathrm{cat,real}}$ values above this value can be regarded as practically unidentifiable, since the uncertainty is larger compared to its intrinsic value. The evolution of 95 % $\mathrm{CI}_{\mathrm{CFD,likelihood}}$ is derived from Figure 6.9 and is represented by the grey region. In theory it is also possible to derive a smooth curve, but the likelihood method requires many evaluations to accurately determine the 95 % CI. The number of evaluations depends on the dimensionality of the problem, but for a one-dimensional problem, it should be possible to obtain an accurate estimatation of the 95 % CI by using about 100 function evaluations. However, this amount of function evaluations has to be performed for each k_{cat} value, requiring a total number of 16 000 (i.e. 100 simulations for all 160 k_{cat} values) CFD simulations for each scenario. To limit the computational requirements, it was decided to perform a "rough" estimation of this 95 % CI by evaluating the objective function at a fixed number of $k_{\mathrm{cat,real}}$ values. As a consequence, the 95 % $\mathrm{CI}_{\mathrm{CFD,likelihood}}$ is here not represented as one value but as a range in which it is located and is therefore represented by the grey region. The 95 % $\mathrm{CI}_{\mathrm{CFD,likelihood}}$ shows quite a similar evolution compared to the 95 % $\mathrm{CI}_{\mathrm{CFD},\mathbf{FIM}}$, but the practically identifiable range is smaller since only $k_{\mathrm{cat,real}}$ values between 3×10^{-4} and 8×10^{-1} L/(g s) are identifiable. This is in agreement with earlier statements in Chapter 4, since the inverse of the **FIM** only yields the lower bound of the parameter uncertainty error covariance matrix (Ljung, 1999). Therefore, the 95 % $\mathrm{CI}_{\mathrm{CFD},\mathbf{FIM}}$ provides more optimistic uncertainties compared to the 95 % $\mathrm{CI}_{\mathrm{CFD,likelihood}}$. The uncertainty ranges only overlap close to the minimum (between 6×10^{-3} and 8×10^{-2} L/(g s)), which is related to the resolution of $k_{\mathrm{cat,real}}$ values. These are evaluated for 161 values between 10^{-4} and 10^{4} L/(g s), more specifically they are evaluated for every $10^{-4+0.05\,i}$ L/(g s) with $i \in 0, 1, \ldots, 160$. As as consequence, the relative difference between every k_{cat} value is about 12.2 %, yielding 95 % $\mathrm{CI}_{\mathrm{CFD,likelihood}}$ which are relatively broad. At very accurate conditions, i.e. close to the minimum of the curve, the 95 % $\mathrm{CI}_{\mathrm{CFD,likelihood}}$ is between 0 and 12.2 %. However, in theory 95 % $\mathrm{CI}_{\mathrm{CFD,likelihood}}$ is always equal or greater than 95 % $\mathrm{CI}_{\mathrm{CFD},\mathbf{FIM}}$. A more accurate estimation of the 95 % $\mathrm{CI}_{\mathrm{CFD,likelihood}}$ could be obtained by reducing the step size, but this would come at a large computational cost. However, in order to construct the 95 % $\mathrm{CI}_{\mathrm{CFD,likelihood}}$, the methodology in Figure 6.7 was performed for 5000 repetitions in order to yield results which are robust with respect to the *in silico* generated noise. As a consequence, the shown 95 % $\mathrm{CI}_{\mathrm{CFD,likelihood}}$ is the combination of the calculated uncertainties for all 5000 repetitions. However, using this approach yields confidence intervals which are about 30 % broader, and thus can be considered as a worst-case scenario.

As a comparison also the 95 % CI using the plug flow model is shown in Figure 6.20 (95 % $\mathrm{CI}_{\mathrm{PF},\mathbf{FIM}}$). At low $k_{\mathrm{cat,real}}$ values ($< 10^{-1}\,\mathrm{L/(g\,s)}$) it coincides with 95 % $\mathrm{CI}_{\mathbf{FIM}}$, which confirms that the CFD model and the plug flow model yield the same results when mass transfer limitations are absent. At high $k_{\mathrm{cat,real}}$ values large deviations occur and the 95 % $\mathrm{CI}_{\mathrm{PF},\mathbf{FIM}}$ curve even starts to decrease, but this will be discussed later in this section.

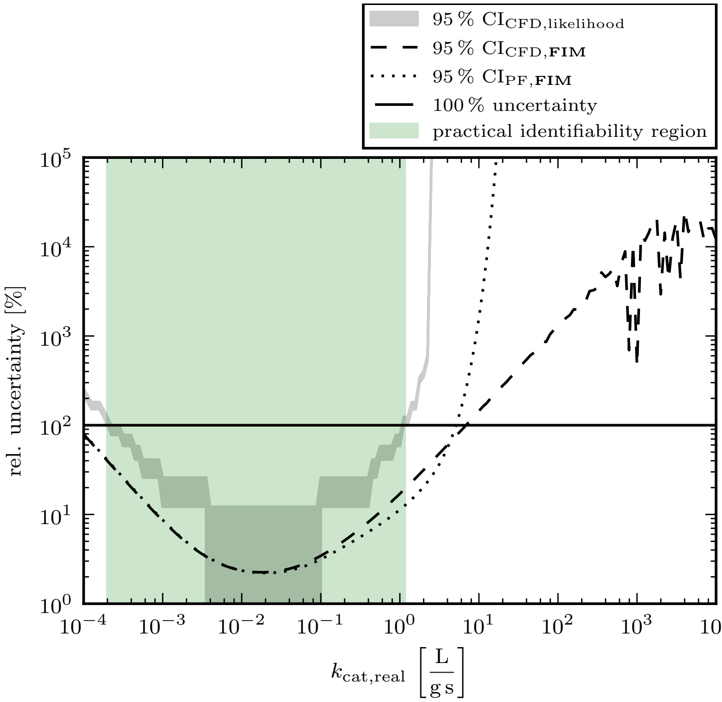

Figure 6.20: The 95 % confidence intervals (CIs) are represented for the nominal case using two different approaches, i.e. likelihood method and the **FIM**. As a reference the 95 % CI for the plug flow model is also shown, but this value is only accurate in absence of mass transfer limitations.

The experimental design in Figure 6.20 can be regarded as optimal for the $k_{\mathrm{cat,real}}$ range between 3×10^{-2} and $10^{-1}\,\mathrm{L/(g\,s)}$. However, in the case that the expected parameter values are located between 10^{-1} and $10^{0}\,\mathrm{L/(g\,s)}$, the relative 95 % $\mathrm{CI}_{\mathrm{CFD,likelihood}}$ is about 77 % which is too high for a parameter estimate to be considered as reliable. Therefore, the experimental design needs to be "optimised" to reduce this uncertainty. In Section 6.4, it was already shown that reducing the residence time from its nominal value (600 s) to 10 s leads to a significant decrease of the uncertainty for the $k_{\text{cat,real}}$ values in the range of interest. The effect of reducing the residence time is shown in Figure 6.21. From this figure, it can be derived that the uncertainty of the $k_{\text{cat,real}}$ values in the range of interest have drastically reduced, i.e. the maximum expected $95\,\%$ $\text{CI}_{\text{likelihood}}$ has reduced from 77 to 26 %. In this case the change in experimental design was performed manually, but from Figure 6.21 it is clear that the minima of the $95\,\%$ $\text{CI}_{\text{CFD,likelihood}}$ and $95\,\%$ $\text{CI}_{\text{CFD},\mathbf{FIM}}$ coincide. Moreover, both curves have similar shapes for $k_{\text{cat,real}}$ values below $10^{-1}\,\text{L/(g s)}$, indicating that the **FIM** might be used as a measure to optimise the experimental design. At higher $k_{\text{cat,real}}$ values, i.e. when the mass transfer limitations become severe, both curves start to deviate and the **FIM** underpredicts the 95 % CI. This illustrates that the **FIM** is probably a good measure to be used as objective function for the optimisation of the experimental design, but shows a persistent underestimation of the parameter uncertainty by at least a factor 2.5. To allow comparison with the **FIM** calculated using the plug flow model (i.e. without mass transfer limitations), the results obtained for that model have also been plotted in Figure 6.21. At low $k_{\text{cat,real}}$ values, the $95\,\%$ $\text{CI}_{\text{CFD},\mathbf{FIM}}$ and $95\,\%$ $\text{CI}_{\text{PF},\mathbf{FIM}}$ should coincide, but some deviation can be found at values below $10^{-3}\,\text{L/(g s)}$. At high $k_{\text{cat,real}}$ values ($> 10^{-1}\,\text{L/(g s)}$), the $95\,\%$ $\text{CI}_{\text{PF},\mathbf{FIM}}$ curve starts to deviate from the $95\,\%$ $\text{CI}_{\text{CFD},\mathbf{FIM}}$ before the minimum is reached. This can be related to the mass transfer limitations which are already significant at this level and thus lead to a major difference between the CFD and plug flow results.

In Figures 6.20 and 6.21 the $95\,\%$ $\text{CI}_{\text{PF},\mathbf{FIM}}$ curve shows a decreasing trend for values above $10^{1}\,\text{L/(g s)}$. This change in trend is not observed in the other two approaches (i.e. $95\,\%$ $\text{CI}_{\text{CFD,likelihood}}$ and $95\,\%$ $\text{CI}_{\text{CFD},\mathbf{FIM}}$), which indicates that the use of the **FIM** for plug flow models at high turnover number cannot be regarded as reliable. In Chapter 4, it was already stated that the application of the **FIM** has its limitations and should always be applied with care. To obtain accurate predictions using the **FIM**, the curvature of the solution locus should be sufficiently small. In Figure 6.22, the *parameter-effects* curvature $c^{\boldsymbol{\theta}}$ for both the nominal and the reduced residence time (i.e. 600 and 10 s respectively) are given. The residual residence s^2 was set equal to 1.256, since this is the expected value of $J(\hat{\boldsymbol{\theta}})/(N-P)$. For the nominal residence time, the *parameter-effects* curvature exceeds the critical value ($\sqrt{F_{\text{crit}}^{-1}}$) around a $k_{\text{cat,real}}$ value of $4 \times 10^{0}\,\text{L/(g s)}$. At the same $k_{\text{cat,real}}$ value in Figure 6.20 the uncertainty trend switches from increasing to decreasing. The same analysis can be made for the reduced residence time, and it can thus be concluded that the decreasing trend at high $k_{\text{cat,real}}$ values is due to the

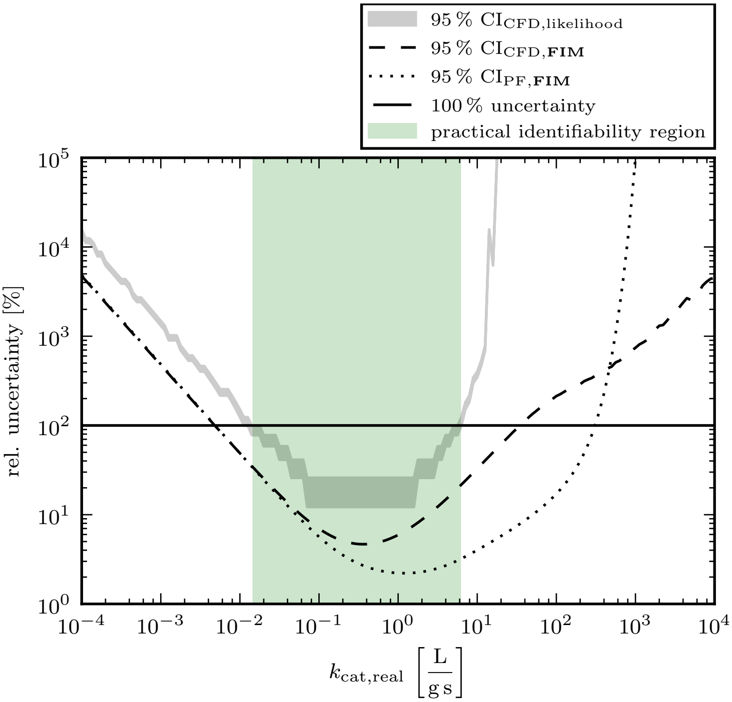

Figure 6.21: The 95 % CIs are represented for the reduced residence time case ($\tau = 10\,\mathrm{s}$) using two different approaches, i.e. likelihood method and the **FIM**. As a reference the 95 % CI for the plug flow model is also shown, but this calculation is only accurate in absence of mass transfer limitations, i.e. for low $k_{\mathrm{cat,real}}$ values.

high curvature. This indicates that by using the **FIM**, attention should be paid to keep the *parameters-effects* curvature below a certain acceptable level. For the two cases evaluated here the 95 % CI$_{\mathrm{CFD},\mathbf{FIM}}$ does not show such trend switches, but there is no guarantee that this cannot happen at different conditions.

6.6 Conclusions

When mass transfer limitations are absent, plug flow models can be used to reliably estimate the intrinsic parameter values. For Da$_{\mathrm{II}}$ values higher than 0.23, mass transfer limitations become too important and the effect on the kinetics can no longer be ignored. Therefore, a model calibration using CFD was performed and showed that even under mass transfer limited conditions it is possible to estimate the intrinsic parameter values accurately. The superiority of the likelihood

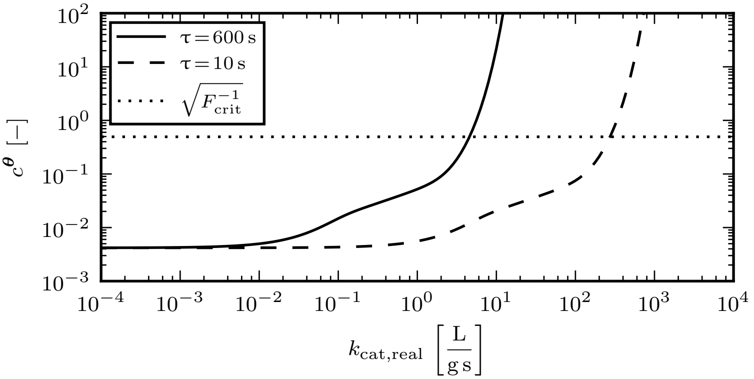

Figure 6.22: The *parameter-effects* curvature c^{θ} as a function of $k_{\mathrm{cat,real}}$ for both the nominal case ($\tau = 600\,\mathrm{s}$) and the reduced residence time case ($\tau = 10\,\mathrm{s}$).

method compared to the **FIM** for estimating the parameter uncertainty was illustrated. However, the current methodology for estimating the likelihood overpredicts the uncertainty, and thus should be regarded as the worst-case scenario for the parameter identifiability. The **FIM** derived from the CFD model shows comparable trends as the likelihood method and thus might be considered as a measure for performing optimal experimental design at a lower computational cost. High *parameter-effects* curvatures were found to be important causes for unreliable uncertainty estimates when using the **FIM**. In an optimisation exercise it will thus be important to keep these curvatures at sufficiently low levels to achieve reliable experimental designs. The results shown in this chapter clearly show that kinetic parameters can be estimated under mass transfer limited conditions. However, the actual experimental design remains an important aspect of the parameter estimation exercise. Moreover, it is illustrated that calculation of the **FIM** for designing experiments should take into account the reactor dimensions, diffusion coefficient values,. . . to allow accurate predictions.

CHAPTER 7

CONCLUSIONS AND PERSPECTIVES

7.1 Research objectives

The objectives of the research performed in this dissertation were formulated as follows:

1. estimate the intrinsic parameter values describing the conversion by ω-TA in an efficient and reliable way,
2. gain fundamental knowledge about the productivity improvements of enzymes in microreactors,
3. determine whether intrinsic parameter values can be estimated properly under mass transfer limited conditions.

To meet these three research objectives, four research questions were formulated to perform the research in a systematic way. These research questions are repeated in the next section and answers will be provided based on the results and experience gathered during the PhD project.

7.2 Research questions

RQ 1. Is the ping-pong bi-bi model identifiable?

To answer this question, it needs to be split up into two separate identifiability questions:

- Structural identifiability question: Can the different model parameters be uniquely estimated when unlimited and perfect (i.e. error-free and unbiased) data are available?
- Practical identifiability question: Can the different model parameters be uniquely estimated when only a limited amount of noise-corrupted data are available?

The structural identifiability question was answered in Chapter 3, and yielded that the plain ping-pong bi-bi model is (at least locally) structurally identifiable. Since a numerical identifiability procedure was used, only the local identifiability could be assessed. However, by using this procedure not only the structural identifiability is investigated but also the performance of the optimisation algorithm. This allows to assess the performance of different optimisation algorithms and, hence, pinpoint potential optimisation issues.

The practical identifiability was investigated for the literature values of Shin and Kim (1998) (Chapter 3) and for the calibrated values using experimental data, which was partially obtained using a robust optimal experimental design procedure (Chapter 4). For the latter, it was shown that all the parameter estimates could be estimated fairly accurately given the experimental uncertainty. In this case, the parameter estimate uncertainty was calculated using the Fisher information matrix. The practical identifiability analysis performed in Chapter 3 yielded the logical result that the measurement uncertainty was of great importance to obtain accurate parameter estimates. Moreover, it was shown that not all parameter values could be estimated properly using the experimental design of Shin and Kim (1998). Although the numerical identifiability procedure should be regarded as a qualitative method, it allows to determine how measurement error and experimental design affect the actual parameter estimate. In this way, deviations and skews can be detected.

RQ 2. Can the uncertainty of kinetic parameter estimates be reduced by optimising the experimental design?

A robust model-based optimal experimental design (rMbOED) was used to identify highly informative regions for the plain ping-pong bi-bi model in Chapter 4. The experimental design strategy also proved useful to identify where the experimental design space was too narrow to obtain proper information for accurately estimating parameter values. Moreover, this approach was compared with the traditional approach where experimentation is performed first and is followed by a parameter estimation. For the model under study, it was shown that for the same experimental effort, the use of rMbOED reduced the 95 % confidence intervals by a factor 2 (Chapter 4). This observation confirms that the application of optimal experimental design methodologies is not only useful for *in silico* problems, but does also prove useful for real-life biocatalytic processes.

The optimal experimental design methodologies were already described in literature, but this cannot be said for the actual code implementations. In this respect, Van Hoey (2016) argued that the unavailability of these implementations makes it difficult to reproduce results and hampers the innovation within the scientific field. To make the optimal experimental design methods accessible for a broader audience, the pyIDEAS package was developed (Section 2.2.9). The aim of this Python package is to encourage the experimentalists, which typically have less experience with mathematical methods, to use OED for the calibration of relatively simple model structures.

RQ 3. How can mass transfer limitations be quantified in (complex) microreactors?

For simple microreactor configurations and first-order kinetics, the mass transfer limitations could already be quantified using dimensionless numbers. However, for more complex microreactors and/or kinetics, which are currently being tested and developed, these dimensionless numbers only provide a rough indication. In Chapter 5, a newly developed generic methodology was presented which is based on the comparison of a CFD model with an ideal plug flow model. This approach was successfully applied to two different microreactor configurations, and nicely coincided with results previously reported in the literature. Moreover, the methodology is independent from the actual microreactor configuration and kinetics under study, and thus can be considered as generally applicable to assess mass transfer limitations for a wide range of microreactor configurations and kinetics. In this respect, unsuitable dimensionless numbers are occasionally used to calculate the level of mass transfer limitations (e.g. by Swarts et al. (2010)). The availability of the generic methodology avoids this kind of misuse and allows the accurate calculation of mass transfer limitations for microreactors and reactions where this was not yet possible for.

RQ 4. Is it possible to (properly) estimate kinetic parameters under mass transfer limited conditions?

In Chapter 6, it was shown that it is possible to perform a reliable kinetic parameter estimation under moderate mass transfer limited conditions. However, under severe mass transfer limited conditions it becomes simply impossible to obtain accurate parameter estimates, and thus the mass transfer needs to be improved in order to yield reliable parameter estimates. The accuracy of the parameter estimate was shown to be highly dependent on the experimental design under mass transfer limited conditions. In this respect, a traditional optimal experimental design typically only considers degrees of freedom which directly influence the kinetic model (e.g. initial substrate and product concentrations, measurement times,...). In order to obtain a suitable experimental design under mass transfer limited conditions, it is important to include the degrees of freedom which influence the mass transfer processes (e.g. the diffusion coefficient value and the microreactor width). To obtain such an optimal design, typically the Fisher information matrix is calculated and its information content is maximised. It was shown that the use of the Fisher information matrix only provided correct estimates when the mass transfer limitations were not severe. At high mass transfer limitations, the nonlinearity of the coupled CFD-kinetic model increases, and thus the Fisher information matrix can no longer be used to reliably calculate parameter estimate uncertainties.

By answering the different research questions, more insight was gathered with respect to the different mass transfer regimes in microreactors and their effect on the practical identifiability of the kinetic parameters. In new biocatalytic studies, this acquired knowledge is readily available to intensify these processes by improving the mass transfer rates. Moreover, the efficient and fast screening of these biocatalysts is important to reduce the lab-to-market time (Tholey and Heinzle, 2002; Garcia et al., 2007; Wirth, 2013). Such a screening allows the fast collection of biocatalyst productivity at different experimental conditions. Once optimal experimental conditions are identified which are also economically viable, the microreactor platform allows to increase the production volume by use of the scale-out approach. The application of this approach avoids the time-consuming process of scale-up (Wohlgemuth et al., 2015). By applying optimal experimental design methods, the required experimental efforts can be decreased significantly and the kinetic parameter reliability can be easily assessed. In this respect, it was shown that it is also possible to reliably estimate parameter values under mass transfer limited conditions. This was not yet possible, and allows to acquire kinetic parameter values which are not dependent on the actual fluid regime. The latter is important, since it will improve the accuracy of upscaling and downscaling calculations.

7.3 Perspectives

Based on the experience build throughout this dissertation, some future perspectives are discussed below.

7.3.1 Kinetic models for enzymes

The kinetic models to describe the enzymatic catalysis are mostly reduced using the quasi steady-state assumption (QSSA). This was also the case in this dissertation, where the quasi steady-state equation representing the plain ping-pong bi-bi mechanism was successfully calibrated. However, the question arises what benefits the quasi steady-state assumption yields. First, the application of the QSSA reduces the system of ODEs to a single algebraic equation. This model reduction makes that the QSSE can be simplified by splitting up the full model structure into submodels, as was done in Chapters 3 and 4. Second, the aim of a model reduction is to reduce the complexity (and the number of parameters) of a model. However, for the plain ping-pong bi-bi model this is not really the case, since the number of parameters is actually the same as the original rate model (Table 7.1).

From Table 7.1, it can be seen that the number of initial conditions for the substrates and products is the same for both models. The actual "simplification" is located within the number of initial conditions of the different enzyme forms. For the quasi steady-state (QSS) model only the total enzyme concentration needs to be set, and can thus be regarded as a parameter since it is fixed in time. On the other hand, the initial concentrations of the four enzyme forms (i.e. E, EA, F,

Table 7.1: Overview of the model complexities of both the rate model and the quasi steady-state model describing the plain ping-pong bi-bi mechanism.

	Rate model	**QSS model**
Parameters	8	8 + 1*
Initial conditions		
- substrates & products	4	4
- enzyme forms	4	1

* K_{eq} is related through the Haldane relationship and should not be calibrated (Segel, 1975).

and FB) need to be set for the rate model. However, it is not clear whether these initial conditions would have a large impact on the model outputs.

It is clear that the application of the quasi steady-state assumption for the plain ping-pong bi-bi mechanism does not yield an important reduction in model complexity. However, for other mechanisms the QSSA has proven to reduce overall model complexity (Briggs and Haldane, 1925; Radulescu et al., 2012), e.g. for the Michaelis-Menten kinetics, the number of parameters is decreased from 3 to 2 and the number of enzyme forms is reduced from 2 to 1.

The question which needs to be answered in the future is whether the use of a quasi steady-state model is needed to describe and calibrate reactions obeying the ping-pong bi-bi mechanism. Moreover, if such a model reduction would be necessary, other (more advanced) model reduction methods are available nowadays (Radulescu et al., 2012; Rao et al., 2014).

7.3.2 Apply generic methodology to assess mass transfer limitations for other (micro)reactors & reactions

The generic methodology to assess mass transfer limitations, which was developed in chapter 5, was only applied to fairly simple microreactor configurations. For other micro- and macroreactor configurations the added value might be even higher, since the use of dimensionless numbers will be practically impossible. However, there might be some issues which have to addressed first for large-scale reactors:

- **Measurement location**
  The generic methodology used measurements at the outlet of the micro-

reactor. In the case of a microreactor, it does not really matter if the measurements would be taken inside the reactor, since these reactors are mostly tubular-like and a measurement location within the reactor can be regarded as a reduction in residence time. However, for larger reactor tanks it might prove impossible to relate a measurement within the reactor with the idealised tank models. Therefore, the fundamental idea of the methodology to compare an ideal model with a CFD model, is probably only applicable for large reactors when performing measurements at the outlet of the reactor.

- **Impact of turbulence**
  Microreactors can be modelled using laminar flow models, but for large reactor tanks the turbulence needs to be taken into account. The choice of the turbulence models and its parameter values can have a great impact. Since turbulent flows generally improve the mass transfer, the effect of the turbulence needs to be described accurately. However, the selection of the proper turbulence model remains a difficult question. Recently, Larsson et al. (2015) compared the performance of RANS turbulence models for different pilot and large-scale reactor configurations. The suitability of a turbulence model was found to be depending on both the reactor configuration and operating conditions, however no general consistency was found. The observation were confirmed by a literature study, which showed that reactors with similar layout and operating conditions were often modelled using different turbulent models (Larsson et al., 2015). This indicates that the selection of the proper turbulence model, although important for the parameter estimation, is not straightforward.

- **Complex reactions**
  In Chapter 5, the generic methodology was applied for a simple pseudo first-order kinetic model. However, in reality more complex kinetic models, involving multiple species and equilibrium reactions, are generally considered. Deriving a single measure indicating the level of mass transfer limitations will prove to be more challenging in such a case.

After addressing these issues, the mass transfer limitations can be calculated for more complex (large-scale) reactors. The generic methodology could be combined with a topology optimisation approach, i.e. the study to optimise the reactor configuration to meet specified performance requirements (Pereira Rosinha et al., 2015). In this respect, the generic methodology could yield additional information regarding the mass transfer limitations, which are expected to decrease during such a topology optimisation.

7.3.3 Automated optimal experimental design for parameter estimation of complex models

Model-based optimal experimental design (MbOED) was only used for part of the model calibration, but the implementations and knowledge are available allowing its direct use in the near future. In this respect, McMullen and Jensen (2011) already presented an automated microfluidic system for the rapid determination of reaction kinetics where model discrimination and parameter estimation were performed sequentially. This approach was applied to a Diels-Alder reaction and was able to discriminate the right model from three other reaction kinetics. Such an automated approach would drastically reduce the time required for performing a proper parameter estimation. To further reduce the experimental effort, the sequential approach used by McMullen and Jensen (2011), can be replaced by an integrated approach where the information for both the parameter estimation and model calibration is collected simultaneously (Donckels, 2009). However, the robustness of such an automated approach needs to be assessed for more complex models like the ping-pong bi-bi QSS model.

7.3.4 Optimal experimental design under mass transfer limited conditions for complex reactions and reactor configurations

Instead of performing an OED study based on the plug flow, the optimisation should better be performed using a CFD model which allows to take into account spatial heterogeneities and mass transfer limitations. However, this approach requires the implementation of the local sensitivity function in the CFD software and is computationally very expensive. Moreover, there are a couple of hurdles which need to be taken before its application can be regarded as reliable.

First, the Fisher information matrix (**FIM**) is typically used to optimise experimental designs. In Chapter 6, the **FIM** was calculated but showed unreliable behaviour under increased mass transfer limitations. This behaviour could be related with the high *parameter-effects* curvature introduced earlier in Chapter 4. In order to obtain reliable experimental designs and parameter estimate uncertainties, Benabbas et al. (2005) proposed a measure in which the *parameter-effects* curvature is kept below a certain maximum during the maximisation of the information content (so-called constrained optimisation).

Second, the application of OED for CFD has only be shown for a kinetic model with a single parameter. Since the convection-diffusion effects will obscure the underlying kinetic parameters and its relations, it can be expected that kinetic models with more parameters will prove more difficult to calibrate. Moreover, kinetic models which are practically identifiable in an ideal reactor configuration, might become practically unidentifiable when taking into account mass transfer limitations.

Third, compared to a “standard” rMbOED, more degrees of freedom are available now. However, that can pose problems since some degrees of freedom are easier to change (e.g. substrate concentration, residence time,. . .) compared to other degrees of freedom (e.g. microreactor width, immobilised enzyme concentration, . . .). Therefore, an objective function needs to be developed which can take into account such limitations.

Despite the fact that there are still some hurdles to be dealt with, the use of OED for CFD-kinetic models looks promising. More specifically, the use of this technique allows to identify highly informative regions where sensors will be more performant. This is especially useful for large-scale reactors like fermentors and wastewater treatment plants.

It should be noted that although OED and topology optimisation both use CFD-kinetic models, the aim of both methods is different. The aim of OED for a CFD-kinetic model, is to optimise the information of the experiments by altering process conditions and (if necessary) the reactor configuration. For a topology optimisation, the aim is to optimise the reactor performance by altering the reactor configuration. A logical optimisation procedure would consist of following steps: First, OED is performed CFD-kinetic model for a standard reactor configuration. If the mass transfer limitations would be too severe to allow a proper parameter estimation, changes in the reactor configuration should be considered. After a successful parameter estimation and uncertainty analysis, the CFD-kinetic model can be used to perform a topology optimisation in order to improve the reactor’s productivity.

7.3.5 Assess hypotheses why enzymes perform better in microreactors

In literature, the enzyme-relative productivity of biocatalytic microreactors is generally higher compared to that in small batch reactors. E.g. Tušek et al. (2012) reported a 30 time higher productivity in the microreactor (6 µL) compared to the cuvette (1 mL). The traditional strengths of microreactors, such as their high surface-to-volume ratio and small diffusion distances, are often referred to in order to explain the observed behaviour. However, these hypotheses are generally left unproven, and thus no additional knowledge and insights are gathered. The focus of most papers is to prove the superiority of these small-scale reactors, while it might be plausible that some productivity problems might already been solved by switching from turbulent flow in batch reactors to the laminar flow in microreactors. In this respect, Maruyama et al. (2003) already raised the question whether the mixing in small batch reactors could result in the denaturation of the enzyme.

When the enzymatic microreactor and batch reactor show a strong difference in productivity, this needs to be assessed using a stepwise approach which should potentially consist of the following steps:

1. Perform additional kinetic experiments in a microreactor. In this respect, the use of an optimal experimental design method will reduce the required experimental effort.
2. Estimate the kinetic parameters using a combined kinetic-CFD model (as shown in Chapter 6), which will allow to obtain the intrinsic parameter values. Moreover, the kinetic parameter uncertainty needs to be calculated.
3. The calibrated kinetic model can now be used to calculate the mass transfer limitations by using the generic methodology introduced in Chapter 5. This step can be regarded as unnecessary, but provides additional information about the mass transfer limitations in the microreactor. Moreover, this step is not calculation intensive, since all the preparative work has already been done in the previous step.
4. Afterwards, a combined kinetic-CFD model needs to be constructed for the batch reactor. Most of the effort done in step 2 can be reused, but a new reactor geometry needs to be implemented and turbulence needs to be included.
5. The kinetic data gathered in the batch reactor can be compared with the model prediction of step 4. If the data and predictions match, the main phenomenon reducing the batch reactor productivity is the lack of mass transfer. Otherwise, additional phenomena like denaturation need to be tested and validated.

The proposed stepwise approach is only a first draft of such a procedure, and should be adapted according to the specificities of the system under study. The kinetic model is calibrated using the data from the microreactor, since it is expected that the uncertainties of the laminar flow model are much lower compared to that of the turbulent flow model. By comparing the integrated CFD-kinetic model for the batch reactor with the corresponding data, information can be gathered and hypotheses can be tested. The use of such a stepwise approach will allow to build a knowledge base about the effect of a specific process operation on the biocatalytic performance.

7.3.6 Modelling of the production of unstable intermediates in microreactors

For the production of unstable intermediates, microreactors prove to outperform traditional large-scale reactors like continuous stirred-tank reactors. In a microreactor it is possible to continuously extract the intermediate at the location where the concentration is the highest (Jensen, 2005). This is also possible for continuously stirred-reactor tanks, but due to mixing effects the effective concentration of the intermediate is lower. In literature, the production of unstable intermediates in microreactors has already been shown experimentally for chemical pathways (Nagaki et al., 2010, 2012a,b). In order to intensify this type of reactions, the mass transfer and the process design need to be improved. The necessary modelling tools, which were partially developed in this dissertation, are now available to achieve this goal.

APPENDIX A

pyIDEAS example

In this appendix, a brief overview is given of the methods currently available within pyIDEAS package and used throughout this dissertation. The pyIDEAS package will be available at `https://github.com/TimothyVD`, where a more extensive documentation is available. The use of the different functionalities is illustrated for the Michaelis-Menten model, introduced earlier in Chapter 2.

A.1 Model definition and simulation

A.1.1 Algebraic model

The Michaelis-Menten equation (Equation 2.15) can be easily implemented using the `AlgebraicModel` class, which is intended for purely algebraic models.

```python
import numpy as np
# import the algebraic model class
from pyideas import AlgebraicModel

# Define model structure
system = {'v': 'Vmax*S/(Km + S)'}

# Set (initial) parameter values
parameters = {'Vmax': 0.25,
              'Km':  20.}

# Initiate an 'AlgebraicModel' object
```

```python
M1 = AlgebraicModel('Michaelis-Menten', system, parameters, ['S'])

# Set the concentration range of the substrate
M1.independent = {'S': np.linspace(0., 100., 1000)}

# Run the model and plot the initial rate v
M1.run()['v'].plot()
```

The final command yields Figure A.1.

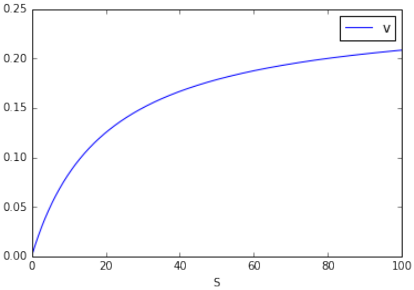

Figure A.1: The reaction rate v as a function of the substrate concentration S for the Michaelis-Menten model.

A.1.2 Differential algebraic model

To describe the evolution of the substrate and product concentrations in a batch reactor, a differential algebraic model needs to be defined. In this case, the Michaelis-Menten equation describes the rate at which the substrate is consumed and the product is being produced.

```python
import numpy as np
# import the differential algebraic model class
from pyideas import Model

# Define model structure
system = {'dP': 'v*E',
          'dS': '-v*E',
          'v': 'Vmax*S/(Km + S)'}

# Set (initial) parameter values
parameters = {'Vmax': 0.25,
              'Km':  20.,
              'E':    4.}

```

```
# Initiate an 'AlgebraicModel' object
M2 = Model('Michaelis-Menten', system, parameters)

# Set the length of the experiment
M2.independent = {'t': np.linspace(0., 100., 1000)}
# Set initial conditions for both the substrate and product
M2.initial_conditions = {'S': 50., 'P': 0.}

# Run the model and plot the initial rate v
M2.run()[['S', 'P']].plot()
```

The final command yields Figure A.2.

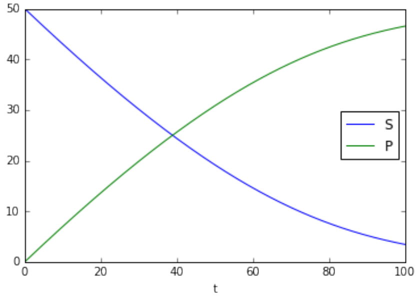

Figure A.2: The substrate and product concentrations as a function of time.

A.2 Parameter estimation

In reality, a model needs to be calibrated using experimental data before it can actually be used for process optimisation. Therefore, some fictitious data with a random white noise of 5 % was generated below. First, the local approach is used to estimate the parameter values. However, local methods are less likely to find the global minimum.

A.2.1 Local optimisation

```
import pandas as pd
from pyideas import Measurements, ParameterOptimisation

# Experimental data
data = np.array([[   0.         ,    0.        ],
                 [  20.         ,    0.138     ],
```

```
                 [  40.        ,    0.168    ],
                 [  60.        ,    0.194    ],
                 [  80.        ,    0.198    ],
                 [ 100.        ,    0.204    ]])

# To use the experimental data, it needs to be
# converted to a pandas dataframe
data = pd.DataFrame(data=data, columns=['S', 'v'])
# The independent variables are set as index
data = data.set_index(['S'])

# Data object is initialised
M1data = Measurements(data)
# Measurement error has std deviation of 5%
# this will be taken into account for the optimisation
M1data.add_measured_errors({'v': 0.05}, method='relative')

# Initiate optimisation object using model and data
M1optim = ParameterOptimisation(M1, M1data)

# Perform a local optimisation using Nelder-Mead
M1optim.local_optimize(method='Nelder-Mead').x
```

The final command yields the following "optimal" parameter values:

```
array([ 14.08076174,   0.23334128])
```

A.2.2 Global optimisation

For more complex problems, a global optimisation might be more suitable since it is more likely to retrieve the global optimum.

```
from pyideas import ModPar

# Set ranges for each parameter which needs to be optimised
parspace = [ModPar('Km',   0., 100., 'randomUniform'),
            ModPar('Vmax', 0.,   5., 'randomUniform')]
M1optim.set_dof_distributions(parspace)

# Perform a particle swarm optimisation (PSO) for 100 particles
population, optim_obj = M1optim.inspyred_optimize(approach='PSO',
                                                  pop_size=100,
                                                  max_eval=10000)
# Extract the most optimal particle for the population
max(population).candidate
```

The final command yields the following “optimal” parameter values, which are really close to those obtained with the local optimisation method.

```
array([ 14.08073538,   0.23334127])
```

A.3 Parameter uncertainty calculations

```python
from pyideas import CalibratedConfidence

# The optimisation is used to construct the confidence object
M1conf = CalibratedConfidence(M1optim)

# Calculate the parameter confidence
M1conf.get_parameter_confidence()

# Calculate the parameter correlation
M1conf.get_parameter_correlation()
```

The parameter estimates obtained from the initial rate data and given the measurement uncertainty standard deviation of 5 % can be regarded as reliable. However, the Michaelis constant K_m is rather uncertain with a 95 % confidence interval of 60 %.

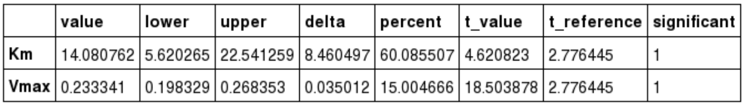

	value	lower	upper	delta	percent	t_value	t_reference	significant
Km	14.080762	5.620265	22.541259	8.460497	60.085507	4.620823	2.776445	1
Vmax	0.233341	0.198329	0.268353	0.035012	15.004666	18.503878	2.776445	1

Figure A.3: The parameter estimates uncertainty of the kinetic parameters of the Michaelis-Menten model, using the Fisher information matrix.

A.4 Model-based optimal experimental design

The question now arises whether more informative experiments could have been designed to allow a better parameter estimation. Two types of optimal experimental design are shortly illustrated in this section, i.e. brute force design and robust design.

A.4.1 Brute force design

The idea behind the brute force design, it to calculate all different design possibilities for one parameter set. The approach is shown below.

```
from pyideas import BaseOED

# Initiate an optimal design object from the calibrated model
M1OED = BaseOED(M1conf, ['S'])

# Set the experimental design ranges for S
M1OED.set_dof_distributions([ModPar('S', 0., 100.0, 'randomUniform')])

# Obtain an optimal design given the practical limitations
indep_out, FIM_end = M1OED.brute_oed({'S': 21}, # Divide range in 21 pieces
                                     5, # Sample 5 most informative experiments
                                     replacement=False, # No replacement of samples
                                     criterion='D') # Use D-criterion for optimisation

# Get optimal sampling locations
indep_out.values[:,0]
```

The final command yields the following optimal experimental design for the parameter values under consideration.

```
array([   5.,   15.,   90.,   95.,  100.])
```

A.4.2 Robust design

Since it is very unlikely that the parameter values are known prior to the parameter estimation, a robust design approach is more suitable. Currently only the maximin approach is implemented within the pyIDEAS package.

```
from pyideas import RobustOED

# Initiate an optimal design object from the calibrated model
# Number of experiments which will be designed is 5
M1rOED = RobustOED(M1conf, 5)

# Set the experimental design ranges for S
M1rOED.set_independent_distributions([ModPar('S', 5., 100.0, 'randomUniform')])

# Set the parameter ranges for both Km and Vmax
M1rOED.set_parameter_distributions([ModPar('Km', 1., 25.0, 'randomUniform'),
```

```
                                                ModPar('Vmax', 0.05, 0.5, 'randomUniform')])

# Calculate the robust optimal experimental design
M1rOED.maximin()
```

The final command yields the following robust optimal experimental design.

```
array([   5.,   5.,   5.,  100.,  100. ])
```

BIBLIOGRAPHY

Al-Haque, N., Santacoloma, P. A., Neto, W., Tufvesson, P., Gani, R., and Woodley, J. M. (2012). A robust methodology for kinetic model parameter estimation for biocatalytic reactions. *Biotechnol Prog*, 28(5):1186–1196.

Aris, R. (1956). On the Dispersion of a Solute in a Fluid Flowing through a Tube. *P Roy Soc A Math Phy*, 235(1200):67–77.

Asano, Y., Togashi, S., Tsudome, H., and Marukami, S. (2010). Microreactor Technology: Innovations in Production Processes. *Pharm Eng*, 30(1).

Asprey, S. and Macchietto, S. (2002). Designing robust optimal dynamic experiments. *J Process Contr*, 12(4):545–556.

Atherton, R. W., Schainker, R. B., and Ducot, E. R. (1975). On the statistical sensitivity analysis of models for chemical kinetics. *AIChE J*, 21(3):441–448.

Bates, D. M. and Watts, D. G. (1980). Relative Curvature Measures of Nonlinearity. *J Roy Stat Soc B Met*, 42(1):1–25.

Bates, D. M. and Watts, D. G. (1988). Curvature Measures of Nonlinearity. In *Nonlinear Regression Analysis and Its Applications*, Wiley Series in Probability and Statistics, pages 232–263. John Wiley & Sons, Inc., Hoboken, NJ, USA.

Bauer, I., Bock, H. G., Körkel, S., and Schlöder, J. P. (2000). Numerical methods for optimum experimental design in DAE systems. *J Comput Appl Math*, 120(12):1–25.

Beale, E. M. L. (1960). Confidence Regions in Non-Linear Estimation. *J Roy Stat Soc B Met*, 22(1):41–88.

Benabbas, L., Asprey, S. P., and Macchietto, S. (2005). Curvature-Based Methods for Designing Optimally Informative Experiments in Multiresponse Nonlinear Dynamic Situations. *Ind Eng Chem Res*, 44(18):7120–7131.

Bodla, V. K., Seerup, R., Krühne, U., Woodley, J. M., and Gernaey, K. V. (2013). Microreactors and CFD as Tools for Biocatalysis Reactor Design: A case study. *Chem Eng Technol*, 36(6):1017–1026.

Breuer, M., Ditrich, K., Habicher, T., Hauer, B., Keßeler, M., Stürmer, R., and Zelinski, T. (2004). Industrielle Verfahren zur Herstellung von optisch aktiven Zwischenprodukten. *Angew Chem*, 116(7):806–843.

Briggs, G. E. and Haldane, J. B. (1925). A Note on the Kinetics of Enzyme Action. *Biochem J*, 19(2):338–339.

Brik Ternbach, M., Bollman, C., Wandrey, C., and Takors, R. (2005). Application of model discriminating experimental design for modeling and development of a fermentative fed-batch L-valine production process. *Biotechnol Bioeng*, 91(3):356–68.

Brun, R., Reichert, P., and Kfinsch, H. R. (2001). Practical identifiability analysis of large environmental simulation. *Water Resour Res*, 37(4):1015–1030.

Çengel, Y. A., Turner, R. H., and Cimbala, J. M. (2008). *Fundamentals of Thermal-Fluid Sciences*. McGraw-Hill, New York, NY 10020, 3 edition.

Chaplin, M. F. and Bucke, C. (1990). *Enzyme Technology*. Cambridge University Press.

Chen, B. H., Hibbert, E. G., Dalby, P. A., and Woodley, J. M. (2008). A new approach to bioconversion reaction kinetic parameter identification. *AIChE J*, 54(8):2155–2163.

Chirico, G., Beretta, S., and Baldini, G. (1999). Conformation of interacting lysozyme by polarized and depolarized light scattering. *J Chem Phys*, 110(4):2297.

Chis, O.-T., Banga, J. R., and Balsa-Canto, E. (2011). Structural identifiability of systems biology models: a critical comparison of methods. *PloS one*, 6(11):e27755.

Constable, D. J. C., Dunn, P. J., Hayler, J. D., Humphrey, G. R., Leazer, Jr., J. L., Linderman, R. J., Lorenz, K., Manley, J., Pearlman, B. A., Wells, A., Zaks, A., and Zhang, T. Y. (2007). Key green chemistry research areasa perspective from pharmaceutical manufacturers. *Green Chem*, 9(5):411–420.

Cornish-Bowden, A. (2004). *Fundamentals of Enzyme Kinetics*. Portland Press Ltd., London, 3 edition.

D'Agostino, R. and Pearson, E. S. (1973). Tests for Departure from Normality. *Biometrika*, 60(3):613.

D'Agostino, R. B. (1971). An omnibus test of normality for moderate and large size samples. *Biometrika*, 58(2):341–348.

Datta, S. and Ghosal, S. (2009). Characterizing dispersion in microfluidic channels. *Lab Chip*, 9(17):2537–50.

De Pauw, D. (2005). *Optimal Experimental Design for calibration of bioprocess models: a validated software toolbox.* PhD thesis, Ghent University, Belgium.

De Pauw, D. J. and Vanrolleghem, P. A. (2006a). Practical aspects of sensitivity function approximation for dynamic models. *Math Comp Model Dyn*, 12(5):395–414.

De Pauw, D. J. W. and Vanrolleghem, P. A. (2006b). Designing and performing experiments for model calibration using an automated iterative procedure. *Water Sci Technol*, 53(1):117–127.

Dixon, M. (1953). The determination of enzyme inhibitor constants. *Biochem J*, 55(1):170–1.

Dochain, D. and Vanrolleghem, P. (2001). *Dynamical Modelling and Estimation in Wastewater Treatment Processes.* IWA Publishing, London, UK.

Docherty, P. D., Chase, J. G., Lotz, T. F., and Desaive, T. (2011). A graphical method for practical and informative identifiability analyses of physiological models: a case study of insulin kinetics and sensitivity. *Biomed Eng OnLine*, 10(39).

Donaldson, J. R. and Schnabel, R. B. (1987). Computational Experience with Confidence Regions and Confidence Intervals for Nonlinear Least Squares. *Technometrics*, 29(1):67–82.

Donckels, B. M. (2009). *Optimal Experimental Design to discriminate among rival dynamic mathematical models.* PhD thesis, Ghent University.

Dowd, J. E. and Riggs, D. S. (1965). A Comparison of Estimates of Michaelis-Menten Kinetic Constants from Various Linear Transformations. *J Biol Chem*, 240(2):863–869.

Dunn, P. J. (2012). The importance of Green Chemistry in Process Research and Development. *Chem Soc Rev*, 41(4):1452–1461.

Eadie, G. S. (1942). The Inhibition of Cholinesterase by Physostigmine and Prostigmine. *J Biol Chem*, 146(1):85–93.

Ehgartner, J., Sulzer, P., Burger, T., Kasjanow, A., Bouwes, D., Krühne, U., Klimant, I., and Mayr, T. (2016). Online analysis of oxygen inside silicon-glass microreactors with integrated optical sensors. *Sensors Actuat B-Chem*, 228:748–757.

Einstein, A. (1956). *Investigations on the Theory of the Brownian Movement.* Dover Publ., Mineola, NY, 1 edition.

Eisenthal, R. and Cornish-Bowden, A. (1974). The direct linear plot. A new graphical procedure for estimating enzyme kinetic parameters. *Biochem J*, 139(3):715–20.

Fedorov, V. V. and Hackl, P. (1997). Convex Design Theory. In *Model-Oriented Design of Experiments*, Lecture Notes in Statistics, page 125. Springer New York, New York, NY.

Fersht, A. (1985). *Enzyme Structure and Mechanism.* W.F. Freeman, New York, second edition.

Fortmann-Roe, S. (2012). Accurately Measuring Model Prediction Error.

Franceschini, G. and Macchietto, S. (2007). Validation of a Model for Biodiesel Production through Model-Based Experiment Design. *Ind Eng Chem Res*, 46(1):220–232.

Franceschini, G. and Macchietto, S. (2008). Novel anticorrelation criteria for model-based experiment design: Theory and formulations. *AIChE J*, 54(4):1009–1024.

Freitas, R. A. J. (2003). *Nanomedicine, Volume IIA: Biocompatibility.* CRC Press, 1 edition.

Frost, C. G. and Mutton, L. (2010). Heterogeneous catalytic synthesis using microreactor technology. *Green Chem*, 12(10):1687–1703.

Gad-el Hak, M. (1999). The Fluid Mechanics of MicrodevicesThe Freeman Scholar Lecture. *J Fluids Eng*, 121(1):5.

Garcia, E., Hasenbank, M. S., Finlayson, B., and Yager, P. (2007). High-throughput screening of enzyme inhibition using an inhibitor gradient generated in a microchannel. *Lab Chip*, 7(2):249–255.

Gervais, T. and Jensen, K. F. (2006). Mass transport and surface reactions in microfluidic systems. *Chem Eng Sci*, 61(4):1102–1121.

Ghislieri, D. and Turner, N. J. (2014). Biocatalytic Approaches to the Synthesis of Enantiomerically Pure Chiral Amines. *Top Catal*, 57(5):284–300.

Goujot, D., Meyer, X., and Courtois, F. (2012). Identification of a rice drying model with an improved sequential optimal design of experiments. *J Process Contr*, 22(1):95–107.

Green, A. P., Turner, N. J., and O'Reilly, E. (2014). Chiral Amine Synthesis Using omega-Transaminases: An Amine Donor that Displaces Equilibria and Enables High-Throughput Screening. *Angew Chem Int Edit*, 53(40):10714–10717.

Gschaider, B. (2010). Automatization with pyFoam.

Gustafson, S.-A. (1983). A Three-Phase Algorithm for Semi-Infinite Programs. In Fiacco, A. V. and Kortanek, K. O., editors, *Semi-Infinite Programming and Applications*, volume 215 of *Lecture Notes in Economics and Mathematical Systems*, pages 138–157. Springer Berlin Heidelberg, Berlin, Heidelberg.

Hanes, C. S. (1932). Studies on plant amylases: The effect of starch concentration upon the velocity of hydrolysis by the amylase of germinated barley. *Biochem J*, 26(5):1406–21.

Hansen, K. B., Balsells, J., Dreher, S., Hsiao, Y., Kubryk, M., Palucki, M., Rivera, N., Steinhuebel, D., Armstrong III, J. D., Askin, D., and Grabowski, E. J. J. (2005). First Generation Process for the Preparation of the DPP-IV Inhibitor Sitagliptin. *Org Process Res Dev*, 9:634–639.

Hartman, R. L., Naber, J. R., Buchwald, S. L., and Jensen, K. F. (2010). Multistep Microchemical Synthesis Enabled by Microfluidic Distillation. *Angew Chem Int Edit*, 49(5):899–903.

He, L. and Niemeyer, B. (2003). A novel correlation for protein diffusion coefficients based on molecular weight and radius of gyration. *Biotechnol. Prog.*, 19(2):544–8.

Herries, D. G. (1984). The computerized derivation of steady-state rate equations for enzyme kinetics. *Biochem J*, 223(2):551–3.

Hessel, V., Löwe, H., and Schönfeld, F. (2005). Micromixers - a review on passive and active mixing principles. *Chem Eng Sci*, 60(8):2479–2501.

Hofstee, B. H. J. (1952). On the Evaluation of the Constants Vm and Km in Enzyme Reactions. *Science*, 116(3013):329–331.

Höhne, M. and Bornscheuer, U. T. (2009). Biocatalytic Routes to Optically Active Amines. *ChemCatChem*, 1(1):42–51.

Hunter, J. D. (2007). Matplotlib: A 2D Graphics Environment. *IEEE Comput Sci Eng*, 9(3):90–95.

Hwang, B.-Y., Cho, B.-K., Yun, H., Koteshwar, K., and Kim, B.-G. (2005). Revisit of aminotransferase in the genomic era and its application to biocatalysis. *J Mol Catal B-Enzym*, 37(1-6):47–55.

Ishikawa, H., Maeda, T., Hikita, H., and Miyatake, K. (1988). The computerized derivation of rate equations for enzyme reactions on the basis of the pseudo-steady-state assumption and the rapid-equilibrium assumption. *Biochem J*, 251(1):175–81.

Jensen, K. F. (2005). Silicon-Based Microreactors. In *Microreactor Technology and Process Intensification*, pages 2–22.

Jones, E., Oliphant, T., Peterson, P., and Others (2001). SciPy: Open source scientific tools for Python. `http://www.scipy.org/`.

Karande, R., Schmid, A., and Buehler, K. (2010). Enzyme catalysis in an aqueous/organic segment flow microreactor: ways to stabilize enzyme activity. *Langmuir*, 26(11):9152–9.

Kennedy, J. and Eberhart, R. (1995). Particle swarm optimization. In *Proceedings of ICNN'95 - International Conference on Neural Networks*, volume 4, pages 1942–1948. IEEE.

Kerby, M. B., Legge, R. S., and Tripathi, A. (2006). Measurements of kinetic parameters in a microfluidic reactor. *Anal Chem*, 78(24):8273–80.

Kheirolomoom, A., Khorasheh, F., and Fazelinia, H. (2002). Influence of external mass transfer limitation on apparent kinetic parameters of penicillin G acylase immobilized on nonporous ultrafine silica particles. *J Biosci Bioeng*, 93(2):125–129.

Kleijn, C. (2012). Numerical Simulation of Flow and Chemistry in Thermal Chemical Vapor Deposition Processes. In *Chemical Physics of Thin Film Deposition Processes for Micro- and Nano-Technologies*, page 363. Springer Science & Business Media.

Kleinstreuer, C. (2003). *Two-Phase Flow: Theory And Applications.* CRC Press.

Kockmann, N. (2008). *Transport Phenomena in Micro Process Engineering*, volume 4. Springer, Berlin, Heidelberg.

Kockmann, N., Engler, M., and Woias, P. (2004). Theoretische und experimentelle Untersuchungen der Mischvorgänge in T-förmigen Mikroreactoren - Teil 3: Konvektives Mischen und chemische Reaktionen. *Chem Ing Tech*, 76(12):1777–1783.

Koo, J. and Kleinstreuer, C. (2003). Liquid flow in microchannels: experimental observations and computational analyses of microfluidics effects. *J Micromech Microeng*, 13(5):568–579.

Kremzner, L. T. and Wilson, I. B. (1964). A Partial Characterization of Acetylcholinesterase *. *Biochemistry*, 3(12):1902–1905.

Larsson, H. K., Krühne, U., Gernaey, K., and Skov, A. L. (2015). *Modelling of Mass Transfer Phenomena in Chemical and Biochemical Reactor Systems using Computational Fluid Dynamics.* PhD thesis.

Laurenti, E. and dos Santos Vianna Jr., A. (2016). Enzymatic microreactors in biocatalysis: history, features, and future perspectives. *Biocatalysis*, 1(1):148–165.

Lawrence, J., O'Sullivan, B., Lye, G. J., Wohlgemuth, R., and Szita, N. (2013). Microfluidic multi-input reactor for biocatalytic synthesis using transketolase. *J Mol Catal B-Enzym*, 95(100):111–117.

Lee, S. (1989). *Methanol Synthesis Technology.* CRC Press.

Lehninger, A. (1982). *Principles of Biochemistry.* Worth, New York.

Leis, J. R. and Kramer, M. A. (1988). The simultaneous solution and sensitivity analysis of systems described by ordinary differential equations. *ACM T Math Software*, 14(1):45–60.

Levenspiel, O. (1972). *Chemical reaction engineering.*

Li, B. Q. (2006). *Discontinuous Finite Elements in Fluid Dynamics and Heat Transfer.* Elsevier.

Lineweaver, H. and Burk, D. (1934). The Determination of Enzyme Dissociation Constants. *J Am Chem Soc*, 56(3):658–666.

Ljung, L. (1999). *System identification - Theory for the User.* Prentice-Hall, 2 edition.

Loffler, D. G. and Schmidt, L. D. (1975). Catalytic activity and selectivity on heterogeneous surfaces with mass transfer. *AIChE J*, 21(4):786–791.

Łyskowski, A., Gruber, C., Steinkellner, G., Schürmann, M., Schwab, H., Gruber, K., and Steiner, K. (2014). Crystal Structure of an (R)-Selective ω-Transaminase from Aspergillus terreus. *PLoS ONE*, 9(1):e87350.

Marques, M. P. C. and Fernandes, P. (2011). Microfluidic devices: useful tools for bioprocess intensification. *Molecules*, 16(10):8368–401.

Marsili-Libelli, S., Beck, M. B., Brunner, P., Croke, B., Guillaume, J., Jakeman, A., Jakeman, J., Keesman, K. J., and Stigter, H. (2014). Practical identifiability analysis of environmental models.

Marsili-Libelli, S., Guerrizio, S., and Checchi, N. (2003). Confidence regions of estimated parameters for ecological systems. *Ecol Model*, 165(2-3):127–146.

Maruyama, T., Uchida, J.-i., Ohkawa, T., Futami, T., Katayama, K., Nishizawa, K.-i., Sotowa, K.-i., Kubota, F., Kamiya, N., and Goto, M. (2003). Enzymatic degradation of p-chlorophenol in a two-phase flow microchannel system. *Lab Chip*, 3(4):308–12.

McKinney, W. (2010). Data Structures for Statistical Computing in Python. In *Proceedings of the 9th Python in Science Conference*, pages 51–56.

McMullen, J. P. and Jensen, K. F. (2011). Rapid Determination of Reaction Kinetics with an Automated Microfluidic System. *Org Process Res Dev*, 15(2):398–407.

Miložič, N., Lubej, M., Novak, U., Žnidaršič-Plazl, P., and Plazl, I. (2014). Evaluation of Diffusion Coefficient Determination using a Microfluidic Device. *Chem Biochem Eng Q*, 28(2):215–223.

Moser, A. (2012). *Bioprocess technology: kinetics and reactors.* Springer Science & Business Media.

Mozharov, S., Nordon, A., Littlejohn, D., Wiles, C., Watts, P., Dallin, P., and Girkin, J. M. (2011). Improved method for kinetic studies in microreactors using flow manipulation and noninvasive Raman spectrometry. *J Am Chem Soc*, 133(10):3601–3608.

Nagaki, A., Kenmoku, A., Moriwaki, Y., Hayashi, A., and Yoshida, J.-i. (2010). Cross-coupling in a flow microreactor: space integration of lithiation and Murahashi coupling. *Angew Chem Int Edit*, 49(41):7543–7.

Nagaki, A., Moriwaki, Y., Haraki, S., Kenmoku, A., Takabayashi, N., Hayashi, A., and Yoshida, J.-I. (2012a). Cross-coupling of aryllithiums with aryl and vinyl halides in flow microreactors. *Chemistry, an Asian journal*, 7(5):1061–8.

Nagaki, A., Takabayashi, N., Moriwaki, Y., and Yoshida, J.-i. (2012b). Flash generation of a highly reactive Pd catalyst for Suzuki-Miyaura coupling by using a flow microreactor. *Chemistry*, 18(38):11871–5.

Nagy, K. D., Shen, B., Jamison, T. F., and Jensen, K. F. (2012). Mixing and dispersion in small-scale flow systems. *Org Process Res Dev*, 16(5):976–981.

Nelder, J. A. and Mead, R. (1965). A simplex method for function minimization. *Comput J*, 7(4):308–313.

Novak, U., Pohar, A., Plazl, I., and Žnidaršič-Plazl, P. (2012). Ionic liquid-based aqueous two-phase extraction within a microchannel system. *Sep Purif Technol*, 97:172–178.

Nugent, T. C. and El-Shazly, M. (2010). Chiral Amine Synthesis - Recent Developments and Trends for Enamide Reduction, Reductive Amination, and Imine Reduction. *Advanced Synthesis & Catalysis*, 352(5):753–819.

Omlin, M. and Reichert, P. (1999). A comparison of techniques for the estimation of model prediction uncertainty. *Ecol Model*, 115(1):45–59.

OpenFOAM (2014). OpenFOAM® - The Open Source Computational Fluid Dynamics (CFD) Toolbox.

O'Sullivan, B., Al-Bahrani, H., Lawrence, J., Campos, M., Cázares, A., Baganz, F., Wohlgemuth, R., Hailes, H. C., and Szita, N. (2012). Modular microfluidic reactor and inline filtration system for the biocatalytic synthesis of chiral metabolites. *J Mol Catal B-Enzym*, 77:1–8.

Pereira Rosinha, I., Woodley, J., Gernaey, K., and Krühne, U. (2015). *Shape and topology optimization of enzymatic microreactors*. PhD thesis.

Pérez, F. and Granger, B. E. (2007). IPython: A System for Interactive Scientific Computing. *IEEE Comput Sci Eng*, 9(3):21–29.

Petersen, B. (2000). *Calibration, Identifiability and Optimal Experimental Design of Activated Sludge Models*. PhD thesis, Ghent University, Belgium.

Plumb, K. (2005). Continuous Processing in the Pharmaceutical Industry. *Chem Eng Res Des*, 83(6):730–738.

Pohar, A., Plazl, I., and Žnidaršič-Plazl, P. (2009). Lipase-catalyzed synthesis of isoamyl acetate in an ionic liquid/n-heptane two-phase system at the microreactor scale. *Lab Chip*, 9(23):3385–90.

Poli, R. (2008). Analysis of the Publications on the Applications of Particle Swarm Optimisation. *J Artif Evol Appl*, 2008:1–10.

Presečki, A. V. and Vasić-Rački, . (2009). Mathematical modelling of the dehydrogenase catalyzed hexanol oxidation with coenzyme regeneration by NADH oxidase. *Process Biochem*, 44(1):54–61.

Press, W., Teukolsky, S., Vetterling, W., and Flannery, B. (1992). *Numerical Recipes in C: the art of scientific computing.* Cambridge University Press, Cambridge, UK, 2 edition.

Pronzato, L. and Walter, E. (1988). Robust experiment design via maximin optimization. *Math Biosci*, 89(2):161–176.

Radulescu, O., Gorban, A. N., Zinovyev, A., and Noel, V. (2012). Reduction of dynamical biochemical reactions networks in computational biology. *Front Genet*, 3:131.

Ranaldi, F., Vanni, P., and Giachetti, E. (1999). What students must know about the determination of enzyme kinetic parameters. *Biochem Educ*, 27(2):87–91.

Rao, S., Schaft, A. V. D., Eunen, K. V., Bakker, B. M., and Jayawardhana, B. (2014). A model reduction method for biochemical reaction networks. *BMC Syst Biol*, 8(52):1–17.

Riedlinger, A., Kretschmer, J., and Möller, K. (2015). On the practical identifiability of a two-parameter model of pulmonary gas exchange. *Biomed Eng OnLine*, 14:1–15.

Ristenpart, W. D. and Stone, H. a. (2012). Michaelis-Menten kinetics in shear flow: Similarity solutions for multi-step reactions. *Biomicrofluidics*, 6(1):14108/1–14108/9.

Ristenpart, W. D., Wan, J., and Stone, H. a. (2008). Enzymatic reactions in microfluidic devices: Michaelis-Menten kinetics. *Anal Chem*, 80(9):3270–6.

Roberge, D. M., Ducry, L., Bieler, N., Cretton, P., and Zimmermann, B. (2005). Microreactor Technology: A Revolution for the Fine Chemical and Pharmaceutical Industries? *Chem Eng Technol*, 28(3):318–323.

Roy, S., Raju, R., Chuang, H. F., Cruden, B. A., and Meyyappan, M. (2003). Modeling gas flow through microchannels and nanopores. *J Appl Phys*, 93(8):4870.

Sablani, S. S., Datta, A. K., Rahman, M. S., and Mujumdar, A. S. (2006). *Handbook of Food and Bioprocess Modeling Techniques.* CRC Press.

Sadana, A. (1988). Enzyme deactivation. *Biotechnol Adv*, 6(3):349–446.

Sahoo, H. R., Kralj, J. G., and Jensen, K. F. (2007). Multistep Continuous-Flow Microchemical Synthesis Involving Multiple Reactions and Separations. *Angew Chem Int Edit*, 119(30):5806–5810.

Savile, C. K., Janey, J. M., Mundorff, E. C., Moore, J. C., Tam, S., Jarvis, W. R., Colbeck, J. C., Krebber, A., Fleitz, F. J., Brands, J., Devine, P. N., Huisman,

G. W., and Hughes, G. J. (2010). Biocatalytic asymmetric synthesis of chiral amines from ketones applied to sitagliptin manufacture. *Science*, 329(5989):305–9.

Schätzle, S., Steffen-Munsberg, F., Thontowi, A., Höhne, M., Robins, K., and Bornscheuer, U. T. (2011). Enzymatic Asymmetric Synthesis of Enantiomerically Pure Aliphatic, Aromatic and Arylaliphatic Amines with (R)-Selective Amine Transaminases. *Adv Synth Catal*, 353(13):2439–2445.

Scott Fogler, H. (2004). *Elements of Chemical Reaction Engineering.* Pearson Education, 4 edition.

Seber, G. A. F. and Wild, C. J. (1989). *Nonlinear Regression.* John Wiley & Sons, Inc.

Segel, I. (1975). Enzyme Kinetics: Behavior and Analysis of Rapid Equilibrium and Steady-State Enzyme Systems. *John Wiley & Sons, New York*, page 957.

Segel, L. A. and Slemrod, M. (1989). The Quasi-Steady-State Assumption: A Case Study in Perturbation. *SIAM Review*, 31(3):446–477.

Sharp, K. V. (2001). *Experimental investigation of liquid and particle-laden flows in microtubes.* Phd, University of Illonois at Urbana-Champaign.

Shengwei (2011). Navier-Stokes vs lattice Boltzmann: will it change the landscape of CFD?

Shin, J. S. and Kim, B. G. (1998). Kinetic modeling of omega-transamination for enzymatic kinetic resolution of alpha-methylbenzylamine. *Biotechnol Bioeng*, 60(5):534–40.

Swarts, J. W., Kolfschoten, R. C., Jansen, M. C., Janssen, A. E., and Boom, R. M. (2010). Effect of diffusion on enzyme activity in a microreactor. *Chem Eng J*, 162(1):301–306.

Taylor, G. (1953). Dispersion of Soluble Matter in Solvent Flowing Slowly through a Tube. *P Roy Soc A Math Phy*, 219(1137):186–203.

Tholey, A. and Heinzle, E. (2002). Methods for Biocatalyst Screening. In *Tools and Applications of Biochemical Engineering Science*, pages 1–19.

Tišma, M., Zelić, B., Vasić-Rački, ., Žnidaršič-Plazl, P., and Plazl, I. (2009). Modelling of laccase-catalyzed l-DOPA oxidation in a microreactor. *Chem Eng J*, 149(1-3):383–388.

Tufvesson, P., Fu, W., Jensen, J. S., and Woodley, J. M. (2010). Process considerations for the scale-up and implementation of biocatalysis. *Food Bioprod Process*, 88(1):3–11.

Tufvesson, P., Lima-Ramos, J., Jensen, J. S., Al-Haque, N., Neto, W., and Woodley, J. M. (2011). Process considerations for the asymmetric synthesis of chiral amines using transaminases. *Biotechnol. Bioeng.*, 108(7):1479–1493.

Turner, N. J. and Truppo, M. D. (2010). Biocatalytic Routes to Nonracemic Chiral Amines. In Nugent, T. C., editor, *Chiral Amine Synthesis: Methods, Developments and Applications*, chapter 14, pages 431–459. Wiley-VCH Verlag GmbH & Co. KGaA, Weinheim, Germany.

Tušek, A., Šalić, A., Kurtanjek, Ž., and Zelić, B. (2012). Modeling and kinetic parameter estimation of alcohol dehydrogenase-catalyzed hexanol oxidation in a microreactor. *Eng Life Sci*, 12(1):49–56.

Van Daele, T., Van Hoey, S., and Nopens, I. (2015). pyIDEAS: an Open Source Python Package for Model Analysis. In *Comput Aided Chem Eng*, volume 37, pages 569–574.

Van Hoey, S. (2016). *Development and application of a framework for model structure evaluation in environmental modelling.* PhD thesis, Ghent University.

Van Sark, W. G. J. H. M., Janssen, G., De Croon, M. H. J. M., and Giling, L. J. (1990). Analytical models for growth by metal organic vapour phase epitaxy: I, II, and III. *Semicond Sci Tech*, 5(1):16–35, 36–44, 291–298.

Vanrolleghem, P., Van Daele, M., and Dochain, D. (1995). Practical identifiability of a biokinetic model of activated sludge respiration. *Water Res*, 29(11):2561–2570.

Verbruggen, S. W., Keulemans, M., van Walsem, J., Tytgat, T., Lenaerts, S., and Denys, S. (2016). CFD modeling of transient adsorption/desorption behavior in a gas phase photocatalytic fiber reactor. *Chem Eng J*, 292:42–50.

Vrentas, J. S. and Vrentas, C. M. (2013). *Diffusion and Mass Transfer.* CRC Press.

Wales, D. and Doye, J. (1998). Global Optimization by Basin-Hopping and the Lowest Energy Structures of Lennard-Jones Clusters Containing up to 110 Atoms. *J Phys Chem A*, 101:5111–116.

Walter, É. and Pronzato, L. (1997). *Identification of parametric models from experimental data.* Springer-Verlag, Heidelberg, xviii edition.

Walter, S., Malmberg, S., Schmidt, B., and Liauw, M. (2005). Mass transfer limitations in microchannel reactors. *Catal Today*, 110(1-2):15–25.

Wiles, C. and Watts, P. (2008). Continuous Flow Reactors, a Tool for the Modern Synthetic Chemist. *Eur J Org Chem*, 2008(10):1655–1671.

Wirth, T. (2013). *Microreactors in organic chemistry and catalysis.* Wiley-VCH.

Wohlgemuth, R., Plazl, I., Žnidaršič-Plazl, P., Gernaey, K. V., and Woodley, J. M. (2015). Microscale technology and biocatalytic processes: opportunities and challenges for synthesis. *Trends Biotechnol*, 33(5):302–14.

Yang, L., Shi, Y., Abolhasani, M., and Jensen, K. F. (2015). Characterization and modeling of multiphase flow in structured microreactors: a post microreactor case study. *Lab Chip*, 15(15):3232–3241.

Zimny, S., Masilamani, K., Jain, K., and Roller, S. (2013). Lattice Boltzmann Simulations on Complex Geometries. In *Sustained Simulation Performance 2013*, pages 49–62. Springer International Publishing, Cham.

Žnidaršič-Plazl, P. and Plazl, I. (2009). Modelling and experimental studies on lipase-catalyzed isoamyl acetate synthesis in a microreactor. *Process Biochem*, 44(10):1115–1121.

CURRICULUM VITAE

Contact and personal information

Name	Timothy Van Daele
Address	Leopold Scheiperslaan 60, 2950 Kapellen
Cell Phone	+32 494 63 44 97
Email	timothy.vandaele@gmail.com
Date of Birth	November 28, 1989
Place of Birth	Ekeren (Antwerp)
Nationality	Belgian

Education

2012 - 2016: PhD student, Ghent University, Belgium
PhD title: Model-based analysis as a tool for intensification of a biocatalytic process in a microreactor

2010 - 2012: MSc in Bioscience Engineering (Environmental Technology), Ghent University, Belgium.
MSc. Thesis: Model reduction in preparation for a PBM for the pharmaceutical granule drying process

2007 - 2010: BSc in Bioscience Engineering (Environmental Technology), University of Antwerp, Belgium.

Additional courses without examination

Transferable skills seminar: Getting started with High Performance Computing (Doctoral Schools, Ghent University, 2012)

Specialist Course: Introduction to Computational Fluid Dynamics (Doctoral Schools, Ghent University, 2012)

Specialist Course: Machine Learning (Ghent University, 2012)

Transferable skills seminar: Effective Scientific Communication (Doctoral Schools, Ghent University, 2013)

BIOPRO World Talent Campus, Intensive course about biotechnology manufacturing (biopro.nu) (Denmark, 2013)

Transferable skills seminar: Authentic Networking (Doctoral Schools, Ghent University, 2014)

MSc. theses supervised

2013 - 2014: Daan Van Hauwermeiren: Model-based analysis of the transaminase process

2013 - 2014: Chaïm De Mulder: Impact of intrinsic and extrinsic parameters on the oxygen kinetic parameters of ammonia and nitrite oxidizing bacteria

2014 - 2015: David Fernandes del Pozo: Effect of mass transfer limitations on enzymatic reactions in microreactors: a model-based analysis

2014 - 2015: Tom Hilderson: Identifiability analysis of the omega-transaminase model

2015 - 2016: Kyrina Denis: Microbial production of antimicrobial compounds from biorefinery sidestreams

Teaching activities

2013 - 2016: Modelling and Simulating 2: Partial differential equations in practice (Part: Introduction to Computational Fluid Dynamics with OpenFOAM)

International Conferences - Symposia

Oral presentations

1. IMTB 2015 - 3rd international conference on Implementation of Microreactor Technology in Biotechnology, Opatija, Croatia, May 10-13, 2015.

   Title: Model-based analysis of mass transfer limitations in microreactors

2. ECCE10 - 10nd European Congress of Chemical Engineering, Nice, France. September 27 - October 1, 2015.

   Title: A case study on robust optimal experimental design for model calibration of ω-transaminase

Poster presentations

1. BIOPRO World Talent Campus, Sorø, Denmark, October 21 - 26, 2013. Title: Modelling of integrated and intensified bioprocesses
2. PSE2015/ESCAPE25 - 12th Process Systems Engineering and the 25th European Symposium on Computer Aided Chemical Engineering, Copenhagen, Denmark, May 31 - June 4, 2015.
   - (a) Title: pyIDEAS: an open source Python package for model analysis
   - (b) Title: A numerical procedure for model identifiability analysis applied to enzyme kinetics
3. IMRET14 - 14th International Conference on Microreactor Technology, Beijing, China, September 12-14, 2016.

   Title: The potential of using microreactors for the enzymatic production of unstable intermediates

4. 2016 AIChE Annual Meeting, San Francisco, USA, November 13-18, 2016.

   Title: Kinetic parameter estimation including uncertainty under mass transfer limited conditions

Publications

A1

1. Mortier, S., Van Daele, T., Gernaey, K.V., De Beer, T., Nopens, I. (2013) Reduction of a single granule drying model: an essential step in preparation of a population balance model with a continuous growth term, *AIChE J*, 59(4), p1127-1138, 10.1002/aic.13907
2. Van Daele, T., Fernandes del Pozo, D., Van Hauwermeiren, D., Gernaey, K.V., Wohlgemuth, R., Nopens, I. (2016) A generic model-based methodology for quantification of mass transfer limitations in microreactors, *Chem Eng J*, 300, p193-208, doi:10.1016/j.cej.2016.04.117
3. Van Daele, T., Gernaey, K.V., Ringborg, R.H., Börner, T., Heintz, S., Van Hauwermeiren, D., Grey, C., Krühne, U., Adlercreutz, P., Nopens, I. Application of Iterative Robust Model-based Optimal Experimental Design for the Calibration of Biocatalytic Models, *in preparation*

P1

1. Van Daele, T., Van Hoey, S., Nopens, I. (2015) pyIDEAS: an open source Python package for model analysis, *Comput Aided Chem Eng*, 37, p569-574, doi:10.1016/B978-0-444-63578-5.50090-6
2. Van Daele, T., Van Hoey, S., Gernaey, K.V., Krühne, U., Nopens, I. (2015) A numerical procedure for model identifiability analysis applied to enzyme kinetics, *Comput Aided Chem Eng*, 37, p575-580, doi:10.1016/B978-0-444-63578-5.50091-8
3. Fernandes del Pozo, D., Van Daele, T., Van Hauwermeiren, D., Gernaey, K.V., Nopens, I. (2016) Quantifying the importance of flow maldistribution in numbered-up microreactors, *Comput Aided Chem Eng*, 38, p1225-1230. 10.1016/B978-0-444-63428-3.50209-5

C1

- Van Daele, T., Fernandes del Pozo, D., Van Hauwermeiren, D., Gernaey, K.V., Nopens, I. (2015) Model-based analysis of mass transfer limitations in microreactors, Implementation of Microreactor Technology in Biotechnology, 3rd International conference (IMTB2015). Opatija, Croatia.

Scientific Consulting

- Van Daele, T., Audenaert, W., Nopens, I., CFD analysis and optimisation of an ion-exchanger (2015-2016) Evides Waterbedrijf, Rotterdam, Netherlands
- Van Daele, T., Rehman, U., Audenaert, W., Nopens, I., CFD analysis of the residence time in a water tower (2016) Pidpa, Antwerp, Belgium